

DISS. ETH NO. 25040

**EARTH PRESSURES IN LANDSLIDES AND
APPLICATIONS OF FIBRE-OPTIC SENSORS IN
GEOMECHANICS**

A thesis submitted to attain the degree of
DOCTOR OF SCIENCES of ETH ZURICH
(Dr. sc. ETH Zurich)

presented by

BALZ ANDREAS FRIEDLI

MSc in Civil Engineering, ETH Zurich

born on *31.10.1986*

citizen of Lützelflüh BE

accepted on the recommendation of

Prof. Dr. Alexander Puzrin
Prof. Dr. Radoslaw Michalowski
Prof. Dr. José Andrade

2018

Abstract

This thesis is concerned with earth pressures in landslides (Part A) and applications of fibre-optic sensors in geomechanics (Part B).

Part A: In stable ground the earth pressures acting on a structure are usually calculated by the evaluation of a limit state of soil failure caused by displacements of the structure. In landslides, in contrast, the soil displaces towards the structure, which implies different loading conditions compared to the stable ground. In this thesis the special kinematic conditions of the soil in the vicinity of a structure in a landslide are investigated. It is shown that, similar to the classical earth pressure theories, also in landslides, and in particular in constrained landslides, after sufficiently large movements, a limit state of soil failure is reached which limits the earth pressures. An attempt to quantify the limit states using limit analysis is made for the cases of a structure constraining the landslide at its lower end and for buildings embedded in the sliding mass. For the former problem upper-bound limit analysis solutions are shown and for the special case of planar landslide with a weak slip surface parallel to the slope the exact solution is derived. For the latter problem the ultimate loads acting on a building in a landslide are limited by a local limit state with soil failure in the vicinity of the building which is quantified using upper-bound limit analysis and the finite-element method. For both cases limit analysis provides practically applicable closed form-solutions for the limiting earth pressures. The presented extensions of the solutions to account for important engineering phenomena, such as wall friction, soil dilation, presence of ground water, etc., and special geometrical conditions of the structures broadens their potential field of application. The solutions are discussed and compared with respect to existing solutions in the literature. The developed earth pressure solutions should provide a tool for engineers for the assessment of existing and the safe design of new structures in landslides and may contribute to future design practice of retaining structures and buildings in landslides.

Part B: Any object touching the ground applies contact forces to the ground surface. These contact forces induce stresses in the subsurface that in turn lead to a deformation of the ground. Measuring such ground deformations enables the detection and possibly identification of objects on the ground surface, opening up several possible applications, such as perimeter security and weigh-in-motion systems. In this part a system using ground-buried distributed fibre-optic strain sensors with very high spatial and strain resolution is presented. The fibre-optic sensors are used to quantify the strain field induced by an object in contact with the ground surface. The contact interactions on the ground surface are calculated from the strain measurements using a mechanical soil model and inverse analysis algorithms similar to those used in image deblurring. The proposed system is tested in a field experiment with different applied load types and magnitudes. In the field experiment highly non-linear mechanical behaviour of the soil at the very small strains caused by small surface loads (such as a pedestrian) was observed. This non-linearity is further investigated in field and laboratory experiments and the results are compared to a finite-element model applying different constitutive models. Buried fibre-optic strain sensors proved to be a suitable tool for the investigation of the mechanical soil behaviour in geotechnical boundary value problems.

Kurzfassung

Die vorliegende Arbeit behandelt in Teil A die Erddrücke welche auf Bauwerke in Rutschungen sowie in Teil B Anwendungen von faseroptischen Sensoren in der Geomechanik.

Teil A: In stabilem Gelände werden die auf eine Struktur wirkenden Erddrücke normalerweise durch die Analyse eines Bruchzustandes im Boden, welcher durch die Verschiebung der Struktur erzeugt wird, berechnet. Im Gegensatz dazu verschiebt sich in Rutschungen der Boden in Richtung der Struktur, was andere Belastungen der Struktur verursacht. In Teil A dieser Arbeit werden die besonderen kinematischen Bedingungen in der Umgebung von Strukturen in Rutschungen untersucht, was zum Schluss führt, dass auch in Rutschungen, unter der Voraussetzung hinreichend grosser Verschiebungen, ein Grenzzustand erreicht wird. Dieser Grenzzustand wird, wie in stabilem Gelände, durch einen Bruchzustandes in der Umgebung der Struktur definiert welcher die Erddrücke auf die Struktur begrenzen. Die Grenzwertbetrachtung der Plastizitätstheorie wird auf das Problem einer Struktur welche die Rutschmasse stabilisiert, sowie auf das Problem eines Gebäudes welches in der Rutschmasse, einer sich gegen unten hin verlangsamenden Rutschung, eingebettet ist angewandt. Für erstgenanntes Problem, welches im deutschen Sprachgebrauch auch unter dem Begriff ‚Kriechdruck‘ bekannt ist, werden obere Grenzwerte für den Erddruck auf eine solche stabilisierende Struktur hergeleitet. Diese Erddrücke ergeben für einen Spezialfall mit hangparalleler Gleitschicht und kohäsionslosem Boden der Rutschmasse die vollständige Lösung, was anhand von Untersuchungen an unteren Grenzwerten gezeigt wird. Beim zweitgenannten Problem werden die Erddrücke an einem Gebäude mit vereinfachter Geometrie anhand von oberen Grenzwerten hergeleitet und mit den Resultaten von Berechnungen anhand der Finite-Elemente-Methode verglichen. Für beide Problemstellungen erlaubt die Grenzwertbetrachtung der Plastizitätstheorie die Herleitung von praktisch anwendbaren geschlossenen Lösungen für die Erddrücke welche im Grenzzustand wirken. Die Lösungen werden erweitert um von den vereinfachenden Annahmen abweichende Randbedingungen, wie zum Beispiel Wandreibung, Dilatanz des Bodens im Bruch, die Anwesenheit von Hangwasser sowie besondere Geometrie der Struktur oder der Rutschung, zu berücksichtigen. Die resultierenden Erddrücke in Rutschungen werden auch anhand von Vergleichen mit anderen Lösungsansätzen in der Literatur diskutiert. Die aufgezeigten Lösungen stellen ein Werkzeug für den mit der Bemessung von Strukturen in Rutschungen beauftragten Ingenieur dar und sie könnten in Zukunft sowohl für die Überprüfung von bestehenden als auch für die Dimensionierung von neuen Bauwerken in Rutschungen benützt werden.

Teil B: Zwischen einem Objekt und der Bodenoberfläche bestehen Kontaktkräfte welche mit einem Spannungsfeld im Untergrund im Gleichgewicht sind und Deformationen des Untergrunds verursachen. Eine Messung dieser Deformationen erlaubt potentiell die Detektion sowie möglicherweise die Identifikation des Objekts an der Bodenoberfläche, was in verschiedenen praktischen Anwendungen, wie in Perimetersicherungssystemen oder dynamischen Waagen im Strassenverkehr, nutzbar wäre. In Teil B dieser Arbeit wird ein System zur Identifikation von Oberflächenlasten mittels vergrabener faseroptischen Dehnungssensoren vorgeschlagen, wobei die Lasten mit Hilfe eines mechanischen Modells des Untergrundes und numerischer

Inversrechnung, vergleichbar Bildschärfungsalgorithmen in der Photographie, aus den Dehnungsmessungen ermittelt werden. In einem Feldversuch konnte eine hohe Genauigkeit bei der Identifikation von verschiedenen Typen von Oberflächenlasten erzielt werden. Die Auswertung der experimentellen Daten zeigte zusätzlich ein stark nicht-lineares Verhalten des Bodens unter den sehr kleinen Dehnungen welche durch kleine Lasten wie Fussgänger erzeugt wurden. Dieses nicht-lineare Verhalten wurde mit weiteren Feld- sowie Laborversuchen vertieft untersucht und die Resultate der Versuche wurden mit den Ergebnissen eines numerischen Bodenmodells unter Anwendung von verschiedenen Stoffmodellen verglichen. Vergrabene faseroptische Dehnungssensoren haben sich als nützliches Werkzeug für die Untersuchung des mechanischen Bodenverhaltens in einem Geotechnischen Randwertproblem erwiesen.

Acknowledgments

I would like to thank and acknowledge all the people who supported me during my PhD. These people made this thesis a successful endeavour and the last five years a pleasant period for me.

I would like to thank Prof. Dr. Alexander Puzrin for giving me the opportunity to pursue my PhD studies in his Geomechanics group. The freedom he gave me to work on my projects and the openness towards new ideas made this thesis possible. I am grateful for all the instructive input and the believing in me.

Many thanks to Prof. Dr. Radoslaw Michalowski and Prof. Dr. José Andrade for accepting to be the co-examiners of my thesis. I highly appreciate their careful reading and their valuable comments.

Special thanks are devoted to the technical staff at IGT, Ernst Bleiker, Heinz Buschor, Andreas Kieper and René Rohr for their support in constructing experimental facilities and instrumenting them with the necessary sensors. Without them the experimental part of this thesis would not have been possible.

The foundation for the success of this thesis was the great spirit and teamwork of the Geomechanics team and I would like to express my gratitude to all the current and former team members for all the fruitful ideas and discussions: Dr. Markus Schwager, Dr. Michael Iten, Dr. Dominik Hauswirth, Dr. Pascal Minder, Frank Fischli, Dr. Rolf Zumsteg, Philipp Oberender, Andreas Stöcklin, David Perozzi, Christian Buss, Simon Hug, Marc Kohler, Roman Hettelingh, Ingrid Mettler, Dr. Carlo Rabaiotti, Dr. Andreas Trabesinger, Dr. Pavel Trapper, Dr. Alessandra Carrera, and Dr. Michael Plötze. Further I would like to thank Luca Pizzetti, Simon Vogler, Martin Kilchsperger, Manuel Stocker, Johannes Schindler, Kallivokas Gerasimos and Athanasios Kontis who all contributed during their student works.

I am deeply grateful to my parents Cornelia and Fritz for always supporting me. None of my achievements would have been possible without their love and care.

My biggest gratitude belongs to my wonderful wife Tamara and my daughter Lisa. You were always by my side and motivated me when my spirit was down. Without you, none of this would have been possible.

Content

Abstract	I
Kurzfassung.....	II
Acknowledgments.....	IV
Content.....	V
1 Introduction.....	1
1.1 Rationale of the thesis.....	1
1.2 Structure of the thesis.....	5
1.3 References	7
PART A: EARTH PRESSURES IN LANDSLIDES	
2 Introduction to limit analysis.....	11
2.1 Concepts and assumptions	12
2.2 Lower-bound theorem	15
2.3 Upper-bound theorem	15
2.4 Notation	17
2.5 References	17
3 Lateral earth pressures in constrained landslides	18
3.1 Abstract	18
3.2 Introduction.....	19
3.3 Problem formulation	22
3.4 Limit analysis solutions.....	23
3.5 The exact solution	29
3.6 Extension of the solution to more general cases	31
3.7 Comparison with existing solutions	35
3.8 Examples.....	37
3.9 Conclusions	40
3.10 Appendix 3-1: Influence of the flow rule	41
3.11 Appendix 3-2: Influence of groundwater.....	43
3.12 Appendix 3-3: Variable thickness of the sliding layer	47
3.13 Appendix 3-4: Comparison of different solutions for passive earth pressures.....	48
3.14 Acknowledgment	48
3.15 Notation	48
3.16 References	50

4	Selected applications of the landslide pressure	52
4.1	Abstract	52
4.2	Arbitrary inclination and strength of the slip surface	53
4.3	Not fully mobilised slip surface close to the structure	59
4.4	Fixed structure not fully embedded in the sliding layer	62
4.5	Conclusions	65
4.6	Notation	66
4.7	References	66
5	Ultimate loads on buildings in landslides.....	67
5.1	Abstract	67
5.2	Introduction.....	68
5.3	Problem formulation	69
5.4	Upper-bound limit analysis	70
5.5	Finite element model	79
5.6	Results.....	80
5.7	Conclusions	87
5.8	Appendix 5-1: Discrete velocity step	89
5.9	Appendix 5-2: Hodographs and weights	89
5.10	Appendix 5-3: Plastic strain magnitude increment plots	92
5.11	Acknowledgment	92
5.12	Notation	93
5.13	References	94
PART B: APPLICATIONS OF FIBRE-OPTIC SENSORS IN GEOMECHANICS		
6	Ground-buried fibre-optic sensors for object identification.....	96
6.1	Abstract	96
6.2	Introduction.....	97
6.3	Experimental setup.....	98
6.4	Inverse Analysis	99
6.5	Results.....	103
6.6	Discussion and conclusions	104
6.7	Appendix 6-1: Description of the fibre-optic sensors.....	106
6.8	Appendix 6-2: Details of the experimental facility	107
6.9	Appendix 6-3: Elastic half space loaded on its free surface.....	108
6.10	Appendix 6-4: Optimisation of the regularisation parameters	110
6.11	Appendix 6-5: Aggregation of loads	112
6.12	Appendix 6-6: Accounting for soil non-linearity	114
6.13	Acknowledgment	116
6.14	Notation	116
6.15	References	117

7	Small strain nonlinearity in Boussinesq’s problem – fibre-optic strain measurements and numerical modelling	119
7.1	Abstract	119
7.2	Introduction	120
7.3	Experiment	121
7.4	Triaxial Tests	125
7.5	Modelling	128
7.6	Model responses in the Boussinesq problem	135
7.7	Conclusions	144
7.8	Appendix 7-1: Details on the triaxial test samples	145
7.9	Appendix 7-2: Grading of the soil	145
7.10	Appendix 7-3: Parameters of the constitutive models	146
7.11	Appendix 7-4: Validation of the finite element solution	147
7.12	Acknowledgment	147
7.13	Notation	148
7.14	References	149
8	Conclusions and outlook.....	151
8.1	Part A: Earth pressures in landslides	151
8.2	Part B: Applications of fibre-optic sensors in Geomechanics.....	154
8.3	References	156
	Curriculum Vitae	157

1 Introduction

The thesis consists of two parts, where part A is concerned with earth pressures in landslides and part B with applications of fibre-optic strain sensors in geomechanics. The introduction is split into these two parts.

1.1 Rationale of the thesis

1.1.1 Part A: Earth pressures in landslides

Landslides are a common geohazard in mountainous areas, endangering a large number of communities and built infrastructure. In Switzerland, for example, more than six percent of the area is prone to slope instability (Lateltin et al. 2005). Infrastructure, like roads or railways, in the mountains often have to cross permanently moving landslides or areas which are prone to slope instability and therefore require retaining structures (*e.g.*, retaining walls). These retaining structures are interacting with the landslide and are in fact stabilizing the moving soil mass, which controls the loads acting on these structures.

In slowly permanently moving landslides, in the literature sometimes referred to as ‘creeping’ (*e.g.*, Puzrin & Schmid 2011; Oberender and Puzrin 2016), the sliding of the soil mass often takes place in narrow zones with reduced strength (Bernander & Olofsson 1981) and the overlaying soil is moving downslope almost intact. This almost intact moving soil mass allowed construction activities in mountainous communities to spread into such unstable areas. Many buildings are embedded within the moving soil mass and at first sight it is not obvious that the movement of the landslide alter the loads acting. However, many buildings in landslides, and in particular in the compression zone of constrained landslides (a landslide moving towards an obstacle at the bottom), exhibit significant damage (*e.g.*, Alexander 1986; Glade et al. 2005; Alonso et al. 2010; Mansour et al. 2011; Cascini et al. 2013), potentially caused by landslide induced loads, which were underestimated in the design of these buildings.

For the assessment of existing and the design of new structures it is important to quantitatively evaluate the potential loads acting on a retaining structure or a building in a landslide. To capture the complex soil structure interaction and the full loading history requires a detailed model of the landslide and the structure which is subjected to many uncertainties. In particular the initial conditions in the sliding body prior to any construction, which control the velocity of the movement and the initial stress field as well as the mostly staged construction are difficult to capture accurately in a soil-structure interaction model. To perform such a complex modelling for every construction in a landslide seems to be an excessive demand and would require a vast amount of high quality data (such as detailed geometry of the landslide, stiffness and strength parameters of the soil, displacements of the landslide).

As a first step towards the solution of this problem the loads acting on structures in landslides (that is, the earth pressures) are investigated similarly to the classical earth pressure theories in

stable ground at the limit state of soil failure. Earth pressures in landslides have usually been calculated using the classical earth pressure theories for stable ground (*e.g.*, Coulomb 1776; Rankine 1857; Müller-Breslau 1906; Caquot & Kérisel 1948; Sokolovskii 1960; Chen 1975; Lancellotta 2002). These theories do, however, not hold for structures in landslides.

In contrast to stable ground, where the retaining structure moves either away from the soil (active case) or towards the soil (passive case) in the landslide case the soil moves towards the retaining structure (Figure 1-1). Based on observations of snow avalanche barriers Haefeli (1944) first realised, that this special kinematic condition has to be taken into account for the evaluation of the earth pressures in landslides. Haefeli developed a limit equilibrium solution which was also used by Brandl and Dalmatiner (1988), can be found in text books (*e.g.*, Brandl 1987, 2001) and is widely used in engineering practice. The solutions is, however, based on some oversimplifying assumptions which led a several authors to seek for alternatives (for example Puzrin & Sterba 2006; Muraro et al. 2015). For a closely related problem of a planar snow or soil sheet under extension or compression (Ziegler 1963; Kupper 1967; Szcypinski 1972) presented rigorous solutions based on limit analysis approaches. The review of the literature has shown that although a number of approaches exist, a need for a rigorous solution of the landslide pressure against a retaining structure exists.

The problem of a building embedded in a permanently moving landslide is closely related to the landslide pressure problem. The difference in stiffness and weight between the building and the landslide disturb the displacement field of the landslide and lead to stress changes within the sliding body which eventually may reach a limit state with failure of the soil in the vicinity of the building or failure of the building. To the author's knowledge no rigorous approach exists to assess this limit state which would provide the ultimate landslide-induced loads acting on the building.

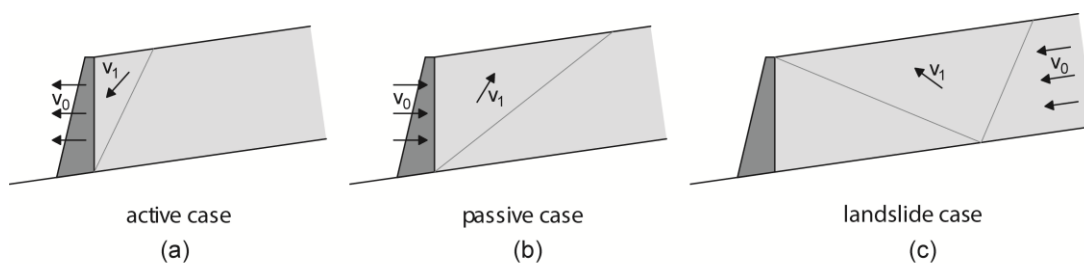


Figure 1-1. Kinematics of different limiting earth pressure situations: (a) active, (b) passive and (c) the landslide case.

1.1.2 Main objectives of part A

The main objectives of this part A are:

- The quantification of the earth pressures acting in a constrained landslide and on the constraining structure (*e.g.*, a rock outcrop or a retaining wall) using limit analysis of plasticity theory.
- The investigation of the limit states in the vicinity of a building embedded in the compression zone of a constrained landslide and quantification of the ultimate loads acting.

In general, the goal of the presented investigation is to provide better understanding of the earth pressures in landslides. The developed earth pressure solutions should provide a tool for engineers for the assessment of existing and the safe design of new structures in landslides. The concepts used to determine the earth pressures in landslides may also be applied to cases with other displacement fields (not only structures in the compression zone of constrained landslides) in future research and practice. Further, the derived solutions may contribute to codes and regulations of retaining structures and buildings in landslides.

1.1.3 Part B: Applications of fibre-optic sensors in geomechanics

Fibre-optic cables are usually used for means of communication. Specialised measurement systems, however, allow the measurement of strain and temperature continuously or distributed along such cables and the whole length of the fibre can be used as a sensor. The first measurement technologies were discovered almost 40 years ago based on Brillouin Optical Time Domain Analysis (BOTDA, Horiguchi et al. (1989)). Since then the techniques have been improved significantly and distributed strain and temperature measurement systems have become commercially available. The most promising technology for geotechnical research on small to middle scales is represented by the swept wavelength interferometry (SWI) to measure Rayleigh scattering (Froggatt & Moore 1998; Froggatt et al. 2006; Gifford et al. 2007). While other technologies enable sensor lengths of tens of kilometres with relatively sparse spatial resolution, SWI is restricted to sensor lengths of some tens of meters but with an unprecedented spatial resolution of a few millimetres and strain resolution of down to ($\sim 1\mu\epsilon$). For dynamic applications SWI with high-temporal-frequency measurements (up to 250 Hz) is already commercially available for sensor lengths smaller than tens of meters (Luna 2013).

At the Geomechanics group of the Institute for Geotechnical Engineering at ETH Zurich fibre-optic sensors (FOSs) have been a research topic for over a decade. Two PhD theses have been devoted to the use of FOSs in geotechnical applications (Iten 2011; Hauswirth 2015). In particular the emplacement of FOSs directly in the soil for geotechnical monitoring was investigated. For this purpose a set of special cables and micro-anchors were developed and tested (*e.g.*, Hauswirth et al. 2010). The cables were applied to the monitoring of landslides, tunnels and anchors (*e.g.*, Iten & Puzrin 2009a, b, 2010; Iten et al. 2009). Since then, FOSs have already been applied successfully in many geotechnical projects in practice for the monitoring of foundations, piles, retaining walls, etc.

In one of the applications of FOSs assessing the ground surface displacements during tunnelling (Hauswirth et al. 2014) distinct measurable strains were detected from pedestrians walking over the ground-buried FOSs in a Park in London. To avoid measurement errors the ground surface above the FOSs was blocked for pedestrians during the measurements. The finding, however, led to the idea of using ground-buried FOSs for the detection and identification of objects at the ground surface. Part B of this thesis deals with the development of such a system, the corresponding inverse analysis and its experimental testing.

The use of FOSs for intrusion-detection systems is not entirely new. (Taylor & Lee 1993) used optical time domain reflectometry and used the frequency shifts induced in the reflected light upon stressing the fibre to detect an intruder passing the buried FOSs. This idea was further improved with different, more quantitative fibre optic interrogating systems (*e.g.*, Kwon et al. 2002; Park & Taylor 2003; Juarez et al. 2005; Kirkendall et al. 2007; Juarez & Taylor 2007; Nikles 2009; Hong et al. 2010; Owen et al. 2012). In a next step towards not only detecting but identifying the intruder the ‘signature’ of specific events was extracted and compared to predefined libraries of signals (Madsen et al. 2007, 2008; Wu et al. 2015).

The system proposed in part B of this thesis is, in contrast to existing intrusion detection systems, based on a mechanical inverse analysis of the contact forces induced by an object moving on the ground surface. The inverse analysis uses a mechanical model of the ground (elastic half space

loaded on its free surface (*e.g.*, Boussinesq 1885)) and algorithms similar to those used in image restoration. The concept of such an object identification system was filed in a patent application (Puzrin et al. 2013).

The nonlinear behaviour of the soil at very small strains revealed in the experimental study of the proposed object identification system is well-known in the field of geomechanics as small-strain nonlinearity (*e.g.*, Burland 1989). This nonlinearity has been extensively investigated on element tests, for example in triaxial tests (Jardine et al. 1984), resonant column tests (*e.g.*, Hardin & Drnevich 1972; Bellotti et al. 1996) and bender element tests (*e.g.*, Dyvik & Madshus 1986) in the laboratory and by means of shear wave velocity measurements in the field (*e.g.*, Stokoe & Woods 1972; Woods 1978). The influence of the small-strain nonlinearity on the behaviour of geotechnical boundary value problems was shown, for example, by Burland & Hancock (1977) and Burland et al. (1979) for the settlements next to deep excavations and tunnels Addenbrooke et al. (1997).

The ground-buried FOSs enable a direct measurement of the nonlinear soil response to increasing strains and therefore represent a tool for interesting insights into the soil behaviour at very small strains in geotechnical boundary value problems.

1.1.4 Main objectives of part B

The main objectives of part B are:

- Development of a system for surface object identification using ground-buried FOSs, including the layout of the FOSs in a shallow trench, the mechanical inverse analysis of the surface loads from the measured strains along the FOSs and the experimental proof-of-concept of the system.
- Investigation of the small-strain-nonlinearity at very small strains in a Boussinesq problem (half space loaded by a surface load) using FOSs. Constitutive modelling of the small-strain behaviour and investigation of the effect of the constitutive behaviour on the response in the Boussinesq problem.

The presented developments in Part B should enable the application of FOSs in a system for surface object identification using FOSs. Additionally the investigations of the small-strain nonlinearity should provide new insights into the behaviour of soils in geotechnical boundary value problems which may be beneficial the assessment of deformations in future geotechnical projects.

1.2 Structure of the thesis

The thesis is structured in two parts:

- Part A: Earth pressures in landslides
- Part B: Applications of fibre-optic sensors in geomechanics

Part A is subdivided into four chapters. In chapter 2 an introduction to limit analysis is provided in order to give the necessary basics for the further derivations shown in chapters 3, 4 and 5. The most important concepts and assumptions of limit analysis are restated briefly.

Chapter 3 deals with the landslide pressure; that is, the earth pressure acting within a constrained landslide and on the constraining obstacle. The landslide pressure is investigated using limit analysis of plasticity theory. A generally applicable upper-bound solution is presented and compared to the lower-bound solution for the special case of a slope parallel slip surface. It is shown that for this special case the exact solution can be found. Further, the limit analysis solutions are extended to account for more general boundary conditions. The solutions are compared to existing approximate solutions from the literature and the applicability is shown and discussed in two practical examples.

In chapter 4 selected applications of the landslide pressure with special boundary conditions not considered in chapter 3 are presented. The solution is extended to arbitrary inclination and strength of the weak slip surface and the potential not fully mobilised slip surface in the vicinity of a retaining structure is discussed. Finally, a structure not fully embedded in the sliding layer of a landslide is investigated and the landslide pressures are quantified and discussed.

In chapter 5 the ultimate loads acting on buildings in landslides are investigated by means of limit analysis and the finite element method (FEM). A generally applicable approach for the assessment of the landslide induced loads, based on the investigation of a local limit state in the vicinity of the building, is presented. This approach is applied to buildings embedded in the sliding soil mass of a constrained landslide. Based on the FEM analyses it is shown that first a local limit state forms in the vicinity of the building followed by a global limit state which resembles the limit state presented in chapter 2. The influence of geometry, weight, and strength of the soil and the building are shown and potential implications on the assessment of existing and the design of new buildings are discussed.

Part B is subdivided into two chapters. Chapter 6 shows an application of ground-buried fibre-optic sensors (FOSs) for object identification. A system for the detection and identification of objects at the ground surface is proposed. The system uses FOSs buried in a shallow trench in the ground. Any object moving at the surface induces contact forces which deform the ground. These deformations are measured with FOSs using swept wavelength interferometry (SWI) to measure the Rayleigh scattering (Froggatt et al. 2006; Gifford et al. 2007). A framework for such a system is established, based on inversely calculating the contact forces acting on the surface from the FOS measurements. The approach for the inverse analysis, which is based on a mechanical model and inverse analysis algorithms similar to those used in image deblurring are presented. An experimental study is described where different static load patterns are identified and the results of the experiment are discussed.

The experiments shown in chapter 6 revealed strongly nonlinear soil behaviour at the very small strains caused by small surface loads (<1 kN). In chapter 7 the experimental investigation of this nonlinearity is presented. An approach to model the experiment using nonlinear hyper-elastic constitutive models implemented into the finite element computing environment ABAQUS (Simulia, Dassault Systèmes, Providence, RI). As independent experimental data on the soil behavior triaxial tests with local strain measurements to capture the small strain nonlinearity are presented. The model results are compared to the experiment and discussed. Particular emphasis is put on the volumetric behavior of the soil at very small strains.

In chapter 8 the main findings are summarised and ideas for potential future research is highlighted.

1.3 References

- Addenbrooke, T.I., Potts, D.M., & Puzrin, A.M. (1997) The influence of pre-failure soil stiffness on the numerical analysis of tunnel construction. *Géotechnique*, **47**, No. 3, 693–712.
- Alexander, D. (1986). Landslide damage to buildings. *Environmental Geology and Water Sciences* **8**, No. 3, 147–151.
- Alonso, E., Pinyol, N. & Puzrin, A.M. (2010) *Geomechanics of Failures – Advanced Topics*, Chapter 1: A Constrained Creeping Landslide: Brattas-St. Moritz Landslide, Switzerland, 3-33, Springer Business & Media, Dordrecht, Heidelberg, London, New York.
- Bellotti, R., Jamiolkowski, M., Lo Presti, D.C.F., & O’Neill, D.A. (1996) Anisotropy of small strain stiffness in Ticino sand. *Géotechnique*, **46**, No. 1, 115–131.
- Bernander, S. & Olofsson, I. (1981). On Formation of Progressive Failures in Slopes. In *Proceedings of the 10th international conference on soil mechanics and foundation engineering*, Stockholm, Sweden, vol. 3, 357–362, Rotterdam, the Netherlands: Balkema.
- Boussinesq, J.V. (1885) *Application des potentiels à l’étude de l’équilibre et du mouvement des solides élastiques*. Gauthiers-Villars, Paris.
- Brandl H. (1987) Retaining Walls and Other Restraining Structures. In *Ground Engineer’s Reference Book* (Bell FG (ed.)). Butterworths, London, Ch. 47, pp. 1–34.
- Brandl H. (2001) Stützbauwerke und konstruktive Hangsicherungen. In *Grundbau-Taschenbuch, Teil. 3 Gründungen*, 6. Edition. (Smolczyk U (ed.)). Ernst & Sohn, pp. 495–651.
- Brandl H. & Dalmatiner J. (1988) *Brunnenfundierungen von Bauwerken in Hängen (insbesondere Brücken)*. Schriftenreihe Strassenforschung des Bundesministeriums für wirtschaftliche Angelegenheiten. Wien, Heft 352, Vienna, Austria.
- Burland, J.B., & Hancock, R.J.R. (1977) Underground Car Park at the House of Commons, London: Geotechnical Aspects. *The Structural Engineer*, **55**, No. 2, 87–100.
- Burland, J.B., Simpson B. & St. John H.D. (1979) Movements around excavations in London Clay. In *Proceedings of the 7th European Conference on Soil Mechanics and Foundation Engineering*, Volume 1. 13–29, Brighton, UK.
- Burland, J.B. (1989) Ninth Laurits Bjerrum Memorial Lecture: ‘Small is beautiful’-the stiffness of soils at small strains. *Canadian Geotechnical Journal*, **26**, No. 4, 499–516.
- Caquot A. & Kérisel J. (1948) *Tableau de poussée et butée et de force portante des fondation*. Gauthiers-Villars, Paris, France.
- Cascini, L., Peduto, D., Pisciotta, G., Arena, L., Ferlisi, S. & Fornaro, G. (2013). The combination of DInSAR and facility damage data for the updating of slow-moving landslide inventory maps at medium scale. *Natural Hazards and Earth System Sciences* **13**, No. 6, 1527–1549.
- Chen, W.-F. (1975). *Limit Analysis and Soil Plasticity*. Amsterdam, the Netherlands: Elsevier Scientific Publishing Co.
- Coulomb, C.A. (1776). Essai sur une application des règles de maximis & minimis à quelques problèmes de statique, relatifs à l’architecture. *Mémoires de Mathématique & de Physique présentés à l’Académie Royale des Sciences par Divers Savans et Lus sans ses Assemblées VII*, 343–382 (in French).

- Dyvik, R., & Madshus, C. (1985) Lab measurements of Gmax using bender elements. *Proceedings of the ASCE Convention, Advances in the Art of Testing Soils Under Cyclic Conditions*, V. Khosla, ed., American Society of Civil Engineers, Detroit, Michigan, USA, 186–196.
- Froggatt, M.E., Gifford, D.K., Kreger, S., Wolfe, M., & Soller, B.J. (2006) Characterization of Polarization-Maintaining Fibre Using High-Sensitivity Optical-Frequency-Domain Reflectometry. *Journal of Lightwave Technology*, OSA, **24**, No. 11, 4149–4154.
- Froggatt, M., & Moore, J. (1998) High-spatial-resolution distributed strain measurement in optical fibre with Rayleigh scatter. *Applied Optics*, **37** No. 10, 1735–1740.
- Gifford, D.K., Froggatt, M.E., Wolfe, M.S., Kreger, S.T., Sang, A.K., & Soller, B. J. (2007) Millimeter Resolution Optical Reflectometry Over Up to Two Kilometers of Fibre Length. *2007 IEEE Avionics, Fibre-Optics and Photonics Technology Conference*, IEEE, Dallas, Texas, USA, 52–53.
- Glade, T., Anderson, M. & Crozier, M.J. (2005). *Landslide hazard and risk*, West Sussex, England: John Wiley & Sons Ltd.
- Haefeli, R. (1944). Zur Erd- und Kriechdruck-Theorie. *Schweizerische Bauzeitung* **124**, No. 20, 256–260 (in German).
- Hardin, B.O., & Drnevich, V.P. (1972) Shear modulus and damping in soils: Design equations and curves. *ASCE Journal of the Soil Mechanics and Foundation Engineering Division*, **98**, No. 118, 667–692.
- Hauswirth, D. (2015) *A study of the novel approaches to soil displacement monitoring using distributed fibre optic strain sensing*. Dissertation No. 22282, ETH Zurich, Switzerland.
- Hauswirth, D., Iten, M. & Puzrin, A.M. (2010) Fibre optic cable an micro-anchor pullout tests in sand, In *Proceedings of the 7th International Conference on Physical Modelling in Geotechnics (ICPMG 2010)* (eds. Springman, S., Laue, J. & Seward, L.), 337-342, Zurich, Switzerland.
- Hauswirth, D., Puzrin, A.M., Carrera, A., Standing, J.R., & Wan, M.S.P. (2014) Use of fibre-optic sensors for simple assessment of ground surface displacements during tunnelling. *Géotechnique* **64**, No 10, 837–842.
- Hong, X., Guo, H., Wu, J., Xu, K., Zuo, Y. Li, Y. & Lin, J. (2010) An intrusion detection sensor based on coherent optical time domain reflector. *Microwave and Optical Technology Letters*, **52**, No. 12, 2746–2748.
- Horiguchi, T., Kurashima, T., & Tateda, M. (1989) Tensile strain dependence of Brillouin frequency shift in silica optical fibers. *IEEE Photonics Technology Letters* **1**, No 5, 107–108.
- Iten, M., (2011) *Novel Applications of Distributed Fibre-optic Sensing in Geotechnical Engineering*. Dissertation No. 19632, ETH Zurich, Switzerland.
- Iten, M., & Puzrin, A.M. (2009a) BOTDA road-embedded strain sensing system for landslide boundary localization. In *Proceedings of the SPIE 7293, Smart Sensor Phenomena, Technology, Networks, and Systems 2009*. Paper No. 729316.

- Iten M, Puzrin A.M., Hauswirth, D., Foaleng-Mafang, S., Beugnot, J.-C. & Thévenaz, L., (2009b) Study of a progressive failure in soil using BEDS. *20th International Conference on Optical Fibre Sensors* (eds. Jones, J., Culshaw, B., Ecke, W., Lopez-Higuera, J.M., & Willsch, R.), Proceedings of SPIE Vol. 7503, Paper No. 75037S.
- Iten, M, & Puzrin, A.M., (2010) Monitoring of stress distribution along a ground anchor using BOTDA. In *Proceedings of the SPIE 7647, Sensors and Smart Structures Technologies for Civil, Mechanical, and Aerospace Systems 2010*. (eds. Tomizuka, M., Yun, C.B., Giurgiutiu, V., Lynch, J.P.), Paper No. 76472J.
- Iten, M., Schmid, A., Hauswirth, D., & Puzrin, A.M. (2009) Defining and monitoring of landslide boundaries using fiber optic systems. *International Symposium on Prediction and Simulation Methods for Geohazard Mitigation (ISO-Kyoto 2009)*, 451-456, Kyoto, Japan.
- Jardine, R.J., Symes, M.J., & Burland, J.B. (1984) The Measurement of soil stiffness in the triaxial apparatus. *Géotechnique* **34**, No 3, 323–340.
- Juarez, J.C., Maier, E.W. & Taylor, H.F., (2005) Distributed fibre-optic intrusion sensor system. *Journal of Lightwave Technology*, **23**, No. 6, 2081–2087.
- Juarez, J.C. & Taylor, H.F. (2007) Field test of a distributed fibre-optic intrusion sensor system for long perimeters. *Applied optics*, **46**, No. 11, 1968–1971.
- Kirkendall, C.K., Bartolo, R., Salzano, J. & Daley, K. (2007) Distributed Fibre Optic Sensing for Homeland Security. *Naval Research Laboratory Review*, 195–196.
- Kupper, W. (1967) Der plastische Grenzzustand in der schiefen ebenen Erd- oder Schneeschicht. *Zeitschrift für angewandte Mathematik und Physik ZAMP* **18**, No 5, 705-736.
- Kwon, I.-B., Baik, S.-J., Im, K., & Yu, J.-W. (2002) Development of fibre optic BOTDA sensor for intrusion detection. *Sensors and Actuators A: Physical*, **101**, No. 1–2, 77–84.
- Lancellotta R. (2002) Analytical solution of passive earth pressure. *Géotechnique* **52**, No 8, 617–619.
- Lateltin, O., Haemmig, C., Raetzo, H. & Bonnard, C. (2005). Landslide risk management in Switzerland. *Landslides* **2**, No. 4, 313–320.
- Luna Inc. (2012) *Optical backscatter reflectometer Model 4600, user guide 6*, OBR 4600, Luna Technologies, Blacksburg, Virginia, USA.
- Madsen, C., Bae, T. & Atkins, R. (2007) Long Fibre-optic Perimeter Sensor: Signature Analysis. *Conference on Lasers and Electro-Optics/Quantum Electronics and Laser Science Conference and Photonic Applications Systems Technologies, OSA*, paper PWA5 Baltimore, Maryland, USA.
- Madsen, C.K., Snider, T., Atkins, R. & Simcik, J. (2008) Real-time processing of a phase-sensitive distributed fibre optic perimeter sensor. In *Proc. SPIE 6943, Sensors, and Command, Control, Communications, and Intelligence (C3I) Technologies for Homeland Security and Homeland Defense VII* (eds. Carapezza, E.M.), Paper No. 694310.
- Mansour, M. F., Morgenstern, N. R. & Martin, C. D. (2011). Expected damage from displacement of slow-moving slides. *Landslides* **8**, No. 1, 117–131.
- Müller-Breslau, H.F.B. (1906). *Erddruck auf Stützmauern*. Stuttgart, Germany: Alfred Körner Verlag (in German).

- Muraro S., Madaschi A. & Gajo A. (2015) Passive soil pressure on sloping ground and design of retaining structures for slope stabilisation. *Géotechnique* **65**, No 6, 507–516.
- Nikles, M. (2009) Long-distance fibre optic sensing solutions for pipeline leakage, intrusion, and ground movement detection. In *Proc. SPIE 7316, Fibre Optic Sensors and Applications VI*. (eds. Udd, E., Du, H.H. & Wang, A.) International Society for Optics and Photonics.
- Oberender P.W. & Puzrin A.M. (2016) Observation-guided constitutive modelling for creeping landslides. *Géotechnique* **66**, No 3, 232–247.
- Owen, A., Duckworth, G. & Worsley, J. (2012) OptaSense: Fibre Optic Distributed Acoustic Sensing for Border Monitoring. In *2012 European Intelligence and Security Informatics Conference*. IEEE, Odense, Denmark, 362–364.
- Park, J. & Taylor, H.F. (2003) Fibre Optic Intrusion Sensor using Coherent Optical Time Domain Reflectometer. *Japanese Journal of Applied Physics*, IOP Publishing, **42**, No. 6, 3481–3482.
- Puzrin, A.M., Friedli, B. & Hauswirth, D. (2013). *Fibre optic based intrusion sensing system*. European Patent Application, Patent No. EP 2987151 A1.
- Puzrin A.M. & Schmid A. (2011) Progressive failure of a constrained creeping landslide. *Proceedings of the Royal Society A: Mathematical, Physical and Engineering Sciences* **467**, No 2133, 2444–2461.
- Puzrin A.M. & Sterba I. (2006) Inverse long-term stability analysis of a constrained landslide. *Géotechnique* **56**, No 7, 483–489.
- Rankine W.J.M. (1857) On the Stability of Loose Earth. *Philosophical Transactions of the Royal Society of London* **147**, 9–27.
- Sokolovskii V.V. (1960) *Statics of soil media*. Butterworths Scientific Publications, London, UK.
- Stokoe, K.H. & Woods, R.D. (1972) In Situ Shear Wave Velocity by Cross-Hole Method. *Journal of the Soil Mechanics and Foundations Division*, ASCE, **98**, No. 5, 443–460.
- Szcepiniski W. (1972) On the motion of flat landslides and avalanches treated as a problem in plasticity. *Archives of Mechanics* **24**, No 5-6, 919-930.
- Taylor, H.F. & Lee, C.E. (1993) *Apparatus and method for fibre optic intrusion sensing*. US Patent, Patent No. US5194847 A.
- Woods, R.D. (1978) Measurement of dynamic soil properties. *Proceedings of the ASCE Geotechnical Engineering Division Specialty Conference – Earthquake Engineering and Soil Dynamics*, Pasadena, California, USA, 91–78.
- Wu, H., Qian, Y., Zhang, W., Hanyu, L. & Xie, X. (2015) Intelligent detection and identification in fibre-optical perimeter intrusion monitoring system based on the FBG sensor network. *Photonic Sensors*, **5**, No. 4, 365–375.
- Ziegler H. (1963). Methoden der Plastizitätstheorie in der Schneemechanik. *Zeitschrift für angewandte Mathematik und Physik ZAMP*, **14**, No 6, 713-737.

PART A: EARTH PRESSURES IN LANDSLIDES

2 Introduction to limit analysis

When a mechanical system is loaded it first exhibits elastic deformations. These deformations are reversible, meaning that in a closed loading unloading cycle the deformation returns to its initial state. If the loads are increased further some irreversible deformations may occur but further loading is still possible. After a certain load is reached the deformations increase without any additional loading (meaning that no elastic deformation occurs anymore). At this point the *collapse state* of the system is reached. The collapse is often studied using the simplifying concept of perfect plasticity.

Historically, in geotechnics the *limit equilibrium method* was applied to investigate the collapse state of stability problems (such as earth pressures, slope stability, bearing capacity, etc.). In this method potential slip lines are presumed and the overall equilibrium of force resultants acting on the slip lines is solved. Additionally the failure criterion in terms of forces is satisfied on the slip lines. In cases which are not statically determinate (that is, all the resultant forces can be calculated from the equilibrium conditions) additional assumptions on the stress distributions along the slip lines have to be made. The limit equilibrium method does not fulfil equilibrium of stresses everywhere nor does it satisfy the failure criterion in the body considered. It therefore represents an approximate method to determine the collapse state of a mechanical system, which, however, is simple to apply to numerous problems in geotechnics and is widely applied for practical problems.

A valid solution of a continuum mechanics system has to fulfil the *stress equilibrium* equations, the *compatibility* equations on the strain and displacements as well as the *constitutive law* which connects stresses and strains. Finding such solutions analytically is, however, a difficult task for general problems, which nowadays is often done using numerical methods (*e.g.*, finite-element method, finite difference method, etc.). For problems concerned only with collapse load of a mechanical system (assuming perfect plasticity, which reduces the complexity of the constitutive law significantly) *limit analysis* provides a powerful tool which enables rigorous statements and is relatively simple to apply also for very complex boundary conditions. In limit analysis the exact solution of the collapse state is bracketed by lower-bounds, which satisfy only the stress equilibrium and the constitutive law (at failure), and upper-bounds, which satisfy only the compatibility and the constitutive law (at failure). If the lower- and upper-bounds are equal the exact solution of the collapse state is found.

Subsequently the most important concepts and assumptions of limit analysis are restated briefly. This chapter is not meant to discuss completely all the aspects of limit analysis and for more details it is referred to (*e.g.*, Hill 1950; Drucker et al. 1952; Chen 1975).

2.1 Concepts and assumptions

2.1.1 Perfect plasticity

The mechanical behaviour of soil is very complex. Before failure occurs it usually shows changes in stiffness of orders of magnitude which additionally depend on the confining stress. The failure stress of soil is generally also stress dependent and the evolution of post-failure strains can be accompanied by a decrease of the resistance, usually called strain-softening behaviour. Capturing all these phenomena of soil behaviour is already difficult on the level of element tests (*e.g.*, triaxial tests, oedometer tests, etc.) but even more on the level of geotechnical boundary value problems and the necessary soil parameters are usually not available in practice.

In many engineering problems the collapse state of a system is of interest and the design ensures a reasonable safety margin against this state. It is therefore convenient to use the concept of perfect plasticity. With this concept at the failure state which is defined by the failure criterion

$$f(\sigma_{ij}) = 0 \quad (2-1)$$

the strain rate is purely plastic

$$\dot{\epsilon}_{ij} = \dot{\epsilon}_{ij}^p \quad (2-2)$$

and the elastic strain rates vanish ($\dot{\epsilon}_{ij}^e = 0$). When the collapse (that is, the limit load) of the whole system is reached no additional loading is possible and all stresses remain constant. Therefore the system deforms under constant surface tractions and body forces acting on the system.

2.1.2 Failure criterion

The failure criterion $f(\sigma_{ij}) = 0$ defines the stress state at which plastic flow can occur. Within the failure criterion (that is, at stress states for which $f < 0$) elastic strain rates occur. Stress states for which $f > 0$ are not possible (Figure 2-1 (a)). Further, it is assumed that the failure criterion is convex. This property of the failure surface is important for the derivation of the limit theorems shown later.

The shear resistance of soils usually depends on the compressive stress. Although many different formulations of failure criteria exist the *Mohr-Coulomb criterion* (Figure 2-1 (b)) initially proposed by Coulomb (1776) and extended for general stress states by Mohr (1906) provides a good fit for soils (*e.g.*, Bishop 1966) and follows a clear concept. The shear resistance is divided into a stress dependent frictional part, and a constant cohesive part. In terms of the shear resistance on a failure plane the criterion reads

$$f = \sigma_n \tan \varphi' + c' - \tau_r = 0 \quad (2-3)$$

where τ_r is the shear resistance, σ_n is the normal stress acting on the failure plane, φ' is the angle of internal friction of the soil and c' is the cohesion of the soil. For the special case of $\varphi' = 0$ the criterion matches the *Tresca failure criterion* which is used for simplified undrained analyses.

The generalisation of the criterion to principal stresses is expressed as

$$f = (\sigma_1 + \sigma_3) \sin \varphi' + 2c' \cos \varphi' - (\sigma_1 - \sigma_3) = 0 \quad (2-4)$$

Where σ_1 and σ_3 are the largest and the smallest principal stresses, respectively, the criterion is independent on the intermediate principal stress σ_2 . The criterion represents, based on all the combinations of principal stresses, six planes in the principal stress space which form together a pyramid with irregular hexagonal base.

2.1.3 Associated flow rule

As at perfectly plastic failure the plastic strains develop without any stress change it is, unlike in elasticity, not possible to define a unique relation between strain and stress. With the concept of the flow rule the vector of the plastic strain rate is defined by a potential surface p except for its magnitude which depends on a positive multiplier $\lambda > 0$.

$$\dot{\varepsilon}_{ij}^p = \lambda \frac{\partial p}{\partial \sigma_{ij}} \quad (2-5)$$

In limit analysis the concept of associated plastic flow is used where the potential surface is equal to the failure surface. Therefore, the plastic strain rates are defined by the plastic multiplier and the derivative of the failure surface (Figure 2-1 (a)).

$$\dot{\varepsilon}_{ij}^p = \lambda \frac{\partial f}{\partial \sigma_{ij}} \quad (2-6)$$

The plastic flow of soils is in general not associated. The associativity is, however, an important assumption for the derivation of the limit analysis theorems.

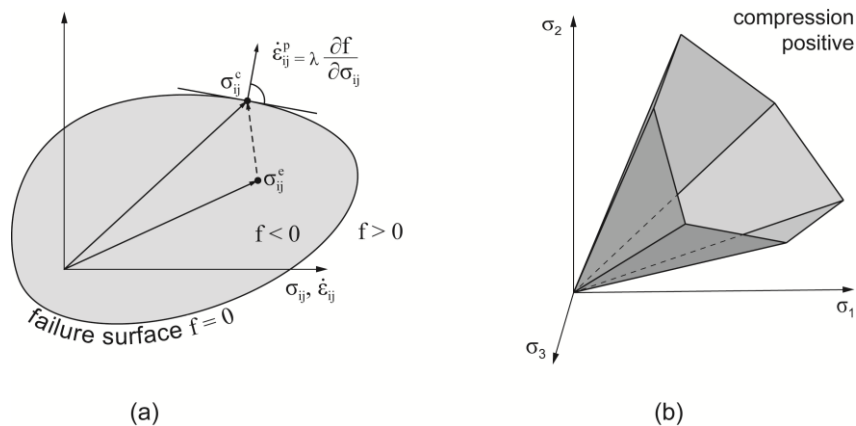


Figure 2-1. (a) Generic failure surface and associated flow (modified from Chen (1975)); (b) Mohr-Coulomb failure surface in the principal stress space.

2.1.4 Virtual work and the principle of maximum dissipation

Assuming *small changes in geometry* at the instant of the collapse allows applying the virtual work equation. The virtual work equation evaluates the work rates of the equilibrium set and a compatibility set. The equilibrium set comprises the tractions T_i on the surface of the body A , the body forces F_i acting within the volume of the body V , and the stress σ_{ij} within the body. The compatibility set comprises the virtual (therefore denoted with an asterisk) displacement rates \dot{u}_i^* and the virtual strain $\dot{\varepsilon}_{ij}^*$.

$$\int_A T_i \dot{u}_i^* dA + \int_V F_i \dot{u}_i^* dV = \int_V \sigma_{ij} \dot{\varepsilon}_{ij}^* dV \quad (2-7)$$

The strain rate on the right hand side of equation (2-7) is composed of elastic and plastic strain rates.

$$\dot{\varepsilon}_{ij} = \dot{\varepsilon}_{ij}^e + \dot{\varepsilon}_{ij}^p \quad (2-8)$$

At the collapse state the elastic strain rates vanish and the right hand side of equation (2-7) corresponds to the plastic dissipation in the body. As no energy can be produced in the system the dissipation is always positive.

$$\dot{D}_i = \int_V \sigma_{ij} \dot{\varepsilon}_{ij}^p dV = \int_V \sigma_{ij} \lambda \frac{\partial f}{\partial \sigma_{ij}} dV \geq 0 \quad (2-9)$$

Note that for purely frictional material (using the Mohr-Coulomb failure surface (2-4) with $c' = 0$ and associated flow) the resultant stress vector on a failure plane and the corresponding plastic strain increment vector are orthogonal. Therefore in this special case the dissipation is zero.

Considering a stress point within the failure surface σ_{ij}^e (i.e., $f(\sigma_{ij}) \leq 0$) and a stress point in the collapse state on the failure surface σ_{ij}^c it follows from the convexity of the failure surface and the associativity of the flow rule that

$$(\sigma_{ij}^c - \sigma_{ij}^e) \dot{\varepsilon}_{ij}^p \geq 0 \quad (2-10)$$

This is resulting from the fact that the maximum angle between the vectors $(\sigma_{ij}^c - \sigma_{ij}^e)$ and $\dot{\varepsilon}_{ij}^p$ cannot be larger than $\pi/2$, which is the case for example on a 'flat' section of the failure surface. The equation can be rewritten as

$$\sigma_{ij}^c \dot{\varepsilon}_{ij}^p \geq \sigma_{ij}^e \dot{\varepsilon}_{ij}^p \quad (2-11)$$

which is known as the *principle of maximum plastic dissipation*, stating that, of all possible stress states the actual collapse state requires the most plastic work.

2.2 Lower-bound theorem

Theorem: If a statically admissible stress field σ_{ij}^e (that is, a stress field fulfilling equilibrium in the body and on its boundaries which is everywhere below the failure surface $f(\sigma_{ij}^e) < 0$) can be found, collapse will not occur under the given loads (surface tractions T_i and body forces F_i). In other words, the loads corresponding to a statically admissible stress field represent a lower-bound for the loads required for the collapse.

Proof: The proof of the theorem is restated following Chen (1975) by assuming it false and showing that this leads to a contradiction. A collapse state with the loading conditions T_i^c, F_i^c and the corresponding actual collapse stress state σ_{ij}^c is considered. Assume a statically admissible stress field σ_{ij}^e which also leads to collapse. From the virtual work equation (2-7):

$$\int_A T_i^c \dot{u}_i^c dA + \int_V F_i^c \dot{u}_i^c dV = \int_V \sigma_{ij}^c \dot{\varepsilon}_{ij}^c dV \quad (2-12)$$

$$\int_A T_i^e \dot{u}_i^e dA + \int_V F_i^e \dot{u}_i^e dV = \int_V \sigma_{ij}^e \dot{\varepsilon}_{ij}^e dV$$

From the equality of the left hand sides of the two states it follows that

$$\int_V (\sigma_{ij}^c - \sigma_{ij}^e) \dot{\varepsilon}_{ij}^c dV = 0 \quad (2-13)$$

However, following equation (2-10)

$$(\sigma_{ij}^c - \sigma_{ij}^e) \dot{\varepsilon}_{ij}^c > 0 \quad (2-14)$$

has to hold and therefore equation (2-13) cannot be true (note that the integral of positive terms has to be positive). This proves the validity of the lower-bound theorem. If the stress state may also lie on the failure surface, $f(\sigma_{ij}^e) = 0$, the body may also be at the actual collapse state.

2.3 Upper-bound theorem

Theorem: If a kinematically admissible (virtual) collapse state $\dot{\varepsilon}_{ij}^{p*}, \dot{u}_i^{p*}$ (that is, a mechanism which satisfies the displacement conditions on the boundaries and the strain rate compatibility conditions within the body) can be found, collapse is in progress or has already taken place. In other words, the loads T_i, F_i determined by equating the rate of external work with the internal dissipation

$$\dot{W}_e = \dot{D}_i = \int_A T_i \dot{u}_i^{p*} dA + \int_V F_i \dot{u}_i^{p*} dV = \int_V \sigma_{ij}^* \dot{\varepsilon}_{ij}^{p*} dV \quad (2-15)$$

will be equal or higher than the actual collapse load.

Proof: The proof of the theorem is restated following Chen (1975) by assuming it false and showing that this leads to a contradiction. It is assumed that the body does not collapse under the loads determined from equation (2-15) and, according to the lower-bound theorem; a corresponding statically admissible stress field σ_{ij}^e exists. From the virtual work equation

$$\int_A T_i \dot{u}_i^{p*} dA + \int_V F_i \dot{u}_i^{p*} dV = \int_V \sigma_{ij}^e \dot{\varepsilon}_{ij}^{p*} dV \quad (2-16)$$

and equation (2-15) it follows that:

$$\int_V (\sigma_{ij}^* - \sigma_{ij}^e) \dot{\varepsilon}_{ij}^{p*} dV = 0 \quad (2-17)$$

However, following equation (2-10)

$$(\sigma_{ij}^* - \sigma_{ij}^e) \dot{\varepsilon}_{ij}^{p*} > 0 \quad (2-18)$$

has to hold and therefore equation (2-17) cannot be true (note that the integral of positive terms is positive). This proves the validity of the upper-bound theorem.

Note that every solution determined from a kinematically admissible collapse state corresponds to a limit equilibrium solution.

Further theorems of limit analysis can be derived, which are not restated here and can be found in (e.g., Drucker et al. 1952; Chen 1975).

2.4 Notation

F_i	Body forces
F_i^c	Body forces at the collapse state
A	Surface area of the body
T_i	Surface tractions
T_i^c	Surface tractions at the collapse state
V	Volume of the body
c'	Cohesion
f	Failure surface
p	Plastic potential
\dot{u}_i	Displacement rates
\dot{u}_i^*	Virtual displacement rates
$\dot{\varepsilon}_{ij}$	Strain increments
$\dot{\varepsilon}_{ij}^p$	Plastic strain increments
$\dot{\varepsilon}_{ij}^c$	(Plastic) strain increments at the collapse state
$\dot{\varepsilon}_{ij}^e$	Elastic strain increments
$\dot{\varepsilon}_{ij}^*$	Virtual strain increments
$\dot{\varepsilon}_{ij}^{p*}$	Virtual plastic strain increments
λ	Plastic multiplier (positive)
σ_{ij}	Stresses
σ_{ij}^c	Stresses at the collapse state
τ_r	Shear resistance
φ'	Angle of internal friction

2.5 References

- Bishop, A.W. (1966) The Strength of Soils as Engineering Materials. *Géotechnique* **16**, No 2, 91–130.
- Chen, W.F. (1975) *Limit Analysis and Soil Plasticity*. Elsevier Scientific Publishing Co., Amsterdam.
- Coulomb, C.A. (1776) Essai sur une application des règles de maximis & minimis à quelques problèmes de statique, relatifs à l'architecture. *Mémoires de mathématiques et de Physique présentés à l'Académie royale des sciences par divers savants, et lus dans ses assemblées* **VII**: 343-382.
- Drucker, D.C., Prager, W. & Greenberg, H.J. (1952) Extended limit design theorems for continuous media. *Quarterly of Applied Mathematics*, **9**, No 4, 381–389.
- Hill, R. (1950) *The mathematical theory of plasticity*, Clarendon Press, Oxford
- Mohr, O. (1906) *Abhandlungen aus dem Gebiete der technischen Mechanik*, Verlag von Wilhelm Ernst & Sohn, Berlin, Germany

3 Lateral earth pressures in constrained landslides

This chapter has been published as an article:

Friedli B., Hauswirth D. & Puzrin A. M., (2017) Lateral earth pressures in constrained landslides. *Géotechnique* **67**, No 10, 890-905.

Republished with permission.

3.1 Abstract

The problem of the limiting landslide pressure on an obstacle was first formulated in 1944 by Robert Haefeli of ETH Zurich, who recognised that kinematics of the problem does not allow for classical active and passive earth pressure theories to be applied. He derived an approximate solution using a limit equilibrium approach with a number of rather arbitrary assumptions and simplifications. Since then, the Haefeli solution has been widely applied for the design and analysis of landslide retaining structures. The chapter revisits this old landslide pressure problem by means of a rigorous upper and lower-bound limit analysis and derives the exact landslide pressure solution for a planar landslide with a weak slip surface parallel to the slope. Being applicable to a wide range of natural and man-made obstacles and, unlike the classical theories, not affected by the wall friction and soil dilation, the upper-bound solution is rather robust. The landslide pressures from this solution increase with the strength of the sliding layer and are significantly higher than the active but much lower than the passive earth pressures. Of even higher practical importance, however, is that due to their oversimplifying assumptions, the widely used approximate solutions appear to get close to the exact solution only over a very narrow range of slope and friction angles. It appears that for mildly inclined weak slip surfaces and high strengths of the sliding layer, analysis and design of retaining structures based on well-known approximate solutions can become dramatically unsafe.

3.2 Introduction

Landslides are a common geohazard in mountainous and alpine regions and have been studied since early times of geotechnical engineering (*e.g.*, Terzaghi 1936; Skempton 1964; Bjerrum 1967). The sliding of the soil mass often takes place along a narrow slip surface with reduced strength in which most of the shear strains are localized (*e.g.*, Bernander and Olofsson 1981). In such cases, the driving component (parallel to the slip surface) of the gravity force acting in the sliding layer is approximately in equilibrium with the shear resistance of the slip surface. The velocity of the sliding soil mass is controlled by fluctuation of the pore water pressures, rate dependent behaviour, strain hardening or softening in the sliding layer and the slip surface, etc. (*e.g.*, Oberender and Puzrin 2016). The velocities may be very small and the process of sliding can extend over decades. Some landslides have been constrained by an obstacle, either natural (a rock outcrop) or artificial (a retaining structure, designed as a mitigation measure). Puzrin and Sterba (2006) and Puzrin and Schmid (2011; 2012) showed that in such constrained landslides the pressure acting in the sliding layer increases towards the obstacle and may reach values producing failure in the sliding layer, causing significant acceleration of the sliding body.

This chapter investigates the limiting landslide pressures acting in the sliding layer and on the constraining obstacle. While the limiting pressure on the retaining structure provides crucial input for the design of retaining structures, the limiting pressure in the sliding layer is in particular important to know when the sliding layer serves as a foundation for buildings and infrastructure, as often is the case with slowly moving landslides in mountainous communities (*e.g.*, Puzrin and Schmid 2011; 2012). The failure at the bottom of the sliding layer affects kinematics of the landslide displacements both, at the location of the failure mechanism (change in the sliding direction) and upslope from it (landslide acceleration), which can be critical for the building and infrastructure performance.

Earth pressures on retaining structures are traditionally estimated as a limiting case where the surrounding soil reaches shear failure (*e.g.*, Coulomb 1776; Rankine 1857). Depending on the relative displacement between the structure and the soil, the failure takes place either in active or passive mode. Several authors refined the earth pressure theory using limit equilibrium and limit analysis, (*e.g.*, Müller-Breslau 1906; Caquot and Kérisel 1948; Sokolovskii 1960, Chen 1975; Lancellotta 2002, etc.). These earth pressure theories are widely used in engineering practice for the design of retaining structures. While for the classical kinematic conditions (wall moving away

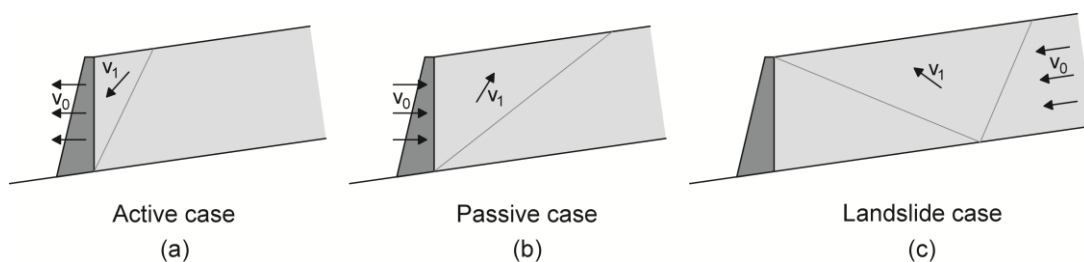


Figure 3-1. Kinematics of different limiting earth pressure situations: (a) active, (b) passive and (c) the landslide case.

or towards the soil, Figure 3-1 (a) and (b)) the calculation of the limiting earth pressures follows well-established techniques, for the special kinematic condition of a slope moving towards a fixed retaining structure or rock outcrop, derivation of the earth pressures remains a subject of ad-hoc procedures often using rather arbitrary assumptions.

Indeed, if the retaining wall were moving downslope faster than the sliding layer, the active failure could take place in the soil behind the wall. In contrast, when the sliding layer moves faster than the retaining structure, this relative movement seems to resemble the classical passive failure case. In reality, however, because the retaining structure or rock outcrop are hardly moving at all, neither of the above two cases applies and kinematic considerations (Figure 3-1 (c)) imply a special case for the earth pressure in constrained planar landslides, denoted in this chapter the ‘landslide pressure’.

Based on his observations of snow avalanche barriers, Haefeli (1944) realised that the sliding mass at the limit state flows over the barrier. He proposed a solution to calculate the landslide pressure acting on a retaining structure based on limit equilibrium and some ad-hoc assumptions (in particular, with respect to the shape of the failure wedge and inclination ϑ of the force acting on this wedge in Figure 3-2 (a)). The value of inclination ϑ has to be postulated within a range between zero and the angle of internal friction φ' , which results in a broad range of the landslide pressure coefficients (Figure 3-2 (b)). It is, therefore, hardly surprising that when Brandl & Dalmatiner (1988) compared the Haefeli solution to field observations, they fell within this range (Figure 3-2 (b)). Considered being ‘confirmed’ by Haefeli’s solution, this measured range has since been broadly used in engineering practice.

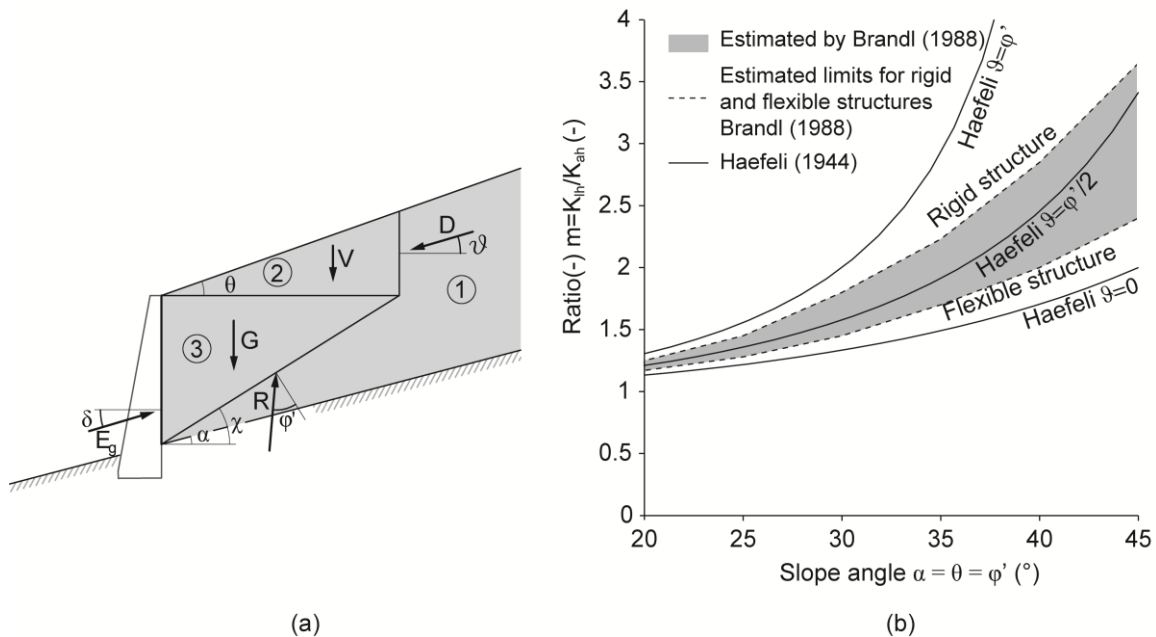


Figure 3-2. Haefeli limit equilibrium solution (a) assumed mechanism, (b) ratio of $m = K_{lh}/K_{ah}$ vs. slope angle for the special case of slope angle equal to the angle of internal friction $\alpha = \varphi'$ (K_{lh} : landslide pressure coefficient; K_{ah} : active earth pressure coefficient for a smooth wall).

In spite of the long history and rather broad application of the Haefeli solution, its arbitrary assumptions remain a subject of concern and have caused a number of authors to seek alternative approaches. For example, for the long-term stability analysis of constrained landslides Puzrin and Sterba (2006) calculated the landslide pressure using the passive case of Rankine's earth pressure theory for planar inclined ground (Rankine 1857, Chu 1991). More recently, Muraro et al. (2015) also concluded, based on numerical calculations (FEM) of the landslide pressure using one specific geometry and a limited parametric study on the effects of the soil-wall friction and soil dilatancy, that their results correspond to Rankine's passive earth pressure. For the slightly different problem of glacier flow Nye (1951) developed stress field solutions for extension and compression of the moving ice body. Ziegler (1963) and Kupper (1967) presented a rigorous analysis of the problem of a snow sheet in an avalanche or a landslide under extension or compression using the Tresca and the Mohr-Coulomb failure criterion, respectively. They found that the stress state in the moving body is limited by an active and passive state and presented analytical expressions for the limit states. Szczepinski (1972) extended their solution to non-dilatative flow and also presents an analytical solution for a landslide body in compression.

The literature dealing with limiting pressures on slope stabilizing piles has mainly focussed on the flow of cohesive soil through the piles (*e.g.*, Ito and Matsui 1975; De Beer 1977; Viggiani 1981; Randolph and Houlsby 1984; Poulos 1995; Kourkoulis et al. 2011 (FEM)) and did not address the case with a continuous wall. Besides these theoretical studies, field measurements of earth pressures in landslides have been provided by Fukuoka (1995).

The review of the literature addressing the landslide pressure acting on retaining structures has shown that although a number of different approaches exist, including rigorous solutions for a particular case, which are not well known in the field of geotechnical engineering, engineers face large uncertainties when applying these approaches to real life landslide problems. The goal of the present work is to provide a more general rigorous solution of the landslide pressure problem based on its consistent formulation within the framework of the upper-bound limit analysis. This solution will then be benchmarked against the existing exact solution for the particular case of a planar slope and its applicability will be extended to account for important engineering phenomena (such as wall friction, wall inclination, soil dilation, presence of the ground water, etc.). After comparing this solution to the approximate solutions used in the engineering practice, two practical examples will be presented.

3.3 Problem formulation

Consider a landslide (Figure 3-3) consisting of a soil layer with the surface inclination θ and the total unit weight γ sliding on a thin layer of weaker soil inclined by angle α with reduced mechanical strength properties (either the same material with residual strength, or a different material, *e.g.*, a thin layer of clay). In this chapter this weak layer is denoted ‘slip surface’. Both, the sliding layer and the slip surface materials are perfectly plastic following the Mohr-Coulomb failure criterion. The sliding layer is characterized by the cohesion c' and the friction angle φ' whereas the slip surface is assumed to be cohesionless with the friction angle of φ'_2 . Below the slip surface, the material is assumed to have a significantly higher strength. If the soil resistance on the slip surface is in equilibrium with the gravitational load of the sliding layer; that is, the friction angle of the slip surface φ'_2 is equal to its inclination α , the sliding layer can move downhill at a constant velocity. The landslide is constrained by an obstacle at the bottom, which may be natural (rock outcrop) or man-made (stabilisation structure, buildings, etc.), has the vertical height H , is inclined to the vertical by angle β and has the friction angle δ at the interface with the soil. If the resistance along the slip surface drops below the driving force, the pressure on the obstacle at the bottom will increase. This can be caused, for example, by fluctuations of the pore water pressures or due to a rate dependent material behaviour on the slip surface (particular mechanisms bringing the slope to the failure state are outside the scope of this chapter, therefore, no ground water table is introduced in the problem formulation, the influence of water is discussed later in the chapter). The constraining obstacle can be compliant or rigid, but cannot move upslope at failure. It is also assumed that the landslide is sufficiently long for the difference between the driving and resisting forces to bring the sliding layer close to the obstacle to failure.

In the considered problem two different limiting landslide pressures are of practical interest: (i) the landslide pressure in the sliding layer (for the slope stability assessment) and (ii) the landslide pressure acting on the retaining structure (for the design criteria). The case of a structure embedded within the sliding layer with no connection to the stable ground beneath the slip surface (*e.g.*, by means of piles or anchors) is outside the scope of the presented work.

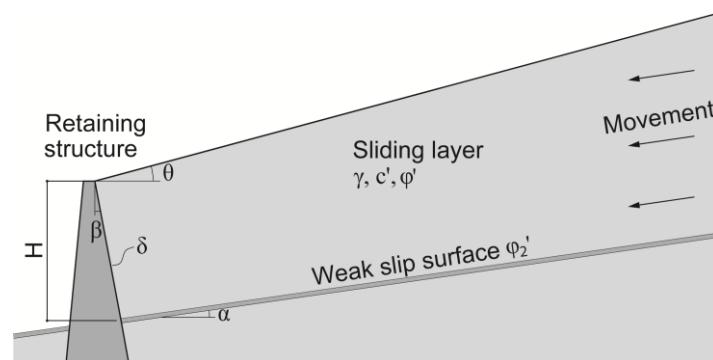


Figure 3-3. Problem formulation, retaining structure in landslide

3.4 Limit analysis solutions

3.4.1 Assumptions

Based on the following assumptions, upper and lower-bound limit analysis solutions are derived in this section, providing, in particular cases, the exact solution for the limiting landslide pressures:

- i. The landslide body is at the state of equilibrium and is moving downslope at a constant velocity (the gravitational shear stress is in equilibrium with the shear resistance: $\varphi'_2 = \alpha$).
- ii. The shear resistance φ'_2 is mobilised along the entire length of the slip surface, all the way down to the obstacle. This condition is satisfied by all compliant retaining structures and by those rigid structures, which were installed after the initial landslide movement took place.
- iii. The soil fails as a perfectly plastic Mohr-Coulomb material with the associated flow rule. Extension of the solutions to a non-associated flow rule will be made later in the chapter.

3.4.2 Upper-bound solution

In order to derive an upper-bound estimate for the landslide pressure, a *kinematically admissible failure mechanism* has to be postulated, where the velocity field satisfies the velocity boundary conditions as well as the strain and strain rate compatibility conditions. For this failure mechanism to be activated, the rate of external work has to be equal (or exceed) the rate of internal dissipation. According to the upper-bound theorem of limit analysis (*e.g.*, Chen 1975), the minimum lateral earth pressure capable of activating such a mechanism will always be larger than the true failure stress in the sliding body.

The kinematically admissible translational mechanism proposed here consists of three rigid blocks, bounded by slip discontinuities with the lengths l_1 and l_2 inclined to the slip surface by angles ω_1 and ω_2 , respectively (Figure 3-4 (a)). According to the associated flow rule, the velocity vector v_1 of Block 1 is inclined to the thin sliding surface by the friction angle φ'_2 . Therefore, in order to satisfy the equilibrium condition $\varphi'_2 = \alpha$, Block 1 has to move horizontally. Block 2 is pushed upwards with velocity v_2 , while Block 3 similarly to Block 1 moves horizontally with the velocity v_3 .

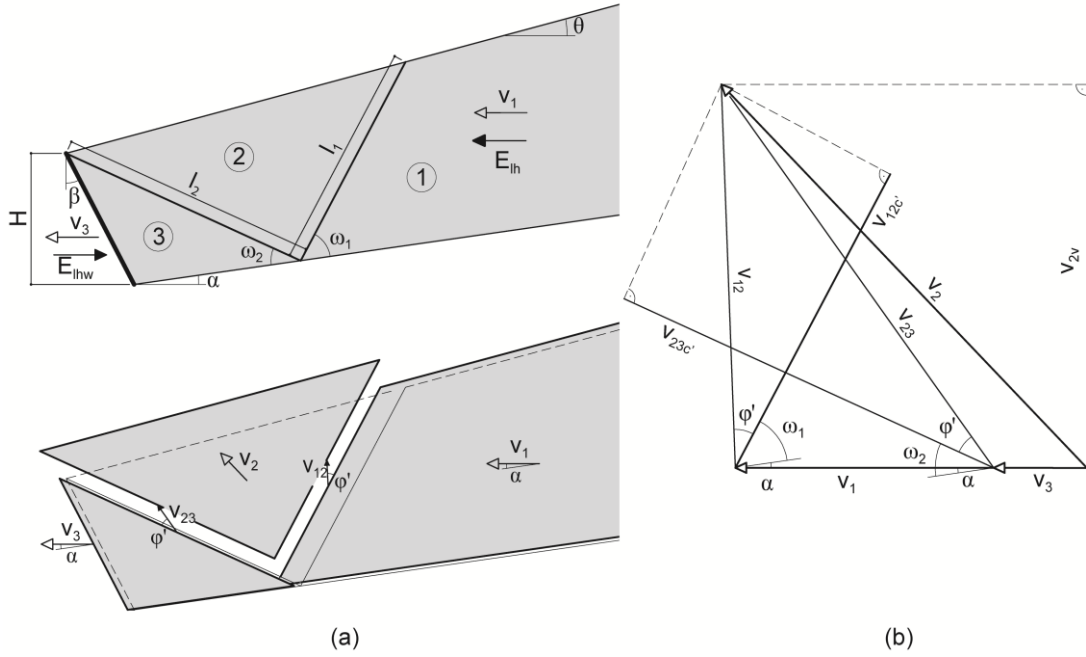


Figure 3-4. (a) Upper-bound mechanism; (b) hodograph

The relations between the velocities of Blocks 1, 2 and 3 are shown in the hodograph in Figure 3-4 (b). For the formulation of the work equation of particular interest are the vertical components v_{2v} of the velocity of Block 2, as well as the relative velocities v_{12} and v_{23} and their components $v_{12c'}$ and $v_{23c'}$ parallel to the corresponding slip discontinuities:

$$\begin{aligned}
 v_{12} &= \frac{(v_1 - v_3) \sin(\varphi' + \omega_2 - \alpha)}{\sin(2\varphi' + \omega_1 + \omega_2)} \\
 v_{23} &= \frac{(v_1 - v_3) \sin(\varphi' + \omega_1 + \alpha)}{\sin(2\varphi' + \omega_1 + \omega_2)} \\
 v_{12c'} &= \frac{(v_1 - v_3) \sin(\varphi' + \omega_2 - \alpha) \cos \varphi'}{\sin(2\varphi' + \omega_1 + \omega_2)} \\
 v_{23c'} &= \frac{(v_1 - v_3) \sin(\varphi' + \omega_1 + \alpha) \cos \varphi'}{\sin(2\varphi' + \omega_1 + \omega_2)} \\
 v_{2v} &= \frac{(v_1 - v_3) \sin(\varphi' + \omega_1 + \alpha) \sin(\varphi' + \omega_2 - \alpha)}{\sin(2\varphi' + \omega_1 + \omega_2)}
 \end{aligned} \tag{3-1}$$

The rate of external work is a sum of the work done by the three external forces - the force in the sliding layer E_{lh} , the reaction of the retaining structure E_{lhw} and the gravity force G - on the corresponding velocities of Blocks 1, 3 and 2, respectively (Figure 3-4 (a)). Note that when $\varphi'_2 = \alpha$, Blocks 1 and 3 move horizontally and the vertical components of the forces acting on these blocks do not contribute to the rate of external work \dot{W}_e , while Block 2 is the only one where the gravity contributes to the external work:

$$\dot{W}_e = v_1 E_{lh} - v_3 E_{lhw} - v_{2v} G_2 \tag{3-2}$$

with the weight of Block 2 given by:

$$G_2 = \frac{H^2 \gamma}{2} \cdot \frac{\cos^2(\alpha - \beta)}{\cos^2 \beta} \cdot \frac{\sin(\omega_2 - \alpha + \theta) \sin(\omega_1 + \omega_2)}{\sin^2 \omega_2 \sin(\omega_1 + \alpha - \theta)} \quad (3-3)$$

The rate of internal dissipation along the slip discontinuity \dot{D}_i is calculated as

$$\dot{D}_i = v_{12c'} c' l_1 + v_{23c'} c' l_2 \quad (3-4)$$

where

$$l_1 = \frac{H \cos(\alpha - \beta) \sin(\omega_2 + \theta - \alpha)}{\cos \beta \sin \omega_2 \sin(\omega_1 - \theta + \alpha)} \quad (3-5)$$

$$l_2 = \frac{H \cos(\alpha - \beta)}{\cos \beta \sin \omega_2}$$

By equating the rate of external work (3-2) and the rate of internal dissipation (3-4), the limiting force in the sliding layer E_{lh} and the corresponding force acting on the retaining structure E_{lhw} can be related depending on the two variable angles of the slip lines ω_1 and ω_2 :

$$E_{lh} - X \cdot E_{lhw} = (1 - X) \cdot f(H, \gamma, \alpha, \beta, \theta, \varphi', c', \omega_1, \omega_2) \quad (3-6)$$

where $X = v_3/v_1$ and

$$f = \frac{H^2 \gamma}{2} \cdot \frac{\cos^2(\alpha - \beta)}{\cos^2 \beta} \cdot \frac{\sin(\omega_2 - \alpha + \theta) \sin(\omega_1 + \omega_2)}{\sin^2 \omega_2 \sin(\omega_1 - \theta + \alpha)} \cdot \frac{\sin(\varphi' + \omega_1 + \alpha) \sin(\varphi' + \omega_2 - \alpha)}{\sin(2\varphi' + \omega_1 + \omega_2)} + \frac{Hc' \cos(\alpha - \beta) \cos(\varphi')}{\cos \beta \sin(2\varphi' + \omega_1 + \omega_2)} \quad (3-7)$$

$$\cdot \left(\frac{\sin(\varphi' + \omega_1 + \alpha)}{\sin \omega_2} + \frac{\sin(\varphi' + \omega_2 - \alpha) \sin(\omega_2 + \theta - \alpha)}{\sin \omega_2 \sin(\omega_1 - \theta + \alpha)} \right)$$

The presented velocity field is only valid for $0 \leq X < 1$ ($X = v_3/v_1 \geq 1$ is anyway not relevant for constrained landslides). In order to quantify both forces E_{lh} and E_{lhw} , equation (3-6) alone is not sufficient and additional considerations are required. One such consideration is that for $0 < X < 1$, that is, in the case of a compliant retaining structure with $v_3 > 0$, the shear resistance φ'_2 will be mobilised along the entire length of the slip surface, all the way down to the structure. Michalowski (1989) and later Drescher and Detournay (1993) demonstrated that if a translational kinematic mechanism forms a statically determinate problem, the limit equilibrium method applied to this mechanism should provide the same upper-bound solution as the work equation. When the shear resistance φ'_2 is mobilised along the entire length of the slip surface (that is, also below Block 3 in Figure 3-4), the kinematic mechanism becomes statically determinate and the same upper-bound landslide pressure can also be found by formulating limit equilibrium of Blocks 1, 2 and 3 (Figure 3-5). It follows that because out of all the external forces acting on the

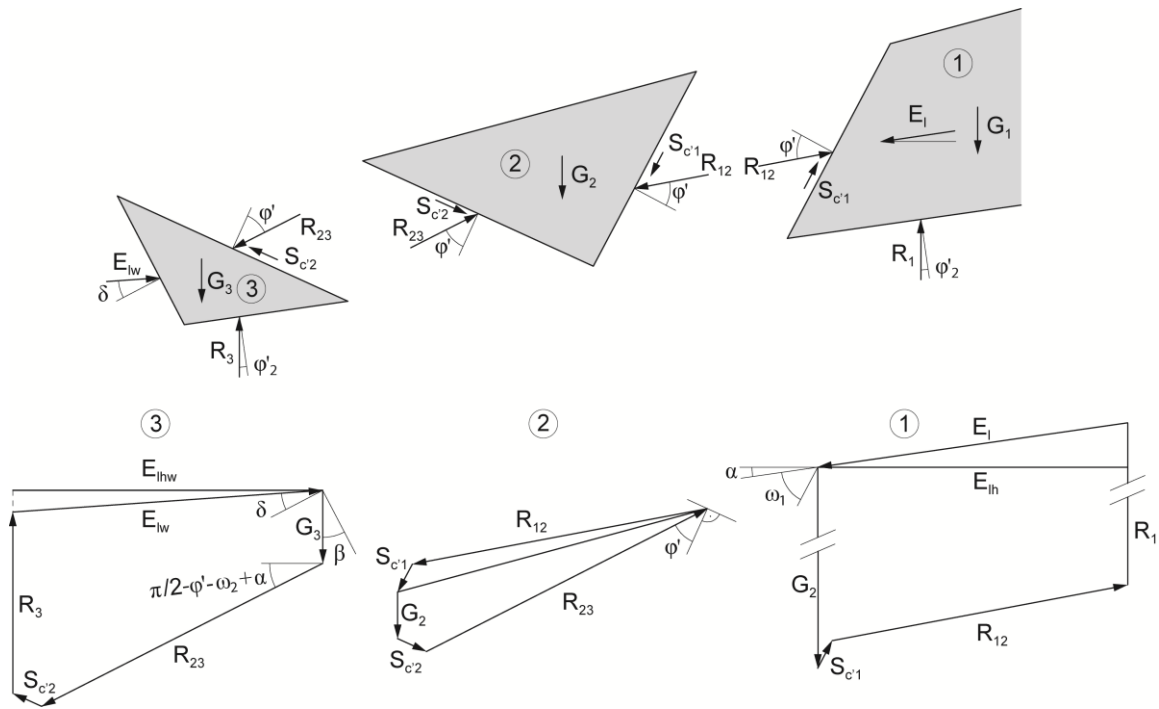


Figure 3-5. Limit Equilibrium and corresponding force polygons.

three blocks ($G_1, G_2, G_3, R_1, R_3, E_l, E_{lw}$) only the latter two have horizontal components, these two components have to be equal, $E_{lh} = E_{lhw}$, to satisfy the equilibrium conditions. When substituted into equation (3-6), this relationship gives

$$E_{lh} = E_{lhw} = f(H, \gamma, \alpha, \beta, \theta, \varphi', c', \omega_1, \omega_2) \quad (3-8)$$

that is, the upper-bounds of the horizontal components of both landslide forces are equal and independent of X for any $0 < X < 1$. Note that the horizontal component of the landslide pressure acting on the wall is independent from the wall-soil interface friction angle δ , unlike in the classical active and passive case. This results from the fact that the only external horizontal forces in the system are E_{lh} and E_{lhw} .

From the above considerations it follows that the special case of $X = 0$, which corresponds to a rigid obstacle with $v_3 = 0$, can also be described by equation (3-8), if this obstacle was installed after the landslide had moved sufficiently far to mobilize the shear resistance φ'_2 along the entire length of the slip surface. If, however, the rigid obstacle existed before the landslide moved, the slip surface resistance in its vicinity will not be mobilized and equation (3-8) can only be used for calculating the landslide force in the sliding layer E_{lh} , while the force on the obstacle $E_{lhw} > E_{lh}$ remains undetermined. The effect of the not fully mobilized resistance φ'_2 can be evaluated approximately by changing the angle of the force R_3 in Figure 3-5. This evaluation is however not within the scope of the present chapter and discussed later in chapter 4.3. While for natural rock outcrops E_{lhw} is of limited practical significance, for man-made structures it represents an

important design factor. However, the fact that they will have to withstand higher pressures than the failure pressure in the sliding layer becomes a strong argument against the use of pre-installed rigid structures as a protection measure against future landslides.

Finally, since in equation (3-2) the term $v_1 E_{lh}$ is positive, the minimum work principle requires E_{lh} to be minimized with respect to the angles ω_1 and ω_2 of the slip discontinuities and E_{lh} obtained from the work equation represents an upper-bound for the landslide force which is required to fail the landslide body in the vicinity of the obstacle. The question remains how good this upper-bound is; that is, how close it is to the exact solution.

3.4.3 Lower-bound solution

A lower-bound solution requires a *statically admissible stress field*; that is, a stress field which is in equilibrium internally, satisfies external stress boundary conditions and does not violate the failure criterion (e.g., Chen 1975). A statically admissible stress field in the present problem with arbitrary slope angle θ , slip surface angle α , inclination of the retaining structure β with frictional-cohesive material is difficult to find. Hence, only the specific case with $\alpha = \theta = \varphi'_2$, $\beta = 0$, $c' = 0$ is considered below, which corresponds to the particular case investigated by Muraro et al. (2015).

The boundary between the sliding layer and the slip surface is introduced as a static discontinuity (that is, the normal σ_n and shear stresses τ_{nt} are continuous but the tangential stress σ_t may be discontinuous). The plane strain equilibrium conditions (bearing in mind $\tau_{nt} = \tau_{tn}$) lead to:

$$\begin{aligned} \frac{\partial \sigma_t}{\partial t} + \frac{\partial \tau_{nt}}{\partial n} - \gamma \sin \alpha &= 0 \\ \frac{\partial \sigma_n}{\partial n} + \frac{\partial \tau_{nt}}{\partial t} - \gamma \cos \alpha &= 0 \end{aligned} \quad (3-9)$$

Assuming constant stresses in the sliding layer in the direction of the slip surface $\partial \tau_{nt} / \partial t = \partial \sigma_t / \partial t = 0$, integrating the equilibrium equations in the normal direction and transforming the normal coordinate $n = z \cos \alpha$ into the depth of the sliding layer z yields

$$\begin{aligned} \sigma_n &= \gamma z \cos^2 \alpha \\ \tau_{nt} &= \gamma z \sin \alpha \cos \alpha \end{aligned} \quad (3-10)$$

which satisfy the boundary condition $\tau_{nt} = \sigma_n \tan \alpha$ on the slip surface (defined by $\varphi'_2 = \alpha$). The slip surface acts as a stress discontinuity and the stress state below the slip surface has to pass the stress point (σ_n, τ_{nt}) in Figure 3-6 (b) and must not violate the failure condition.

Combined with the failure criterion for the soil in the sliding layer (Figure 3-6 (a)), equation (3-10) allows definition of the stress field from the Mohr circle shown in Figure 3-6 (b). The large circle represents the stress state in the sliding layer and the small circle represents the stress state in the slip surface. Substituting the stress state defined by equations (3-10) into the equation of the Mohr circle gives

$$(\sigma_m - \sigma_n)^2 + \tau_{nt}^2 = r^2 = \sigma_m^2 \sin^2 \varphi' \quad (3-11)$$

which can be resolved with respect to the mean stress σ_m :

$$\sigma_m = \sigma_n \frac{1 \pm \sqrt{1 - \cos^2 \varphi' (1 + \tan^2 \alpha)}}{\cos^2 \varphi'} \quad (3-12)$$

The horizontal normal stress σ_x and the corresponding shear stress τ_{xz} acting on a vertical plane are also related via the Mohr circle equation:

$$(\sigma_x - \sigma_m)^2 + \tau_{xz}^2 = r^2 = \sigma_m^2 \sin^2 \varphi' \quad (3-13)$$

Because on the slip surface $\varphi'_2 = \alpha$ and $\tau_{nt} = \sigma_n \tan \alpha$, the pole P of the Mohr circle in Figure 3-6 (b) is located on the straight line with inclination α passing through the origin, so that:

$$\tau_{xz} = \sigma_x \tan \alpha \quad (3-14)$$

that is, the force E_{lw} acting on the vertical wall has the same inclination as the slope.

Solving equation (3-13) and (3-14) results in the horizontal normal stress acting on a vertical plane

$$\sigma_x = \sigma_m \frac{1 \pm \sqrt{1 - \cos^2 \varphi' (1 + \tan^2 \alpha)}}{1 + \tan^2 \alpha} \quad (3-15)$$

where only the case with higher horizontal stress is of interest. The total force on the wall is found by substituting the mean stress from equation (3-12) into (3-15) and integrating this stress over the thickness of the sliding layer. A lower-bound for the landslide pressure coefficient K_{lhw} is then given by

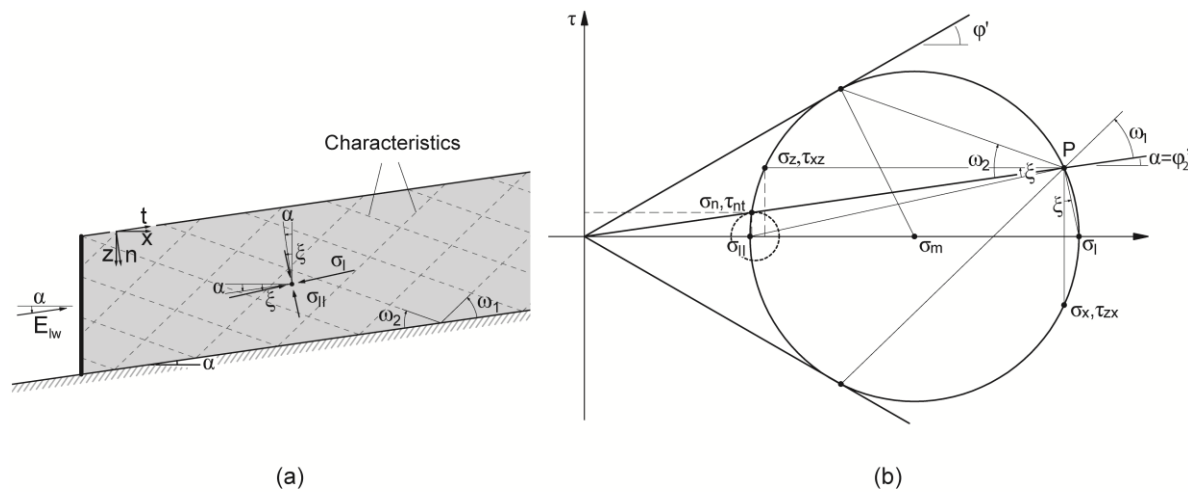


Figure 3-6. (a) Statically admissible stress field for slope parallel slip surface and vertical wall (b) Mohr circle of the stress state on the slip surface (small) and in the sliding layer (large circle).

$$K_{lhw} = \frac{\sigma_x}{\gamma z} = \frac{2E_{lhw}}{\gamma H^2} = \frac{\cos^4 \alpha}{\cos^2 \varphi'} \cdot \left(1 + \sqrt{1 - \cos^2 \varphi' (1 + \tan^2 \alpha)}\right)^2 \quad (3-16)$$

Algebraically, this solution corresponds exactly to another lower-bound solution, which Rankine (1857) proposed for a rather different problem of the classical passive earth pressure in inclined planar ground (Figure 3-1 (b)). This is due to the fact that in both problems the same assumption (3-10) has been adopted for the planes parallel to the slope surface, although the implications of this assumption are very different for the two problems. Indeed, whereas in the Rankine passive pressure formulation (with homogeneous soil of strength φ') this assumption does not produce the true stress field, in the landslide pressure problem, the same assumption (3-10) allows for the true failure state to be achieved at the slope parallel slip surface with a lower strength $\varphi'_2 = \alpha$. It is, therefore, hardly surprising that for the problem it was originally supposed to solve (that is, the wall moving towards the soil), this Rankine lower-bound appeared to be only useful for special cases (*e.g.*, $\alpha = 0$, $\delta = 0$), providing in general values which are significantly below the exact solution. In particular for steep slopes, where the true passive earth pressures should increase with increasing slope inclination, the values given by this lower-bound solution decrease. A comparison of the Rankine passive pressure with other solutions for passive earth pressure is shown in Appendix 3-4. In contrast, as is shown in the following section, for the problem of landslide pressures this not optimal lower-bound from a different problem appears to provide the exact solution.

3.5 The exact solution

For the special case of $\alpha = \theta$ and $c' = 0$, $\beta = 0$, it can be shown that the above presented upper and lower-bound solutions become identical, providing the exact solution for the problem of the landslide pressure, as had been demonstrated by Kupper (1967) and Szczepinski (1972). Indeed, for this case the upper-bound solution (3-8) simplifies to:

$$E_{lhw} = \frac{H^2 \gamma \cos^2 \alpha}{2} \cdot \frac{\sin(\omega_1 + \omega_2)}{\sin \omega_2 \sin \omega_1} \cdot \frac{\sin(\varphi' + \omega_1 + \alpha) \sin(\varphi' + \omega_2 - \alpha)}{\sin(2\varphi' + \omega_1 + \omega_2)} \quad (3-17)$$

In order to find the lowest upper-bound, in general critical inclinations of the slip discontinuities ω_1 and ω_2 in Figure 3-4 have to be found. Let us consider a case where these two inclinations are not independent and related via the same relationship

$$\omega_1 + \omega_2 = \frac{\pi}{2} - \varphi' \quad (3-18)$$

as the inclinations of the failure planes in the lower-bound solution (see Mohr's circle in Figure 3-6 (b)).

This relation further simplifies the upper-bound solution to:

$$E_{lhw} = \frac{H^2 \gamma \cos^2 \alpha}{2} \cdot \frac{\sin(\omega_1 + \varphi' + \alpha) \cos(\omega_1 + \alpha)}{\sin \omega_1 \cos(\omega_1 + \varphi')} \quad (3-19)$$

Solving equation $dE_{lhw}(\omega_1)/d\omega_1 = 0$ with respect to ω_1 gives the critical inclination

$$\begin{aligned} \omega_1 &= \frac{1}{2} [\arccos(t) - \varphi' - \alpha] \\ t &= -\frac{\sin \alpha}{\sin \varphi'} \end{aligned} \quad (3-20)$$

providing the lowest upper-bound for the landslide force under assumption (3-18):

$$\begin{aligned} E_{lhw} &= \frac{H^2 \gamma \cos^2 \alpha}{2} \cdot \frac{\sin(\arccos(t) + \alpha) + \sin(\varphi')}{\sin(\arccos(t) - \alpha) - \sin(\varphi')} \\ &= \frac{H^2 \gamma \cos^4 \alpha}{2 \cos^2 \varphi'} \cdot \left(1 + \sqrt{1 - \cos^2 \varphi' (1 + \tan^2 \alpha)}\right)^2 \end{aligned} \quad (3-21)$$

which is identical to the lower-bound solution (3-16), therefore, representing the *rigorous exact solution* of the landslide pressure problem for the particular case of $\alpha = \theta$ and a vertical retaining structure in cohesionless soil. This result is consistent with the findings of Muraro et al. (2015), who, based on the results of the finite element analysis of a particular case of the wall and slope geometry (using linear elastic - perfectly plastic constitutive model), found that the numerically calculated earth pressures were close to those obtained using Rankine's solution for passive pressure.

Assuming linear pressure distribution in the sliding layer, the exact landslide pressure coefficients K_{lhw} for five different friction angles are plotted in Figure 3-7 as a function of the slope angle α , together with active and passive earth pressure coefficients for inclined planar ground and frictionless vertical wall ($\delta = \beta = 0$), derived from Coulomb (1776) and Müller-Breslau (1906) solutions.

Although it is of little practical significance to calculate landslide pressures for very mild slope angles (only very few terrestrial landslides have slope angles below 15°), it is interesting to compare their theoretical pressure coefficients to the classical earth pressure theory. It appears that for the mildest (horizontal) slope, the landslide pressure coefficient is identical to that for the passive earth pressure, while for another extreme case, of the steepest (unstable) slope with $\alpha = \varphi'$, the landslide pressure is equal to the active earth pressure, given by $K_{ah}(\varphi' = \alpha) = \cos^2 \alpha$. However, as is seen in Figure 3-7, in between these two extreme cases there is a significant difference between the landslide pressure and both, the active and passive pressures. While passive pressure coefficients are overly conservative, using active pressure values as an estimate of the landslide pressure is in particular unsafe, since they predict decrease in the earth

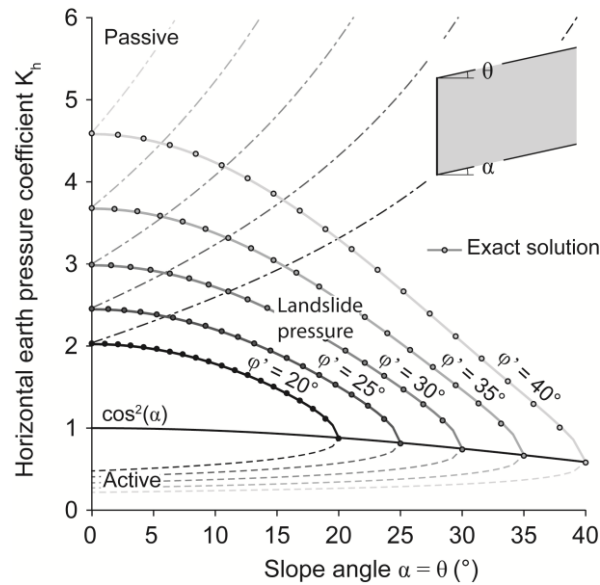


Figure 3-7. Earth pressure coefficients on retaining structures: solid lines correspond to the exact solution for the landslide pressure, plotted together with the active and the passive earth pressure coefficients for planar inclined ground and a smooth vertical wall, according to (Coulomb 1776) and (Müller-Breslau 1906) (dashed and dash-dotted lines, respectively).

pressure coefficients with increasing strength of the sliding layer φ' , whereas the true landslide pressures are seen to increase with strength.

It follows that the minimized upper-bound from equation (3-8) degenerates, in a particular case, to the known exact solution, providing some confidence for the application of this upper-bound to more general cases. It appears, however, that the application of the limit analysis solutions can also be extended to account for more realistic soil and wall conditions.

3.6 Extension of the solution to more general cases

In fact, the exact solution (3-21) derived for the special case of the vertical wall, with the limitations imposed on the flow rule and the wall-soil friction, can be extended to more general cases in cohesionless soil $c' = 0$ and $\alpha = \theta$. Note that each extension is only valid for the whole range of corresponding parameters when it is considered individually.

3.6.1 Extension to arbitrary wall friction

Note, that while in the upper-bound solution (3-8) the horizontal component of the landslide force E_{lhW} does not depend on the wall friction δ , in the lower-bound solution the stress state at the vertical wall (3-14) results in the resultant force E_{lW} parallel to the slope. This implies that the wall-soil interface friction angle should be higher than the slope inclination ($\delta \geq \alpha$), limiting the applicability range of the exact solution (3-21).

3.6.2 Extension to arbitrary wall inclination

The upper-bound solution for arbitrary wall inclination β is given by equation (3-8). If it was possible to find a lower-bound solution, identical to equation (3-8), it would provide the exact solution for arbitrary wall inclination. From a stress field in Figure 3-8 it follows that the only horizontal components of stresses act on the wall with inclination β (left) and the vertical cut (right). Hence, the horizontal force components E_{lh} and E_{lhw} have to be equal and the corresponding landslide pressure coefficients $K_{lh}(\beta = 0)$ and $K_{lhw}(\beta)$ are related via the squared ratio between the heights H and H_z :

$$K_{lhw}(\beta) = \frac{H_z^2}{H^2} \cdot K_{lh}(\beta = 0) \quad (3-22)$$

where:

$$H_z = H \cdot \frac{\cos(\alpha - \beta)}{\cos \alpha \cos \beta} \quad (3-23)$$

It follows that the lower-bound landslide pressure coefficient $K_{lhw}(\beta)$ can be expressed using the lower-bound solution (3-16) for $K_{lh}(\beta = 0)$ in the case of the vertical wall.

$$\begin{aligned} K_{lhw}(\beta) &= \frac{\cos^2(\alpha - \beta)}{\cos^2 \alpha \cos^2 \beta} \cdot K_{lh}(\beta = 0) \\ &= \frac{\cos^2(\alpha - \beta)}{\cos^2 \beta} \cdot \frac{\cos^2 \alpha}{\cos^2 \varphi'} \cdot \left(1 + \sqrt{1 - \cos^2 \varphi' (1 + \tan^2 \alpha)}\right)^2 \end{aligned} \quad (3-24)$$

On the other hand, in the upper-bound solution (3-8) for $c' = 0$, the wall inclination β is only present inside the proportionality coefficient for the landslide force. Therefore, the optimal inclination of the slip lines ω_i is not affected by the wall inclination resulting in the same optimisation as in equations (3-17) - (3-21). The resulting upper-bound appears to be identical to the lower-bound given by equation (3-24), providing the exact solution for the case of $\beta \neq 0$.

If a large inclination of the wall β is accompanied by a low wall-soil friction it is possible that the landslide pressure is different from the presented exact solution. In such a case it might be 'easier' for the landslide body to fail directly on the soil-wall-interface. A limiting condition is shown after which the exact solution will not be valid anymore. The expression is derived by

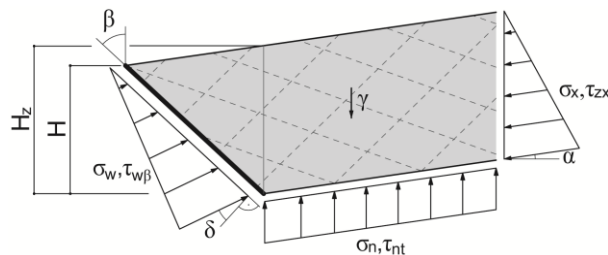


Figure 3-8. Extension of the lower-bound solution to arbitrary wall inclination β .

comparison of the landslide force of the exact solution (3-21) with a modified landslide force formulated using a mechanism involving the wall-soil interface as second slip discontinuity.

$$\begin{aligned}
 E_{lh} &= \min\{E_{lh2}, E_{lh1}\} \\
 E_{lh2} &= \frac{H^2\gamma}{2} \cdot \frac{\cos(\alpha - \beta) \cos(\beta - \delta)}{\cos^2 \beta} \\
 &\quad \cdot \frac{\sin(2 \arctan(\Gamma) - \alpha + \beta) - \sin(\varphi' + \beta)}{\sin(\varphi' + \alpha + \delta - \beta) + \sin(2 \arctan(\Gamma) - \delta + \beta)} \\
 E_{lh1} &= \frac{H^2\gamma}{2} \cdot \frac{\cos^2(\alpha - \beta)}{\cos^2 \beta} \cdot \frac{\cos^2 \alpha}{\cos^2 \varphi'} \cdot \left(1 + \sqrt{1 - \cos^2 \varphi' (1 + \tan^2 \alpha)}\right)^2
 \end{aligned} \tag{3-25}$$

With

$$\begin{aligned}
 \Gamma &= \frac{-\sin(\varphi' + \alpha) \sin(\alpha + \delta - 2\beta)}{\sin(\alpha - \delta) - \sin(\varphi' + \alpha) \cos(\alpha + \delta - 2\beta) - \sin(\varphi' + \delta)} \\
 &\quad + \left(\frac{\sin^2(\varphi' + \alpha) + 2 \sin(\varphi' + \alpha) \cos(\alpha + \delta - 2\beta) \sin(\varphi' + \delta)}{\sin(\alpha - \delta) - \sin(\varphi' + \alpha) \cos(\alpha + \delta - 2\beta) - \sin(\varphi' + \delta)} \right. \\
 &\quad \left. + \frac{(\sin^2(\varphi' + \delta) - \sin^2(\varphi' - \delta))}{\sin(\alpha - \delta) - \sin(\varphi' + \alpha) \cos(\alpha + \delta - 2\beta) - \sin(\varphi' + \delta)} \right)^{(1/2)}
 \end{aligned} \tag{3-26}$$

For cases where the exact solution is not valid anymore, the modified landslide force E_{lh2} can be used as an upper-bound for the force acting on the retaining structure.

3.6.3 Extension to arbitrary soil dilation

In order to fulfil the conditions of limit theorems, the associated flow rule has been assumed, which for real soils is not a good approximation of the constitutive behaviour at failure, in particular, on the slip surface where a significant amount of shearing leads to the critical state condition. It is, however, very likely that the present problem is not affected by soil dilation significantly and that the proposed exact solution is also valid for a non-associated flow rule. One way to support this statement is to follow the general argument of Drescher and Detournay (1993) by using the fact that the same force values can also be calculated, without accounting for the flow rule, from the limit equilibrium analysis of the statically determinate, translational kinematic mechanism in Figure 3-5. Another argument is that the finite element parametric study by Muraro et al. (2015) has also shown practically no influence of dilation on the landslide pressures. Finally, in Appendix 3-1 it is demonstrated that for the assumption of linear slip discontinuities and the corresponding linear stress field, the non-associated solution is equivalent to the exact solution with the associated flow rule.

3.6.4 Cases with variable thickness of the sliding layer and cohesive soils

For $\theta > \alpha$ and $c' > 0$ the presented upper-bound solution does not necessarily represent the exact solution. However, since the general upper-bound solution (3-8) overestimates the landslide pressures, it can still be used for the design of retaining structures. While this is a safe solution for the retaining structure, it is an unsafe solution if used as the limiting stabilisation force in a

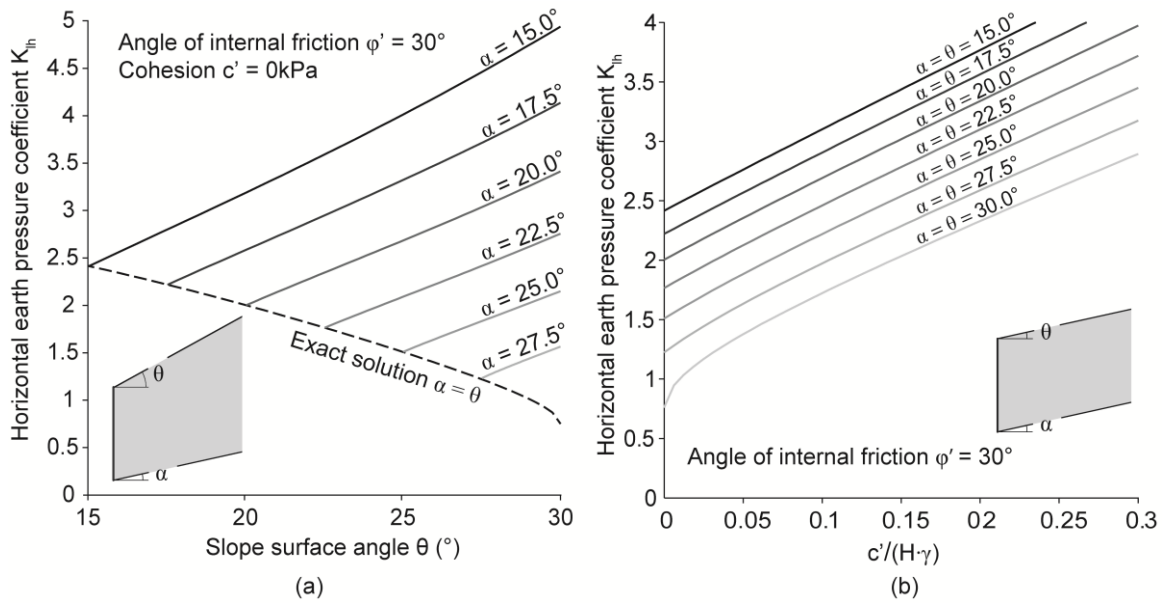


Figure 3-9. (a) Influence of variable thickness of the sliding layer $\theta \geq \alpha$ shown for the case of $\varphi' = 30^\circ$ in the upper-bound solution; (b) influence of the cohesion c' for the case of $\varphi' = 30^\circ$ in the upper-bound solution.

slope stability calculation. For a fixed friction angle of $\varphi' = 30^\circ$, Figure 3-9 shows the landslide earth pressure coefficient K_{lh} for sliding layers with (a) variable thickness (also see Table 3-2 in Appendix 3-3) and (b) cohesion. Compared to the special case of $\alpha = \theta$, the landslide pressure increases significantly with increasing slope surface angles θ . Soil cohesion in the sliding layer is also seen to increase the landslide pressure coefficient.

3.6.5 Accounting for ground water

Planar landslides normally exhibit a slope parallel ground water flow (Figure 3-10 (a), case i). However, in the vicinity of the obstacle the flow may deviate from the slope parallel case, for example due to the drainage of the water at a retaining wall (Figure 3-10 (a), case ii). Since the permeability of the soil is often anisotropic and may be spatially variable, estimating the exact transient flow field in the vicinity of the obstacle may prove difficult. The real phreatic surface and the corresponding water pressures will often lie between the dry case (Figure 3-10 (a), case iii), and the case with slope parallel flow (Figure 3-10 (a), case i). Therefore, also the landslide pressures will lie between the dry and the slope parallel flow cases and provide practically applicable bounds for the design of retaining structures and the assessment of constrained landslides. For the dry case, the pressures are provided by the exact solution (3-21). For the slope parallel case, derivation of the upper and the lower-bound solutions is presented in Appendix 3-2.

Note, that for the slope parallel case the presence of the ground water reduces the effective stresses and therefore the strength of the slip surface φ'_2 has to be larger than its inclination to fulfil the condition of constant velocity of the sliding layer:

$$\tan \varphi'_2 = \tan \alpha \cdot \frac{\gamma H}{\gamma H - \gamma_w H_w} \quad (3-27)$$

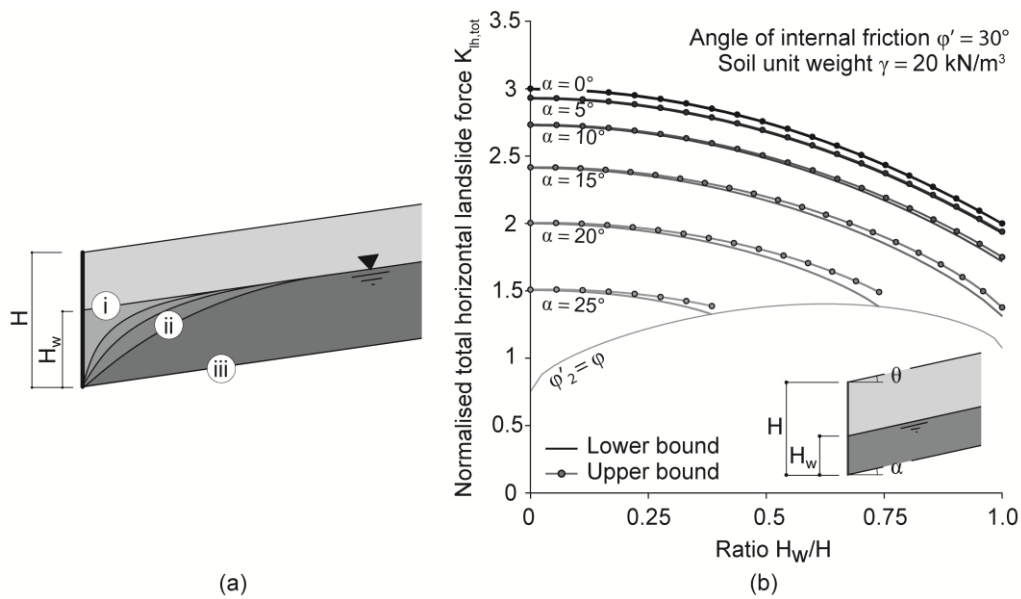


Figure 3-10. (a) Schematic sketch of possible groundwater flow in a landslide: (i) slope parallel flow; (ii) drained flow; (iii) no groundwater in the sliding layer. (b) Normalised total horizontal landslide force acting on a vertical wall with slope parallel groundwater flow for $\phi' = 30^\circ$ and $\gamma = 20 \text{ kN/m}^3$

In other words the landslide is only activated when the phreatic surface reaches the height H_w . The results of the upper and lower-bound limit analysis solutions from Appendix 3-2 are shown

in Figure 3-10 (b) for the total normalised landslide force $K_{lh,tot} = 2E_{lh,tot}/(H^2\gamma)$ depending on the ratio H_w/H for six different slope angles α . The two solutions are not anymore identical for the whole range of parameters and, therefore, they do not represent the exact solution. However, it can be concluded that the presence of water will always weaken the sliding body and the force needed to fail the soil in the vicinity of a constraining obstacle will always be smaller than the one of a landslide in dry condition. Therefore, the use of the presented exact solution for dry condition (3-21) represents a safe estimate for the design of a retaining structure. However, if used as the limiting stabilisation force in a slope stability calculation this solution is not safe, and a more complex lower-bound solution for the slope parallel flow should be used as a safe estimate.

3.7 Comparison with existing solutions

The problem of lateral landslide pressures was first studied by Haefeli (1944). He identified the special kinematical situation to which the classical active and passive pressure solutions are not applicable and tried to derive a solution for the landslide pressures using limit equilibrium. This solution is widely applied in the practice of geotechnical engineering in order to assess the landslide pressure acting on retaining structures. Brandl and Dalmatiner (1988) used Haefeli's solution for the special case of a slope angle equal to the angle of internal friction $\alpha = \phi'$ and compared it to field observations. They found out that the landslide pressure depends on the stiffness of the retaining structure and compares well to the solution of Haefeli. Their findings are published in textbooks (Brandl 1987; Brandl 2001) and are frequently used in engineering practice. In this section these solutions and their assumptions are compared to the presented exact solution.

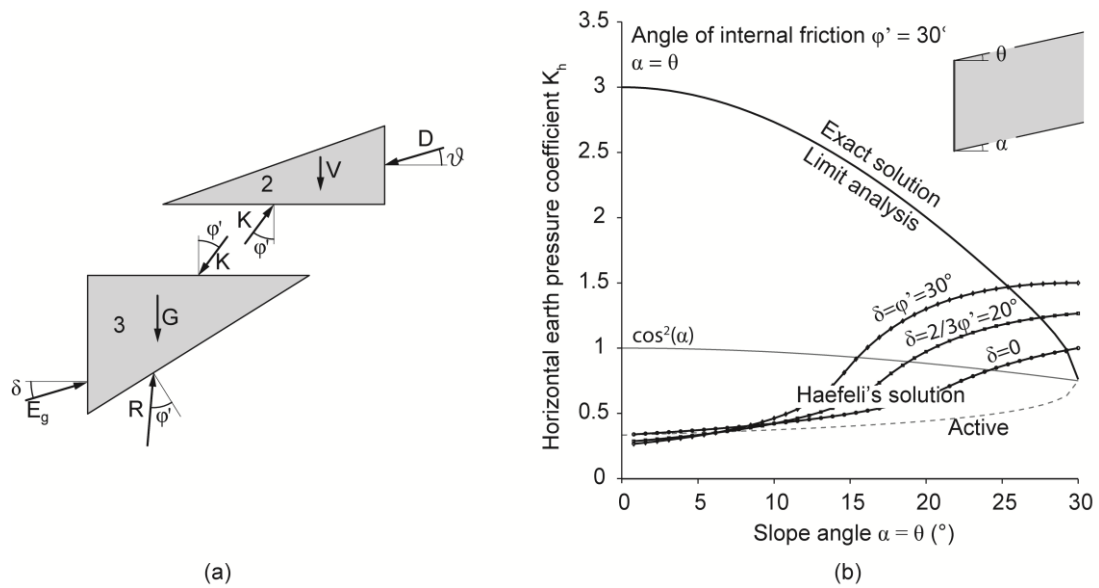


Figure 3-11. Haefeli limit equilibrium solution (a) blocks with edge forces; (b) comparison to the exact solution.

Haefeli (1944) assumed the failure mechanism shown in Figure 3-2 (a). A sliding layer on a rock surface was considered. Although the soil mass has to slide towards the retaining structure, no localised weak slip surface was introduced (it is not clear why the slide would occur if the strength of soil is higher than the slope angle). The solution is based on the formulation of limit equilibrium for Block 2 and Block 3 in Figure 3-11 (a), introducing some arbitrary assumptions:

- The slip surface between Blocks 2 and 3 is fixed as horizontal, which does not allow the solution to be optimised.
- On the vertical boundary of Block 2, inclination ϑ of the force D is a free parameter, while the proper application of limit equilibrium would require failure on this slip surface, that is, $\vartheta = \varphi'$.

Equilibrium on Blocks 2 and 3 gives the following expression for the Haefeli landslide force acting on the retaining structure:

$$E_g = \frac{\gamma H^2}{2} \cdot \frac{\tan \theta}{\tan^2 \chi \cos \delta} \cdot \left(\frac{1}{\cot \varphi' - \tan \delta} + \frac{1 + \frac{\tan \chi}{\tan \theta}}{\tan \delta + \cot(\chi - \varphi')} \right) \quad (3-28)$$

The subscript g is chosen according to the original publication by Haefeli (1944), it refers to the word ‘gleit’, german for ‘slide’. The force depends on the angle χ and has to be maximised with respect to χ , which is constrained by the rock surface angle $\chi \geq \alpha$. In the case of a slope parallel rock surface $\theta = \alpha$ with an inclination close to the angle of internal friction φ' , the angle χ is usually taken equal α .

In Figure 3-11 (b) Haefeli’s solution is shown for the case of slope parallel rock surface for three different wall-soil frictions δ . For comparison, the horizontal component of the landslide force E_{gh} is normalised assuming a linear pressure distribution at the wall. In contrast to the exact

solution (3-21) from limit analysis, where the earth pressure drops significantly with increasing slope angle α , Haefeli's solution is close to the active earth pressure at low slope angles and grows with increasing slope. Another difference is the significant influence of the wall friction δ : while the exact solution is, at least within certain bounds (*e.g.*, $\delta \geq \alpha$ for $\beta = 0$), independent of δ , the Haefeli solution at steep slope angles may vary by as much as 50%. Comparison with the exact solution shows that for realistic slope and friction angles in the sliding layer, of around $\alpha = 20^\circ$ and $\varphi' = 30^\circ$, respectively, Haefeli's solution underestimates landslide pressures significantly and has to be treated with care.

It is also seen in Figure 3-11 (b) that as the slope angles get closer to the friction angle, Haefeli's solution approaches the exact one, but for the special case of a slope angle α equal to the angle of internal friction φ' , the landslide pressures of Haefeli's solution can become significantly higher than those of the exact limit analysis solution. Although this case is rather hypothetical, because it implies that every single soil element in the sliding layer has reached the failure state (rarely the case in planar slides), for some reason Brandl and Dalmatiner (1988) have chosen this special case of Haefeli's solution to compare to their field observations. This comparison is shown in Figure 3-2 (b), where the horizontal landslide pressure coefficient K_{lhw} is normalised by the horizontal active earth pressure for a smooth wall $K_{ah}(\delta = 0) = \cos^2 \alpha$. While the comparison looks rather favourable for Haefeli's solution (subject of the correct guess of the inclination ϑ), the same cannot, unfortunately, be said about the exact solution $m = K_{lhw}/K_{ah} = 1$, which unlike Brandl's observations and Haefeli's solution does not exhibit in this special case any increase with increasing slope (and friction) angle.

How is it possible that an approximate solution fits the field observations better than the exact solution derived within the framework of limit analysis? The most likely explanation of this paradox is the inaccuracy of the extreme $\varphi' = \alpha$ assumption. In fact, by relaxing the $\alpha = \varphi'$ constraint, a good fit of the exact solution to Brandl's estimate for flexible structures (Figure 3-2 (b)) can be achieved by the slight increase of 5-10% in friction angle of the sliding layer φ' over the slope angle α . This implies that the sliding most likely took place on a weak slope parallel slip surface, which seems to be more realistic than Brandl's assumption of the global failure in the sliding layer. A more detailed analysis requires the exact knowledge of boundary conditions of every measured landslide, which at this stage is outside the scope of the presented work.

3.8 Examples

This section demonstrates the application of the derived solutions to two practical examples Figure 3-12: (a) Case 1 of a constrained creeping landslide with a slope parallel weak layer and (b) Case 2 of a retaining wall with a mildly inclined weak layer.

3.8.1 Constrained creeping landslide with a slope parallel weak layer

First a constrained creeping landslide with a slope parallel weak layer is investigated (Figure 3-12 (a)). The thickness of the sliding layer is 20 m, which corresponds to a vertical height $H_z = 21.3$ m. At the bottom of the slope the landslide meets a rock outcrop. Due to this constraint the pressure in the sliding layer increases towards the toe and might at some point in time reach failure. Such a situation is common in mountainous areas and there are also cases where buildings are constructed on the landslide (*e.g.*, Puzrin and Schmid 2012). For this particular case

the landslide pressure coefficient can be calculated using the exact solution (3-16) as $K_{lh} = 2.0$, while the landslide pressure acting on the rock outcrop K_{lhw} is higher and cannot be determined from the presented solutions. Note that the limiting landslide force acting in the sliding layer is independent from the inclination of the rock outcrop β and can be calculated using the vertical height of the sliding layer $H_z = 21.3\text{m}$:

$$E_{lh} = \frac{\gamma H_z^2 K_{lh}}{2} = 9073 \text{ kN/m} \quad (3-29)$$

The critical mechanism for this geometry is shown in Figure 3-12 (a). Its length measured in horizontal direction results to 77.6 m, which is significantly higher than the thickness of the sliding layer and can involve a significant amount of structures within the landslide compression zone, which could be more damaged by differential displacements than those located further uphill on the practically uniformly sliding layer.

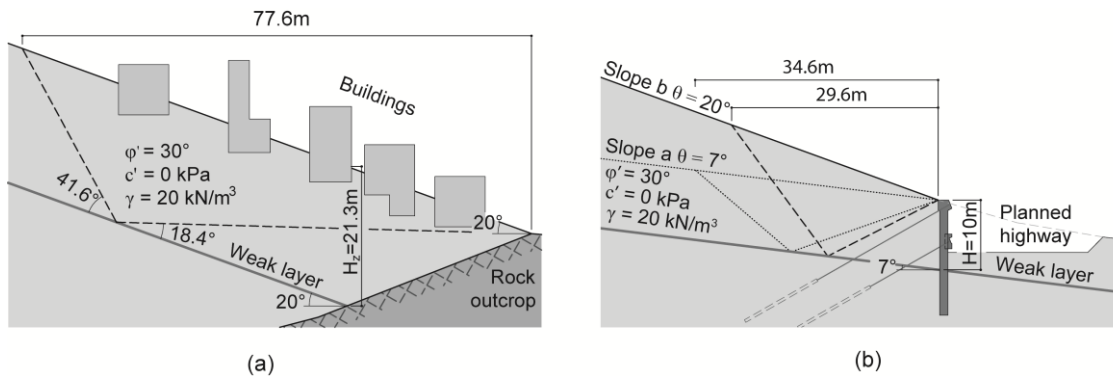


Figure 3-12. (a) Case 1: constrained creeping landslide; (b) Case 2: retaining wall for highway. (slope a: $\theta = 7^\circ$, slope b: $\theta = 20^\circ$)

3.8.2 Retaining wall with a mildly inclined weak layer

The second case is more exotic but certainly possible. It is chosen to show the influence of a mildly inclined weak layer, first in the case 2a with constant thickness of the sliding layer (Figure 3-12 (b), slope a) and then in the case 2b with variable thickness of the sliding layer (Figure 3-12 (b), slope b). A planned highway requires a retaining wall at the foot of a slope where a weak bentonite layer with an inclination of $\alpha = 7^\circ$ is located at the depth of $H = 10\text{m}$, measured at the wall. The landslide can take place if the friction angle in the weak layer drops to the angle of the layer inclination $\phi'_2 = \alpha = 7^\circ$, which is close to the residual friction angle of a pure bentonite (e.g., Lupini et al. 1981; Maio and Fenellif 2015). The parameters of the sliding layer are taken the same as in case 1 above.

In the case 2a of constant thickness of the sliding layer $\theta = \alpha = 7^\circ$ (slope a), the exact solution can be used to calculate the landslide pressure and the corresponding force acting on the retaining wall. Due to the milder inclination of the weak layer, the landslide pressure coefficient $K_{lhw} = 2.9$ increases by 45% compared to case 1 and the resulting landslide force acting on the retaining wall becomes:

$$E_{lhw} = \frac{\gamma H^2 K_{lhw}}{2} = 2867 \text{ kN/m} \quad (3-30)$$

Higher strength of the sliding layer allows for steeper slope inclinations than those of the weak layer. To illustrate the effect of the variable thickness on the landslide pressure, case 2b with a slope inclination of $\theta = 20^\circ$ (Figure 3-12 (b), slope b) has been investigated. The fact that $\theta \neq \alpha$ excludes the application of the exact solution and a possibly more conservative upper-bound solution (3-8) has to be used (Table 3-2 in Appendix 3-3). In this case due to the mild inclination of the slip surface the lowest landslide pressure coefficient calculated from the general upper-bound solution (3-8) is $K_{lhw} = 5.4$, which is significantly higher than the one in the case 2a with the slope parallel slip surface. The resulting total horizontal landslide force acting on the retaining wall is:

$$E_{lhw} = \frac{\gamma H^2 K_{lhw}}{2} = 5394 \text{ kN/m.} \quad (3-31)$$

While this upper-bound result is conservative for the design of the retaining wall, it provides an insight into how enormous the landslide forces can become for variable thickness of the sliding layer with low inclination of the slip surface and emphasises a need for more detailed analysis.

3.8.3 Comparison

Comparison of the two case studies shows that there is a significant influence of the geometry on the landslide pressure coefficient. A low inclination of the weak slip surface increases the landslide pressure coefficient significantly, in particular with variable thickness of the sliding layer (see Table 3-1, also showing Haefeli's solution and the active and passive coefficients according to Müller-Breslau 1906). This comparison reveals that in both cases Haefeli's solution underestimates the earth pressures significantly. While for case 1 and case 2a the classical passive earth pressure is too high compared to the exact limit analysis solution it is quite close to the upper-bound solution for case 2b, at least when a frictionless wall is assumed.

Table 3-1. Comparison of the horizontal earth pressure coefficients for the two case studies for different soil-wall frictions (note that the sign of the soil-wall friction angles δ corresponding to the kinematic conditions chosen, that is, negative for the passive case).

Soil-wall friction angle δ	Exact solution		Upper-bound	Haefeli $\theta = 20^\circ$	Active $\theta = 20^\circ$	Passive $\theta = 20^\circ$
	Case 1:	Case 2:				
	$\alpha = \theta = 20^\circ$	Slope a: $\alpha = 7^\circ,$ $\theta = 7^\circ$	Slope b: $\alpha = 7^\circ,$ $\theta = 20^\circ$			
$\delta=0^\circ$	2.0	2.9	5.4	0.63	0.44	5.74
$\delta=2/3\varphi'=20^\circ$				0.97	0.39	21.96

3.9 Conclusions

The problem of the limiting landslide pressure on an obstacle was first formulated by Haefeli (1944), who recognised that the kinematics of the problem does not allow for classical active and passive earth pressure theories to be applied. He derived an approximate solution using a limiting equilibrium approach with a number of rather arbitrary assumptions and simplifications. Since then, the Haefeli solution has been widely applied for design and analysis of landslide retaining structures.

This chapter revisits the old landslide pressure problem by means of a rigorous upper-bound limit analysis, which has been shown for a special case of a planar landslide to produce the known exact landslide pressure solution. The proposed approach also allows extending the limit analysis solutions to account for arbitrary wall friction and inclination, as well as the soil dilatancy and ground water effects, significantly broadening its field of application. Algebraically, this solution corresponds exactly to another lower-bound solution, which William Rankine proposed in 1857 for a rather different problem of the classical passive earth pressure in inclined planar ground assumed to be homogeneous (that is, without a weaker slip surface). Ironically, while for the problem it was originally supposed to solve (that is, the wall moving towards the soil) this Rankine lower-bound did appear to be useful only for special cases (*e.g.*, $\alpha = 0$), providing in general values significantly below the exact solution, for the problem of landslide pressures this suboptimal lower-bound from a different problem appears to provide the exact solution! This finding explains the ‘paradox’, why some numerical finite element solutions of this problem (*e.g.*, Muraro et al. 2015) happen to be close to the Rankine solution.

If the full shear resistance is mobilised along the entire length of the slip surface, all the way down to the obstacle, the exact solution allows for derivation of both the landslide pressure acting on the obstacle and the (identical to it) landslide failure pressure in the sliding layer. This condition is satisfied by all compliant retaining structures and by those rigid structures, which were installed after the initial landslide movement took place. If, however, the rigid obstacle existed before the landslide moves, the exact solution provides only the landslide failure pressure in the sliding layer, with the (higher) landslide force on the obstacle remaining undetermined. While for natural rock outcrops the latter force is of limited practical significance, for man-made rigid structures it represents an important design factor. However, the fact that they will have to withstand higher pressures than the failure pressure in the sliding layer becomes a strong argument against the use of such pre-installed rigid structures as a protection measure against future landslides.

The landslide pressures from the exact limit analysis solution increase with the strength of the sliding layer and appear to be significantly higher than the classical active but much lower than the classical passive earth pressures. Of even higher practical importance is that due to their oversimplifying assumptions, the well-established approximate limit equilibrium solutions (*e.g.*, Haefeli 1944; Brandl and Dalmatiner 1988) seem to get close to the exact limit analysis solution only over a very narrow range of slope and friction angles of the sliding layer. It follows that for mildly inclined weak slip surfaces and high strengths of the sliding layer, analysis and design of retaining structures based on these approximate solutions can become dramatically unsafe.

3.10 Appendix 3-1: Influence of the flow rule

In case of non-associated flow the failure load will always be equal or lower than the one derived using associated flow (*e.g.*, Chen 1975). To derive a solution using the non-associated flow rule the work dissipated along the slip discontinuities has to be calculated. In contrast to the associated flow this dissipation is non-zero even for purely frictional material. For this reason, in such a case both, a kinematically admissible velocity field and a corresponding statically admissible stress field have to be postulated (*e.g.*, Drescher and Detournay 1993; Smith 2012). In the special case of slope parallel slip surface, the stress field from the lower-bound solution Figure 3-6 and the mechanism shown in Figure 3-13 are used to derive the limiting landslide pressure for the case of a non-associated flow in the sliding layer and a non-dilatant flow on the slip surface. Consequently, Block 1 in Figure 3-13 (a) moves parallel to the slip surface and the hodograph changes (Figure 3-13 (b)), note that also the vertical component of the landslide force contributes to the rate of external work.

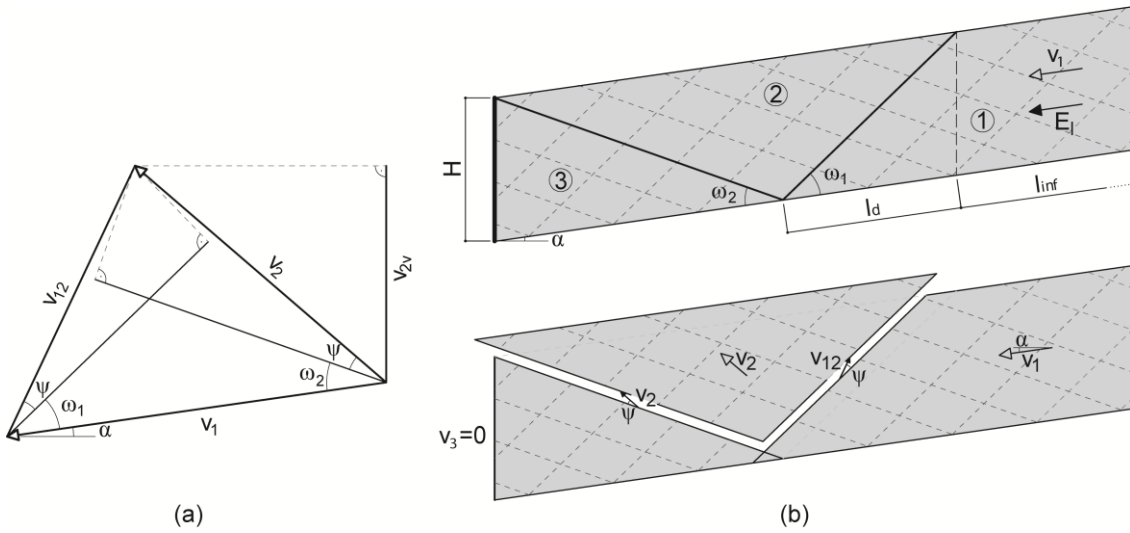


Figure 3-13. (a) Upper-bound mechanism for non-associated flow in the sliding layer and non-dilatant flow on the slip surface (b) the corresponding hodograph

From the hodograph in Figure 3-13 (b), using the constraint on the angles of the slip discontinuities $\omega_1 + \omega_2 = \frac{\pi}{2} - \varphi'$ the velocities are related by:

$$\begin{aligned}
 v_2 &= \frac{v_1 \sin(\omega_1 + \psi)}{\cos(2\psi - \varphi)} \\
 v_{12} &= \frac{v_1 \cos(\omega_1 + \varphi' - \psi)}{\cos(2\psi - \varphi)} \\
 v_{2v} &= \frac{v_1 \sin(\omega_1 + \psi) \cos(\omega_1 + \alpha + \varphi' - \psi)}{\cos(2\psi - \varphi)}
 \end{aligned} \tag{3-32}$$

and the lengths of the slip discontinuities are:

$$\begin{aligned}
l_1 &= \frac{H \cos \alpha}{\sin \omega_1} \\
l_2 &= \frac{H \cos \alpha}{\cos(\omega_1 + \varphi')} \\
l_d &= \frac{H \cos(\omega_1 + \alpha)}{\sin \omega_1}
\end{aligned} \tag{3-33}$$

The rate of external work is calculated as:

$$\dot{W}_e = \frac{v_1 E l h}{\cos \alpha} + v_1 \sin \alpha G_1 - v_2 v G_2 \tag{3-34}$$

where

$$\begin{aligned}
G_1 &= H\gamma \cdot \left(\cos \alpha l_{inf} + \frac{H \cos \alpha \cos(\omega_1 + \alpha)}{2 \sin \omega_1} \right) \\
G_2 &= \frac{H^2 \gamma}{2} \cdot \frac{\cos^2 \alpha \cos \varphi'}{\cos(\omega_1 + \varphi') \sin \omega_2}
\end{aligned} \tag{3-35}$$

The rate of internal dissipation is calculated from the scalar product of the relative velocities and the resulting failure stress on the slip discontinuities in the sliding layer and the slip surface, respectively:

$$\begin{aligned}
\dot{D}_i &= (\tan \varphi' \cos \psi - \sin \psi) \cdot \left(\int_0^{l_1} \sigma_f v_{12} dl + \int_0^{l_2} \sigma_f v_2 dl \right) \\
&\quad + \sigma_{n,ss} \tan \alpha v_1 (l_{inf} + l_d)
\end{aligned} \tag{3-36}$$

Since the normal stress acting on the slip discontinuities in the sliding layer σ_f is distributed linearly, the rate of internal dissipation simplifies to:

$$\dot{D}_i = \sigma_{f,b} (\tan \varphi' \cos \psi - \sin \psi) \cdot \frac{(v_{12} l_1 + v_2 l_2)}{2} + \sigma_{n,ss} \tan \alpha v_1 (l_{inf} + l_d) \tag{3-37}$$

Where $\sigma_{f,b}$ denotes the normal stress in the slip discontinuities at the bottom of the sliding layer and $\sigma_{n,ss}$ is the normal stress acting on the slip surface.

$$\begin{aligned}
\sigma_{f,b} &= \sigma_{m,b} \cos^2 \varphi' = H\gamma \cos^2 \alpha \cos^2 \varphi' \cdot \frac{1 + \sqrt{1 - \cos^2 \varphi' (1 + \tan^2 \alpha)}}{\cos^2 \varphi'} \\
\sigma_{n,ss} &= H\gamma \cos^2 \alpha
\end{aligned} \tag{3-38}$$

Equating the rates of external work and internal dissipation $\dot{W}_e = \dot{D}_i$ and solving for the landslide force leads to the horizontal component of the landslide force:

$$E_{lh} = \frac{\cos \alpha}{v_1} \cdot \left[\sigma_{f,b} (\tan \varphi' \cos \psi - \sin \psi) \cdot \frac{(v_{12}l_1 + v_2l_2)}{2} + \sigma_{n,ss} \tan \alpha v_1 (l_{inf} + l_d) - v_1 \sin \alpha G_1 + v_{2v}G_2 \right] \quad (3-39)$$

Since the dissipation rate along the infinite length of the landslide l_{inf} and the corresponding rate of external work of this part are equal, the landslide pressure is independent of this unknown landslide length. Inserting the stresses, velocities, weights and geometric parameters (equations (3-32)-(3-35)) and rearranging (3-39) leads to the same expression for the landslide force as the exact solution (3-21) derived assuming associated flow.

3.11 Appendix 3-2: Influence of groundwater

Consider a slope parallel ($\theta = \alpha$) cohesionless ($c' = 0$) landslide with slope parallel groundwater flow and the total saturated soil unit weight equal to the total moist soil unit weight. It is assumed that the landslide is only activated when the phreatic level of the groundwater reaches a certain height H_w . In this case the strength of the slip surface is higher than the slope inclination and has to fulfil condition (3-27).

The formulation of an upper-bound limit analysis solution follows the same procedure as without water, except that the work done against the pore water pressures caused by expansion of a body (due to dilatancy) as well as the work done by external water pressures has to be taken into account, e.g., Michalowski (1995). The assumed mechanism corresponds to the one without water and consists of two slip discontinuities, Figure 3-15 (a). For the sake of simplicity, block 3 is assumed to remain rigid and at rest in front of the obstacle. The velocities v_{2v} , v_{12u} , v_{23u} are derived from the hodograph, Figure 3-15 (b), and the water forces U_{12} , U_{23} are calculated by integration of the water pressure along the slip discontinuities, Figure 3-15 (a).

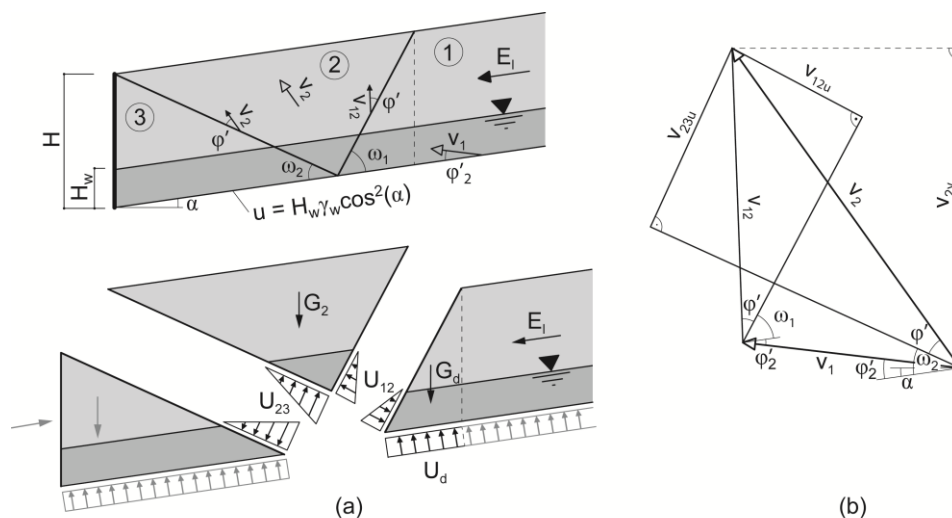


Figure 3-14. (a) Upper-bound mechanism with water; (b) corresponding hodograph

$$\begin{aligned}
v_{2v} &= \frac{v_1 \sin(\varphi' + \omega_1 + \varphi'_2) \sin(\varphi' + \omega_2 - \alpha)}{\sin(2\varphi' + \omega_1 + \omega_2)} \\
v_{12u} &= \frac{v_1 \sin(\varphi' + \omega_2 - \varphi'_2) \sin \varphi'}{\sin(2\varphi' + \omega_1 + \omega_2)} \\
v_{23u} &= \frac{v_1 \sin(\varphi' + \omega_1 + \varphi'_2) \sin \varphi'}{\sin(2\varphi' + \omega_1 + \omega_2)} \\
U_{12} &= \frac{H_w^2 \gamma_w \cos^3 \alpha}{2 \sin \omega_1} \\
U_{23} &= \frac{H_w^2 \gamma_w \cos^3 \alpha}{2 \sin \omega_2}
\end{aligned} \tag{3-40}$$

The weight of block 2, G_2 , is not affected by the water and remains as in equation (3-3). Note, that due to $\varphi'_2 \geq \alpha$, block 1 does not move horizontally. However, because the work done by the infinite part of block 1 equals exactly the work done by the pore pressure on the slip surface, only the work done against the weight of the triangular block G_d between the first slip discontinuity and the vertical dashed line in Figure 3-14 (a) as well as the corresponding pore pressure U_d on the slip surface enters the equation for the landslide force.

$$\begin{aligned}
U_d &= \frac{H \gamma_w H_w \cos^2 \alpha \cos(\alpha + \omega_1)}{\sin \omega_1} \\
G_d &= \frac{\gamma H^2 \cos \alpha \cos(\alpha + \omega_1)}{2 \sin \omega_1}
\end{aligned} \tag{3-41}$$

The resulting total horizontal force required to fail the soil in the vicinity of the constraining obstacle is calculated from the work equation to:

$$E_{lh} = \frac{v_{2v} G_2 + v_1 \sin(\varphi'_2 - \alpha) G_d - v_{12u} U_{12} - v_{23u} U_{23} - v_1 U_d \sin \varphi'_2}{v_1 \cos \varphi'_2} \cos \alpha \tag{3-42}$$

Similar to the dry solution, it depends on the two unknown angles of the slip discontinuities ω_1 and ω_2 . The best upper-bound solution is again found by minimizing the total landslide force E_{lh} . Since the equations are rather cumbersome, this minimisation is done numerically and the results for some special cases are shown in Figure 3-10 (b).

A lower-bound limit analysis solution can be found by dividing the stress field in the landslide body into two regions. The upper region 1 is dry and the lower region 2 is wet, see Figure 3-15 (a). In the dry part the solution (3-16) is still valid. In the wet part a stress field solution is derived below.

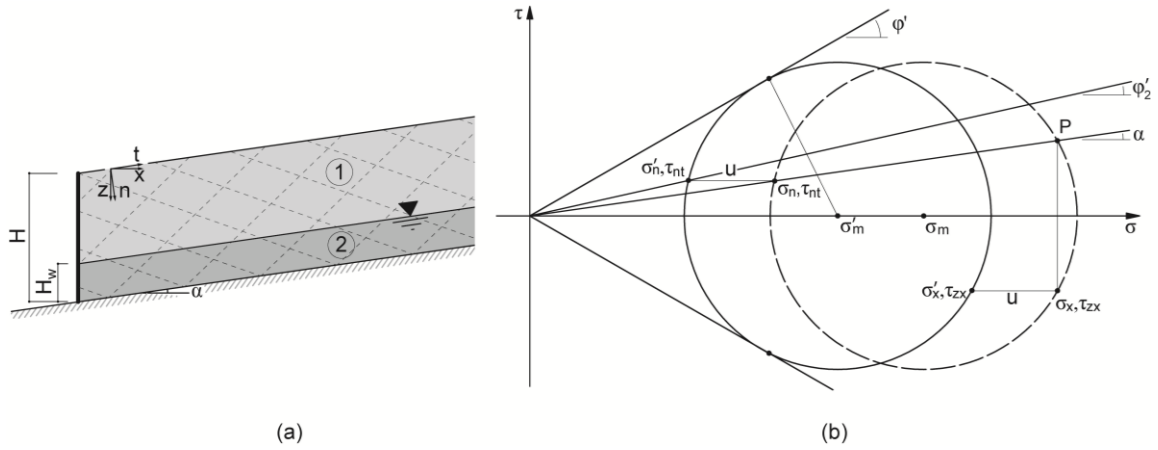


Figure 3-15. (a) Statically admissible stress field for slope parallel slip surface and vertical wall with water. (b) Mohr circle of the stress state in the wet layer (solid line: effective stress state; dashed line: total stress state).

The equilibrium conditions for the effective stresses depend on the water pressure u and lead to:

$$\frac{\partial \sigma'_t}{\partial t} + \frac{\partial \tau_{nt}}{\partial n} - \gamma \sin \alpha + \frac{\partial u}{\partial t} = 0 \quad (3-43)$$

$$\frac{\partial \sigma'_n}{\partial n} + \frac{\partial \tau_{nt}}{\partial t} - \gamma \cos \alpha + \frac{\partial u}{\partial n} = 0$$

Where the water pressure is given by

$$u = \gamma_w \cos \alpha (n - (H - H_w) \cos \alpha) \quad (3-44)$$

Assuming constant stresses in the sliding layer in the direction of the slip surface $\partial \tau_{nt} / \partial t = \partial \sigma'_t / \partial t = 0$, integrating the equilibrium equations in the normal direction and transforming the normal coordinate $n = z \cos \alpha$ into the depth of the sliding layer z yields

$$\sigma'_n = \cos^2 \alpha ((\gamma - \gamma_w)z + (H - H_w)\gamma_w) \quad (3-45)$$

Since for the total stresses the equilibrium conditions (3-9) are still valid, also their expression (3-10) does not change.

$$\begin{aligned} \sigma_n &= \gamma z \cos^2 \alpha \\ \tau_{nt} &= \gamma z \sin \alpha \cos \alpha \end{aligned} \quad (3-46)$$

On the slip surface ($z = H$), the ratio $\tau_{nt} / \sigma'_n = \tan \alpha \frac{\gamma H}{\gamma H - \gamma_w H_w}$ fulfils condition (3-27). Substitution of equations (3-45) and (3-46) into the Mohr circle of the effective stress state gives

$$(\sigma'_m - \sigma'_n)^2 + \tau_{nt}^2 = r^2 = \sigma'^2_m \sin^2 \phi' \quad (3-47)$$

which can be resolved with respect to the mean effective stress:

$$\sigma'_m = \frac{\sigma'_n \pm \sqrt{\sigma_n'^2 - \cos^2 \varphi' (\sigma_n'^2 + \tau_{nt}^2)}}{\cos^2 \varphi'} \quad (3-48)$$

The total horizontal normal stress σ_x and the corresponding shear stress τ_{xz} acting on a vertical plane are also related via the Mohr circle equation:

$$(\sigma_x - \sigma_m)^2 + \tau_{xz}^2 = r^2 = \sigma_m'^2 \sin^2 \varphi' \quad (3-49)$$

Because the total stresses are still related by (3-14), the pole P of the Mohr circle describing the total stress state in Figure 3-16 (b) is located on the straight line with inclination α passing through the origin. Solving equation (3-49), using equation (3-14), results in the total horizontal normal stress acting on a vertical plane

$$\sigma_x = \frac{\sigma_m \pm \sqrt{\sigma_m^2 - (1 + \tan^2 \alpha)(\sigma_m^2 - \sigma_m'^2 \sin^2 \varphi')}}{1 + \tan^2 \alpha} \quad (3-50)$$

Where the total mean stress is $\sigma_m = \sigma'_m + u$. The effective stress acting on a vertical plane is calculated from the total stress using $\sigma'_x = \sigma_x - u$. The total landslide force acting on a vertical plane is determined by integrating (3-50) over the thickness of the sliding layer. The resulting normalised total landslide forces are shown in Figure 3-10 (b) depending on the ratio H_w/H for six slope inclinations α .

3.12 Appendix 3-3: Variable thickness of the sliding layer

Table 3-2. Landslide pressure coefficients K_{lh} for vertical walls ($\beta = 0$) in cohesionless soil ($c'=0$), varying slope angle θ , slip surface inclination α and angle of internal friction in the sliding layer φ' (in general upper-bound solution, values corresponding to the exact solution $\alpha = \theta$ marked in bold).

$\varphi'=20^\circ$						
$\alpha, ^\circ$	$\theta, ^\circ$					
	5.0	8.0	11.0	14.0	17.0	20.0
5.0	1.98	2.27	2.56	2.85	3.15	3.47
8.0		1.88	2.17	2.45	2.73	3.01
11.0			1.75	2.03	2.29	2.55
14.0				1.57	1.84	2.10
17.0					1.33	1.63
20.0						0.88

$\varphi'=25^\circ$						
$\alpha, ^\circ$	$\theta, ^\circ$					
	5.0	9.0	13.0	17.0	21.0	25.0
5.0	2.40	2.93	3.47	4.06	4.71	5.42
9.0		2.26	2.77	3.28	3.83	4.43
13.0			2.05	2.53	3.00	3.50
17.0				1.77	2.21	2.66
21.0					1.43	1.87
25.0						0.82

$\varphi'=30^\circ$						
$\alpha, ^\circ$	$\theta, ^\circ$					
	5.0	10.0	15.0	20.0	25.0	30.0
5.0	2.93	3.84	4.85	6.01	7.39	9.05
10.0		2.73	3.59	4.52	5.58	6.82
15.0			2.42	3.19	4.02	4.95
20.0				2.00	2.69	3.39
25.0					1.51	2.10
30.0						0.75

$\varphi'=35^\circ$						
$\alpha, ^\circ$	$\theta, ^\circ$					
	5.0	11.0	17.0	23.0	29.0	35.0
5.0	3.61	5.16	7.02	9.38	12.45	16.54
11.0		3.33	4.75	6.44	8.53	11.22
17.0			2.86	4.12	5.55	7.32
23.0				2.27	3.31	4.46
29.0					1.59	2.41
35.0						0.67

$\varphi'=40^\circ$						
$\alpha, ^\circ$	$\theta, ^\circ$					
	5.0	12.0	19.0	26.0	33.0	40.0
5.0	4.51	7.13	10.65	15.67	23.08	34.49
12.0		4.10	6.48	9.60	13.95	20.26
19.0			3.43	5.44	8.00	11.49
26.0				2.58	4.15	6.08
33.0					1.67	2.79
40.0						0.59

3.13 Appendix 3-4: Comparison of different solutions for passive earth pressures

In Figure 3-16 the landslide pressure solution for the special case of slope parallel slip surface and cohesionless soil, which coincides with the Rankine (1857) passive earth pressure solution, is compared to other solutions for the passive earth pressure. Additional to Rankine's lower-bound the stress field solution of Lancellotta (2002), extended for sloping ground, and two upper-bound solutions of limit analysis (the wedge solution of Coulomb (1776) and the solution derived from a log-sandwich mechanism by Chen (1975)) are shown. The exact solution is bracketed by the lower-bound using the modified Lancellotta and the upper-bound using the log-sandwich mechanism and increases with increasing slope inclination. It is shown that Rankine's solution is a very low lower-bound solution for passive earth pressure, which is a result of the assumption that the stress field does not change in slope parallel direction and requires the (mobilised) soil-wall friction to be equal to the slope inclination. On the other hand this assumption is the reason why it provides the exact solution to the landslide pressure problem.

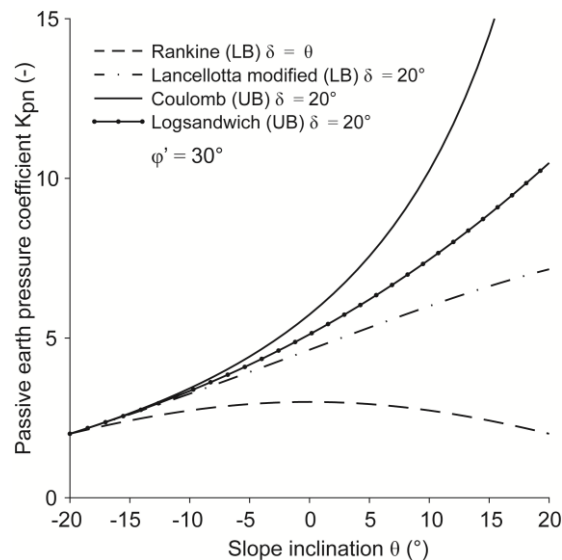


Figure 3-16. Comparison of two upper and two lower-bound solutions for passive earth pressure acting on a vertical wall with $\varphi' = 30^\circ$ and soil-wall friction $\delta = 20^\circ$.

3.14 Acknowledgment

I would like to thank my co-authors D. Hauswirth and A. Puzrin as well as my colleagues Pascal Minder, Andreas Stöcklin, Philipp Oberender, Luca Pizzetti, David Perozzi, Manuel Stocker, Johannes Schindler, Kallivokas Gerasimos and Athanasios Kontis (all ETH Zurich, Switzerland) for valuable discussions on the topic.

3.15 Notation

- c' cohesion of the sliding layer
 D force acting on the mechanism in Haefeli's solution

\dot{D}_i	rate of internal dissipation
E_l	limiting landslide force in the sliding layer
E_{lh}	limiting landslide force in the sliding layer
E_{lw}	limiting landslide force acting on the retaining structure
E_{lhw}	horizontal landslide force acting on the retaining structure
E_g	landslide force in Haefeli's solution (Figure 3-2)
E_{gh}	horizontal landslide force in Haefeli's solution
G	weight of block 1 in the Haefeli's solution
G_i	weight of the blocks in the upper-bound solution
H	vertical height of the retaining structure above the slip surface
H_z	vertical height of the sliding layer
H_w	vertical height of the water table in the sliding layer
K_l	landslide pressure coefficient
K_{lh}	horizontal landslide pressure coefficient
l_i	length of the slip discontinuity
m	ratio of the landslide pressure and the active earth pressure coefficients $m = K_{lh}/K_{ah}$
R_i	resulting frictional resistance force
S_i	cohesive resistant force
V	weight of block 2 in Haefeli's solution
v_i	virtual velocity
\dot{W}_e	rate of external work
X	ratio v_3/v_1
α	inclination of slip surface
β	inclination of the retaining structure
γ	unit weight of soil
γ_w	unit weight of water
δ	soil-wall interface friction angle ($\neq \delta_{mob}$)
ψ	dilation angle in the sliding layer
θ	inclination of slope surface
ϑ	inclination of the force D in Haefeli's solution
φ'	angle of internal friction in the sliding layer
φ'_2	angle of internal friction in the slip surface
σ_i	total normal stress
σ'_i	effective normal stress
τ_{ij}	shear stress
χ	inclination of the slip discontinuity in Haefeli's solution
ω_i	angle of the slip discontinuity, in the upper-bound solution the following constraints have to be fulfilled: $\pi - \omega_2 - 2\varphi > \omega_1 > \max\{0, \theta - \alpha\}$ and $0 < \omega_2 < \max\{\frac{\pi}{2} - \beta + \alpha, \frac{\pi}{2} - \varphi' + \alpha\}$, the lower-bound solution constrains the two angles by $\omega_1 + \omega_2 = \pi/2 - \varphi'$.

3.16 References

- Bernander, S. & Olofsson, I. (1981) On Formation of Progressive Failures in Slopes. In *Proceedings of the 10th Int. Conference on Soil Mechanics and Foundation Engineering*, Vol. 3. Stockholm, pp. 357–362, Rotterdam, the Netherlands, Balkema.
- Bjerrum, L. (1967) Progressive failure in slopes of overconsolidated plastic clay and clay shales. *ASCE Journal of Soil Mechanics and Foundation Engineering Division* **93**, No 5, 3–49.
- Brandl, H. (1987) Retaining Walls and Other Restraining Structures. In *Ground Engineer's Reference Book* (Bell, F.G. (ed.)). Butterworths, London, Ch. 47, 1–34.
- Brandl, H. (2001) Stützbauwerke und konstruktive Hangsicherungen. In *Grundbau-Taschenbuch, Teil. 3 Gründungen*, 6. Edition. (Smoltzyk, U. (ed.)). Ernst & Sohn, 495–651.
- Brandl, H. & Dalmatiner, J. (1988) *Brunnenfundierungen von Bauwerken in Hängen (insbesondere Brücken)*. Schriftenreihe Strassenforschung des Bundesministeriums für wirtschaftliche Angelegenheiten. Wien, Heft 352, Vienna, Austria.
- Caquot, A. & Kérisel, J. (1948) *Tableau de poussée et butée et de force portante des fondation*. Gauthiers-Villars, Paris, France.
- Chen, W.F. (1975) *Limit Analysis and Soil Plasticity*. Elsevier Scientific Publishing Co., Amsterdam.
- Chu, S.C. (1991) Rankine's analysis of active and passive pressures in dry sands. *Soils and Foundations* **31**, No 4, 115–120.
- Coulomb, C.A. (1776) Essai sur une application des règles de maximis & minimis à quelques problèmes de statique, relatifs à l'architecture. *Mémoires de mathématiques et de Physique présentés à l'Académie royale des sciences par divers savants, et lus sans ses assemblées VII*: 343-382.
- De Beer, E. (1977) Piles subjected to static lateral loads. In *Proceedings of the Speciality Session 10, 9th Int. Conference on Soil Mechanics and Foundation Engineering, speciality session 10*. Tokyo, 1–14.
- Drescher, A. & Detournay, E. (1993) Limit load in translational failure mechanisms for associative and non-associative materials. *Géotechnique* **43**, No 3, 443–456.
- Fukuoka, M. (1995) Earth pressure in moving soil mass. In *Proceedings of the Bengt B Broms Symposium on Geotechnical Engineering*, Singapore, 135–147.
- Haefeli, R. (1944) Zur Erd- und Kriechdruck-Theorie. *Schweizerische Bauzeitung* **124**, 256–260.
- Ito, T. & Matsui, T. (1975) Methods to estimate lateral force acting on stabilizing piles. *Soils and Foundations* **15**, No 4, 43–59.
- Kourkoulis, R., Gelagoti F., Anastasopoulos I. & Gazetas G. (2011) Slope Stabilizing Piles and Pile-Groups: Parametric Study and Design Insights. *Journal of Geotechnical and Geoenvironmental Engineering* **137**, No 7, 663–677.
- Kupper, W. (1967) Der plastische Grenzzustand in der schiefen ebenen Erd-oder Schneeschicht. *Zeitschrift für angewandte Mathematik und Physik ZAMP* **18**, No 5, 705-736.
- Lancellotta, R. (2002) Analytical solution of passive earth pressure. *Géotechnique* **52**, No 8, 617–619.
- Lupini, J.F., Skinner, A.E. & Vaughan, P.R. (1981) The drained residual strength of cohesive soils. *Géotechnique* **31**, No 2, 181–213.

- Nye, J.F. (1951). The flow of glaciers and ice-sheets as a problem in plasticity. *Proceedings of the Royal Society A: Mathematical, Physical and Engineering Sciences* **207**, No 1091, 554-572.
- Di Maio, C. & Fenellif, G.B. (2015) Residual strength of kaolin and bentonite: the influence of their constituent pore fluid. *Géotechnique* **44**, No 2, 217-226.
- Michalowski, R.L. (1989) Three-dimensional analysis of locally loaded slopes. *Géotechnique* **39**, No 1, 27-38.
- Michalowski, R.L. (1995). Slope stability analysis: a kinematical approach. *Géotechnique*, **45**, No 2, 283-293.
- Müller-Breslau, H.F.B. (1906) *Erddruck auf Stützmauern*. Alfred Kröner Verlag, Stuttgart, Germany.
- Muraro, S., Madaschi, A. & Gajo, A. (2015) Passive soil pressure on sloping ground and design of retaining structures for slope stabilisation. *Géotechnique* **65**, No 6, 507–516.
- Oberender, P.W. & Puzrin, A.M. (2016) Observation-guided constitutive modelling for creeping landslides. *Géotechnique* **66**, No 3, 232–247.
- Poulos, H.G. (1995) Design of reinforcing piles to increase slope stability. *Canadian Geotechnical Journal* **32**, No 5, 808–818.
- Puzrin, A.M. & Schmid, A. (2011) Progressive failure of a constrained creeping landslide. *Proceedings of the Royal Society A: Mathematical, Physical and Engineering Sciences* **467**, No 2133, 2444–2461.
- Puzrin, A.M. & Schmid, A. (2012) Evolution of stabilised creeping landslides. *Géotechnique* **62**, No 6, 491–501.
- Puzrin, A.M. & Sterba I. (2006) Inverse long-term stability analysis of a constrained landslide. *Géotechnique* **56**, No 7, 483–489.
- Randolph, M.F. & Houlsby, G.T. (1984) The limiting pressure on a circular pile loaded laterally in cohesive soil. *Géotechnique* **34**, No 4, 613–623.
- Rankine, W.J.M. (1857) On the Stability of Loose Earth. *Philosophical Transactions of the Royal Society of London* **147**, 9–27.
- Skempton, A.W. (1964) Long-term stability of clay slopes. *Géotechnique* **14**, No 2, 77–102.
- Smith, C. (2012) Limit loads for a shallow anchor/trapdoor embedded in a non-associative Coulomb soil. *Géotechnique* **62**, No 7, 563–571.
- Sokolovskii, V.V. (1960) *Statics of soil media*. Butterworths Scientific Publications, London, UK.
- Szcepiniski, W. (1972) On the motion of flat landslides and avalanches treated as a problem in plasticity. *Archives of Mechanics* **24**, No 5-6, 919-930.
- Terzaghi, K. (1936) Stability of slopes of natural clay. In *Proceedings of the First Int. Conference on Soil Mechanics and Foundation Engineering*, Vol. 1. Cambridge, 161–165.
- Viggiani, C. (1981) Ultimate lateral load on piles used to stabilise landslides. In *Proceedings of the 10th Int. Conference on Soil Mechanics and Foundation Engineering*, Vol. 3. Stockholm, 555–560.
- Ziegler, H. (1963). Methoden der Plastizitätstheorie in der Schneemechanik. *Zeitschrift für angewandte Mathematik und Physik ZAMP*, **14**, No 6, 713-737.

4 Selected applications of the landslide pressure

4.1 Abstract

In chapter 3 the limiting earth pressure acting on a retaining structure in a landslide was derived using upper- and lower-bound limit analysis (Friedli et al. 2017). The formulation of these limit states required simplifying assumptions on the geometry and the strength of the slip surface, the mobilisation of the friction along the slip surface as well as the embedment of the retaining structure. These assumptions seem, from a practical point of view, a bit restrictive. In this chapter an attempt is made to extend the application of the landslide pressure to some selected boundary conditions deviating from the considered ones in chapter 3. First, the restriction of the equality of inclination and strength of the slip surface is released and the corresponding landslide force is evaluated using upper-bound limit analysis and discussed with respect to the special case shown in chapter 3. It is shown that a difference between inclination and strength of the slip surface has an effect on the landslide pressure and that the pressure, in contrast to the solution in chapter 3, depends on the wall-friction. Next, the influence of a not fully mobilised friction along the slip surface in the vicinity of the retaining structure is investigated and discussed. It is shown that if the slip surface is not fully mobilised the pressures acting on the retaining structure can be significantly higher compared to the fully mobilised case. Finally, the case of a structure which does not reach down to the slip surface but is horizontally pinned is studied using upper-bound limit analysis. It is shown that depending on the embedment of the structure either a classical passive earth pressure mechanism or the landslide pressure mechanism shown in chapter 3 will form. The switchover condition between the two mechanisms is shown and discussed.

4.2 Arbitrary inclination and strength of the slip surface

4.2.1 Introduction

The landslide pressure solution, presented in chapter 3, (Friedli et al. 2017), is derived for the special case of a landslide which is exactly at the edge of stability (that is, the friction angle of the slip surface φ'_2 is assumed to be equal to the inclination of the slip surface α). This simplification, which is representative for many landslides, allows the derivation of the exact solution of limit analysis for the landslide pressure in cohesionless material with slope parallel slip surface and upper-bound solutions for more general cases. Further, it could be shown that in this special case the landslide pressure acting on a retaining structure is independent of the wall-friction. In reality, however, cases exist where a retaining structure is placed in a steep or a flat section of a landslide, where the simplifying condition of $\varphi'_2 = \alpha$ does not hold anymore. In this section the influence of arbitrary inclination and strength of the slip surface is investigated using upper-bound limit analysis.

4.2.2 Problem formulation

Consider a landslide consisting of a cohesionless sliding layer with the total unit weight γ and the angle of internal friction φ' moving on a weak slip surface with angle of internal friction φ'_2 . The slope surface has an arbitrary geometry and so does the weak slip surface (Figure 4-1). If the landslide is permanently moving the overall safety factor has to be close to 1 (that is, the driving gravity forces are close to the resistance along the weak slip surface). For a potential structure at location 1 in Figure 4-1 the assumption of constant friction along the weak slip surface leads to conditions with higher inclination of the slip surface, α_1 compared to φ'_2 . In contrast, for a potential structure at location 2 the inclination of the slip surface α_2 is lower than φ'_2 .

It is assumed that the landslide is sufficiently long above the potential structure for the difference between the driving and the resisting forces to bring the sliding layer to failure in the vicinity of the structure. The water table is assumed to be below the slip surface, therefore only dry conditions are considered. In this section only vertical structures are investigated.

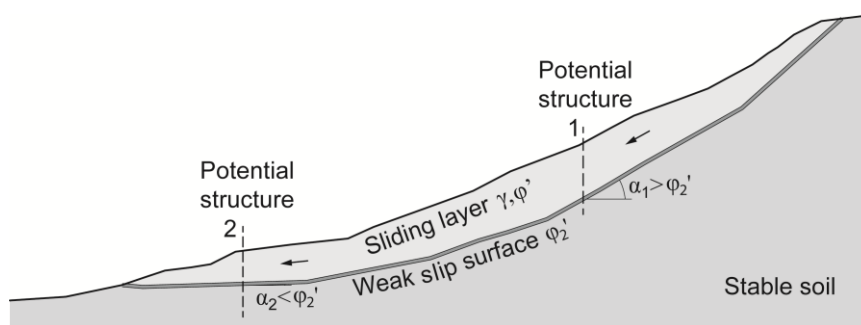


Figure 4-1. Problem formulation: schematic landslide with arbitrary geometry and strength of the slip surface with potential structures at different locations along the slope.

4.2.3 Upper-bound solution for the landslide force

Similar to the landslide pressure solution (Friedli et al. 2017) a kinematically admissible translational mechanism is proposed where the velocity field satisfies the velocity boundary conditions as well as the strain rate compatibility conditions. According to the upper-bound theorem (e.g., Chen 1975) the landslide force required to fail such a mechanism will always be larger than the true failure force in the sliding layer. The mechanism consists of three rigid blocks (Figure 4-2 (a)) which are bounded by slip discontinuities with the angles ω_1 and ω_2 . In contrast to the mechanism in shown in chapter 3 (Friedli et al. 2017), in case of $\varphi'_2 \neq \alpha$ the weight of block 1 contributes to the external work. As only the landslide force required to fail the sliding layer is of interest the length of block 1 is limited to an infinitely small value $dl \rightarrow 0$. Therefore the weight of block 1 vanishes and only the landslide force E_l contributes to the external work. Note that with the simplification, $\varphi'_2 = \alpha$, in chapter 3 (Friedli et al. 2017) the weight of block 1 also does not contribute to the external work due to the velocity being horizontal which is caused by the associated flow on the slip surface. According to the associated flow rule the velocity vector of block 1 is inclined to the slip surface by the friction angle φ'_2 , block 2 moves upwards with the velocity v_2 according to the hodograph in Figure 4-2 (b) and block 3 including the retaining structure is assumed to be at rest, $v_3 = 0$.

The relations between the velocities of blocks 1 and 2 are shown in the hodograph in Figure 4-2 (b). For the formulation of the work equation the component of the velocity of block 1 in the direction of the landslide force (which is inclined by ξ to the inclination of the slip surface), $v_{1\xi}$, and the vertical component of the velocity of block 2, v_{2v} , are of interest.

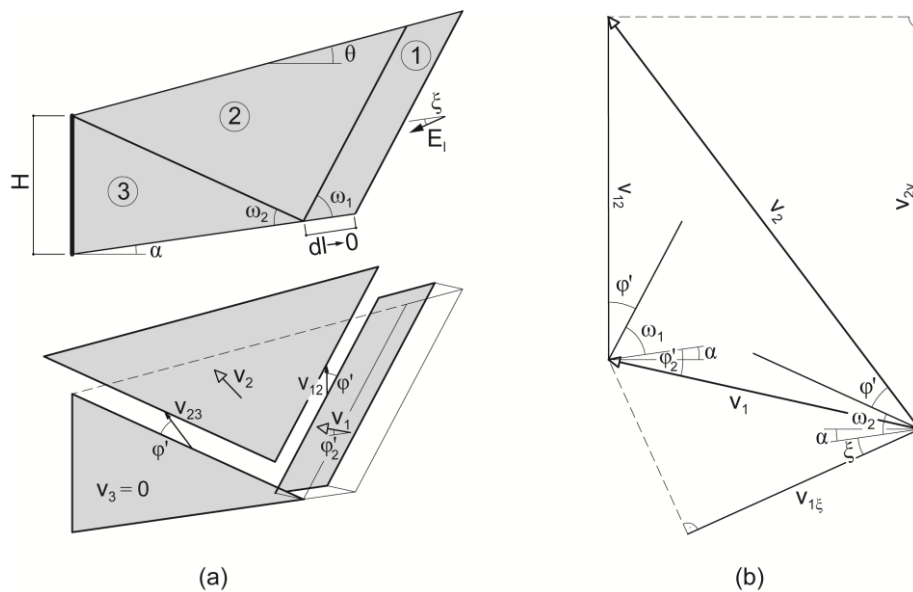


Figure 4-2. (a) Upper-bound mechanism and (b) corresponding hodograph.

The relations of the velocities of blocks 1 and 2 read

$$\begin{aligned}
 v_2 &= v_1 \frac{\sin(\varphi' + \varphi'_2 + \omega_1)}{\sin(2\varphi' + \omega_1 + \omega_2)} \\
 v_{2v} &= v_1 \frac{\sin(\varphi' + \varphi'_2 + \omega_1) \sin(\varphi' + \omega_2 - \alpha)}{\sin(2\varphi' + \omega_1 + \omega_2)} \\
 v_{1\xi} &= v_1 \cos(\varphi'_2 + \xi)
 \end{aligned} \tag{4-1}$$

As the soil friction has to be mobilised along the slip discontinuities the inclination of the landslide force has to fulfil the following condition.

$$\xi = \omega_1 + \varphi' - \frac{\pi}{2} \tag{4-2}$$

As cohesionless material is considered the dissipation is zero and the work equation reads:

$$\dot{W}_e = \dot{D}_i = v_{1\xi} E_l - v_{2v} G_2 = 0 \tag{4-3}$$

with the weight of block 2

$$G_2 = \frac{H^2 \gamma}{2} \cdot \frac{\cos^2 \alpha \sin(\omega_2 - \alpha + \theta) \sin(\omega_1 + \omega_2)}{\sin^2 \omega_2 \sin(\omega_1 + \alpha - \theta)} \tag{4-4}$$

Solving the work equation for the landslide force leads to:

$$\begin{aligned}
 E_l &= \frac{H^2 \gamma}{2} \cdot \frac{\sin(\varphi' + \varphi'_2 + \omega_1) \sin(\varphi' + \omega_2 - \alpha)}{\sin(2\varphi' + \omega_1 + \omega_2) \sin(\varphi' + \omega_1 + \varphi'_2)} \\
 &\cdot \frac{\cos^2 \alpha \sin(\omega_2 - \alpha + \theta) \sin(\omega_1 + \omega_2)}{\sin^2 \omega_2 \sin(\omega_1 + \alpha - \theta)}
 \end{aligned} \tag{4-5}$$

which depends on the two *a priori* not known angles of the velocity discontinuities ω_1 and ω_2 . The lowest upper-bound solution is found by optimising (4-5) with respect to these angles. The optimisation is done numerically and the results are shown and discussed later in the results section.

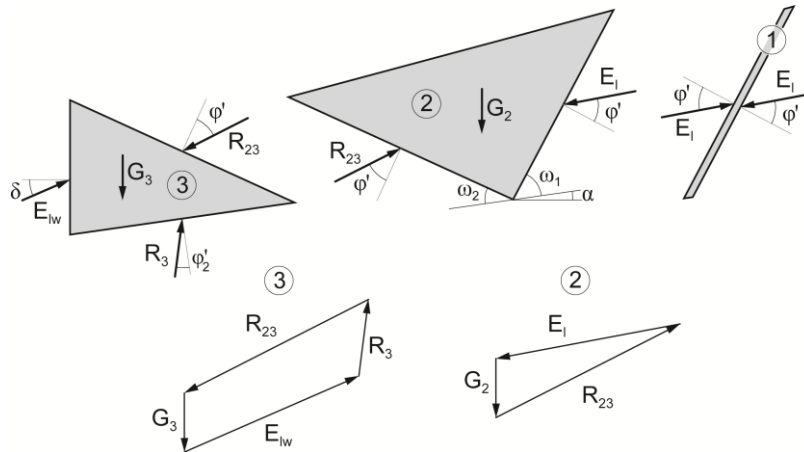


Figure 4-3. Limit equilibrium on the landslide pressure mechanism.

4.2.4 Force acting on the wall

From the upper-bound considerations only the landslide force acting in the sliding layer above the mechanism is evaluated. As block 3 is assumed to be at rest the force acting on the retaining structure cannot be defined from the work equation. As for translational mechanisms which are statically determinate (that is, all the forces acting can be calculated from the equilibrium conditions and the failure criterion) the limit equilibrium method provides a solution which is equivalent to an upper-bound limit analysis solution (e.g., Michalowski 1989; Drescher and Detournay 1993), the evaluation of this force is done using limit equilibrium under the assumption that the friction on the slip surface is mobilised all the way down to the retaining structure. As shown in chapter 3 (Friedli et al. 2017) this is the case for compliant structures. The limit equilibrium on blocks 1, 2 and 3 and the corresponding force polygons are shown in Figure 4-3. The landslide force acting on the wall reads

$$E_{lw} = \frac{G_3 \tan(\varphi'_2 - \alpha) + R_{23} [\cos(\varphi' + \omega_2 - \alpha) \tan(\varphi'_2 - \alpha) - \sin(\varphi' + \omega_2 - \alpha)]}{\sin \delta \tan(\varphi'_2 - \alpha) - \cos \delta} \quad (4-6)$$

with

$$R_{23} = \frac{E_l \sin(\omega_1 + \varphi' + \alpha)}{\sin(\omega_2 + \varphi' - \alpha)} \quad (4-7)$$

$$G_3 = \frac{H^2 \gamma}{2} \cdot \frac{\cos \alpha \cos(\omega_2 + \alpha)}{\sin \omega_2}$$

Note that the landslide force acting on the wall depends on the wall friction angle δ , unlike in the special case discussed in chapter 3, (Friedli et al. 2017).

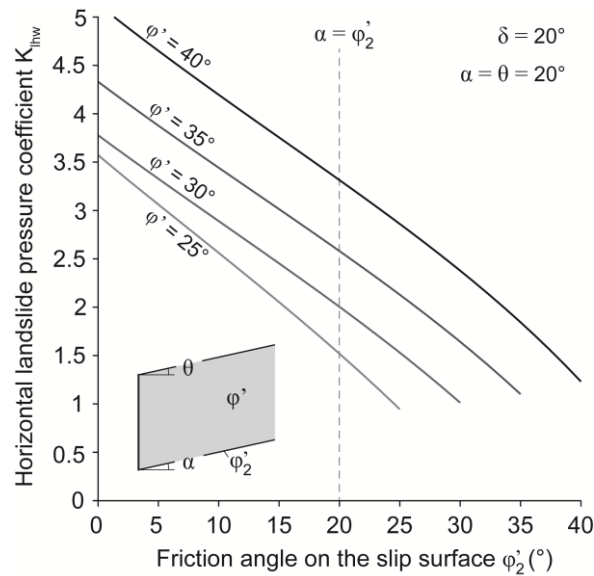


Figure 4-4. Landslide pressure coefficient depending on the friction angle on the slip surface, φ'_2 , for four different angles of internal friction in the sliding layer, φ' , at a slope inclination of $\alpha = \theta = 20^\circ$ and wall friction of $\delta = 20^\circ$.

4.2.5 Results

The results of the landslide pressure calculations are presented in a normalised form, which corresponds to the assumption of a linear stress distribution at the wall. The horizontal landslide pressure coefficient acting on the wall is defined as:

$$K_{lhw} = \frac{2E_{lw} \cos \delta}{\gamma H^2} \quad (4-8)$$

The minimisation of the landslide force (4-5) with respect to the angles ω_1 and ω_2 is done numerically with a constrained nonlinear optimisation.

In Figure 4-4 the horizontal landslide pressure coefficient K_{lhw} is shown depending on the friction angle of the slip surface, φ'_2 , for a case with slope parallel slip surface, $\alpha = \theta = 20^\circ$ and wall-friction angle $\delta = 20^\circ$ and four different angles of internal friction of the sliding layer, φ' . The landslide pressure acting on the retaining structure increases significantly with a reduction of φ'_2 . For the investigated angles of internal friction in the sliding layer the influence of φ'_2 is comparable (that is, the slope of the curves is similar).

As already shown in equation (4-6) the force acting on the retaining structure depends on the (mobilised) wall-friction δ . This influence is shown in Figure 4-5 (a) for a case with $\varphi' = 30^\circ$ and a slope parallel slip surface with inclination $\alpha = \theta = 20^\circ$. The influence of the wall-friction on the landslide pressure depends on the difference between the inclination of the slip surface, α , and the friction angle on the slip surface, φ'_2 . While in cases where $\varphi'_2 < \alpha$ higher wall-friction leads to lower pressures, in cases where $\varphi'_2 > \alpha$ the wall-friction has the opposite effect. Note that with $\varphi'_2 = \alpha$, as shown in chapter 3, the landslide pressure acting on the retaining structure is independent from the wall-friction.

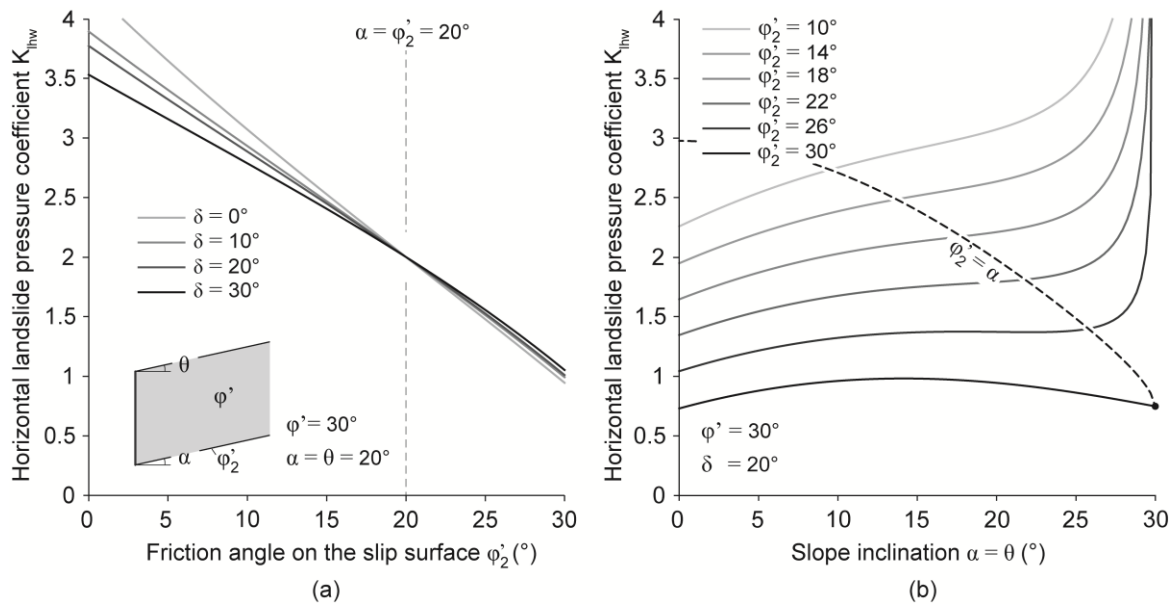


Figure 4-5. (a) Landslide pressure coefficient depending on the friction angle on the slip surface, φ'_2 , for four different δ with $\alpha = \theta = 20^\circ$ and $\varphi' = 30^\circ$; (b) Landslide pressure coefficient depending on the slope inclination, $\alpha = \theta$, for six different friction angles on the slip surface, φ'_2 , with $\varphi' = 30^\circ$ and $\delta = 20^\circ$, for comparison the special case of $\varphi'_2 = \alpha$ is also shown (dashed line).

The influence of the slope inclination on the landslide pressure at different friction angles of the slip surface is illustrated in Figure 4-5 (b) for a case with $\varphi' = 30^\circ$ and $\delta = 20^\circ$. In contrast to the solution with $\varphi'_2 = \alpha$ (dashed line in Figure 4-5 (b)) the pressure generally increases with increasing slope inclination. However, at low slope inclinations the pressure first increases only slowly with increasing slope but as it approaches the angle of internal friction in the sliding layer the pressures increase strongly, for cases with lower friction on the slip surface φ'_2 . In such cases, where α is close to φ' , the optimised angle ω_2 tends towards zero (can be shown by inserting $\alpha = \varphi'$ in equations (3-18) and (3-20)) and block 3 becomes very large which increases resistance force on the slip surface (R_3 in Figure 4-3). Due to the small φ'_2 with respect to α this force has a downhill component and leads to additional loads on the retaining structure. Except for these extreme cases the landslide pressure deviates only little from the solution with $\varphi'_2 = \alpha$ for the investigated friction angles on the slip surface φ'_2 .

4.2.6 Discussion

In cases where $\varphi'_2 < \alpha$ and in particular when α is close to φ' the landslide pressure acting on a retaining structure can be significantly higher compared to the solution of the special case shown in chapter 3. The presented solution is an upper-bound for the force acting on the structure. It is therefore possible that the high values for $\alpha \rightarrow \varphi'$ are overly conservative for the design of the structure. In contrast to the solution shown in chapter 3, where $\varphi'_2 = \alpha$, with $\varphi'_2 \neq \alpha$ the landslide pressure acting on the retaining structure depends on the wall-friction δ . However, the influence of the wall-friction on the landslide pressure is limited and depends on the value of φ'_2 with respect to α . As the case of $\varphi'_2 < \alpha$ is usually closer to the top end of a landslide it is possible that the difference between the driving gravity forces of the sliding layer and the resistance on the slip surface are not sufficient to bring the whole sliding layer to failure. In this case the load acting on the retaining structure is limited by this difference and will therefore be lower than the presented values resulting from upper-bound limit state considerations.

The case with $\varphi'_2 > \alpha$ is not possible in a landslide with slope parallel slip surface. In this case the force in the sliding layer decreases in downslope of the point where $\varphi'_2 = \alpha$. Therefore, if the force is sufficiently high, the sliding layer will fail at this point and not in the vicinity of the structure. In this case the landslide pressure at the point where $\varphi'_2 = \alpha$ can be used as a safe estimate for the load acting on the structure. A further reduction of the force in the sliding layer towards the structure is possible due to the higher φ'_2 compared to α . If, however, the thickness of the sliding layer reduces from the point where $\varphi'_2 = \alpha$ towards the structure, the overall resistance of the sliding layer reduces and it is still possible to reach the limit state in the vicinity of the structure or somewhere in between.

The calculation of the landslide pressure acting on the wall in case of $\varphi'_2 > \alpha$ requires therefore accurate knowledge of the geometry of the landslide and its strength parameters to determine the point where the sliding layer will reach the limit state first. Furthermore, as the sliding layer will most probably not reach a failure state anymore in the vicinity of the structure, the pressures cannot be derived from the evaluation of a limit state of soil failure and the complete elastic-plastic loading history has to be accounted for. As the derived values are upper-bound solutions they still represent a safe estimate for the design of the retaining structure but they might be overly conservative.

4.3 Not fully mobilised slip surface close to the structure

4.3.1 Introduction

For the investigation of the landslide pressure in chapter 3 (Friedli et al. 2017) a three block translational mechanism was assumed. As at the limit state of perfectly plastic soil failure the force acting on the retaining structure does not change anymore, the velocity of the structure and the adjacent block 3 vanish. Therefore the force acting on the retaining structure does not contribute to the work equation and cannot be calculated. It was shown that the force acting on the retaining structure E_{lw} can be determined using the assumption of a fully mobilised friction on the slip surface under block 3 and the limit equilibrium method. This assumption is fulfilled for compliant structures which allow sufficient mobilisation movement before the sliding layer reaches failure. However, in general cases this does not have to hold. In this section an attempt is made to quantify the effects of a not fully mobilised slip surface under block 3.

4.3.2 Problem formulation

The problem formulation follows in general chapter 3 and is restated here briefly. The sliding layer with surface inclination θ and the total unit weight γ moves downslope on a weak slip surface inclined by the angle α . The friction angle on the slip surface equals its inclination, $\varphi'_2 = \alpha$. The landslide is constrained by a retaining structure with the height H , the inclination β to the vertical and a wall-soil interface friction angle δ . Underneath block 3 only a part of the friction is mobilised $\varphi'_{2,mob} < \varphi'_2$. If the retaining structure moved upslope (for example by very large pre-stressing forces from anchors) the mobilised friction under block 3 may even change its sign. This possibility is also investigated.

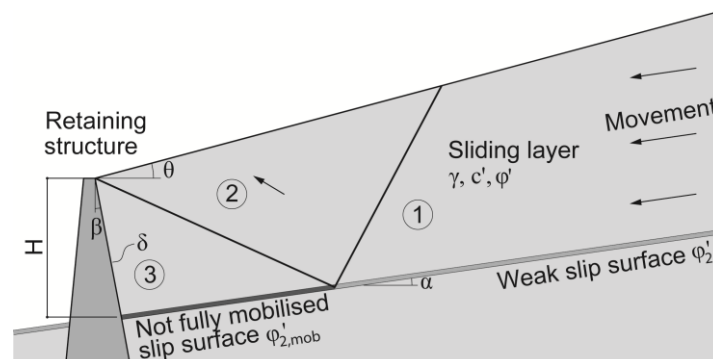


Figure 4-6. Problem formulation: landslide with retaining structure and not fully mobilised slip surface close to the structure underneath block 3.

4.3.3 Limit equilibrium solution

The landslide force acting in the sliding layer, E_l , is not altered by the not fully mobilised slip surface under block 3. Therefore the landslide force acting on the structure with a not fully mobilised slip surface under block 3 can be calculated from limit equilibrium on block 3 with the force polygon shown in Figure 4-7 to:

$$E_{lw} = \frac{R_{23}(\cos(\varphi' + \omega_2 - \alpha) \tan(\alpha - \varphi'_{2,mob}) + \sin(\varphi' + \omega_2 - \alpha)) + G_3 \tan(\alpha - \varphi'_{2,mob})}{\sin(\delta + \beta) \tan(\alpha - \varphi'_{2,mob}) + \cos(\delta + \beta)} + \frac{S_{c'2}(\cos(\omega_2 - \alpha) - \sin(\omega_2 - \alpha) \tan(\alpha - \varphi'_{2,mob}))}{\sin(\delta + \beta) \tan(\alpha - \varphi'_{2,mob}) + \cos(\delta + \beta)} \quad (4-9)$$

With

$$R_{23} = \frac{E_{lh} - S_{c'2} \cos(\omega_2 - \alpha)}{\sin(\varphi' + \omega_2 - \alpha)}$$

$$S_{c'2} = l_2 c' = \frac{H \cos(\alpha - \beta)}{\cos \beta \sin \omega_2} c' \quad (4-10)$$

$$G_3 = \frac{H^2 \gamma}{2} \cdot \frac{\cos(\alpha - \beta - \omega_2)}{\cos \beta}$$

E_{lh} is the horizontal component of the landslide force acting in the sliding layer which is independent from the mobilised friction under block 3. Under the assumption of $\varphi'_2 = \alpha$ along the slip surface of the landslide, this force is calculated following equations (3-7) and (3-8) in chapter 3 which simplifies to the exact solution shown in equation (3-21) in case of a slope parallel slip surface, cohesionless sliding layer and vertical wall. In this case the optimised angle ω_2 according to equations (3-18) and (3-20) can be used. For cases with $\varphi'_2 \neq \alpha$ and cohesionless sliding layer the horizontal component of the force E_l in equation (4-5) can be used and ω_2 has to be optimised numerically. Note that similar to cases with $\varphi'_2 \neq \alpha$, discussed previously in section 4.2, the landslide force acting on the retaining structure depends on the wall friction angle δ if the slip surface is not fully mobilised under block 3.

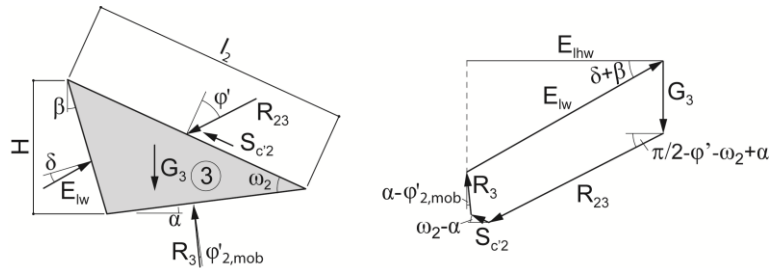


Figure 4-7. Limit equilibrium on block 3 and corresponding force polygon.

4.3.4 Results

Only the special case with $\varphi'_2 = \alpha$ on the slip surface underneath block 1 and not fully mobilised slip surface, $\varphi'_{2,mob}$ underneath block 3 with cohesionless sliding layer and a vertical, frictionless wall is evaluated numerically. The results are presented in normalised form according to equation (4-8). The horizontal landslide pressure coefficient increases significantly with a reduction of the mobilised friction angle on the slip surface from the special case investigated in chapter 3 (dots in Figure 4-8).

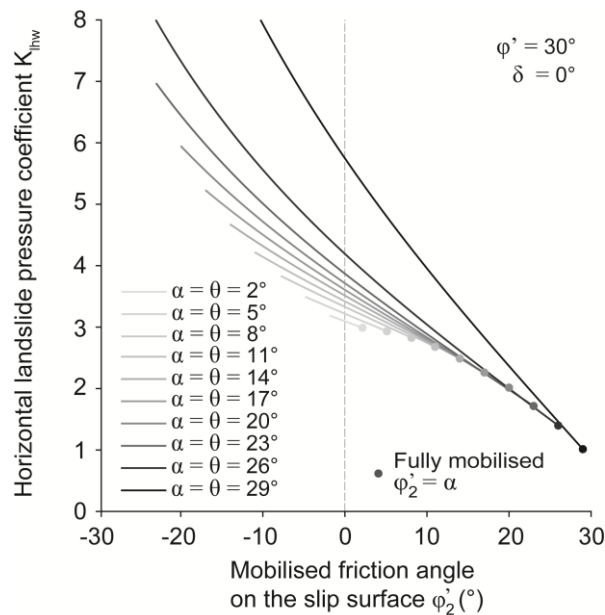


Figure 4-8. Horizontal landslide pressure coefficient depending on the mobilised friction angle on the slip surface underneath block 3 for the case of $\alpha = \theta$ with $\varphi' = 30^\circ$ and $\delta = 0^\circ$.

4.3.5 Discussion

The results of the limit equilibrium calculations show that the pressures acting on the structure can be significantly higher if the slip surface is not fully mobilised in the vicinity of the retaining structure. For a retaining structure which is installed in an already active permanently moving landslide it is, however, hardly possible that the slip surface underneath block 3 is not fully mobilised. This is only possible if a very stiff structure was installed before the landslide had moved and the movement started either due to increase of porewater pressure or softening of the slip surface material. However, as already stated in chapter 3, regarding the earth pressures a structure has to withstand, this is an argument for compliant retaining structures in landslides (that is, structure which displace slightly during loading). On the other hand to keep the landslide displacements small it would be favourable to install very stiff structures.

4.4 Fixed structure not fully embedded in the sliding layer

4.4.1 Introduction

The landslide pressure solution was derived for structures founded below the weak slip surface of a landslide. In this case the structure stabilises a wedge of the landslide adjacent to the structure above which the mechanism forms and the whole sliding layer fails. If, however, the structure does not reach all the way down to the slip surface but is horizontally pinned (for example a bridge foundation where the bridge girder forms the stabilisation or a structure which is anchored below the slip surface into stable ground) it is possible that not the whole sliding layer fails. In this case a part of the sliding layer will keep moving underneath the retaining structure. This problem was already discussed by Haefeli (1944) who suggested that for structures not reaching down to the slip surface a passive earth pressure mechanism is formed. Haefeli argued with a Coulomb wedge forming adjacent to the structure but did not compare the passive earth pressure to the landslide pressure and did not investigate how deep a structure has to be embedded in order to fail the whole sliding layer. Consequently, in this section the landslide pressure solution is compared to a good passive earth pressure upper-bound solution.

4.1.1 Problem formulation

Consider a landslide consisting of a sliding layer with slope inclination θ , angle of internal friction φ' and soil unit weight γ sliding on a weak slip surface with inclination α and resistance $\varphi'_2 = \alpha$. The landslide with vertical height H moves towards a retaining structure with vertical height H_{wall} (Figure 4-9). It is assumed that the retaining structure is infinitely thin and only the part of the sliding layer upslope of the retaining structure is considered, the possible active failure state downslope of the structure is not within the scope of this section.

In case of a sufficiently deep retaining wall the whole sliding layer fails, evoking the landslide pressure mechanism (Figure 4-9 (a)) discussed in chapter 3. In this case the force acting on the retaining structure E_l is calculated from equations (3-7) and (3-8) and in the special case with a slope parallel slip surface, cohesionless soil and a vertical structure, the exact solution (3-19) can be used.

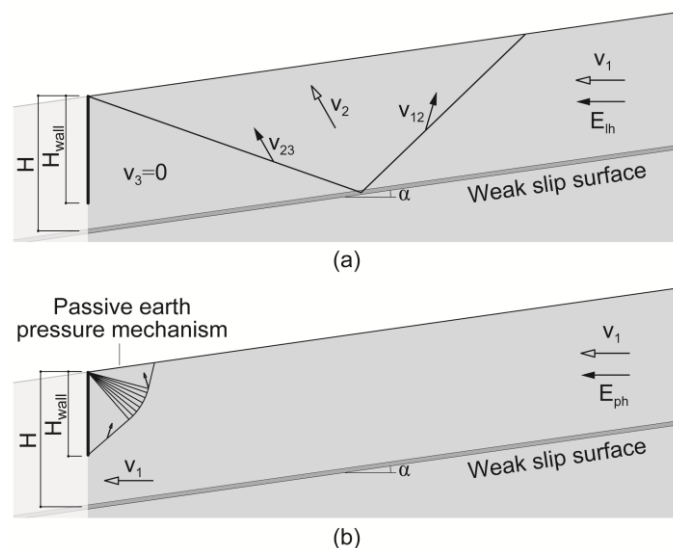


Figure 4-9. (a) Structure with large embedment evoking failure of the whole sliding layer; (b) structure with small embedment evoking a passive failure mechanism adjacent to the structure.

If the embedment depth of the retaining wall is sufficiently small a local mechanism above the retaining structure might be more favourable compared to the landslide pressure mechanism (Figure 4-9 (b)). The sliding layer under the structure is not influenced by such a mechanism and keeps moving. It can be shown that the external work done on the passive earth pressure mechanism, in contrast to the landslide pressure mechanism, is only depending on the relative velocity of the sliding layer with respect to the structure. This was already observed by Haefeli (1944) with limit equilibrium considerations. Therefore the limiting earth pressure acting on such a structure corresponds to the classical passive earth pressure. Subsequently the passive earth pressure is calculated according to the log-sandwich mechanism presented in (Chen 1975), which is known to provide good upper-bound values. This mechanism consists of two triangular blocks bracketing a log-spiral shearing zone and depends on two free parameters ρ and ψ which are to be optimised numerically. Note that the wall-friction δ , unlike in the landslide pressure case, affects the limit load significantly. The wall-friction can be introduced as an associated frictional failure or as non-associated frictional failure. In the latter case, which is used in the following calculations, the wall-friction produces a dissipation term which depends on the passive force. If, however, the structure can move vertically the wall-friction will not be mobilised and δ has to be set to zero. The expression for the passive earth pressure coefficient for cohesionless soil according to Chen (1975) is restated here for completeness.

$$\begin{aligned}
 K_p = & \frac{\sec \delta}{\cos \beta + \tan \delta \sin \beta - \frac{\tan \delta \sin(\beta + \rho)}{\cos \rho}} \\
 & \cdot \left\{ \frac{\tan \rho \cos(\rho + \varphi') \sin(\beta + \rho)}{\cos \beta \varphi'} + \frac{\cos^2(\rho + \varphi')}{\cos \rho \cos \beta \cos^2 \varphi' (1 + 9 \tan^2 \varphi')} \right. \\
 & \cdot [\sin(\beta + \rho) [3 \tan \varphi' + (3 \tan \varphi' \cos \psi + \sin \psi) \exp(-3\psi \tan \varphi')]] \\
 & + \cos(\beta + \rho) [1 + (-3 \tan \varphi' \sin \psi - \cos(\psi)) \exp(-3\psi \tan \varphi')]] \\
 & \left. + \frac{\cos^2(\rho + \varphi') \cos(\beta + \rho + \psi - \theta) \sin(\beta + \rho + \psi) \exp(-3\psi \tan \varphi')}{\cos \varphi' \cos \beta \sin(\beta + \rho + \psi + \varphi' - \theta) \cos \rho} \right\}
 \end{aligned} \tag{4-11}$$

Note that the slope inclination θ and the wall inclination β are used corresponding to the problem formulation in chapter 3.3.

The comparison of the external work required for the passive failure adjacent to the structure or failure of the whole sliding layer allows for the determination of the governing mechanism. This comparison can be equivalently done on the level of the force acting in the landslide body at the limit state and the mechanism with the lower force will be more favourable.

4.4.2 Results

The results are presented in normalised form according to equation (4-8). As it is assumed that the whole landslide force at the limit state is carried by the structure the normalisation is done using the height of the structure H_{wall} instead of H . Only the case with slope parallel slip surface, vertical structure and cohesionless sliding layer is considered.

In Figure (4-10) the normalised horizontal force acting on the structure is shown for a particular case depending on the embedment ratio of the structure H_{wall}/H . At low embedment ratios the passive earth pressure mechanism is governing and the resulting normalised force acting on the structure is equal to the passive earth pressure coefficient. For this reason the normalised force remains constant with increasing embedment ratio, at the same time the required force in the sliding layer increases with H_{wall}^2 up to the point where the landslide force to fail the whole sliding layer is equal or smaller (the forces are equal at the kink in Figure 4-10 (a)). Increasing the embedment ratio after this point does not affect the total force; therefore the decreasing normalised force is an effect of the increasing height of the structure and follows a parabola.

The evaluation of the normalised force for seven different slope inclinations in Figure 4-10 (a) shows that, in contrast to the landslide pressure, the passive pressure increases with increasing slope. This leads to a shift of the point where the switch between the two mechanisms takes place from high to low embedment ratios with increasing slope inclination. The embedment ratio at this switch is hereafter denoted 'critical embedment ratio' and is shown in Figure 4-10 (b) depending on the slope inclination for different angles of internal friction in the sliding layer.

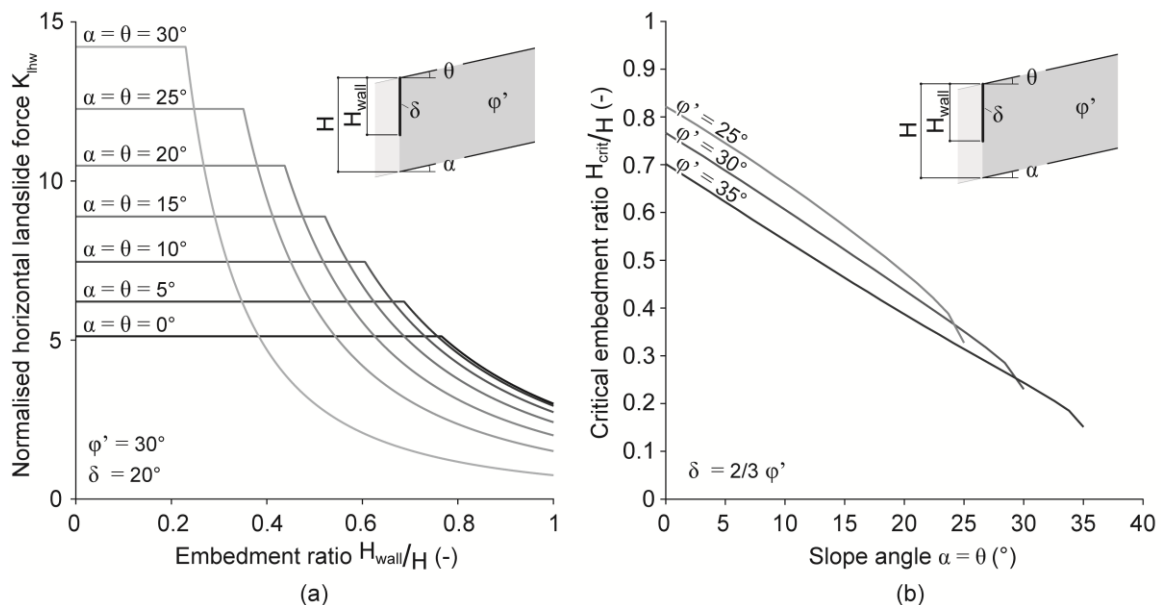


Figure 4-10. (a) Normalised horizontal force acting on the wall depending on the embedment ratio of the wall H_{wall}/H for the case of $\phi' = 30^\circ$ and $\delta = 20^\circ$ at seven slope inclinations; (b) Critical embedment ratio above which the whole sliding layer fails (that is, the landslide pressure mechanism becomes governing) for different ϕ' with corresponding $\delta = 2/3 \phi'$.

4.4.3 Discussion

The results of the above considerations show that in landslides with low slope inclination structures reaching almost down to the slip surface are required to reach the limit state where the whole sliding layer fails. With increasing slope inclination this critical embedment ratio reduces and for extreme cases where the slope inclination is close to the angle of internal friction in the sliding layer already quite shallow structures provide sufficiently high passive resistance to fail the whole sliding layer.

Provided that the landslide is sufficiently long, structures which are smaller than the critical height will not induce the highest possible stabilisation force. In such cases the sliding layer fails adjacent to the structure but keeps moving below the structure. The stabilisation using such structures does therefore not represent an optimum solution. On the other hand the stabilisation force does not increase anymore with deeper retaining structures. Note that a potential width of the retaining structure will increase the passive resistance due to friction at its base, in particular if a significant vertical force is acting (for example resulting from inclined anchors). This would lead to smaller critical heights of the retaining structure required to evoke the global failure of the whole sliding layer.

4.5 Conclusions

Three selected applications of the landslide pressure solution to broader geometrical and strength boundary conditions were presented. The restrictive assumption of equal inclination and friction of the weak slip surface does not have to hold for any structure in a landslide. The upper-bound considerations allowed the derivation of the landslide force acting on a retaining structure also in this more general case. It was shown that for a wide range of arbitrary inclinations of the slip surface the resulting landslide force does not deviate strongly compared to the solution from chapter 3. For very steep slopes and low friction of the slip surface, however, the force which the structure has to withstand may increase significantly. Further, it is interesting to note that if the inclination and the friction of the slip surface are not equal the landslide force on the retaining structure depends on the wall-friction.

Rigid structures which were installed prior to the landslide movement may prevent the mobilisation of the slip surface in their vicinity. The investigation of the effect of such a not fully mobilised friction shows that the corresponding landslide force acting on the structure may be significantly higher compared to the fully mobilised case. Although in practice structures in landslides will usually show some compliance and deform with increasing landslide pressures the results of this small study is a strong argument against pre-installed rigid structures.

In the investigation of structures which are not founded below the slip surface but are horizontally pinned (for example using anchors) the considerations shown by Haefeli (1944) could be confirmed. If a shallow structure is considered a passive failure mechanism forms and the sliding layer keeps moving under the structure. The corresponding earth pressures are limited by the passive resistance. If the structure reaches a certain critical embedment the whole sliding layer fails at the limit state and the landslide pressure mechanism can be evoked. While structures

shallower than this critical embedment can only provide a limited stabilisation force, with deeper structures the stabilisation force cannot be increase further. Therefore the critical embedment can be regarded as an optimum solution.

4.6 Notation

\dot{D}_i	Rate of internal dissipation
E_l	Limiting landslide force in the sliding layer
E_{lh}	Limiting landslide force in the sliding layer
E_{lw}	Limiting landslide force acting on the retaining structure
E_{lhw}	Horizontal landslide force acting on the retaining structure
G_i	Weight of the blocks in the upper-bound solution
H	Vertical height of the sliding layer above the slip surface
H_{wall}	Vertical height of the retaining structure
K_{lh}	Horizontal landslide pressure coefficient
R_i	Resulting frictional resistance force
v_i	Virtual velocity
\dot{W}_e	Rate of external work
α	Inclination of slip surface
γ	Unit weight of soil
δ	Soil-wall interface friction angle
ρ	Angle between the wall and the log-spiral shearing zone in the passive earth pressure mechanism
θ	Inclination of slope surface
φ'	Angle of internal friction in the sliding layer
φ'_2	Angle of internal friction in the slip surface
ρ	Angle of the log-spiral shearing zone in the passive earth pressure mechanism
ω_i	Angle of the slip discontinuities

4.7 References

- Chen, W.F. (1975) *Limit Analysis and Soil Plasticity*. Elsevier Scientific Publishing Co., Amsterdam.
- Drescher, A. & Detournay, E. (1993) Limit load in translational failure mechanisms for associative and non-associative materials. *Géotechnique* **43**, No 3, 443–456.
- Friedli, B., Hauswirth, D. & Puzrin, A.M., (2017) Lateral earth pressures in constrained landslides. *Géotechnique* **67**, No 10, 890-905.
- Haefeli, R. (1944) Zur Erd- und Kriechdruck-Theorie. *Schweizerische Bauzeitung* **124**, 256–260.
- Michalowski, R.L. (1989) Three-dimensional analysis of locally loaded slopes. *Géotechnique* **39**, No 1, 27-38.

5 Ultimate loads on buildings in landslides

This chapter has been published as an article:

Hug S., Friedli B., Oberender P., & Puzrin A. M., (2017) Ultimate loads on buildings in landslides. *Géotechnique*, Published ahead of print: <https://doi.org/10.1680/jgeot.17.P.134>

Republished with permission.

5.1 Abstract

Existing buildings embedded in permanently moving landslides often exhibit significant damage. This damage is mostly caused by excessive loads acting on the building due to relative displacements of the landslide. For buildings in the compression zone of a landslide the existing classical earth pressure and landslide pressure solutions are not capable of describing the loads adequately. In this chapter it is shown that accumulated loads acting on a building eventually lead first to a local limit state with failure in the vicinity of the building, followed by a global limit state where the whole sliding body reaches failure. Both limit states are analysed by means of limit analysis, resulting in analytical solutions for the ultimate loads for general cases, and the finite element method, resulting in the loading history for particular cases, respectively. The derived solutions are practically applicable for the assessment and potential retrofitting of existing buildings as well as for the design of new ones, possibly preventing future damage.

5.2 Introduction

Landslides are one of the major natural hazards endangering a large number of communities in mountainous regions. In Switzerland, for example, studies assess that more than six percent of the area is prone to slope instability (Lateltin et al. 2005). The landslide hazards are typically classified (*e.g.*, Cruden & Varnes 1996) into fast moving catastrophic mass movements, representing a dynamic event, and slow, permanently moving landslides, in the literature sometimes referred to as ‘creeping’ (*e.g.*, Puzrin & Schmid 2011). As in such permanently moving landslides the sliding often takes place in narrow zones with reduced strength (Bernander & Olofsson 1981), the overlaying sliding body is moving downslope almost intact. For this reason and because the displacement rates can be very small, construction activities have often spread into such instable areas. Regulations for the design of buildings in these conditions remain vague, which often leads to structural damage (*e.g.*, Cascini et al. 2013; Alexander 1986; Glade et al. 2005; Mansour et al. 2011) potentially caused by the underestimation of the landslide induced loads.

Past research focused on the correlation of occurred damage on existing structures to the displacement field of landslides (*e.g.*, Mansour et al. 2011; Picarelli 2011; Lateltin et al. 2005; Urciuoli 2008; FOEN 2016; Palmisano et al. 2016). These authors found that in particular the cumulated displacements (absolute downslope displacements of the landslide) and the relative displacements (difference of the displacements between two points on the landslide) are important parameters for vulnerability analyses of structures. In addition, the type of construction (*e.g.* statically determined or redundant) as well as the orientation towards the landslide movement was identified to influence their damage. While these studies allow for a qualitative assessment of existing structures based on empirical relations, only little work has been done to quantify the loads acting on such structures. The knowledge of these loads, however, is crucial for the design of new buildings and the potential strengthening of existing buildings.

The loads induced on buildings in landslides are commonly assessed using the same earth pressure theories as in stable slopes (*e.g.*, Rankine 1857; Coulomb 1776; Müller-Breslau 1906; Caquot & Kérisel 1948; Sokolovskii 1960). While active earth pressure is probably a non-safe estimate, using passive earth pressures for the design may be overly conservative. A solution for the earth pressure acting on natural or artificial obstacles that constrain the movement of a landslide was presented by Haefeli (1944) and Brandl & Dalmatiner (1988) using limited equilibrium. A rigorous limit analysis solution for this problem was recently published by Friedli et al. (2017), (chapter 3 of this thesis). These solutions, however, are only valid for structures embedded below the slip surface. In contrast, buildings embedded in the sliding body are moving together with the landslide and have to be treated differently.

The difference in stiffness and weight between the sliding body and a structure disturbs the displacement field of the landslide. This disturbance leads to stress changes which eventually result in one of the following limit states:

- i. Failure of the soil in the vicinity of the structure (local failure)
- ii. Failure of the whole sliding body (global failure)
- iii. Structural failure

Investigating the limit states of local and global failure allows evaluating the ultimate loads acting on a building in a landslide and preventing its structural failure by an appropriate design. In the present chapter this concept is applied to buildings embedded in the compression zone of a sliding body. Such conditions are present, for example if the sliding body is constrained at the bottom by an obstacle which can be artificial (retaining structure) or natural (rock outcrop), leading to decreasing displacement rates downslope towards the obstacle (*e.g.*, Puzrin & Schmid 2012; Oberender & Puzrin 2016; Puzrin & Sterba 2006). The ultimate loads acting on the building at local failure and in the sliding body at global failure are quantified by means of the kinematic method of limit analysis which has proven to be a suitable tool for geotechnical problems (*e.g.*, Chen 1975; Michalowski 1989; Randolph & Houlsby 1984; Smith 1998) and the finite element method (FEM).

5.3 Problem formulation

Consider a landslide with a slope surface inclination θ . The sliding takes place along a narrow weak zone, denoted ‘slip surface’, inclined by α (Figure 5-1). The problem is considered to have infinite dimension in the out of-plane direction (plane strain assumption). The slope and the slip surface are assumed to be planar in the vicinity of the building. The soil of the sliding body is assumed to be cohesionless and is characterised only by its angle of internal friction φ' and the unit weight γ . As permanently moving landslides are studied, the friction angle on the slip surface φ'_2 is assumed to be equal to the surface inclination α . The displacements of the landslide decrease downslope causing compression of the sliding body. The velocity field is assumed constant over the depth of the sliding body.

A building with the total weight G_b is embedded within the sliding body. Its cross-sectional geometry is simplified by a rectangular shape with embedment depths d_1 and d_2 at the up- and downhill sides, respectively; the vertical thickness of the sliding body t is measured at the uphill edge of the building. The interface friction between the building and the surrounding soil is δ . Further, it is assumed that the building is stiffer than the surrounding soil of the sliding body and does not collapse before the failure state is reached in the soil.

For the design of new buildings and the assessment of existing ones, the ultimate horizontal loads on the uphill and the downhill walls (that is, the ultimate earth pressure) are of main interest.

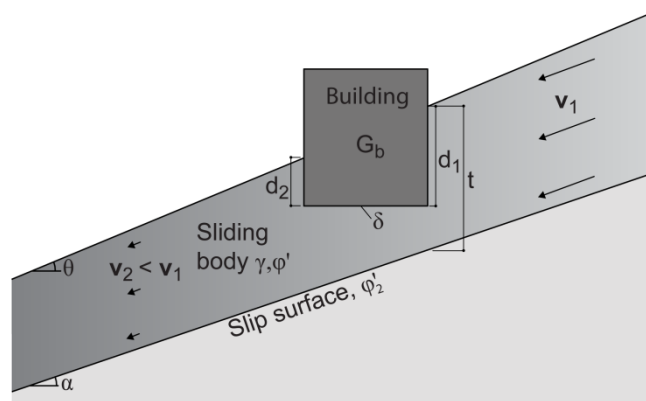


Figure 5-1. Geometry of the slope and the embedded building.

5.4 Upper-bound limit analysis

To calculate the ultimate loads acting on a building embedded in the compression zone of a landslide the kinematic method of limit analysis is used. For the application of this method, it is assumed that the soil failure is perfectly plastic following to the Mohr-Coulomb failure criterion with associated flow. The implications of a non-associated flow are discussed in the results section by comparison with the FEM solution.

To formulate an upper-bound solution, a kinematic admissible failure mechanism has to be found (*e.g.*, Chen 1975). At the limit state the rates of external work \dot{W}_e and the internal dissipation rates \dot{D}_i have to be equal which allows solving for the loads acting on the building (local failure) or in the sliding body (global failure). While for a global failure the kinematic method is applicable directly, in the case of local failure it cannot be applied in a straightforward manner, because only a part of the sliding body (that is, the soil in the vicinity of the building) is at the limit state. Despite this difficulty, it is still possible to evaluate the local limit state using the kinematic method. This is shown later in this chapter and the kinematic admissibility is proven in Appendix 5-1. In the following, first two local mechanisms and later two global mechanisms are introduced which allow the derivation of the corresponding ultimate loads.

5.4.1 Local failure mechanisms

The local failure is investigated using two families of mechanisms. In the first family (Figure 5-2 (a)) the building slips on the interface between its base and the surrounding soil. It consists of the uphill part of the sliding body (block 1) moving downslope, the downhill part of the sliding body (block 2), the building and a connected uphill soil wedge (block 3) and a soil wedge at the downhill wall (block 4).

In the second family (Figure 5-2 (c)) the velocity discontinuity does not occur in the interface beneath the building. It consists of the uphill and downhill part of the sliding body (blocks 1 and 2) and one translating block including the building, an uphill soil wedge and a part of soil beneath the building (block 3). With the two *a priori* unknown angles of the wedges ω_1 and ω_2 both mechanisms have two degrees of freedom which have to be optimised. Note that both angles count positive in anti-clockwise direction.

Both types of mechanisms are divided into two subtypes A and B depending on the uphill velocity discontinuity between blocks 1 and 3. While in subtype A shear failure of the soil occurs, forming a soil wedge on the uphill side of the building, in subtype B the failure occurs in the soil-structure interface at the uphill wall. In Figure 5-2 only the subtype A is illustrated. Note that in subtype B, $\omega_1 = \pi/2$ is determined and reduces the degrees of freedom to one.

In reality as long as no global failure has occurred, the soil beneath the building experiences a gradually decreasing velocity field causing changes in elastic strain energy due to the compression of the soil. The exact formulation of this energy rate is rather cumbersome, but can be replaced with the equivalent work rate of an internal force \mathbf{R}_{12} acting on a vertical 'velocity step' in the sliding body. This velocity step, which is not to be confused with the velocity discontinuities of the mechanisms, is illustrated in Figure 5-2 (a) and (c) as an interpenetration of block 1 into block 2. The kinematic admissibility of the velocity step is demonstrated in Appendix 5-1.

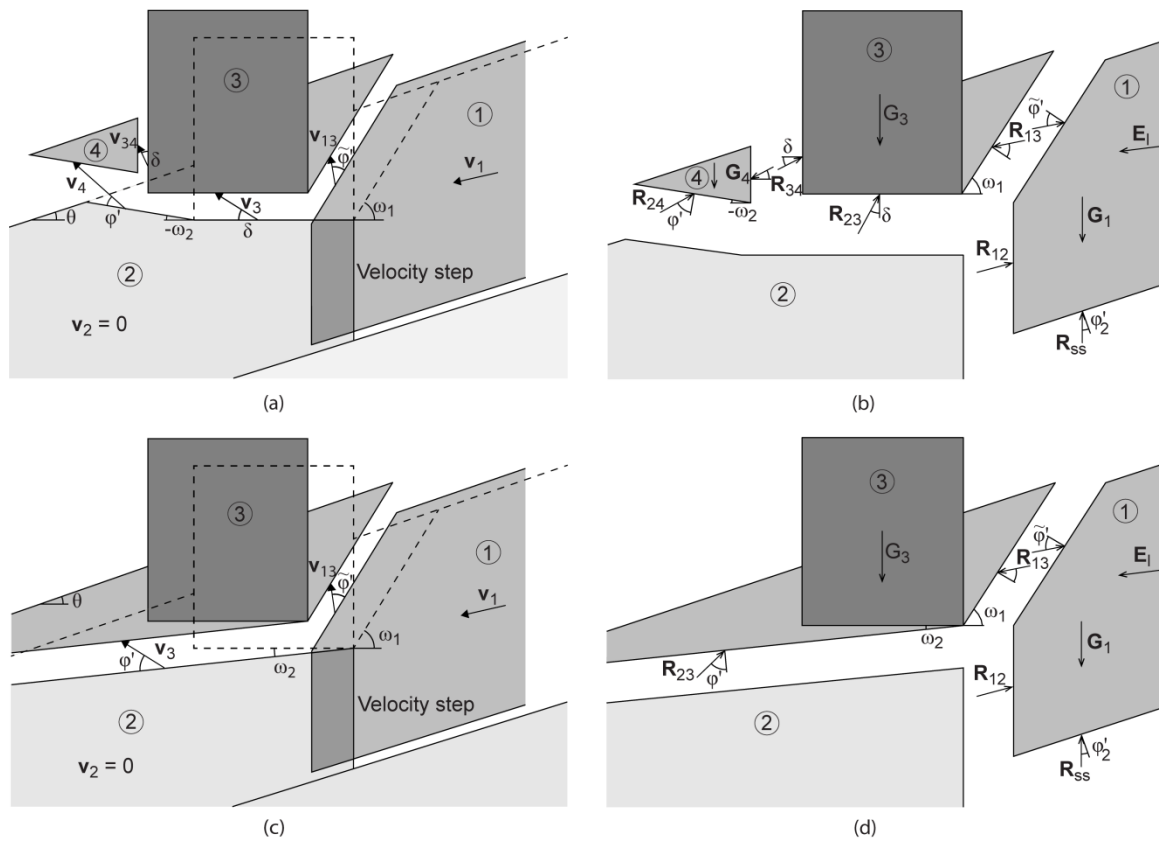


Figure 5-2. (a) Local mechanism type 1A and (b) the corresponding free body diagram; (c) local mechanism type 2A and (d) the corresponding free body diagram.

As only relative displacements lead to increasing loads on the building, the downhill part of the sliding body (block 2) is introduced to be at rest, $v_2 = 0$, in both mechanism families. In contrast the part of the sliding body on the uphill side of the building (block 1) moves with the velocity v_1 . Note that according to the associated flow rule the direction of velocity v_1 is defined by the frictional strength on the slip surface and in this case the solution represents a rigorous upper-bound. In Appendix 5-2 it is shown that the local mechanisms are independent on the direction of v_1 and result in the same ultimate loads. Block 3 and block 4 move with their velocities v_3 and v_4 according to the associated flow rule.

As cohesionless soil is assumed the dissipation rate \dot{D}_i is zero. Consequently the work equation is calculated from the external work rates done on blocks 1, 3, 4 against gravity (G_1 , G_3 and G_4), the work rates done by the force in the uphill sliding body, E_l , the internal force in the velocity step, R_{12} , and the resistance force on the slip surface, R_{SS} .

$$\dot{W}_e = (E_l + R_{SS} + G_1 + R_{12}) \cdot v_1 + G_3 \cdot v_3 + G_4 \cdot v_4 = \dot{D}_i = 0 \quad (5-1)$$

The work equation (5-1) is also valid for the local mechanism type 2 with $G_4 = 0$.

In addition to equation (5-1), all the forces acting on block 1, including the internal force \mathbf{R}_{13} , have to be in equilibrium (Figure 5-2 (b) and (d)).

$$\mathbf{E}_l + \mathbf{R}_{SS} + \mathbf{G}_1 + \mathbf{R}_{12} = \mathbf{R}_{13} \quad (5-2)$$

Inserting equation (5-2) into (5-1) allows solving for the internal force \mathbf{R}_{13} . The horizontal component of the force on the uphill wall of the building P_{uh} results from the horizontal component of \mathbf{R}_{13} , (Figure 5-2 (b)).

For the first family of mechanisms evaluating the work equation (5-1) and inserting the weights and the velocities according to the geometry of Figure 5-2 (a), allows solving for P_{uh} . Detailed derivations of the weights and the velocities can be found in Appendix 5-2.

$$P_{uh1} = \left(G_b + \frac{\gamma d_1^2}{2} \frac{1}{\tan \omega_1 - \tan \theta} \right) \cdot \frac{\sin \delta \sin(\tilde{\varphi}' + \omega_1)}{\sin(\tilde{\varphi}' + \delta + \omega_1)} + \frac{\gamma d_2^2}{2} \cdot \frac{\sin(\varphi' - \omega_2) \cos 2\delta \sin(\tilde{\varphi}' + \omega_1)}{(\tan \theta - \tan \omega_2) \cos(\varphi' + \delta - \omega_2) \sin(\tilde{\varphi}' + \delta + \omega_1)} \quad (5-3)$$

Where the angle of friction in the velocity discontinuity between block 1 and 3, $\tilde{\varphi}'$, corresponds to the soil friction angle φ' (local mechanism type 1A) or the interface friction δ (local mechanism type 1B) depending on the value of the angle ω_1 .

$$\tilde{\varphi}' = \begin{cases} \varphi', & \omega_1 < \pi/2 \\ \delta, & \omega_1 = \pi/2 \end{cases} \quad (5-4)$$

The force on the downhill wall follows from equilibrium on the building. The horizontal component of this force results in

$$P_{dh1} = \frac{\gamma d_2^2}{2} \cdot \frac{\tan(\varphi' - \omega_2)}{(\tan \theta - \tan \omega_2)(1 - \tan(\varphi' - \omega_2) \tan \delta)} \quad (5-5)$$

Equation (5-3) is to be optimised with respect to the angles of the velocity discontinuities ω_1 and ω_2 , with the following constraints, which follow from geometric (Figure 5-2 (a)) and kinematic considerations Figure 5-11 (a)).

$$\theta \leq \omega_1 \leq \min \left\{ \pi - \varphi' - \delta; \frac{\pi}{2} \right\} \quad (5-6)$$

$$\varphi' + \delta - \frac{\pi}{2} \leq \omega_2 \leq \varphi' - \delta$$

For the second family of local mechanisms (Figure 5-2 (c) and (d)) the horizontal component of the force on the uphill wall is calculated analogously to

$$P_{uh2} = \left[\frac{\gamma d_1^2}{2} \left(\frac{1}{\tan \omega_1 - \tan \theta} + \frac{1}{\tan \theta - \tan \omega_2} \right) - \frac{\gamma(d_1^2 - d_2^2)}{2} \cot \theta + G_b \right] \cdot \frac{\sin(\phi' - \omega_2) \sin(\tilde{\varphi}' + \omega_1)}{\sin(\phi' + \tilde{\varphi}' + \omega_1 - \omega_2)} \quad (5-7)$$

Where $\tilde{\varphi}'$ still depends on ω_1 according to equation (5-4) and divides the mechanism into the subtypes 2A and 2B. The angles of the velocity discontinuities have to be optimised with the following constraints, which follow from geometric (Figure 5-2 (c)) and kinematic considerations (Figure 5-11 (b)).

$$\theta \leq \omega_1 \leq \min \left\{ \pi - \phi' - \delta; \frac{\pi}{2} \right\} \quad (5-8)$$

$$0 \leq \omega_2 \leq \theta$$

Note that in this mechanism no failure occurs along the downhill wall and the base of the building (Figure 5-2 (d)) and therefore the force acting on the downhill wall cannot be determined.

5.4.2 Global failure mechanisms

After reaching the local failure in the vicinity of the building the landslide can be loaded further until global failure of the whole sliding body is reached. This limit state is closely related to the solution presented in chapter 3, Friedli et al. (2017). The building, however, introduces additional constraints on the mechanism and possibly alters the weight of the sliding body, which allows the formation of at least two possible failure configurations. While for buildings lighter than the excavated soil a mechanism including the building may occur (type 1, Figure 5-3 (a)), heavier ones may prevent such a mechanism and lead to failure further elsewhere along the slope, excluding the building (type 2, Figure 5-3 (b)).

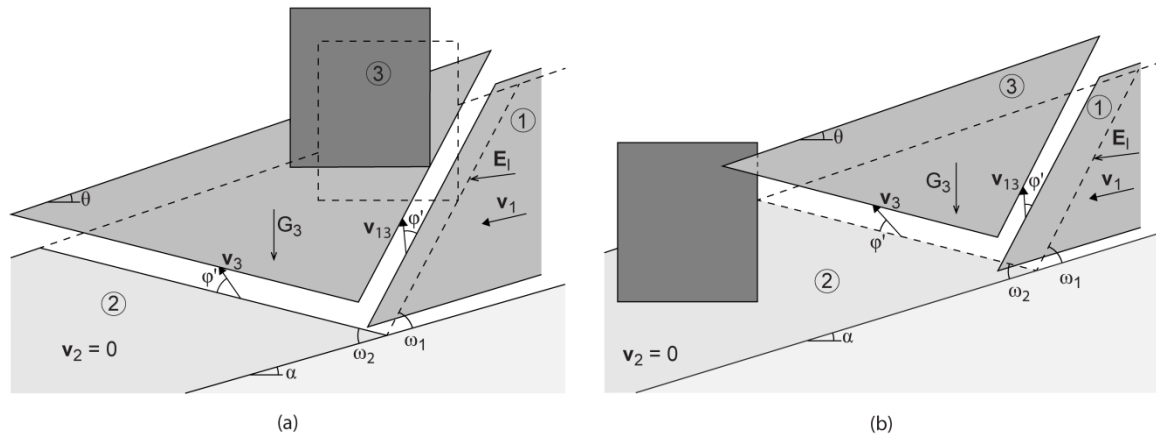


Figure 5-3. (a) Geometry of the global mechanism type 1; (b) geometry of the global mechanism type 2.

Both global mechanisms consist of three blocks bounded by two velocity discontinuities inclined by ω_1 and ω_2 to the slip surface. Block 1 moves downslope with velocity \mathbf{v}_1 , block 2 is at rest, $\mathbf{v}_2 = 0$, and block 3 consists of either the building and the surrounding soil (type 1, Figure 5-3 (a)) or only a soil wedge (type 2, Figure 5-3 (b)) which is pushed upwards with velocity \mathbf{v}_3 . The derivation of the velocities from the hodograph and the expressions for the weights contributing to the work equation are presented in Appendix 5-2. Formulating the work equation

$$\dot{W}_e = \mathbf{E}_l \cdot \mathbf{v}_1 + \mathbf{G}_3 \cdot \mathbf{v}_3 = \dot{D}_i = 0 \quad (5-9)$$

allows solving for the force required to cause global failure of the sliding body \mathbf{E}_l . Note that the force \mathbf{E}_l acts along the velocity discontinuity between block 1 and 3.

For the global mechanism type 1 the horizontal component of this force results in

$$\begin{aligned} E_{lh1} = & \left\{ \frac{\gamma}{2} \left[\left(t + \frac{(t-d_1)(\tan \alpha - \tan \theta)}{\tan(\alpha + \omega_1) - \tan \alpha} \right)^2 \right. \right. \\ & \cdot \left. \left(\frac{1}{\tan(\alpha + \omega_1) - \tan(\theta)} + \frac{1}{\tan \theta + \tan(\omega_2 - \alpha)} \right) \right] \\ & \left. - \frac{\gamma(d_1^2 - d_2^2)}{2} \cot \theta + G_b \right\} \cdot \frac{\sin(\varphi' - \alpha + \omega_2) \sin(\varphi' + \alpha + \omega_1)}{\sin(2\varphi' + \omega_1 + \omega_2)} \end{aligned} \quad (5-10)$$

This force has to be optimised with the following constraints on the angles of the velocity discontinuities, which follow from geometric (Fig. 3) and kinematic considerations (see Fig. 11 (c) later in the chapter).

$$\begin{aligned} \max\{0; \theta - \alpha\} &\leq \omega_1 \leq \frac{\pi}{2} - \alpha \\ \max\{0; \alpha - \theta\} &\leq \omega_2 \leq \frac{\pi}{2} - \varphi' + \alpha \\ 2\varphi' + \omega_1 + \omega_2 &\leq \pi \\ \omega_2 - \left[\alpha + \arctan \left(\frac{\tan(\alpha + \omega_1)}{\frac{d_1 - d_2}{t - d_1} \cot \theta (\tan(\alpha + \omega_1) - \tan \alpha) - 1} \right) \right] &\leq 0 \end{aligned} \quad (5-11)$$

The horizontal component of the force required to cause failure of the sliding body according to the global mechanism type 2 (Figure 5-3 (b)), corresponds to the solution presented in chapter 3, Friedli et al. (2017):

$$\begin{aligned} E_{lh2} = & \frac{\gamma t^2}{2} \cdot \frac{\cos^2 \alpha \sin(\theta - \alpha + \omega_2) \sin(\varphi' - \alpha + \omega_2)}{\sin \omega_2 \sin(\alpha - \theta + \omega_1) \sin(2\varphi' + \omega_1 + \omega_2)} \\ & \cdot \frac{\sin(\omega_1 + \omega_2) \sin(\varphi' + \alpha + \omega_1)}{\sin \omega_2 \sin(\alpha - \theta + \omega_1) \sin(2\varphi' + \omega_1 + \omega_2)} \end{aligned} \quad (5-12)$$

The angles of the velocity discontinuities in (5-12) have to fulfil the first three constraints of equation (5-11).

5.4.3 Optimisation

The angles of the velocity discontinuities have to be optimised to derive the most critical mechanism. In the presented case the kinematic method provides an upper-bound solution for the load acting on the loads acting on the building. The lowest upper-bound has to be found by optimisation of the solution. Before presenting the optimised loads, a normalisation of the geometry and the weight of the building with respect to the landslide is introduced below.

The ratio between the embedment depth of the downhill wall d_2 and the uphill wall d_1 , is denoted 'embedment ratio' λ :

$$\lambda = \frac{d_2}{d_1} \quad (5-13)$$

The ratio between the embedment depth of the uphill wall d_1 and the thickness of the sliding body t , is denoted 'relative embedment depth' η :

$$\eta = \frac{d_1}{t} \quad (5-14)$$

The ratio between the weight of the building G_b and the weight of the excavated soil of the sliding body, is denoted 'weight compensation ratio' β :

$$\beta = \frac{2G_b}{\gamma(d_1^2 - d_2^2) \cot \theta} \quad (5-15)$$

This ratio is equal to unity, $\beta = 1$, for buildings which exactly compensate the weight of the excavated soil, denoted 'weight compensation' in this chapter.

The force on the uphill wall of the building, derived for the local mechanisms in equations (3) and (5-7) is also normalised

$$K_{uh} = \frac{2P_{uh}}{\gamma d_1^2} \quad (5-16)$$

and can be interpreted as earth pressure coefficient K_{uh} corresponding to a linearly distributed stress increasing with depth. The force on the downhill wall is normalised similarly using the embedment depth d_2 . As the ultimate force required to cause global failure acts over the whole thickness of the sliding body t , equations (5-10) and (5-12) are normalised as follows

$$K_{lh} = \frac{2E_{lh}}{\gamma t^2} \quad (5-17)$$

In the following sections the normalised expressions for the load on the building at local failure and the load in the sliding body at global failure are presented including the respective optimised angles of the velocity discontinuities.

5.4.3.1 Local failure mechanism type 1A

In case of $\omega_1 < \pi/2$ the normalised load on the uphill wall of the building is

$$K_{uh1A} = \left[\sin \delta \left(\cot \theta (1 - \lambda^2) \beta + \frac{1}{\tan \omega_1 - \tan \theta} \right) + \frac{\lambda^2}{\tan \theta - \tan \omega_2} \frac{\sin(\varphi' - \omega_2) \cos 2\delta}{\cos(\varphi' + \delta - \omega_2)} \right] \cdot \frac{\sin(\varphi' + \omega_1)}{\sin(\varphi' + \delta + \omega_1)} \quad (5-18)$$

with the optimised angle ω_1

$$\omega_1 = -\varphi' + \arccot \left(\cot(\varphi' + \theta) + \frac{\tan \varphi' + \cot(\varphi' + \theta)}{\chi(\tan \varphi' + \tan \theta) - 1} \right) \cdot \left[1 - \sqrt{1 + \frac{\chi(\tan \varphi' + \tan \theta) - 1}{\tan(\varphi') + \cot(\varphi' + \theta)} (\cot(\varphi' + \theta) + \cot \delta)} \right] \quad (5-19)$$

where χ is

$$\chi = \cot \theta (1 - \lambda^2) \beta + \frac{\lambda^2 \sin(\varphi' - \omega_2) \cos 2\delta}{(\tan \theta - \tan \omega_2) \cos(\varphi' + \delta - \omega_2) \sin \delta} \quad (5-20)$$

The optimised angle ω_2 is

$$\omega_2 = \varphi' - \arccot \left(-\tan \varphi' + \sqrt{(\cot(\varphi' - \theta) + \tan \varphi')(\tan \varphi' + \tan \delta)} \right) \quad (5-21)$$

The normalised horizontal force on the downhill wall is

$$K_{dh1} = \frac{\tan(\varphi' - \omega_2)}{(1 - \tan(\varphi' - \omega_2) \tan \delta)(\tan \theta - \tan \omega_2)} \quad (5-22)$$

The angle of the second velocity discontinuity ω_2 given in equation (5-21) also optimises the force on the downhill wall.

5.4.3.2 Local failure mechanism type 1B

In case of $\omega_1 = \pi/2$ the normalised load is

$$K_{uh1B} = \frac{\cos \delta}{\cos 2\delta} \left[\sin \delta \cot \theta (1 - \lambda^2) \beta + \frac{\lambda^2 \sin(\varphi' - \omega_2) \cos 2\delta}{(\tan \theta - \tan \omega_2) \cos(\varphi' + \delta - \omega_2)} \right] \quad (5-23)$$

where the optimised expression for ω_2 given in equation (5-21) is still valid and the normalised force on the downhill wall is still described by (5-22).

5.4.3.3 Local failure mechanism type 2A

Similarly for the mechanism type 2 in case of $\omega_1 < \pi/2$ the normalised load on the building is

$$K_{uh2A} = \left[\left(\frac{1}{\tan \omega_1 - \tan \theta} + \frac{1}{\tan \theta - \tan \omega_2} \right) + \cot \theta (1 - \lambda^2)(\beta - 1) \right] \frac{\sin(\varphi' - \omega_2) \sin(\varphi' + \omega_1)}{\sin(2\varphi' + \omega_1 - \omega_2)} \quad (5-24)$$

For this case the angles of the velocity discontinuities, ω_1 and ω_2 , have been optimised numerically. A closed solution can only be presented for the special case of weight compensation, $\beta = 1$

$$\omega_1 = \frac{1}{2} \left[\arccos \left(-\frac{\sin \theta}{\sin \varphi'} \right) - \varphi' + \theta \right] \quad (5-25)$$

$$\omega_2 = \omega_1 + \varphi' - \frac{\pi}{2}$$

provided that the angle of the second velocity discontinuity is inclined downslope $\omega_2 > 0$.

5.4.3.4 Local failure mechanism type 2B

In case of $\omega_1 = \pi/2$ the normalised load is

$$K_{uh2B} = \left[\left(\frac{1}{\tan \theta - \tan \omega_2} \right) + \cot \theta (1 - \lambda^2)(\beta - 1) \right] \frac{\sin(\varphi' - \omega_2) \cos \delta}{\cos(\varphi' + \delta - \omega_2)} \quad (5-26)$$

And the corresponding optimised angle of the velocity discontinuity is

$$\omega_2 = \varphi' - \arccot \left(-\tan \varphi' + \sqrt{(\cot(\varphi' - \theta) + \tan \varphi')(\tan \varphi' + \tan \delta)} \right) \quad (5-27)$$

5.4.3.5 The critical local failure mechanism

As these normalised loads of the building are all upper-bounds, the mechanism leading to the minimum load represents the most critical mechanism. Therefore the minimum value among the solutions given by equations (5-18), (5-23), (5-24) and (5-26) is used depending on the geometry, weight and strength parameters.

$$K_{uh} = \min\{K_{uh1A}, K_{uh1B}, K_{uh2A}, K_{uh2B}\} \quad (5-28)$$

The ultimate force on the downhill wall is only defined in the local mechanism types 1A and 1B by equation (5-22), which corresponds to the passive earth pressure coefficient using a translational mechanism (*e.g.*, Coulomb 1776; Müller-Breslau 1906).

5.4.3.6 Global failure mechanisms

For the global mechanism type 1, involving the building, the normalised force in the sliding body is derived from equation (5-10).

$$K_{lh1} = \frac{\sin(\varphi' - \alpha + \omega_2) \sin(\varphi' + \alpha + \omega_1)}{\sin(2\varphi' + \omega_1 + \omega_2)} \cdot \left[\left(1 + (1 - \eta) \frac{\tan \alpha - \tan \theta}{\tan \omega_1 - \tan \alpha} \right)^2 \left(\frac{1}{\tan(\alpha + \omega_1) - \tan \theta} + \frac{1}{\tan \theta + \tan(\omega_2 - \alpha)} \right) - \eta^2 \cot \theta (1 - \lambda^2)(1 - \beta) \right] \quad (5-29)$$

In this case the optimised angles of the velocity discontinuities could not be derived in closed-form, therefore they have to be optimised numerically.

For the global mechanism type 2 the normalised force is derived from equation (5-12).

$$K_{lh2} = \frac{\cos^2 \alpha \sin(\theta - \alpha + \omega_2) \sin(\varphi' - \alpha + \omega_2) \sin(\omega_1 + \omega_2) \sin(\varphi' + \alpha + \omega_1)}{\sin^2 \omega_2 \sin(\alpha - \theta + \omega_1) \sin(2\varphi' + \omega_1 + \omega_2)} \quad (5-30)$$

For general slope and slip surface inclinations the optimised angles of the velocity discontinuities could also not be derived analytically. However, in the special case of slope parallel slip surface ($\alpha = \theta$) the angles

$$\omega_1 = \frac{1}{2} \left(\arccos \left(-\frac{\sin \theta}{\sin \varphi'} \right) - \varphi' - \theta \right) \quad (5-31)$$

$$\omega_2 = \frac{\pi}{2} - \varphi' - \omega_1$$

optimise equation (5-30) and the corresponding normalised force acting in the sliding body results in

$$K_{lh2}(\alpha = \theta) = \frac{\cos^4 \theta}{\cos^2 \varphi'} \left(1 + \sqrt{1 - \cos^2 \varphi' (1 + \tan^2 \theta)} \right)^2 \quad (5-32)$$

which corresponds to the exact solution of the ‘landslide pressure’ coefficient presented in chapter 3, Friedli et al. (2017).

5.5 Finite element model

The above presented upper-bound solutions allow only the evaluation of the limit state and no conclusion can be drawn regarding the evolution of the loads on a building either before or after reaching the local failure. Furthermore, for local failure, the velocity step had to be introduced beneath the building which is a simplification of the actual elastic-plastic compression of the sliding body. To validate the assumptions and the results, the loading process of a building in a landslide was modelled using the FEM.

The commercial FEM Code Abaqus/Standard (Dassault Systèmes Simulia Corp., RI, USA) was used to model the landslide with the embedded building in plane strain conditions. The geometry of the model is shown schematically in Figure 5-4. Only the case with slope parallel slip surface $\theta = \alpha$ was investigated with the FEM. The material of the sliding body was modelled using a linear elastic – perfectly plastic constitutive law with the Mohr-Coulomb failure criterion. Note, that the built-in Mohr-Coulomb model in Abaqus uses a smooth plastic potential surface (Menétrey & Willam 1995) which does not allow modelling associated flow in the deviatoric plane and only approximates associated flow in the meridional planes. To model associated flow, the dilation parameter ψ was chosen to match as close as possible the plastic potential to the failure surface in the meridional plane. The influence of the flow rule has been analysed by comparing the results in additional simulations where only half of the dilation was used. The embedded building was modelled as linear elastic, with significantly higher stiffness than the soil body; the contact between the building and the surrounding soil was modelled with frictional interfaces. The interfaces in Abaqus use a non-dilative flow rule. At the uphill end of the model an elastic block was tied to the sliding body to prevent failure at this boundary. Note that due to the used constitutive model for the soil and the interfaces, the FEM simulations do not fully match the assumptions of limit analysis for the flow rule.

The initial stress state in the model was introduced by applying the gravity loading as a body force both to the soil and the building. The exact stresses depend therefore on this loading and the elasto-plastic constitutive model and strongly depend on the Poisson ratio which was chosen as $\nu = 0.3$. Note that the apparent initial earth pressure coefficients at the uphill and the downhill

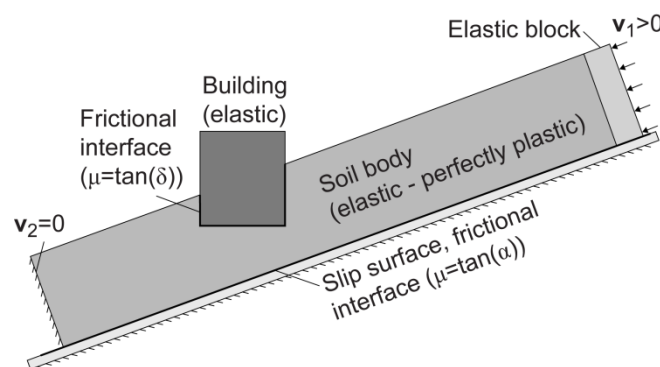


Figure 5-4. Geometry and boundary conditions of the finite element model in ABAQUS.

walls in the model are not identical because the wall heights differ (otherwise equilibrium of forces would not be fulfilled). After applying the gravity loading, the entire sliding body was displaced downslope ($v_1 = v_2 > 0$) to mobilise the interface resistance along the full length of the slip surface. Then the bottom of the landslide was kept at rest ($v_2 = 0$) and the sliding body was compressed applying a velocity boundary condition on the elastic block ($v_1 > 0$) until first local and afterwards global failure occurred. During this process the contact pressure at the interfaces around the building, the horizontal force in the remaining part of the sliding body beneath the building as well as the horizontal force at the top of the landslide were evaluated.

5.6 Results

5.6.1 Loads on the uphill wall

The limit analysis solutions are shown in Figure 5-5 (a) (solid thick lines) for the special case of weight compensation, $\beta = 1$, and a constant embedment ratio, $\lambda = 0.5$, for three different angles of internal friction of the sliding body, φ' . It is shown that increasing strength of the sliding body leads to increasing ultimate loads on the building which is a result of the increased resistance against local failure. The zones 1A and 2A show the regions where the corresponding local mechanism provides the lowest upper-bound. At low slope inclinations the local mechanism type 1A dominates and the corresponding loads are high, only capped by the passive earth pressure (that is, formation of a classical passive failure on the uphill wall of the building). The passive earth pressure shown in Figure 5-5 (a) corresponds to the log-sandwich upper-bound solution according to Chen (1975). With increasing slope inclination the loads decrease and for moderate slopes the local mechanism 1A and 2A result in the same loads (shaded region in Figure 5-5 (a)). At steeper slopes, characterised by the condition

$$\theta \geq \operatorname{arccot} \left(\frac{1 + \sin^2 \varphi'}{\sin \varphi' \cos \varphi'} \right) \quad (5-33)$$

the mechanism 2A becomes solely governing and the normalised force K_{uh} coincides with the landslide pressure coefficient (5-32), (chapter 3, Friedli et al. 2017). Note that the landslide pressure solution results from a global mechanism and it is normalised over the height of the sliding body t , whilst the normalisation of the forces from the local mechanisms is done over the embedment depth of the uphill

wall d_1 . In Figure 5-5 the normalised force K_{uh} derived from the local mechanisms is equal or higher than the normalised force from the global mechanism. However, considering the relative embedment depth $\eta=0.5$, the total force acting on the building is actually lower than the total force derived from the landslide pressure. At low slope inclination and high relative embedment depth η it is possible that the landslide pressure mechanism is reached before local failure could appear. This scenario did not appear to be relevant in the investigated cases.

Similar to the strength of the soil, increasing the interface strength between the building and the sliding body results in significantly higher ultimate loads on the building (Figure 5-5 (b)). In cases with low interface friction and high slope inclination the normalised force calculated using the local mechanisms may even drop below the active earth pressure coefficient, which means that the building would slip under active earth pressure.

Note that in Figure 5-5 (a) and (b) the embedment ratio, λ , is kept constant which means that the width of the building increases with decreasing slope inclination. This explains the significant increase of the normalised force at low slope inclination. For a building with constant width, λ increases with decreasing slope and the corresponding loads are lower. However, for the presented special case with $\beta = 1$ and $\delta = \varphi'$ the results shown in Figure 5-5 (a) actually hold for any λ as long as the local mechanism type 2A is governing and therefore the width of the building has no influence. This is shown in Figure 5-5 (c) where the loads are presented depending on the weight compensation ratio β for different λ . Further it is shown that for buildings lighter than the excavated soil, $\beta < 1$, the ultimate loads decrease, while for heavier buildings, $\beta > 1$ they increase.

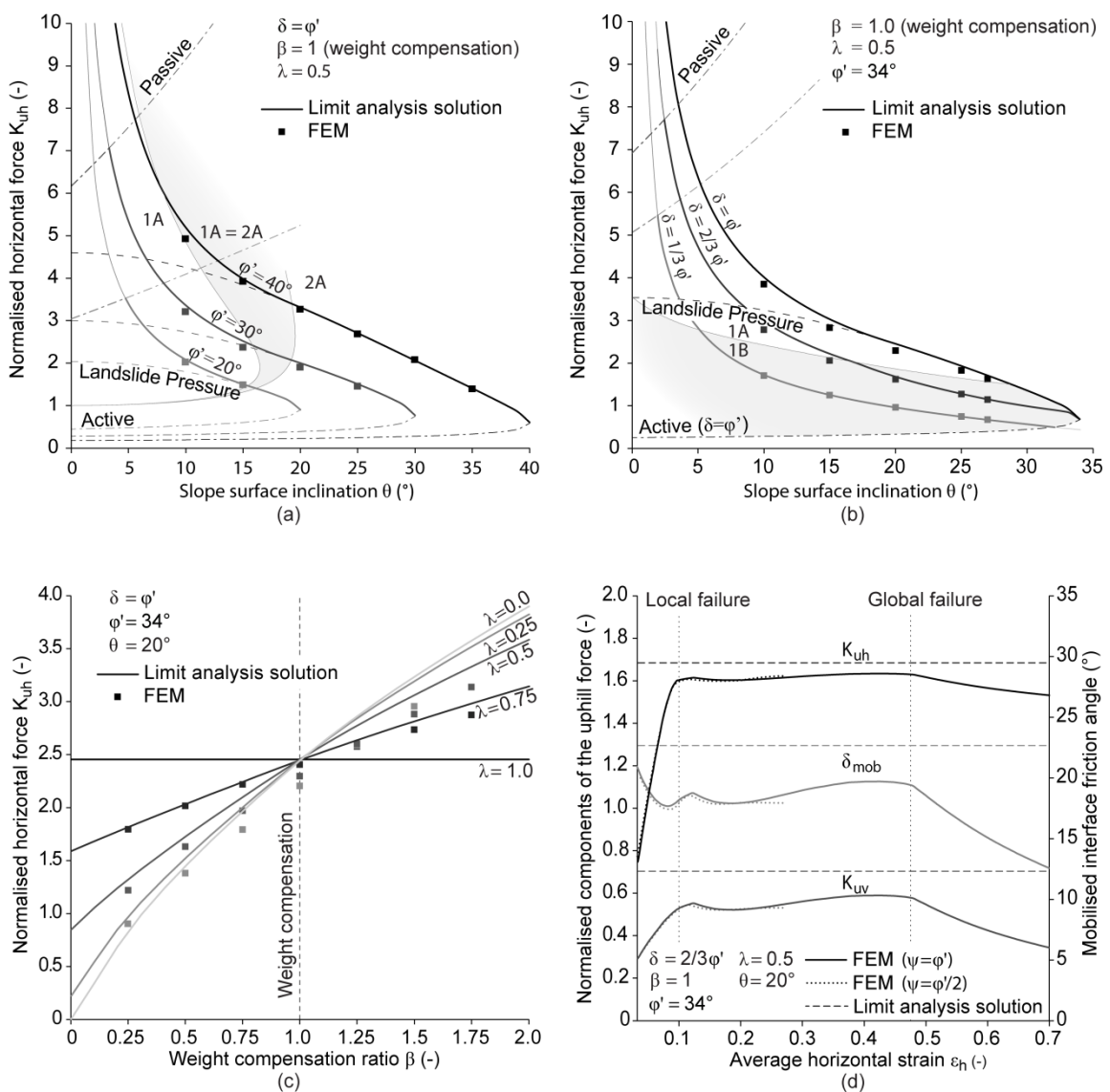


Figure 5-5. Normalised horizontal force K_{uh} on the uphill wall ($\eta = 0.5$): (a) depending on the slope inclination θ for three different φ' ; (b) depending on the slope inclination θ for three different interface friction ratios δ/φ' ; (c) depending on the weight compensation ratio β for different embedment ratios λ ; (d) evolution of the components of K_u in the FEM model.

In Figure 5-5 (d) the evolution of the loads on the uphill wall of the building (depending on the average horizontal strain ε_h in the vicinity of the building) is presented for one particular set of parameters according to the FEM simulation. The average horizontal strain, ε_h , is calculated as the ratio of the relative horizontal displacement of the sliding layer between two points, chosen uphill and downhill from the building outside the expected range of the local mechanism, and the horizontal distance between these two points. Starting from an initial loading, which in our analysis is rather low ($K_0 \approx 0.4$), the horizontal (K_{uh}) and the vertical components (K_{uv}) of the force on the uphill wall increase to the point when local failure is reached. Afterwards, further compression of the landslide does not lead to increasing forces on the building until eventually the whole sliding body fails. Once this global failure has occurred a redistribution of the forces from the uphill wall to the remaining part of the sliding body beneath the building can take place. This leads to a slight decrease in the wall force and confirms that the local mechanism determines the ultimate load on a building in a landslide. Plots of the plastic strain magnitudes at local and global failure are shown in Appendix 5-3. The loads calculated with a non-associated flow rule ($\psi = \varphi'/2$) are similar to the other solutions (load evolution is indicated with a dotted line in Figure 5-5 (d)). The influence of the dilatancy is limited because the problem is not overly constrained.

The results of the FEM simulations at local failure are also presented in (Figure 5-5 (a), (b) and (c)). These results are quite close to the developed upper-bound solutions using limit analysis and represent some validation of the results. For heavy buildings, the solution deviates more from the FEM simulations (Figure 5-5 (c)). This is a shortcoming of the considered translational mechanisms which are not able of capturing local bearing capacity failure beneath the downhill edge of the building, observed in the FEM simulations.

5.6.2 Loads on the downhill wall

The force on the downhill wall calculated from the local mechanisms type 1 is presented in Figure 5-6 (a) depending on the slope inclination θ with $\varphi' = 34^\circ$ for different interface frictions δ . Since in the local mechanisms type 2 no interface failure occurs between the downhill wall and the soil, limit analysis does not allow evaluating the force acting on this wall. Similar to the uphill wall the force decreases with increasing slope inclination and the values lie closely to the classical passive earth pressure.

In Figure 5-6 (b) the evolution of the force components acting on the downhill wall are presented for the same set of parameters used for Figure 5-5 (d). Similarly, the horizontal component (K_{dh}) and the vertical component (K_{dv}) of the force increase until local failure is reached. After this point the force remains constant even when reaching global failure. The interface friction is mobilised almost over the whole depth of the downhill wall, only close to the downhill edge the stress field is disturbed which slightly reduces the vertical component of the force.

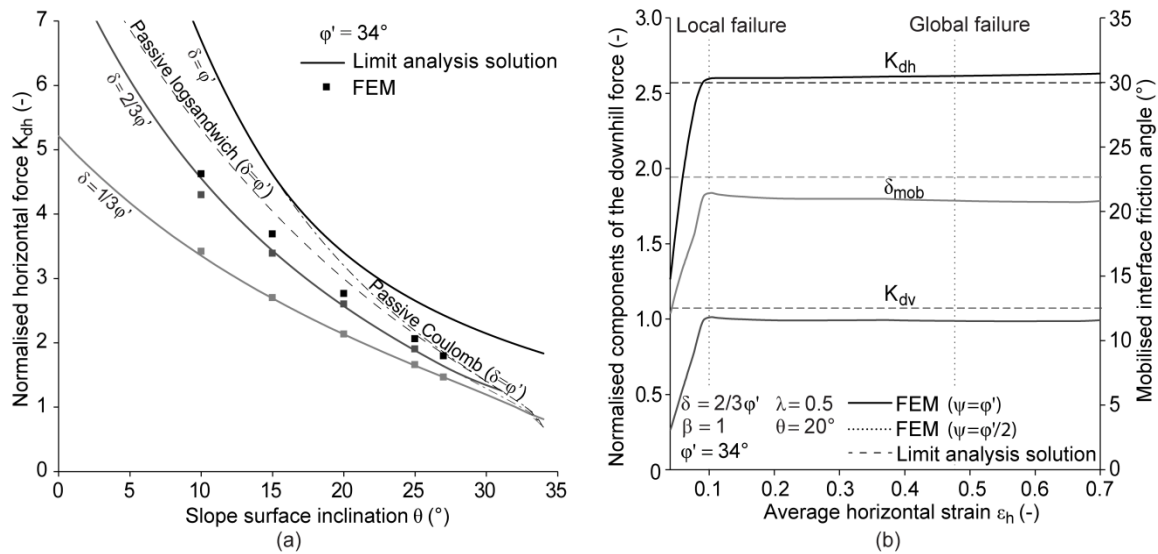


Figure 5-6. Normalised horizontal force K_{dh} acting on the downhill wall: (a) depending on the slope inclination θ for different interface friction ratios δ/ϕ' ; (b) evolution of the components of K_d in the FEM model using the same parameters as in Figure 5 (d).

The comparison of the FEM results with the upper-bound solution is also shown in Figure 5-6 (a). While the two models compare well for low interface friction angles, δ , the proposed local mechanism overestimates the forces significantly for $\delta = \phi'$. As the mechanism consists of one translational wedge at the downhill wall, it is basically identical to the classical Coulomb passive earth pressure mechanism (Coulomb 1776). However, the single degree of freedom, together with the associated flow rule overly constrains the mechanism at higher slope inclinations. This is reflected in higher load values compared to the Coulomb solution. Introducing more degrees of freedom, for example, by using a log-sandwich mechanism (*e.g.*, Chen 1975) to calculate the passive earth pressure, provides an upper-bound closer to the FEM solution. This leads to the conclusion that the ultimate load on the downhill wall should be calculated using the best available passive earth pressure solution.

5.6.3 Force on the building base

In case of the local mechanism type 1 the force acting on the building base, \mathbf{R}_{23} , can be derived from equilibrium of forces on the building (Figure 5-2 (b)). Using upper-bound limit analysis does only allow finding the total force on the base but not its distribution. Note that in local mechanism type 2 no failure occurs along the downhill wall and the base of the building (Figure 5-2 (d)) and therefore the force acting along these interfaces cannot be determined.

5.6.4 Force in the sliding body

The influence of the relative embedment depth, η , on the ultimate force in the sliding body is illustrated in Figure 5-7 (a) depending on the slope inclination θ for a light ($\beta = 0.5$) and a heavy ($\beta = 1.5$) building. The normalised force of the global failure mechanism type 2 (that is, the landslide pressure) is independent of the building properties. In contrast the force of the global mechanism type 1 strongly depends on the size and the weight of the building, as it contributes to the external work.

For a heavy building ($\beta > 1$) the force according to the global mechanism type 1 increases with increasing embedment depth η . However, for such buildings the global mechanism type 2 always provides lower forces. Therefore all values of mechanism type 1 that lie above the line for the global mechanism type 2 (landslide pressure) in Figure 4-7 (a) cannot be reached. For a light building ($\beta < 1$), in moderate to steep slopes, the force decreases with increasing embedment depth. In mildly inclined slopes the building acts as a geometrical constraint and therefore even light buildings cause a significant increase of the force, potentially exceeding the landslide pressure. At weight compensation ($\beta = 1$) the force given by both global mechanisms is equal and therefore this point represents the switchover between the two mechanisms (Figure 5-7 (b)). However, for strongly embedded buildings in mild slopes, where the geometrical constraint of the building increases the force, the landslide pressure becomes governing also for buildings lighter than those with weight compensation (Figure 5-7 (b), $\theta = 10^\circ$).

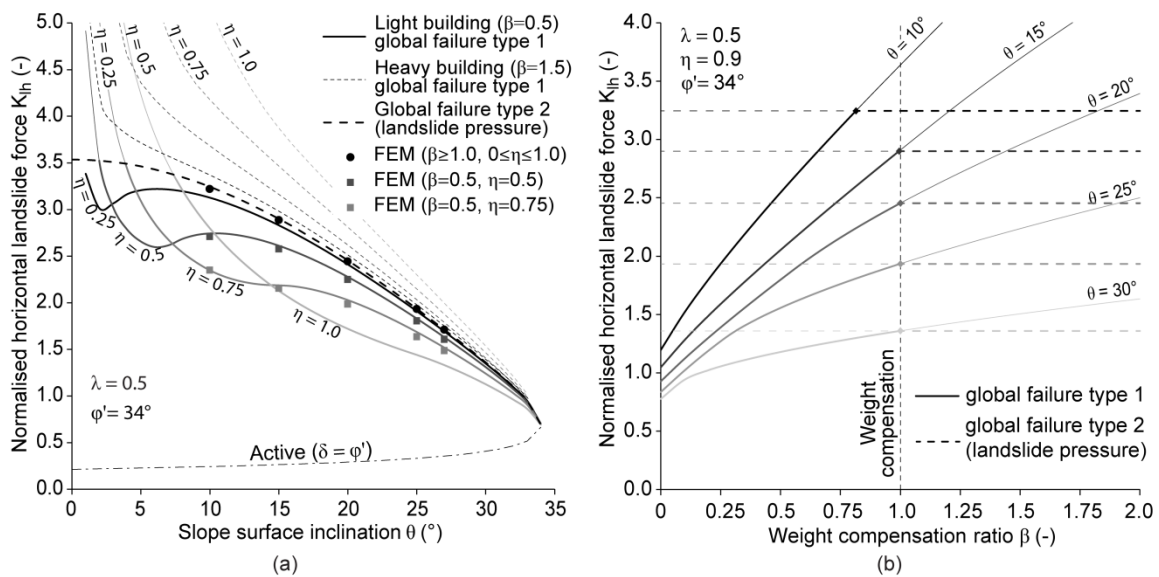


Figure 5-7. Normalised horizontal forces in the sliding body K_{lh} at global failure: (a) depending on the slope inclination θ , the weight compensation ratio β and the relative embedment depth η ; (b) depending on the weight compensation ratio β and the slope inclination θ .

The results of the FEM analysis (Figure 5-8) show the evolution of the total normalised horizontal force in the sliding body upslope of the building K_{lh} , the normalised horizontal force on the building $2P_{uh}/(\gamma t^2)$ and the normalised horizontal force in the remaining part of the sliding body beneath the building $2R_{12h}/(\gamma t^2)$. Note that all forces are normalised using the thickness of the sliding body t . Starting from the initial conditions all three forces increase until the force on the building reaches its maximum at local failure. All additional loading caused by the landslide is redistributed through the remaining part of the sliding body beneath the building until a plateau is reached. At this point the global mechanism has fully developed and no further loading is possible (see plastic strain increment plot in Appendix 5-3). Nevertheless, a further redistribution from P_{uh} to R_{12h} is possible which leads to a slight unloading of the wall. In the FEM analyses this redistribution was only observed in cases with reduced interface strength.

The FEM analysis shown in Figure 5-8 was performed with reduced interface friction $\delta = 2/3 \varphi'$. A part of the failure took place along the base of the building (see Appendix 5-3, Figure 5-12 (b)) and therefore the total force is slightly lower compared to the analytical solution. For not reduced interface friction, however, the limit analysis solution is close to the FEM results (Figure 5-7 (a)). Note that in the case of heavy buildings, $\beta > 1$, the global failure mechanism does not include the building and coincides with the landslide pressure. Therefore, the FEM results coincide with the results of a building with weight compensation, $\beta = 1$.

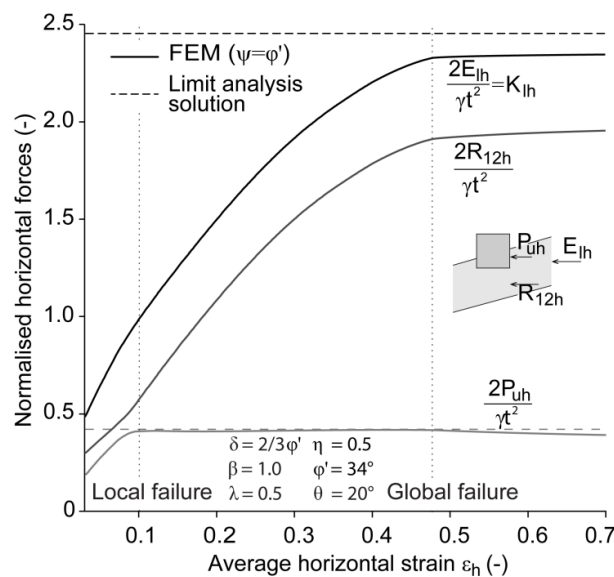


Figure 5-8. Evolution of normalised horizontal forces in the FEM model using the same parameters as in Figure 5-5 (d).

5.6.5 Approximation of the time to local failure

Though the upper-bound solution allows estimating the ultimate loads on a building at the limit state, the time necessary to reach this state remains an open question. With a parametric study using the FEM the strain needed to reach this state was investigated (Figure 5-9). For different average soil stiffness the necessary mean horizontal strain in the vicinity of the building to reach local failure was evaluated.

If the strain rate in a landslide is known, the critical average horizontal strain ε_{hf} in the vicinity of the building can be transformed into the time needed to reach local failure. For example in the Brattas landslide in St. Moritz, Switzerland, an average compression strain rate of $0.2 \text{ mm}/(\text{m} \cdot \text{year})$ has been observed in large parts of the built-up area (internal report IGT 1994), leading to the local failure times provided in the second ordinate of Figure 5-9. In this example, for reasonable ranges of the building weight and the stiffness of the sliding body the local failure is reached after 3÷30 years, which is likely to be within the lifetime of a building. Only very heavy buildings require more time to reach local failure. Note that the time to failure increases with decreasing initial stresses. In the FEM analysis the initial stresses were rather low ($K_0 \approx 0.4$) therefore the analysis represents an upper estimate for the time until local failure is reached.

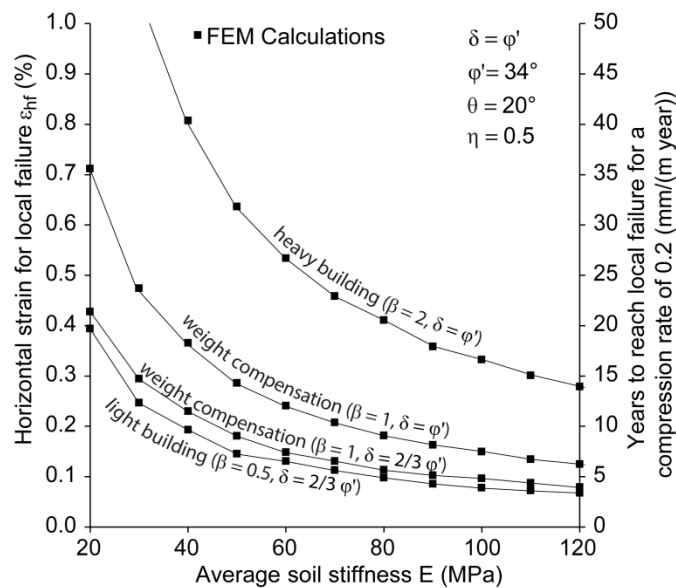


Figure 5-9. Critical horizontal strain needed to reach local failure depending on the stiffness of the soil for an example case.

5.7 Conclusions

The loads on the buildings embedded in permanently moving landslides increase over time, eventually leading to a local limit state where the soil in the vicinity of the building fails. In this work the ultimate loads have been quantified for the special case of a building in the compression zone of a landslide. The applied limit analysis and the FEM proved to be suitable tools for the evaluation of the limit loads and the loading history, respectively.

It was demonstrated that, compared to stable slopes, the loads on a building in a landslide can be significantly higher. As the analytical solutions are derived using the kinematic method they represent upper-bounds of the loads. The solutions are applicable for the assessment of existing and the design of new buildings in landslides, potentially preventing future damage. In addition to the geometry of the building and the slope, the only parameters needed for such an analysis are the soil friction, the interface friction, the weight of the soil and the building. Note that, from equations (5-18), (5-23), (5-24) and (5-26) it follows that the ultimate load on the building is independent of the depth and inclination of the slip surface.

Further compression of the landslide after the local limit state leads to a global failure of the whole sliding body. Buildings lighter than the excavated soil may evoke such a failure in their vicinity at a lower force in the sliding body and therefore earlier in time.

The results of the local and global failure mechanisms allow the discussion of the following design concepts for buildings in the compression zone of permanently moving landslides.

- (i) Preventing the local limit state during the lifetime of a building should keep the relative displacements low in its vicinity. This might reduce damage to connected non-ductile structures such as pipes or electrical lines. However, it was shown that significant delay in local failure can only be achieved for heavy buildings resulting in higher ultimate loads.
- (ii) Light buildings with low interface friction experience lower ultimate loads resulting in a cheaper structure. It may, however, lead to accelerated global failure in the vicinity of the building and therefore such a weakening of the sliding body should be avoided.
- (iii) The results derived from the local and global failure mechanisms suggest that in order to avoid premature global failure and at the same time minimise the loads acting on the building, it should be designed to imitate the sliding body by using weight compensation and high interface strength.

For the proposed design case of not reduced interface strength ($\delta = \varphi'$) and weight compensation ($\beta = 1$), in average to steep slopes the ultimate loads on the uphill wall of a building coincide with the landslide pressure calculated using equation (5-32). In other cases the minimum load derived from the four local mechanisms, equation (5-28), is to be applied. In contrast the limit state of the soil at the downhill wall corresponds to the classical passive earth pressure problem

and therefore these well-known solutions can be used. The ultimate loads on the uphill and the downhill wall can be used to design the bending and shear capacity of the respective walls. Furthermore, it should be noted that the load transfer between these exterior walls and the bottom plate has to be studied carefully. The solutions for the ultimate loads on a rectangular building where derived on the assumption of plane strain conditions, homogeneous soil and constant velocity field over the depth of the sliding body, imposing some limitations on their application. The presented approach of investigating the local and global limit states, however, could be extended to more general building and slope geometries, other velocity fields (for example in extension zones or shear zones) and 3D situations.

5.8 Appendix 5-1: Discrete velocity step

The solution of the local limit state requires the introduction of a discrete velocity step in the sliding body beneath the building. Here, the influence of a continuous velocity gradient is investigated (Figure 5-10 (a)). The velocity decreases between the uphill edge of the building, point A, and a certain point along the base, point D. While above the building the sliding body moves at the velocity v_1 it is at rest downslope of point D, $v_2 = 0$. The construction of the hodograph (Figure 5-10 (b)) shows that only between point D and E, where the underlying soil is at rest, the relative velocities coincide with the absolute velocity of the building v_3 . Between point A and D the relative velocities are inclined with respect to the absolute velocity of the building resulting in a tension crack in the interface. The admissibility of this tension crack is shown in Figure 5-10 (c) and as cohesionless material was considered no internal dissipation has to be taken into account. The position of point D can be shifted along the base of the building with the two extremes of point D equal to point A or point E, in any case the velocity field remains kinematically admissible. Note that the absolute velocity of the building is not altered by the location of point D, which leads to the conclusion that the exact velocity field in the sliding body has no influence on the external work rate done by the building.

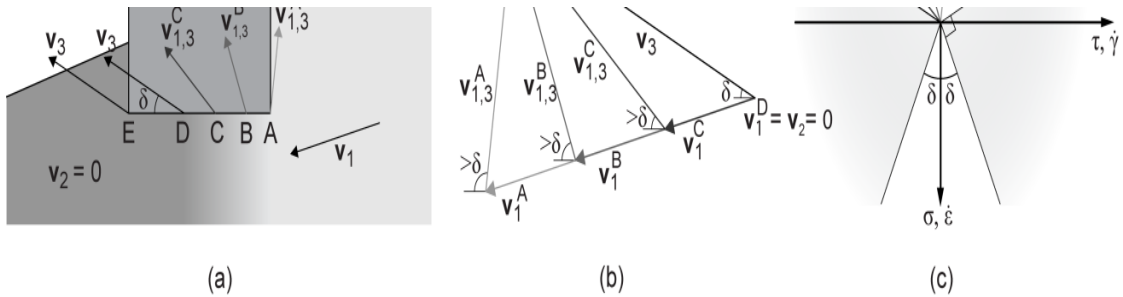


Figure 5-10. Velocity step beneath the building for the local failure mechanism type 1: (a) geometry, velocity field and relative velocity along the base; (b) hodograph; (c) velocity vectors in the $\tau - \sigma$ space.

5.9 Appendix 5-2: Hodographs and weights

To derive the work equation the velocities of all the moving blocks are expressed as a function of the geometry and the velocity of the landslide v_1 . The hodographs are illustrated in Figure 5-11 (a) for the local mechanism type 1, in Figure 5-11 (b) for the local mechanism type 2 and in Figure 5-11 (c) for both types of global mechanisms. The velocity of the uphill part of the sliding body is inclined by ζ with respect to the horizontal.

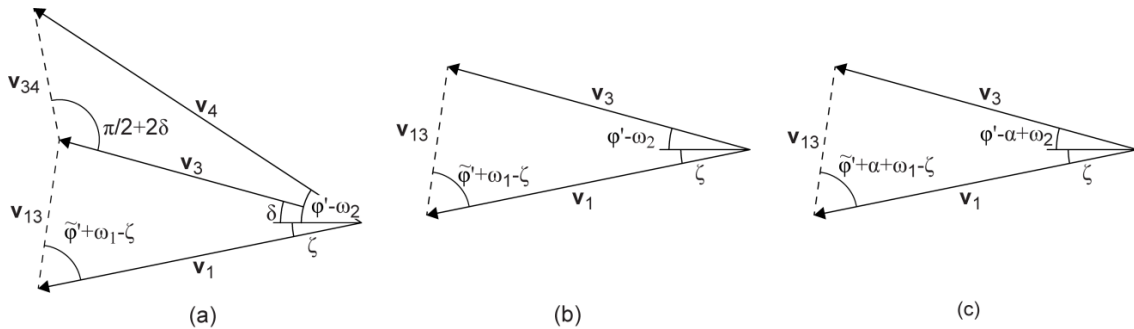


Figure 5-11. Hodographs for: (a) the local failure mechanism type 1; (b) the local failure mechanism type 2; (c) the global failure mechanism type 1 and type 2

5.9.1 Local failure mechanisms

For the local mechanism type 1 the velocity ratios between block 3 and 1 is derived to

$$\frac{|v_3|}{|v_1|} = \frac{\sin(\tilde{\varphi}' + \omega_1 - \zeta)}{\sin(\tilde{\varphi}' + \delta + \omega_1)} \quad (5-34)$$

and between block 4 and 1 it is

$$\frac{|v_4|}{|v_1|} = \frac{\cos 2\delta}{\cos(\varphi' + \delta - \omega_2)} \frac{\sin(\tilde{\varphi}' + \omega_1 - \zeta)}{\sin(\tilde{\varphi}' + \delta + \omega_1)} \quad (5-35)$$

The weight of block 3 is the sum of the weight of the building G_b and the weight of the uphill wedge. Block 4 only consists of a single soil wedge.

$$\begin{aligned} |G_3| &= G_b + \frac{\gamma d_1^2}{2} \frac{1}{\tan \omega_1 - \tan \theta} \\ |G_4| &= \frac{\gamma d_2^2}{2} \frac{1}{\tan \theta - \tan \omega_2} \end{aligned} \quad (5-36)$$

For the local mechanism type 2 only the velocity ratio

$$\frac{|v_3|}{|v_1|} = \frac{\sin(\tilde{\varphi}' + \omega_1 - \zeta)}{\sin(\tilde{\varphi}' + \varphi' + \omega_1 - \omega_2)} \quad (5-37)$$

and the sum of the weight of the building and both soil wedges is required

$$|G_3| = G_b + \frac{\gamma d_1^2}{2} \left(\frac{1}{\tan \omega_1 - \tan \theta} + \frac{1}{\tan \theta - \tan \omega_2} \right) - \frac{\gamma(d_1^2 - d_2^2)}{2} \cot \theta \quad (5-38)$$

For both local failure mechanisms the work equation can be written as follows (for mechanism type 2 set $|G_4| = 0$):

$$|R_{13}| \sin(\tilde{\varphi}' + \omega_1 - \zeta) - |G_3| \frac{|v_3|}{|v_1|} \sin \delta - |G_4| \frac{|v_4|}{|v_1|} \sin(\varphi' - \omega_2) = 0 \quad (5-39)$$

Note that $|R_{13}|$ is independent of ζ when the expressions for the velocity ratios from above are applied.

5.9.2 Global failure mechanisms

The velocity ratios of the two global mechanisms are equal and can be derived with Figure 5-11 (c).

$$\frac{|v_3|}{|v_1|} = \frac{\sin(\varphi' + \alpha + \omega_1 - \zeta)}{\sin(2\varphi' + \omega_1 + \omega_2)} \quad (5-40)$$

The expression for the weight of the block 3 for the global mechanism type 1 results in

$$|G_3| = G_b + \frac{\gamma}{2} \left[\left(t + \frac{(t - d_1)(\tan \alpha - \tan \theta)}{\tan(\alpha + \omega_1) - \tan(\alpha)} \right)^2 \cdot \left(\frac{1}{\tan(\alpha + \omega_1) - \tan \theta} + \frac{1}{\tan \theta + \tan(\omega_2 - \alpha)} \right) - (d_1^2 - d_2^2) \cot \theta \right] \quad (5-41)$$

and for the global mechanism type 2 it is

$$|G_3| = \frac{\gamma t^2 \cos^2 \alpha \sin(\theta - \alpha + \omega_2) \sin(\omega_1 + \omega_2)}{2 \sin^2 \omega_2 \sin(\alpha - \theta + \omega_1)} \quad (5-42)$$

For both global failure mechanisms the work equation can be written as follows

$$|E_l| \sin(\varphi' + \alpha + \omega_1 - \zeta) - |G_3| \frac{|v_3|}{|v_1|} \sin(\varphi' - \alpha + \omega_2) = 0 \quad (5-43)$$

Similar to the local mechanisms the ultimate force in the sliding body at global failure is independent of ζ .

5.10 Appendix 5-3: Plastic strain magnitude increment plots

In Figure 5-12 the plastic strain increments are illustrated for (a) local failure and (b) global failure, considering a building with weight compensation ($\beta = 1$) and reduced interface strength ($\delta = 2/3 \varphi'$). In (c) and (d) local and global failures are illustrated for a heavy building ($\beta = 1.25$) with not reduced interface strength ($\delta = \varphi'$). The analytically derived velocity discontinuities are shown with solid lines for comparison, fitting closely the plastic strain increments of the FEM solutions.

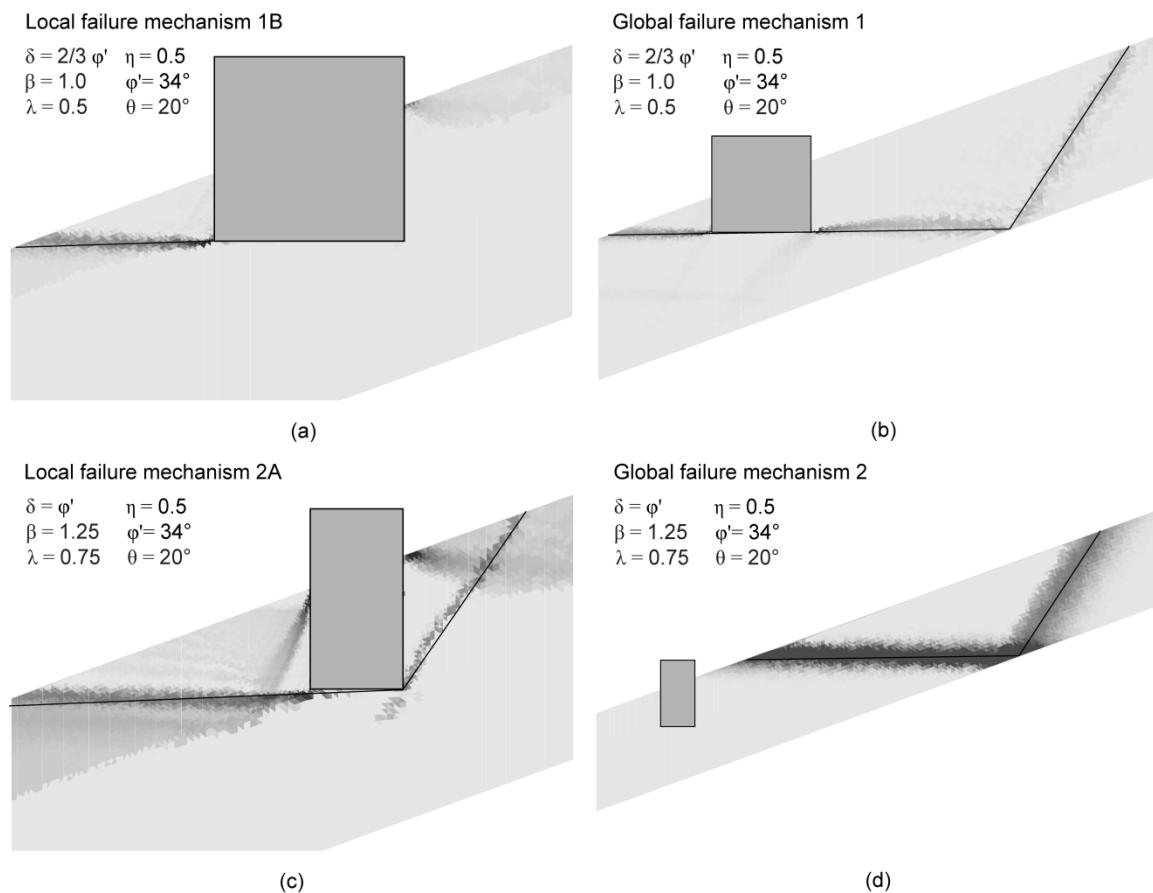


Figure 5-12. Plastic strain magnitude increments: (a) local and (b) global failure for a building with weight compensation and reduced interface friction; (c) local and (d) global failure for a heavy building with not reduced interface friction. Solid lines represent the analytical velocity discontinuities.

5.11 Acknowledgment

I would like to thank my co-authors S. Hug, P. Oberender and A. Puzrin for their help on the derivations of the solutions, the parametric studies and the editing of the manuscript as well as for valuable discussions on the topic.

5.12 Notation

\dot{D}_i	Internal dissipation rate
d_1	Embedment depth of the building at the uphill wall
d_2	Embedment depth of the building at the downhill wall
E	Young's modulus in the FEM Model
\mathbf{E}_l	Total force in the sliding body
E_{lh}	Horizontal component of the force in the sliding body for the global failure mechanisms
G_b	Weight of the building
\mathbf{G}_i	Weight of the rigid blocks in the mechanisms
K_0	At rest earth pressure coefficient
K_{dh}	Normalised horizontal component of the downhill wall force
K_{dv}	Normalised vertical component of the downhill wall force
K_{lh}	Normalised horizontal component of the force in the sliding body
K_{uh}	Normalised horizontal component of the uphill wall force
K_{uv}	Normalised vertical component of the uphill wall force
P_{dh}	Horizontal components of the downhill wall forces
P_{uh}	Horizontal components of the uphill wall forces
\mathbf{R}_{ij}	Internal resistance forces in the mechanisms
R_{ijh}	Horizontal component of an internal resistance force in the mechanism
\mathbf{R}_{ss}	Resistance force on the slip surface
t	Vertical thickness of the sliding body at the uphill wall of the building
\mathbf{v}_i	Velocity for the limit state analysis and velocity of a boundary in the FEM model
\dot{W}_e	External work rate
α	Inclination of slip surface
β	Weight compensation ratio $\beta = 2G_b / ((d_1^2 - d_2^2)\gamma \cot(\theta))$
γ	Unit weight of soil
δ	Soil-building interface friction angle
ε_h	Average horizontal strain in the sliding body (measured between two points outside the range of the local mechanism)
ε_{hf}	Average horizontal strain in the sliding body when reaching local failure
ζ	Inclination of the velocity vector v_1
η	Relative embedment depth $\eta = d_1/t$
λ	Embedment ratio $\lambda = d_2/d_1$
ν	Poisson ratio in the FEM model
θ	Inclination of slope surface
φ'	Angle of internal friction in sliding body
φ'_2	Angle of internal friction in slip surface
$\tilde{\varphi}'$	Friction angle at the uphill velocity discontinuity in the local failure mechanism
ψ	Angle of dilatancy in the FEM model
ω_i	Angle of the velocity discontinuity
χ	Substitution parameter in the solution of the local failure mechanism

5.13 References

- Alexander, D. (1986) Landslide damage to buildings. *Environmental Geology and Water Sciences* **8**, No. 3, 147–151.
- Bernander, S. & Olofsson, I. (1981) On Formation of Progressive Failures in Slopes. In *Proceedings of the 10th international conference on soil mechanics and foundation engineering*, Stockholm, Sweden, vol. 3, 357–362, Rotterdam, the Netherlands: Balkema.
- Brandl, H. & Dalmatiner, J. (1988) *Brunnenfundierungen von Bauwerken in Hängen (insbesondere Brücken)*, Strassenforschung Heft 352. Vienna, Austria: Bundesministerium für Wirtschaftliche Angelegenheiten (in German).
- Caquot, A. & Kérisel, J. (1948) *Tableau de poussée et butée et de force portante des fondation*. Paris, France: Gauthiers-Villars (in French).
- Cascini, L., Peduto, D., Pisciotta, G., Arena, L., Ferlisi, S. & Fornaro, G. (2013) The combination of DInSAR and facility damage data for the updating of slow-moving landslide inventory maps at medium scale. *Natural Hazards and Earth System Sciences* **13**, No. 6, 1527–1549.
- Chen, W.-F. (1975) *Limit Analysis and Soil Plasticity*. Amsterdam, the Netherlands: Elsevier Scientific Publishing Co.
- Coulomb, C.A. (1776) Essai sur une application des règles de maximis & minimis à quelques problèmes de statique, relatifs à l'architecture. *Mémoires de Mathématique & de Physique présentés à l'Académie Royale des Sciences par Divers Savans et Lus sans ses Assemblées* **VII**, 343–382 (in French).
- Cruden, D.M. & Varnes, D.J. (1996) Landslide types and processes. In *Landslides: Investigation and Mitigation*. (eds A.K. Turner and R.L. Schuster), Transportation Research Board Special Report 247, Chapter 3, 36-75. Washington, DC, USA.
- Friedli, B., Hauswirth, D. & Puzrin, A.M. (2017) Lateral earth pressures in constrained landslides. *Géotechnique*, **67**, No 10, 890-905.
- Glade, T., Anderson, M. & Crozier, M.J. (2005) *Landslide hazard and risk*, West Sussex, England: John Wiley & Sons Ltd.
- Haefeli, R. (1944) Zur Erd- und Kriechdruck-Theorie. *Schweizerische Bauzeitung* **124**, No. 20, 256–260 (in German).
- IGT (Institute for Geotechnical Engineering) (1994) *Vorschriften über das Bauen im Brattas-Hang*. Internal Report No. 3922/24, Institute for Geotechnical Engineering, ETH Zurich, Zürich, Switzerland (in German).
- Lateltin, O., Haemmig, C., Raetzo, H. & Bonnard, C. (2005) Landslide risk management in Switzerland. *Landslides* **2**, No. 4, 313–320.
- Mansour, M. F., Morgenstern, N. R. & Martin, C. D. (2011) Expected damage from displacement of slow-moving slides. *Landslides* **8**, No. 1, 117–131.
- Menétrey, Ph. & Willam K.J. (1995) Triaxial Failure Criterion for Concrete and its Generalization, *ACI Structural Journal* **92**, No.3, 311–318.

- Michalowski, R. L. (1989) Three-dimensional analysis of locally loaded slopes. *Géotechnique*, **39**, No. 1, 27–38.
- Müller-Breslau, H.F.B. (1906) *Erddruck auf Stützmauern*. Stuttgart, Germany: Alfred Körner Verlag (in German).
- Oberender, P.W. & Puzrin, A.M. (2016) Observation-guided constitutive modelling for creeping landslides. *Géotechnique* **66**, No. 3, 232–247.
- Palmisano, F., Vitone, C. & Cotecchia, F. (2016) Methodology for Landslide Damage Assessment. *Procedia Engineering*, **161**, 511–515.
- Picarelli, L. (2011) Discussion to the paper “Expected damage from displacement of slow-moving slides” by M. F. Mansour, N. R. Morgenstern and C. D. Martin. *Landslides* **8**, No. 4, 553–555.
- Puzrin, A.M. & Schmid, A. (2011) Progressive failure of a constrained creeping landslide. *Proceedings of the Royal Society A: Mathematical, Physical and Engineering Sciences*, 467(2133), 2444–2461.
- Puzrin, A.M. & Schmid, A. (2012) Evolution of stabilised creeping landslides. *Géotechnique* **62**, No. 6, 491–501.
- Puzrin, A.M. & Sterba, I. (2006) Inverse long-term stability analysis of a constrained landslide. *Géotechnique* **56**, No. 7, 483–489.
- Raetzo, H. & Loup, B. (2016) *Protection against Mass Movement Hazards, UV-1608-E*. Bern, Switzerland: Federal Office for the Environment (FOEN).
- Randolph, M.F. & Houlsby, G.T. (1984) The limiting pressure on a circular pile loaded laterally in cohesive soil. *Géotechnique*, **34**, No. 4, 613–623.
- Rankine, W.J.M. (1857) On the Stability of Loose Earth. *Philosophical Transactions of the Royal Society of London* **147**, No. 84, 9–27.
- Smith, C.C. (1998) Limit loads for an anchor/trapdoor embedded in an associative coulomb soil. *International Journal for Numerical and Analytical Methods in Geomechanics*, **22**, No. 11, 855–865.
- Sokolovskii, V.V. (1960) *Statics of soil media*. London, UK: Butterworths Scientific Publications.
- Urciuoli, G. & Picarelli, L. (2008) Interaction between landslides and man-made works. In *Landslides and Engineered Slopes – From the past to the future. Proceedings of the 10th International Symposium on Landslides and Engineered Slopes* (eds. Z. Chen, K. Ho, F.Q., WU, Z.K. & Li, W. Zheng), vol. 2, 1301–1307, London, UK: Taylor & Francis Group.

PART B: APPLICATIONS OF FIBRE-OPTIC SENSORS IN GEOMECHANICS

6 Ground-buried fibre-optic sensors for object identification

This chapter has been submitted as an article:

Friedli B., Pizzetti L., Hauswirth D. & Puzrin A.M., (2018) Ground-buried fibre-optic sensors for object identification, *ASCE Journal of Geotechnical and Geoenvironmental Engineering*, under review, manuscript submitted 09/05/2017.

6.1 Abstract

Currently available perimeter-security systems use ground-buried fibre-optic sensors to detect objects on the ground surface, and some of them compare the observed signal patterns with those in a predefined library to identify specific types of objects. Such qualitative approaches neglect, however, a wealth of information contained in the measured signal. Here a more rational approach is presented that uses ground-buried distributed fibre-optic strain sensors with very high spatial and strain resolution to quantify the strain field induced by an object in contact with the ground surface. The contact interactions on the ground surface are calculated from the strain measurements using a mechanical soil model and inverse analysis algorithms similar to those used in image deblurring. The approach should enable a variety of applications where the knowledge of contact interactions on the ground surface is beneficial, from biodiversity survey, perimeter security and weigh-in-motion systems to biomechanical applications and sports medicine.

6.2 Introduction

Any object touching the ground applies contact forces to the ground surface. These contact forces induce stresses in the subsurface that in turn lead to a deformation of the ground. Measuring such ground deformations enables the detection and possibly identification of objects on the ground surface, opening up several possible applications. One of them is perimeter security, where ground-buried fibre-optic sensors (FOSs) are used already and offer a number of advantages compared to conventional systems such as ultrasonic, radar or photo-electric sensors. In general, FOSs have high sensitivity, long-distance sensing capabilities and are immune to electro-magnetic interference. They are relatively easy to install in a trench in the ground and they do not require electrical power at the sensing location.

Early intrusion-sensing systems used conventional optical time-domain reflectometry (OTDR) and ground-buried FOSs (Taylor & Lee 1993) to detect frequency shifts induced in the reflected light upon stressing the fibre. This idea was improved on by combining the buried FOSs with different, more quantitative interrogation modalities, including phase-sensitive or coherent OTDR (ϕ -, C-OTDR, Park & Taylor 2003; Owen et al. 2012; Hong et al. 2010; Juarez et al. 2005; Kirkendall et al. 2007; Juarez & Taylor 2007) and Brillouin OTDR (BOTDR, Kwon et al. 2002; Nikles 2009). In a next step towards identifying an intruder, the ‘signature’ of specific events was extracted (Madsen et al. 2007; Madsen et al. 2008). More recently, it was proposed to train the system using a predefined library of signals corresponding to events of interest (Wu et al. 2015). A measured event is then compared to those stored in the system. However, such systems are only able to classify previously known events and may be prone to misclassification caused by environmental influences, such as rain or snow, or seasonal changes in the mechanical behaviour of the ground. Another interesting application of FOSs lies in the detection of underground tunnels (built for smuggling) using BOTDR (Klar & Linker 2010) and swept wavelength interferometry (SWI, Klar et al. 2014) where the tunnels are detected using wavelet decomposition of the measured strain signals.

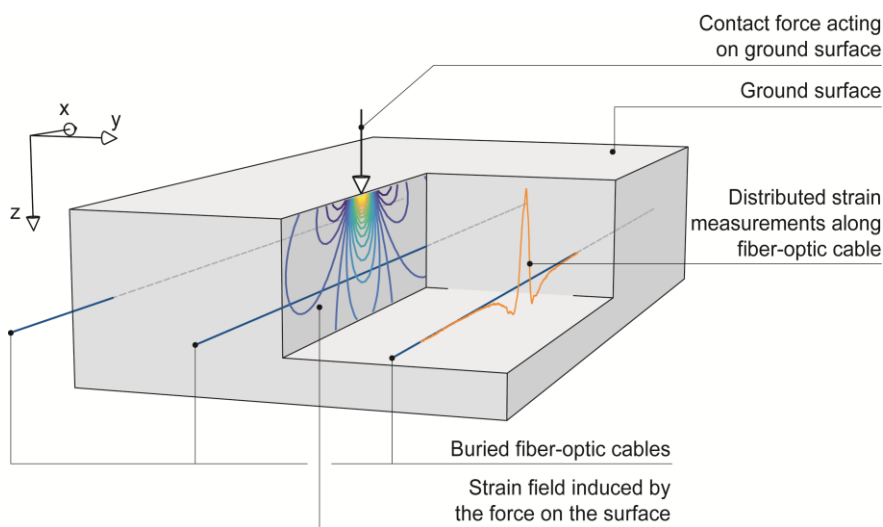


Figure 6-1. Basic principle of object identification with buried fibre-optic cables measuring the strain field induced by surface loads.

To overcome the limitations of currently available intrusion detection systems, distributed FOSs based on SWI to measure Rayleigh scattering (Gifford et al. 2007; Froggatt et al. 2006) in standard single-mode optical fibres are used to quantitatively measure the strain field in the ground (which corresponds to the derivative of the displacement field with respect to the sensor coordinate). Such a strain-sensing system is commercially available (optical backscatter reflectometer (OBR) 4600, Luna Inc., Roanoke VA, US) and enables measuring deformations with an unprecedented strain and spatial resolution of $< 1 \mu\epsilon$ and 5 mm, respectively (Gifford et al. 2007), providing an accurate image of the strain field in the ground along the fibre axis. Here a framework for using such a system for quantitative object identification is established, based on inversely calculating the contact forces acting on the surface from the FOS measurements and a mechanical model of the ground (Figure 6-1). As practical applications are often based on linear systems (for example in perimeter security or in weigh-in-motion of road traffic), the FOSs are buried in a parallel layout in a shallow trench in the ground. Calculating the contact forces acting on the ground surface enables the identification and classification of objects based on their respective contact-force patterns. A patent on the idea of object identification has been filed (Puzrin et al. 2013).

6.3 Experimental setup

For the proof-of-concept demonstration, a test site consisting of a shallow trench in the field was developed; where FOSs have been buried in a serpentine layout with five parallel sections of sensor cables (Figure 6-2). The length of each section is approx. 6 m, the spacing between them 0.25 m and the burial depth 0.4 m. Tight-buffered single-mode fibres with polyethylene coating to ensure mechanical safety in the rather rough conditions within the trench were used (details to the sensor cables are presented in Appendix 6-1). The sensor cables were further protected by thin sand layers within the refilled and compacted soil material. Three different cable types were installed to test the influence of different longitudinal stiffness and surface corrugation of the cables. Here only the results using the most promising sensor cables are presented. The end of the sensor cable that is connected to the OBR 4600 enters the soil through a shaft whereas the second, free end is installed in a shaft at the other end of the experimental site.

During the experiment the ground surface was loaded with polyvinylchloride cylinders of 0.1 m diameter filled with lead. The lead filling allowed realizing different masses between 10 kg and 50 kg. The loading cylinders were placed on a thin sand cushion to flatten the natural ground surface and ensure better contact. First a reference measurement without loading was performed before arranging the cylinders on the ground and measuring under load. To avoid undesired loading of the ground surface, the cylinders were placed from a bridge structure spanning across the test site (for further information, see the Appendix 6-2).

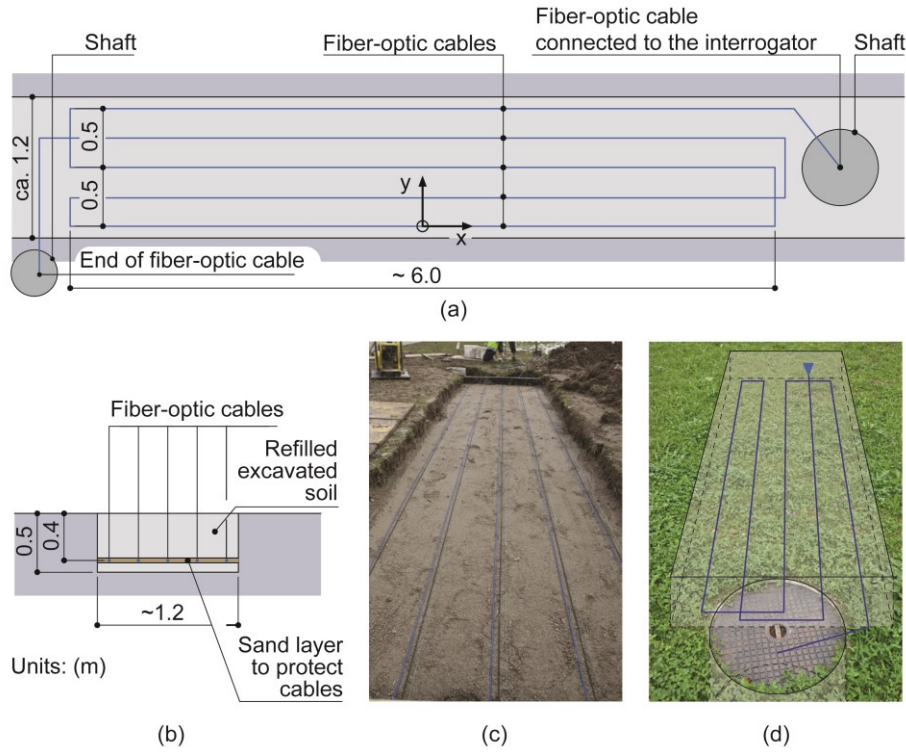


Figure 6-2. Experimental setup of the buried FOSs; (a) plan view; (b) cross-section; (c) FOSs during installation in the trench; (d) layout of the experiment after refilling the trench and grass grown over it.

6.4 Inverse Analysis

Calculation of a strain field at the level of the ground-buried FOSs, caused by contact forces between the object and the ground, requires a mechanical model of the ground. For normal traction, this problem can be mathematically formulated as a half space loaded on its free surface (shear traction is assumed to be negligible.) Although the constitutive behaviour of soil is in general nonlinear and anisotropic, the assumption of linear isotropic elasticity is a first-step approximation that enables using an efficient numerical solution of the inverse problem. The effects of soil nonlinearity are discussed below. For the problem of a linear isotropic half space loaded on its free surface, a well-known analytical solution exists (Boussinesq 1885; Green & Zerna 1968). The strain field in the ground follows from the solution of the Laplace equation for the potential function of the displacements ϕ ,

$$\Delta\phi = 0 \quad (6-1)$$

For the boundary condition of a normal point force acting at the origin on the free surface and using Cartesian coordinates (x, y, z) , the solution of the potential function takes the form

$$\phi = -\frac{P(1+\nu)}{2\pi E} \ln(R+z); \quad R = \sqrt{x^2 + y^2 + z^2} \quad (6-2)$$

where P is the magnitude of the point force and E and ν the Young's modulus and the Poisson ratio of the half space, respectively.

This solution has a singularity at the origin, which could be lifted by applying finite-strain theory. However, for the problem at hand, only displacements at the depth of the buried FOS are of interest, and these are sufficiently far away from the origin. The horizontal strains ε_{xx} are calculated by differentiating the potential function with respect to the in-plane coordinate x and the vertical coordinate z (for the full derivation of the elastic strain function see Appendix 6-3).

$$\begin{aligned}\varepsilon_{xx} &= (1 - 2\nu)\phi_{,xx} + z\phi_{,xxz} \\ &= \frac{P}{E} \cdot \frac{(1 + \nu)}{2\pi} \left[\frac{(1 - 2\nu) \left(2 + \frac{z}{R}\right) x^2}{R^2(R + z)^2} - \frac{(1 - 2\nu)}{R(R + z)} + \frac{(R^2 - 3x^2)z}{R^5} \right] \\ &= \frac{P}{E} \cdot f(x, y, z, \nu)\end{aligned}\quad (6-3)$$

As linear elastic behaviour of the soil is assumed, the superposition principle holds and the strain field caused by an arbitrary force distribution on the surface, $q(x_p, y_p)$, is determined by the convolution of the force distribution with the strain mapping function from equation (6-3):

$$\varepsilon_{xx} = \int_{-\infty}^{\infty} \int_{-\infty}^{\infty} \frac{q(x_p, y_p)}{E} \cdot f(x_c - x_p, y_c - y_p, z_c, \nu) dy_p dx_p \quad (6-4)$$

where x_p, y_p denote the coordinates of the force distribution on the surface and x_c, y_c, z_c are the coordinates of the point in the ground where the strain is evaluated. In the inverse problem, the force distribution acting on the surface can be found from equation (6-4) by deconvolution. This

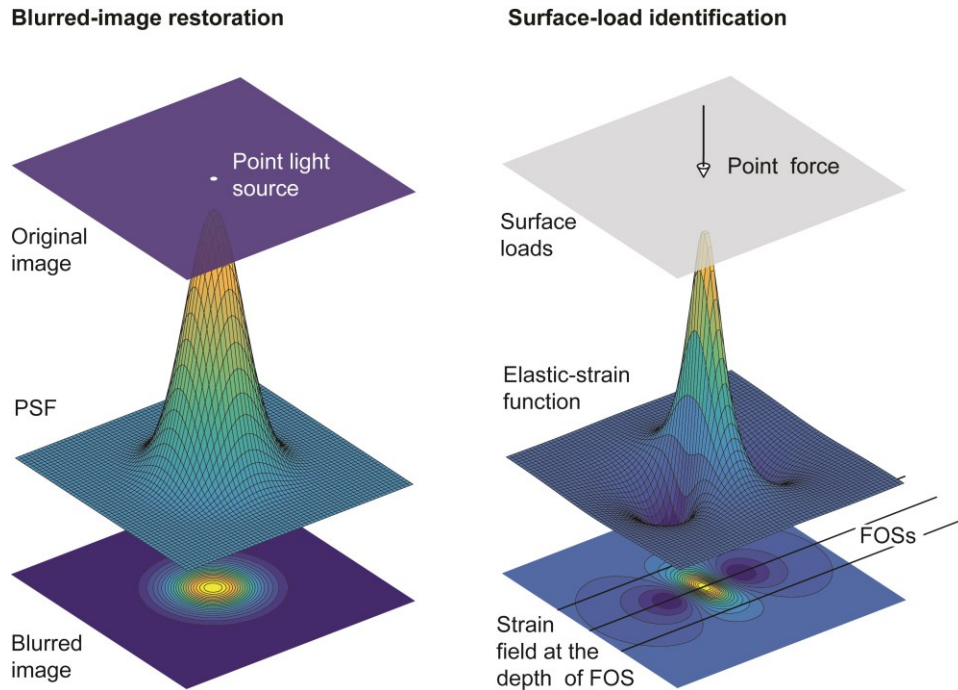


Figure 6-3. Analogy of surface-load identification to blurred-image restoration.

problem is ill-posed; that is, whereas a unique solution does exist if more than one FOS with non-zero spacing is used, the stability of the solution is sensitive to small errors in the strain measurements (Hadamard 1902). It turns out, however, that the present problem has an analogy in the restoration of blurred images in photography, where distortions (for example, due to unwanted or engineered imperfections in the camera system) lead to a blurred image as the real image is convoluted with a point spread function (PSF). Numerous numerical approaches have been developed to deblur images based on prior knowledge of the PSF. In our case, the strain field at the depth of the FOS can be regarded as the blurred image of the surface forces, and the elastic strain mapping function $1/E \cdot f(x, y, z, \nu)$ in equation (6-3) is analogous to the PSF in image restoration (Figure 6-3). However, because the strain field only along discrete linear sections is measured, not the entire planar image is available.

The identification of surface loads from real strain measurements requires the discretisation of the inverse problem into single point loads acting on a grid at the surface (Figure 6-4). The discrete strain measurements and the load distribution are transformed into vectors $\boldsymbol{\varepsilon}_{xx}$ and \boldsymbol{p} , respectively, and the elastic-strain mapping function becomes the mapping matrix \boldsymbol{A} . The forward problem is then described as a system of linear equations where the matrix \boldsymbol{A} is found from mapping point forces with coordinates x_p, y_p at the surface to discrete strain points on the FOS cables with coordinates x_c, y_c, z_c (Figure 6-4) using the elastic-strain mapping function given in equation (6-3):

$$\boldsymbol{\varepsilon}_{xx} = \boldsymbol{A}\boldsymbol{p} \quad (6-5)$$

Tikhonov regularisation (Hansen 1992; Tikhonov 1943) and a fast non-negative least-squares algorithm (Lawson & Hanson 1974; Zdunek 2011; Bro & De Jong 1997) is used to solve numerically for the optimal load vector \boldsymbol{p}_{opt} . The non-negativity constraint is used as no tension forces can exist between an object and the ground surface. This constraint enhances the stability of the solution significantly as it prevents force oscillation around zero, providing an additional regularizing effect. The problem therefore becomes

$$\boldsymbol{p}_{opt} = \underset{\boldsymbol{p} \geq 0}{\operatorname{argmin}} \{ \|\boldsymbol{A}\boldsymbol{p} - \boldsymbol{\varepsilon}_{xx}\|_2^2 + \lambda \|\boldsymbol{L}\boldsymbol{p}\|_2^2 \} \quad (6-6)$$

where λ is the regularisation parameter, which we optimised using simulations with synthetically produced strain data (the full optimisation procedure is described in Appendix 6-4). \boldsymbol{L} is a penalty matrix, which can contain prior information on the position of surface forces. A matrix of ones $\boldsymbol{L}_{ij} = 1$ is used, prescribing that every load and corresponding magnitude in the grid is equally probable. Other penalty matrices (based on fitting the strain data perpendicular to the cables with a Gaussian or a Lagrangian polynomial) have been tested. While raising computational cost, they did not improve the quality of the inverse analysis significantly. For the results shown in this chapter, a discretisation grid for the surface loads with $N = 10'000$ nodes on an area of 4 m x 4 m was used. It is possible that multiple neighboring loads on the grid approximate the strains caused by one load in the experiment better than one single load acting at one grid node. The loads that

are closer to each other than the diagonal of the square in the grid are aggregated to a single equivalent static load, leading to a sub-grid resolution of the load location (see Appendix 6-5).

For the successful identification of surface loads, the two elastic parameters of the strain-mapping function have to be known *a priori*. This can be ensured by determining these parameters using laboratory tests on a soil sample or by calibrating them inversely by performing on site strain measurements with known loads. Such a calibration, however, is complicated by the fact that the stiffness of the soil is strongly nonlinear at the very low strains present in our problem (Friedli & Puzrin 2015). (This phenomenon is known in geomechanics as small-strain nonlinearity (*e.g.*, Burland 1989)). In general, soils do not even behave elastically; that is, after removal of the loads a small irreversible strain remains. Accounting for this nonlinear constitutive behaviour in the half-space model would affect the analytical expression for the strain-mapping function and prevent the use of the superposition principle. Therefore, as an approximation it is assumed that the entire soil behaves as a linear elastic half space and correct for the nonlinearity based on the magnitude of the applied load. Equation (3) shows that the strain field is linearly dependent on the Young's modulus E , which means that each calculated load has only to be corrected to account for the nonlinear Young's modulus E , assuming that the Poisson ratio remains constant (which is approximately the case in our experiment). In a first step the load distribution is calculated for an average constant Young's modulus. Because the stiffness depends on strain and therefore on load, in a second step each load is corrected to be compatible with the load-dependent stiffness. The loads are corrected by using a characteristic curve that correlates the magnitude of each load P to the corresponding soil stiffness $E(P)$. This curve is obtained experimentally by loading the ground surface in steps over the entire expected load range and inversely optimising the 'pseudo-elastic' stiffness parameters (for details, see the Appendix 6-6). Although the approach does not solve the true nonlinear strain field for all calculated loads, it was found to perform well in accurately identifying their magnitudes.

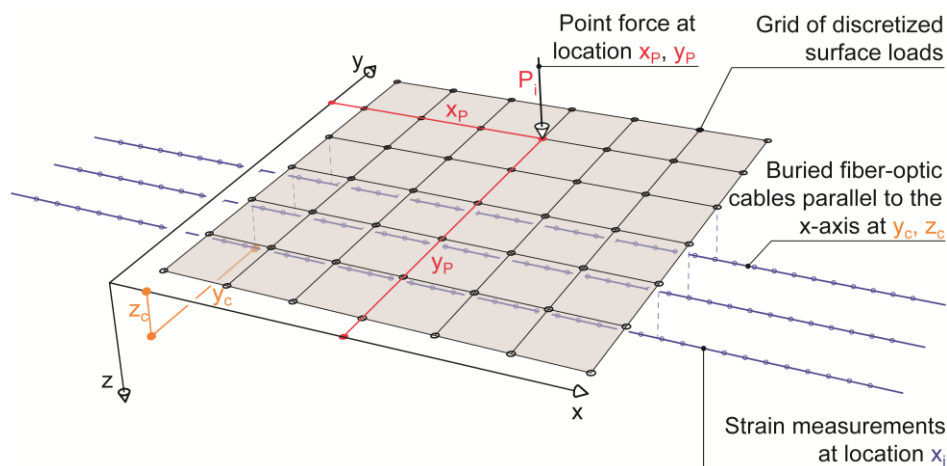


Figure 6-4. Discretisation of the surface loads in a grid.

6.5 Results

The three different load patterns tested in the experimental study are presented in Figure 6-5 (a)-(c), with the corresponding results of the inverse analysis given in Figure 6-5 (d)-(f). Where both the shape of the loads and their location are captured reasonably well, the reconstructed magnitudes show small deviations from the real values. The study shows that the accuracy of the calculated loads is higher for loads placed within the perimeter of the buried cables, in particular for the line load configuration (Figure 6-5 (b), (e)). Loads placed outside this perimeter are reconstructed with lower accuracy in both position and magnitude. This can be explained by the smaller amount of available measured strain data (that is, a smaller part of the strain image is captured by the FOSs). For the circle load configuration (Figure 6-5, (c), (f)) the inverse analysis yields a lower number of loads than have been present in the experiment. This is a direct result of

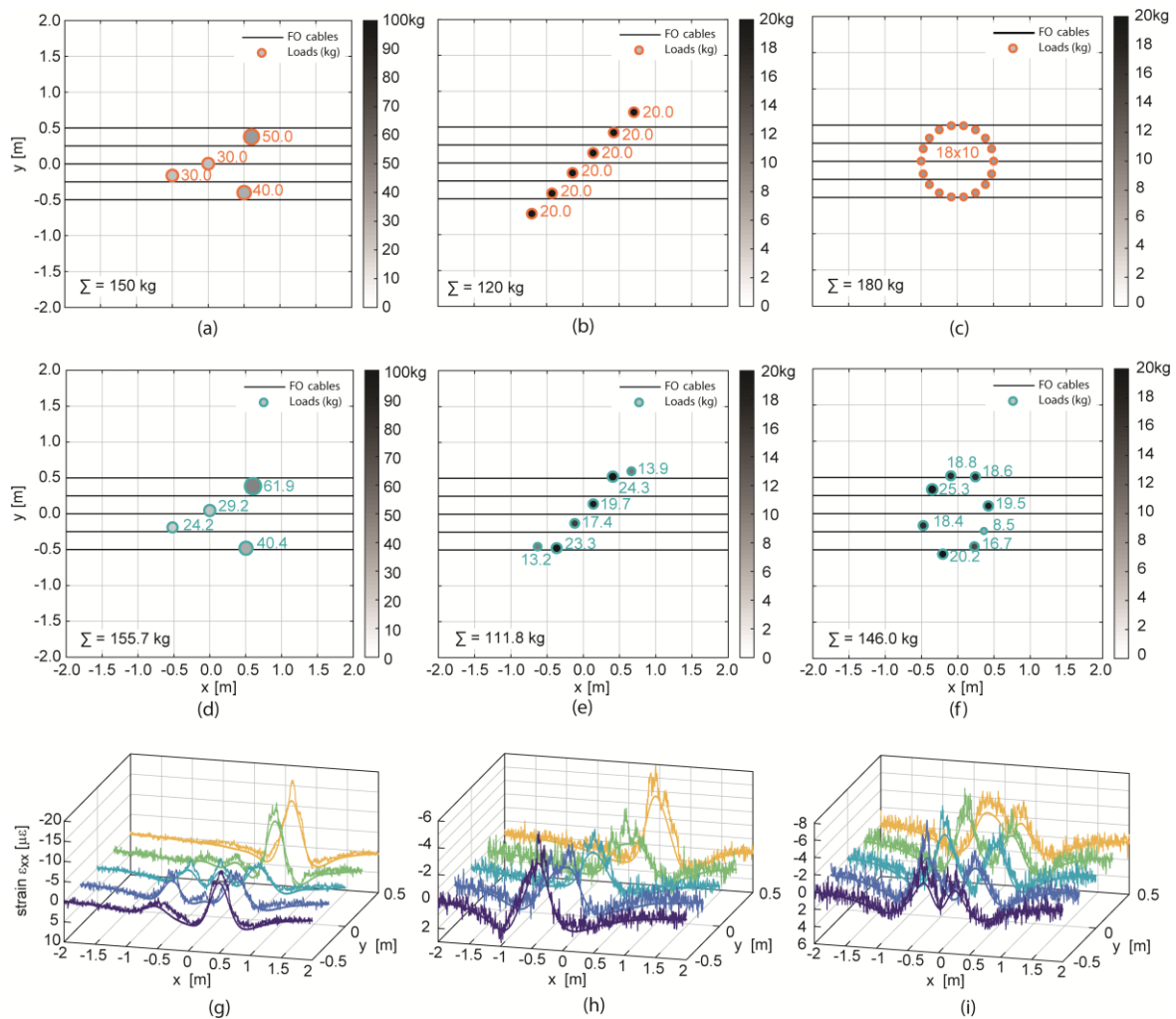


Figure 6-5. (a)-(c) Experimental load patterns, (a) point, (b) line, (c) circle. (d)-(f) Reconstructed load patterns, (d) point, (e) line, (f) circle (dot size and shading indicate the load magnitude). (g)-(i) Measured and reconstructed strain along FOS, (g) point, (h) line, (i) circle; the reconstructed strain corresponds to the inversely calculated loads in (d)-(f).

the regularisation and the aggregation of loads, which prefers solutions with a low number of loads and high magnitudes.

For practical applications, the point load configuration (Figure 6-5 (a), (d)) is probably the most realistic one, as objects moving on the ground usually consist of a small number of feet or wheels, leading to a sparse contact-force pattern on the surface.

6.6 Discussion and conclusions

The inversely calculated surface loads (Figure 6-5 (g)-(i)) induce theoretical strains that match well the measured ones. However, there are some deviations, most likely as a result of soil inhomogeneity (that is, spatially variable stiffness). The measured strain magnitudes for all three load cases are very small (5–15 $\mu\epsilon$) and the corresponding noise levels in the measurements are therefore rather high. The tiny strain magnitudes and the resulting low signal-to-noise ratio (SNR) for the circular load pattern are another possible explanation for the accuracy loss affecting the inverse analysis in that case. Nonetheless, the accuracy of the inverse analysis of surface loads seems rather remarkable, considering that the mechanical system (that is, the ground) is made of non-engineered natural material.

Ground-buried FOSs with high-resolution SWI strain sensing provides a powerful tool for the identification of surface loads. Despite some inaccuracies in load magnitude and position outside the area of buried cables, the framework introduced here enables capturing successfully and accurately different load patterns. A combination of such a system with high-temporal-frequency sensing (which is already commercially available for sensing lengths smaller than tens of meters) should provide a dynamic-load identification system. The spatial and temporal distributions of contact forces attained in this way could be used as an input for pattern recognition with machine learning, to identify objects moving on the ground surface. The knowledge of the contact-force distributions provides more information about the object compared to correlating measurements to a pre-defined library of signals. One of the main issues towards real-time identification is the computational time of the inverse analysis. One possible approach to reducing it is to use already reconstructed load patterns of past time frames as prior estimators for the reconstruction of the current measurement frame under load, for example using the penalty matrix L in equation (6-6). Further improvements of the reconstruction could be achieved by using FOSs buried in shallower depth, leading to more favourable SNRs; a drawback of this approach, however, is that the elastic-strain function is narrower and that therefore less information can be gathered by one FOS, thus reducing the robustness of the reconstruction for loads outside the perimeter of the FOSs. Therefore the optimal depth has to be found for a particular application depending on the expected magnitude of loads, the stiffness of the soil and the desired width of reliable identification around the FOSs.

6.6.1 Outlook

Further improvement of distributed strain sensing, and therefore longer sensing distances with comparable high strain and spatial resolution, would open up a path for several practical

applications. In particular, the ability to identify the number and magnitudes of contact forces makes it possible to discriminate, for example, between bipedal humans and quadrupedal animals, which should reduce the number of false alarms in perimeter-security systems. Such systems would strongly benefit if, in addition to their detection, intruders could also be classified based on their contact-force pattern. In biodiversity measurements, the step lengths and corresponding contact-force magnitudes, which differ from species to species, can be used to discriminate between different species. In this way the number of animals of each species could be counted as they cross a line perpendicular to their common migration path. Based on the identification of load magnitudes, dynamic weigh-in-motion systems for road traffic and airports could be developed, where the FOSs are embedded into the asphalt. The ability to measure the contact forces for each wheel independently should facilitate the classification of vehicles, such that in addition to the load of the entire truck also that of individual axes — caused, for instance, by improper placement of the freight — could be checked. Finally, in biomechanical applications and sports medicine, the contact-force patterns could provide new insights regarding stresses on an athlete's body during training and competition.

6.7 Appendix 6-1: Description of the fibre-optic sensors

6.7.1 Fibre-optic sensor (FOS) cables

In the experiment three different FOS cables were used, which vary in their structure, material, diameter and longitudinal stiffness. All three cables consist of a standard single mode fibre, which is coated with different plastic material to strengthen its behaviour in rough conditions in the ground (Table 6-1). The thinnest cable, GR, is rather vulnerable to mechanical damage and was only used to validate the other two. While the RU cable, which turned out to be the most promising in our application, has only a Polyethylene coating, the V9 cable has an additional metal jacket which makes it robust but also much stiffer.

Table 6-1. FO cables used in the experiment

Name	GR	RU	V9
Diameter (mm)	0.9	2.9	3.2
Longitudinal stiffness (kN)	1.0	5.0	59
Surface	Smooth	Smooth	Corrugated

6.7.2 Swept wavelength interferometry (SWI)

The technique uses the Rayleigh backscattering caused by small random variations of the density and the refractive index in the fibre (e.g., Froggatt & Moore 1998). A laser source sweeps over a defined wavelength range and the backscattered light is measured using an optical interferometer. By performing a cross correlation analysis of the reference measurement and the measurement in the tested sensor, the spectral shift is found which linearly depends on the applied temperature and strain change (Figure 6-6), (Gifford et al. 2007).

A commercially available interrogator from Luna Inc., (Luna 2012) was used. This device allows measuring strain and temperature with sensing ranges up to 70 m on single-ended fibres. In this study a spatial resolution of 5 mm was used, which allows strain resolution in the range of $<1 \mu\epsilon$.

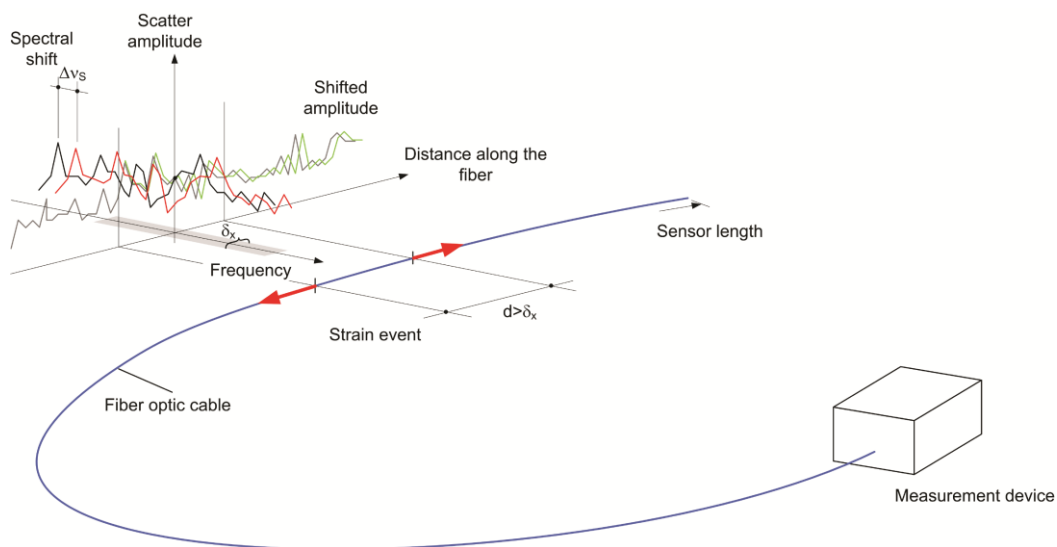


Figure 6-6. Basic principle of swept wavelength interferometry, from Hauswirth (2015).

6.8 Appendix 6-2: Details of the experimental facility

6.8.1 Pre-tensioned cables

Figure 6-7 (a) shows the FOS cables in the trench of the experimental facility before its refilling by the excavated material. The three different cables were placed close to each other in a serpentine layout to form five parallel sections. The cables have to be pre-tensioned in order to measure strain changes accurately and ensure that the sections are straight. In particular, in order to measure compressive strains, a sufficiently high pre-tensioning level has to be reached.



Figure 6-7. (a) Photo of the trench with pre-tensioned fibre-optic cables. Note, while here cables at a depth of 0.2 m are shown the presented experiment data is measured using FOS at a depth of 0.4 m; (b) Detail of the pre-tensioning of the FOS cables.

In Figure 6-7 (b) the fixations used for the pre-tensioning are shown. All the cables were pre-tensioned to a strain level of approximately $1500 \mu\epsilon$ before the excavated material was refilled. After refilling and compacting the trench, the pre-tensioning fixations were released, therefore at both ends of each section the pre-tensioning is zero. However, the friction between the cables and the surrounding soil allows for building up of the necessary tension forces for the pre-tensioning over in a middle part of the experimental facility (Hauswirth 2015), where the loading of the ground surface during the experiment is applied.

6.8.2 Three different cables

A loading test on the three different cables was performed and the corresponding strain measurements are shown in Figure 6-8 (a). The most sensitive thin GR cable, which cannot be used under realistic harsh conditions in soil, is utilised here as a reference measurement. This cable captures the true strain of the soil most exactly due to its very low stiffness. While the stiffer cable RU differs only slightly at the peak strain value, the V9 cable with metal jacket dampens the measured strain peak significantly. This dampened measurement is most likely a result of the large longitudinal stiffness of the V9 cable which prevents the cable to follow exactly the deformations of the soil. It is concluded that the RU cable represents a good choice for the applications considered in this chapter; therefore the experiments are performed using only the measurements in this cable.

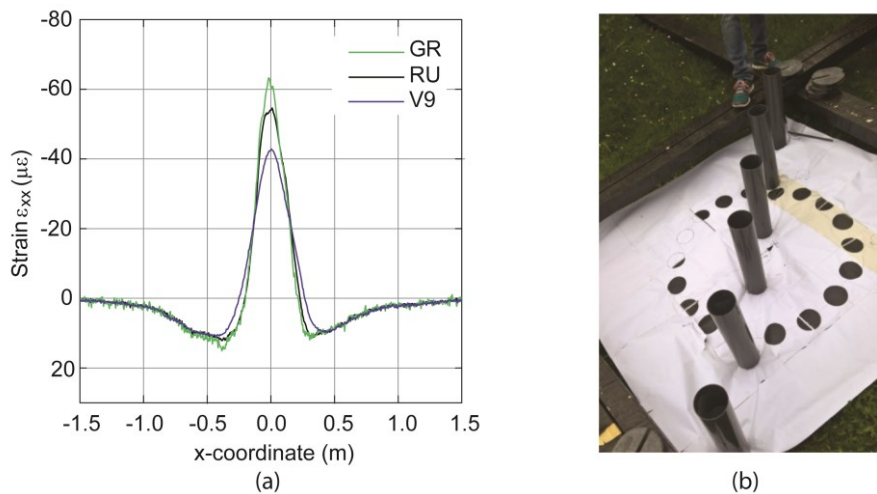


Figure 6-8. (a) Measured strain along the three different FOS cables for a point load of 85 kg placed directly above the cables. (b) Arrangement of the cylinders on the ground surface using a printed template for the correct placing (line load example).

6.8.3 Loading of the ground surface

The ground surface was loaded using Polyvinylchloride cylinders with an outer diameter of 100 mm which are filled with lead balls. On the ground surface a thin sand cushion ensures good contact. The cylinders were placed on the ground surface using a bridge structure to prevent loading of the ground during placement of the loads. To ensure a correct arrangement of the loading cylinders a template was placed on the ground. The location and rotation of the poster were referenced with respect to fix points besides the experimental facility. This procedure allows positioning of the loading cylinders on the ground surface with an accuracy of approximately 1 cm.

6.9 Appendix 6-3: Elastic half space loaded on its free surface

For completeness, the derivation of the strain field in a homogeneous isotropic linear elastic half space (Boussinesq 1885) is revisited here. More general derivations are found in several textbooks on elasticity theory, *e.g.*, Green & Zerna (1968). The stresses and strains are described in a Cartesian coordinate system since in the final application strains along a line are needed. The derivation is done using index notation. As only the change of strains due to surface loads is of interest, body forces are neglected. The equilibrium conditions are

$$\begin{aligned}\sigma_{ij,i} &= 0 \\ \sigma_{ij} &= \sigma_{ji}\end{aligned}\tag{6-7}$$

In the problem of interest only small displacement gradients $\frac{\partial u_i}{\partial x_j} \ll 1$ occur, therefore linearised Cauchy strain is used.

$$\varepsilon_{ij} = \frac{1}{2}(u_{i,j} + u_{j,i})\tag{6-8}$$

As mentioned above, isotropic linear elastic constitutive behaviour is assumed. The constitutive law is written here in terms of the Lamé constants (Lamé 1852).

$$\sigma_{ij} = \lambda I_1 \delta_{ij} + \mu \varepsilon_{ij} \quad (6-9)$$

where I_1 denotes the first invariant of the strain tensor $I_1 = \varepsilon_{ii}$ and δ_{ij} is the Kronecker delta. By inserting (6-9) and (6-8) into (6-7), special cases of the Navier equations are derived.

$$(\lambda + \mu)I_{1,i} + \mu \Delta u_i = 0 \quad (6-10)$$

Introducing a potential function ϕ from which the displacements are calculated by

$$\begin{aligned} u_x &= \frac{\mu}{\lambda + \mu} \phi_{,x} + z \phi_{,xz} \\ u_y &= \frac{\mu}{\lambda + \mu} \phi_{,y} + z \phi_{,yz} \\ u_z &= -\frac{\mu}{\lambda + \mu} \phi_{,z} + z \phi_{,zz} \end{aligned} \quad (6-11)$$

reduces the number of unknowns to a single function. Substituting the displacements (6-11) into equation (6-10) leads to the condition that the potential function has to satisfy the Laplace equation.

$$\Delta \phi = 0 \quad (6-12)$$

For the special case of a point load acting at the origin on the surface of a half space, the potential function

$$\phi = -\frac{P}{4\pi\mu} \ln \left(z + \sqrt{x^2 + y^2 + z^2} \right) \quad (6-13)$$

fulfils (6-12) and the stress boundary conditions on the free surface of the half space.

$$\begin{aligned} \sigma_{zz}(z=0) &= 0, \quad x, y \in \mathbb{R} \setminus \{0\} \\ \int_{-\infty}^{\infty} \int_{-\infty}^{\infty} \sigma_{zz}(z=0) dx dy &= -P. \end{aligned} \quad (6-14)$$

The horizontal displacements are derived from the first equation in (6-11) and the Lamé constants are substituted by the Young's-modulus E and the Poisson's ratio ν :

$$\begin{aligned} u_x &= \frac{Px(1+\nu)}{4\pi E} \left(\frac{z}{R^3} - \frac{2\nu}{R(z+R)} \right) \\ u_y &= \frac{Py(1+\nu)}{4\pi E} \left(\frac{z}{R^3} - \frac{2\nu}{R(z+R)} \right) \\ R &= \sqrt{x^2 + y^2 + z^2} \end{aligned} \quad (6-15)$$

Linear strains are calculated by differentiating the corresponding displacements with respect to x or y . The horizontal strain along the x -coordinate reads:

$$\varepsilon_{xx} = u_{x,x} = \frac{P}{E} \cdot \frac{(1+\nu)}{2\pi} \left[\frac{(1-2\nu) \left(2 + \frac{z}{R} \right) x^2}{R^2(R+z)^2} - \frac{(1-2\nu)}{R(R+z)} + \frac{(R^2 - 3x^2)z}{R^5} \right] \quad (6-16)$$

6.10 Appendix 6-4: Optimisation of the regularisation parameters

To optimise the regularisation parameter λ and the load grid of the inverse analysis a suite of synthetic experiments was performed. It was assumed that the ground behaves as an isotropic linear elastic material with a Young's modulus $E=35$ MPa and Poisson ratio $\nu=0.22$. These stiffness parameters have been determined as average values in a preliminary field experiment. Synthetic strain measurements were produced using the half space solution shown in equation (6-16). To simulate the random measurement error, a Gaussian noise was added. The parameters of the Gaussian noise were calibrated using a field measurement with zero load.

For the assessment of the influence of the regularisation parameters two different error estimators were used:

- Error 1: Force resultant error; this error describes the accuracy of the inversely calculated resultant load $P_{res,calc}$ with respect to the synthetically applied true load $P_{res,true}$. This error estimator includes information on the accuracy of the magnitude of the surface load distribution.

$$error\ 1 = \left\| \frac{P_{res,true} - P_{res,calc}}{P_{res,true}} \right\| \quad (6-17)$$

- Error 2: 2D strain error; this error estimator describes the accuracy of the calculated strain field in the whole plane at the depth of the FOS $\epsilon_{xx,calc}(x, y, z_c)$ with respect to the forward calculated strain $\epsilon_{xx,synth}(x, y, z_c)$ resulting from the synthetically applied loads and additional Gaussian noise. This error estimator includes information on the accuracy of the 'shape' of the surface load distribution.

$$error\ 2 = \left\| \frac{\epsilon_{xx,synth}(x, y, z_c) - \epsilon_{xx,calc}(x, y, z_c)}{\epsilon_{xx,synth}(x, y, z_c)} \right\| \quad (6-18)$$

These error estimators were calculated for varying regularisation parameters λ and the three load patterns (point, line and ring load) and are shown in Figure 6-9 (a)-(d). In Figure 6-9 (c) the computational time is shown depending on λ . The choice of the regularisation parameter is a trade-off between accuracy and computational time. In Figure 6-9 (d)-(e) the influence of the grid density on the error estimators is presented. It is shown that a denser grid increases the stability of the inverse analysis. However, this comes with increasing computational cost. For the presented experiment a grid with $N=10^7$ nodes is used. In Figure 6-9 (f)-(g) the influence of the Poisson ratio on the error estimators is presented for varying λ . These considerations constrain the useful range of the regularisation parameter between $2.5 \cdot 10^{-11}$ and $5 \cdot 10^{-11}$. In the presented experimental study $\lambda = 4 \cdot 10^{-11}$ was used.

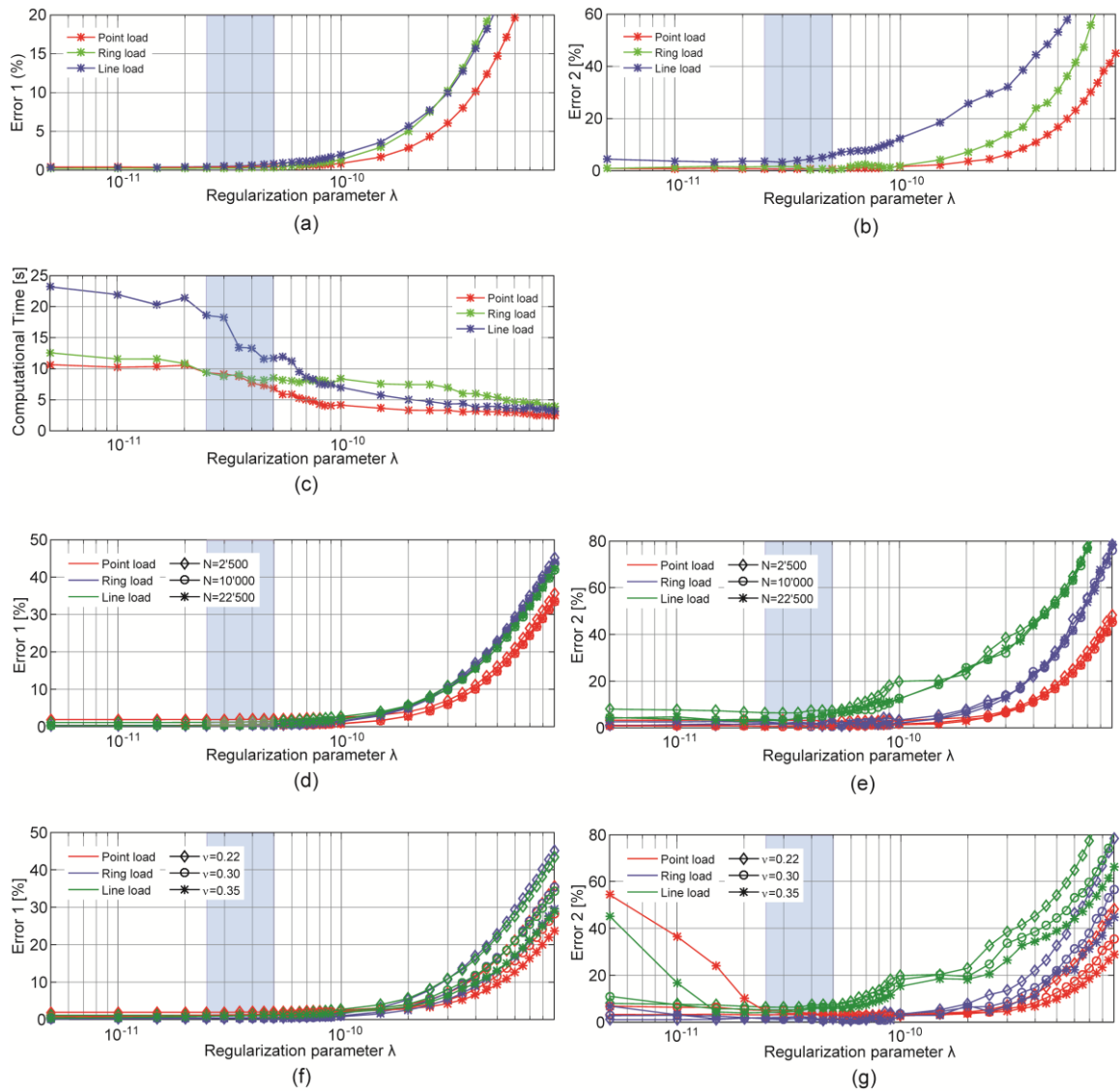


Figure 6-9. Error calculations and computation time for varying regularisation parameter λ based on synthetic experiments: (a) Regularisation parameter λ vs. Error 1 for the three load types. (b) Regularisation parameter λ vs. Error 2 for the three load types. (c) Regularisation parameter λ vs. computational time for the three load types. (d) Regularisation parameter λ vs. Error 1 for the three load types with three grid densities. (e) Regularisation parameter λ vs. Error 2 for the three load types with three grid densities. (f) Regularisation parameter λ vs. Error 1 for the three load types with three Poisson ratios. (g) Regularisation parameter λ vs. Error 2 for the three load types with three Poisson ratios.

6.11 Appendix 6-5: Aggregation of loads

Here it is shown how multiple loads located close to each other in the grid are aggregated into one single static equivalent load. An algorithm similar to a k-d-tree is used which checks the distance of all non-zero forces to each other. The solution set merges all the loads which are within a certain distance from each other. Figure 6-10 shows schematically how this aggregation works. While load 4 is not aggregated, loads 1, 2 and 3 are aggregated to the new static equivalent load A. In the experimental study presented in the chapter the loads are aggregated which are closer to each other than the diagonal of one grid square. With $N=10'000$ nodes on an area of 4×4 m this distance corresponds to $\sqrt{2} \cdot 0.04$ m.

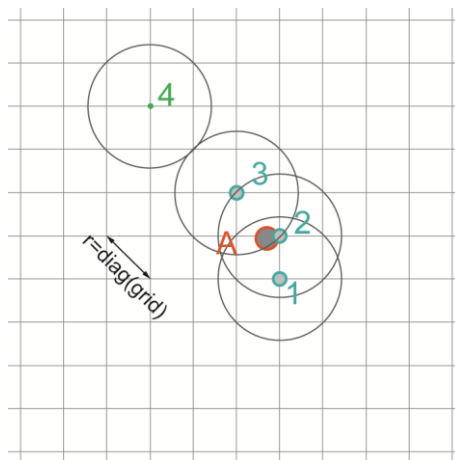


Figure 6-10. Schematic sketch of the aggregation of surface loads.

The inverse analysis, although regularised, often produces some small artefact loads which have to be excluded from the solution set. Synthetic experiments were performed where the magnitude of a point load at the origin was increased gradually. The corresponding error estimators are presented in Figure 6-11. At low load magnitudes the signal to noise ratio is low which leads to high errors, *i.e.*, for our inverse analysis small load artefacts are likely to be caused by measurement errors. The error decreases strongly after reaching a load magnitude of $P > 4-5$ kg. Therefore a threshold value of 5 kg was introduced below which the calculated loads are excluded from the solution set.

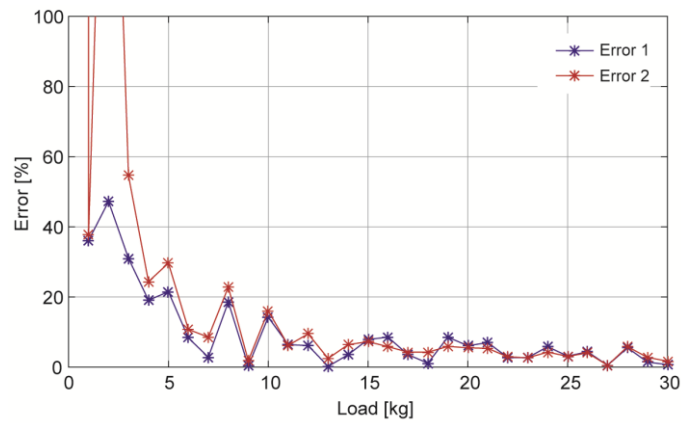


Figure 6-11. Error estimators of error 1 and error 2 depending on the load magnitude in the synthetic experiment with Gaussian noise

In Figure 6-12 the inversely calculated loads are shown of the presented experimental study before (a)-(c) and after aggregation (d)-(f). It is shown that before the aggregation the correct loads are approximated by a number of small loads which are then merged. Additionally, the small artefact loads are removed by the threshold value of 5 kg. The aggregation proves to be a powerful tool to merge the inversely calculated loads in to a set which is close to the applied ones. Note, that this aggregation may impose errors if the applied loads are not sparse, which in practical applications are relatively unlikely to occur.

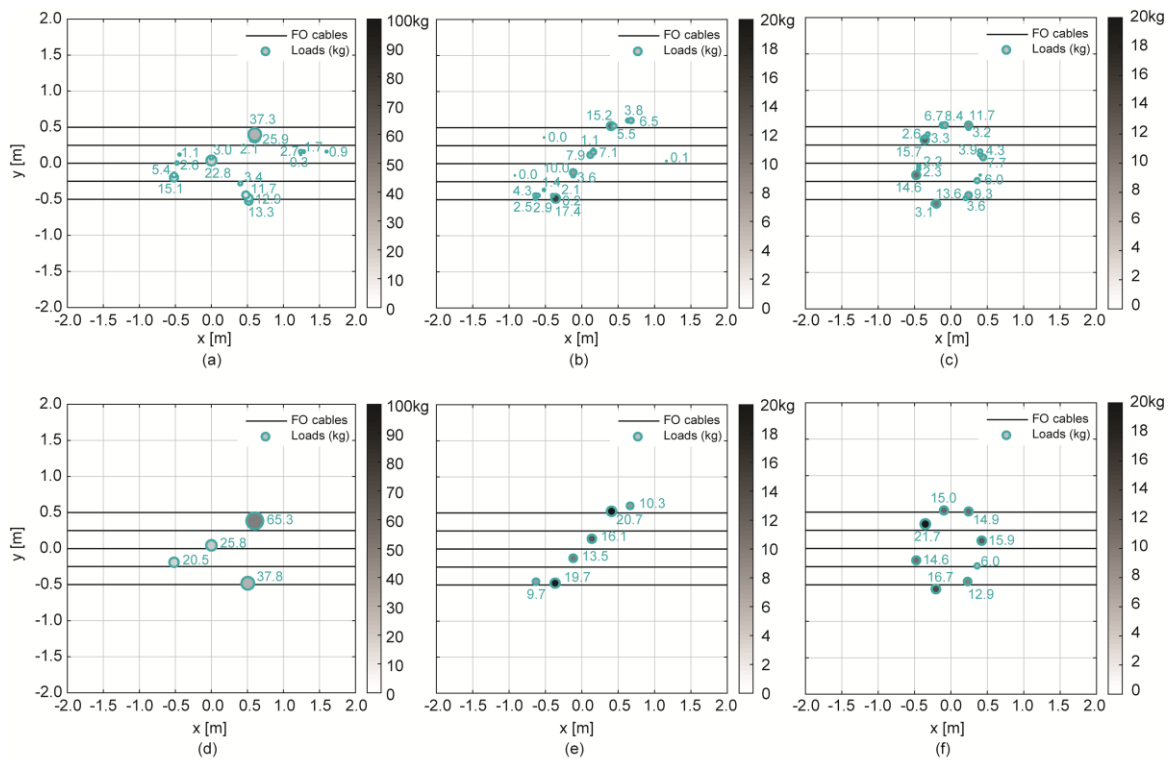


Figure 6-12. Calculated loads before aggregation; (a) points, (b) line, (c) ring; Aggregated loads which pass the threshold value, (d) points, (e) line, (f) ring.

6.12 Appendix 6-6: Accounting for soil non-linearity

It is shown how soil non-linearity influences the measured strain caused by a point load acting on the ground surface. The load magnitude was stepwise increased from zero to 100 kg. After each loading step a strain measurement was performed, the results of these measurements are shown in Figure 6-13.

For each load step the equivalent Young's modulus is optimised by comparing measured strain $\epsilon_{xx,meas}$ with calculated strain $\epsilon_{xx,calc}$ which is a function of E and ν :

$$E_{opt}, \nu_{opt} = \arg \min_{E, \nu} \|\epsilon_{xx,meas} - \epsilon_{xx,calc}(E, \nu)\| \quad (6-19)$$

This evaluation shows that the stiffness drops with increasing load, which is a result of the nonlinear soil stiffness (known as small strain non-linearity (Burland 1989)), Figure 6-13 (b). In contrast, the Poisson ratio remains relatively constant, which is reflected in Figure 6-13 (a) by the fact that the location of the zero strain point (approx. $x = \mp 0.15$ m) remains constant for all the load steps (indeed, the theoretical coordinate of this point only depends on the Poisson ratio). Therefore it is concluded that the equivalent Poisson ratio is almost independent from the load magnitude.

In our approximate method to account for the soil non-linearity the Poisson ratio is set to a constant value $\nu = 0.18$ and optimise only the Young's modulus which captures the measured strain best for each load step. This correlates the point load magnitude P to the corresponding equivalent Young's modulus resulting in a characteristic curve $E(P)$. In the inverse analysis of surface loads, the first iteration calculates initial values of the loads on the surface P_0 using a mid-range Young's modulus E_0 .

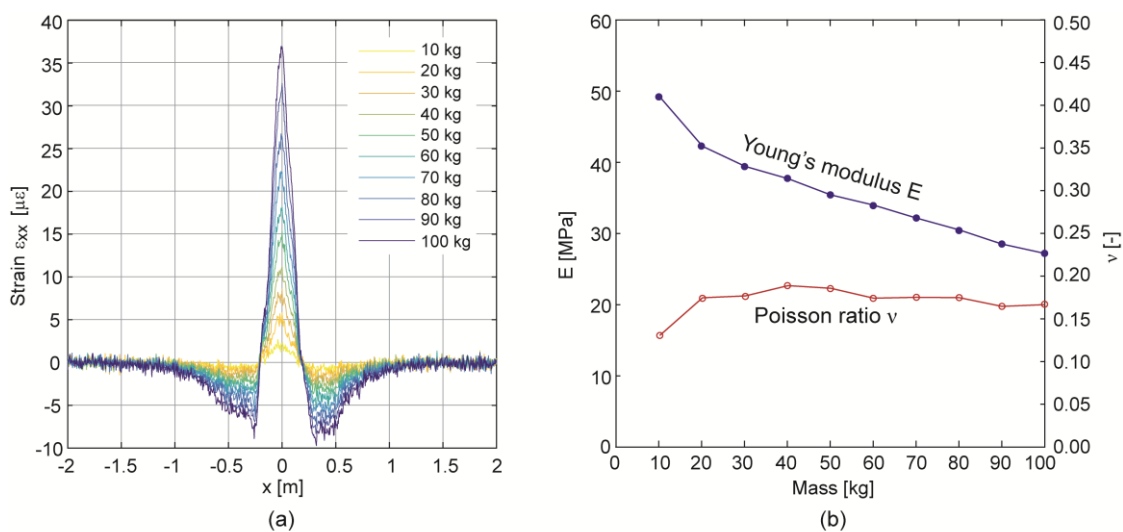


Figure 6-13. (a) Strain caused by a stepwise increased point load above the cable. (b) Young's modulus and Poisson ratio depending on the load magnitude.

Since strains are proportional to the ratio of the load magnitude and the Young's modulus (equation (6-16)), the load magnitude of each load can be corrected by solving

$$\varepsilon_{xx,meas} = \frac{P_0}{E_0} \cdot f(x, y, z, v = const.) = \frac{P_{corr}}{E(P_{corr})} \cdot f(x, y, z, v = const.) \quad (6-20)$$

with respect to the corrected load P_{corr} . The Young's modulus is also depending on the load magnitude and is only known piece-wise, which would require an iterative procedure to find the correct pair of the corrected load and Young's modulus $\frac{P_{corr}}{E(P_{corr})}$. Therefore the characteristic curve is converted to depend on the maximum strain caused by the corresponding load magnitude (Figure 6-14).

$$\varepsilon_{xx,max}(E) = \frac{P_{applied}}{E(P_{applied})} \cdot f(x = 0, y, z, v = const.) \quad (6-21)$$

This allows solving directly for the corrected load magnitude:

$$P_{corr} = \frac{P_0 E(\varepsilon_{xx,max})}{E_0} \quad (6-22)$$

Note, that since the soil non-linearity prevents the use of the analytical solution (6-16) and the superposition principle, this approach induces certain errors if multiple surface loads are close to each other. An additional error comes from the distance of a load perpendicular to the FOS cable since the characteristic curve is evaluated for a load placed directly above the FOS. The used approach proves, however, to be powerful in identifying accurately the load magnitude for sparse load distributions even if they deviate strongly from the initial calibration of the Young's modulus.

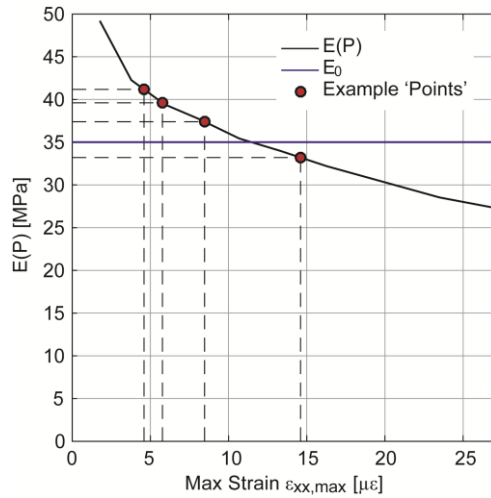


Figure 6-14. Young's modulus depending on the maximum strain value caused by a corresponding point load directly above the FOS. Yellow points show the example of the point load layout.

6.13 Acknowledgment

I would like to thank my co-authors L. Pizzetti, D. Hauswirth and A. Puzrin as well as my colleagues M. Schwager, P. Minder, P. Oberender and A. Stoecklin (Institute for Geotechnical Engineering, ETH Zurich) for valuable discussions on the topic, R. Rohr and H. Buschor (Institute for Geotechnical Engineering, ETH Zurich) for their help in constructing the experimental setup and A. Trabesinger for discussions on the manuscript and its linguistic review.

6.14 Notation

\mathbf{A}	Strain transfer matrix
E	Young's modulus
E_{opt}	Optimised Young's modulus
E_0	Mid-range (initial) Young's modulus
I_1	First invariant of the strain tensor ε_{ii}
\mathbf{L}	Penalty matrix for the regularisation
N	Number of load nodes at the surface
P	Load magnitude
P_0	Initial guess of the load values
P_{corr}	Corrected load values
$\mathbf{P}_{res,true}$	True load vector
$\mathbf{P}_{res,calc}$	Calculated load vector
R	Radial distance to the origin $\sqrt{x^2 + y^2 + z^2}$
\mathbf{p}	Load vector
\mathbf{p}_{opt}	Optimised load vector
$q(x_p, y_p)$	Load distribution at the surface
u	Displacement
x_c	x-coordinate of a point on the cable
x_p	x-coordinate of the load
y_c	y-coordinate of a point on the cable
y_p	y-coordinate of the load
z_c	z-coordinate of a point on the cable
δ_{ij}	Kronecker delta
ε_{ij}	Strain tensor
ε_{xx}	Horizontal strain in x-direction
$\boldsymbol{\varepsilon}_{xx}$	Strain vector along the cable
$\boldsymbol{\varepsilon}_{xx,calc}$	Inversely calculated strain vector
$\boldsymbol{\varepsilon}_{xx,synth}$	Synthetically, forward calculated strain vector
λ	Regularisation parameter, (in Appendix 6-3: Lamé parameter)
$\mu\varepsilon$	microstrain $\mu m/m$
μ	Lamé parameter
σ_{ij}	Stress tensor
ν	Poisson ratio
ν_{opt}	Optimised Poisson ratio
ϕ	Potential function for the displacements

6.15 References

- Boussinesq, J.V. (1885) *Application des potentiels à l'étude de l'équilibre et du mouvement des solides élastiques*. Gauthiers-Villars, Paris, France.
- Bro, R. & De Jong, S. (1997) A fast non-negativity-constrained least squares algorithm. *Journal of Chemometrics*, **11**, No. 5, pp.393–401.
- Burland, J.B. (1989) Ninth Laurits Bjerrum Memorial Lecture: 'Small is beautiful'-the stiffness of soils at small strains. *Canadian Geotechnical Journal*. **26**, No. 4, 499–516.
- Friedli, B. & Puzrin, A.M. (2015). Investigation of Soil Nonlinearity at Very Small Strains Using Ground Buried Fibre Optic Sensors. In *Proceedings of the 6th International Symposium on Deformation Characteristics of Geomaterials*, (eds. Rinaldi, V.A., Zeballos, M.E. & Clariá, J.J.) Buenos Aires, Argentina, 608–614.
- Froggatt, M. & Moore, J. (1998) High-spatial-resolution distributed strain measurement in optical fibre with Rayleigh scatter. *Applied Optics*, **37**, No. 10, 1735–1740.
- Froggatt, M.E., Gifford, D.K., Kreger, S., Wolfe, M., and Soller, B.J. (2006) Characterization of Polarization-Maintaining Fibre Using High-Sensitivity Optical-Frequency-Domain Reflectometry. *Journal of Lightwave Technology*, OSA, **24** No. 11, 4149–4154.
- Gifford, D.K., Froggatt, M.E., Wolfe, M.S., Kreger, S.T., Sang, A.K., and Soller, B. J. (2007) Millimeter Resolution Optical Reflectometry Over Up to Two Kilometers of Fibre Length. *2007 IEEE Avionics, Fibre-Optics and Photonics Technology Conference*, IEEE, Dallas, Texas, USA, 52–53.
- Green, A. E., & Zerna, W. (1968). *Theoretical Elasticity*. Oxford University Press.
- Hadamard, J. (1902) Sur les problèmes aux dérivées partielles et leur signification physique. *Princeton University Bulletin*, 49–52.
- Hansen, P.C. (1992) Analysis of Discrete Ill-Posed Problems by Means of the L-Curve. *SIAM Review*, **34**, No.4, 561–580.
- Hauswirth, D. (2015) *A study of the novel approaches to soil displacement monitoring using distributed fibre optic strain sensing*. Dissertation No. 22282, ETH Zurich, Switzerland.
- Hong, X., Guo, H., Wu, J., Xu, K., Zuo, Y. Li, Y. & Lin, J. (2010) An intrusion detection sensor based on coherent optical time domain reflector. *Microwave and Optical Technology Letters*, **52**, No. 12, 2746–2748.
- Juarez, J.C., Maier, E.W. & Taylor, H.F., (2005) Distributed fibre-optic intrusion sensor system. *Journal of Lightwave Technology*, **23**, No. 6, 2081–2087.
- Juarez, J.C. & Taylor, H.F., (2007) Field test of a distributed fibre-optic intrusion sensor system for long perimeters. *Applied optics*, **46**, No. 11, 1968–71.
- Kirkendall, C.K., Bartolo, R., Salzano, J. & Daley, K. (2007) Distributed Fibre Optic Sensing for Homeland Security. *Naval Research Laboratory Review*, 195–196.
- Klar, A., Dromy, I. & Linker, R., (2014) Monitoring tunneling induced ground displacements using distributed fibre-optic sensing. *Tunnelling and Underground Space Technology*, **40**, 141–150.

- Klar, A. & Linker, R., (2010) Feasibility study of automated detection of tunnel excavation by Brillouin optical time domain reflectometry. *Tunnelling and Underground Space Technology*, **25**, No. 5, 575–586.
- Kwon, I.-B., Baik, S.-J., Im, K., & Yu, J.-W. (2002) Development of fibre optic BOTDA sensor for intrusion detection. *Sensors and Actuators A: Physical*, **101**, No. 1–2, 77–84.
- Lamé, M.G., (1852) *Leçons sur la théorie mathématique de l'élasticité des corps solides*, Gauthiers-Villars, Paris, France.
- Lawson, C.L. & Hanson, R.J., (1974) *Solving Least Squares Problems*, Prentice-Hall, Englewood Cliffs, New Jersey, USA.
- Luna Inc. (2012) *Optical backscatter reflectometer Model 4600, user guide 6*, OBR 4600, Luna Technologies, Blacksburg, Virginia, USA.
- Madsen, C., Bae, T., & Atkins, R. (2007) Long Fibre-optic Perimeter Sensor: Signature Analysis. *Conference on Lasers and Electro-Optics/Quantum Electronics and Laser Science Conference and Photonic Applications Systems Technologies, OSA*, paper PWA5 Baltimore, Maryland, USA.
- Madsen, C.K., Snider, T., Atkins, R., & Simcik, J. (2008) Real-time processing of a phase-sensitive distributed fibre optic perimeter sensor. In *Proc. SPIE 6943, Sensors, and Command, Control, Communications, and Intelligence (C3I) Technologies for Homeland Security and Homeland Defense VII* (eds. Carapezza, E.M.), 694310.
- Nikles, M. (2009) Long-distance fibre optic sensing solutions for pipeline leakage, intrusion, and ground movement detection. In *Proc. SPIE 7316, Fibre Optic Sensors and Applications VI*. (eds. Udd, E., Du, H.H. & Wang, A.), International Society for Optics and Photonics.
- Owen, A., Duckworth, G. & Worsley, J. (2012) OptaSense: Fibre Optic Distributed Acoustic Sensing for Border Monitoring. In *2012 European Intelligence and Security Informatics Conference*. IEEE, Odense, Denmark 362–364.
- Park, J., & Taylor, H.F. (2003) Fibre Optic Intrusion Sensor using Coherent Optical Time Domain Reflectometer. *Japanese Journal of Applied Physics*, IOP Publishing, **42**, No. 6, 3481–3482.
- Puzrin, A.M., Friedli, B., & Hauswirth, D. (2013). *Fibre optic based intrusion sensing system*. European Patent Application, EP 2987151 A1.
- Taylor, H.F., & Lee, C.E. (1993) *Apparatus and method for fibre optic intrusion sensing*. US Patent, US5194847 A.
- Tikhonov, A.N. (1943) On the stability of inverse problems. *Doklady Akademii Nauk SSSR*, **39** No 5, 176–179.
- Wu, H., Qian, Y., Zhang, W., Hanyu, L. & Xie, X. (2015) Intelligent detection and identification in fibre-optical perimeter intrusion monitoring system based on the FBG sensor network. *Photonic Sensors*, **5**, No. 4, 365–375.
- Zdunek, R., 2011. Regularized NNLS Algorithms for Nonnegative Matrix Factorization with Application to Text Document Clustering. In *Computer Recognition Systems 4, Advances in Intelligent and Soft Computing*, **95**, (eds. Burduk, R., Kurzyński, M., Woźniak, M. & Żolnierok, A.). Springer, Berlin, Heidelberg, 757–766.

7 Small strain nonlinearity in Boussinesq's problem – fibre-optic strain measurements and numerical modelling

7.1 Abstract

The ground deforms under the action of normal forces on its surface (loaded half space, Boussinesq problem). During such loading the soil shows strongly nonlinear behaviour known as small strain nonlinearity. The chapter studies this nonlinearity at very small strains using ground buried distributed fibre-optic strain sensors in a field experiment which was initially developed to identify objects on the ground surface by inverse analysis. The results of the fibre-optic measurements are compared to the response of a finite-element half space model using four different linear and nonlinear elastic constitutive models. The same nonlinearity is observed in triaxial tests using local strain measurement which serve as independent verification of the constitutive models and their parameters. It is shown that not only the nonlinear deviatoric but also the nonlinear volumetric behaviour is important to capture the response of the soil in the Boussinesq boundary value problem.

7.2 Introduction

An object moving on the ground applies a load to its surface. The stresses induced by these loads result in deformations of the ground which can be measured using buried distributed fibre-optic sensors (FOSs) (Figure 7-1). Starting from the measured strain in the ground the loads acting on the surface can be calculated using a mechanical model (*e.g.*, half space loaded on its surface) and inverse analysis algorithms. Knowing the contact forces induced by an object moving on the surface over the buried FOSs enables applications ranging from biodiversity survey, perimeter security to weigh-in-motion systems. The concept of such an inverse analysis was presented in chapter 6, Friedli et al. (2017) based on the works of Juarez et al. (2005); Kwon et al. (2002); Madsen et al. (2007; 2008); Nikles (2009); Owen et al. (2012); Park and Taylor (2003); Taylor and Lee (1993) on intrusion sensing systems using FOSs, further a patent application was filed (Puzrin et al. 2013).

The experimental study on the inverse analysis of static surface loads (Friedli et al. 2017), shown in chapter 6 revealed significantly nonlinear behaviour of the soil at the very small loads applied corresponding to a mass between 10 kg and 100 kg. This nonlinearity is most likely an effect of the well-known degradation of soil stiffness at low strains (Burland 1989) which was investigated extensively in laboratory and/or field tests. In the laboratory triaxial tests with local strain measurements (*e.g.*, Jardine et al 1984), resonant column tests (*e.g.*, Bellotti et al. 1996; Hardin and Drnevich 1972) and bender element tests (*e.g.*, Dyvik and Madshus 1985) were used. In field tests the small-strain stiffness was mainly measured by means of shear wave velocity (*e.g.*, Stokoe and Woods 1972; Woods 1978). The influence of the small-strain nonlinearity in geotechnical boundary value problems was shown to be crucial for the correct assessment of settlements caused by deep excavations (*e.g.*, Burland and Hancock 1977) or tunneling (*e.g.*, Addenbrooke et al. 1997).

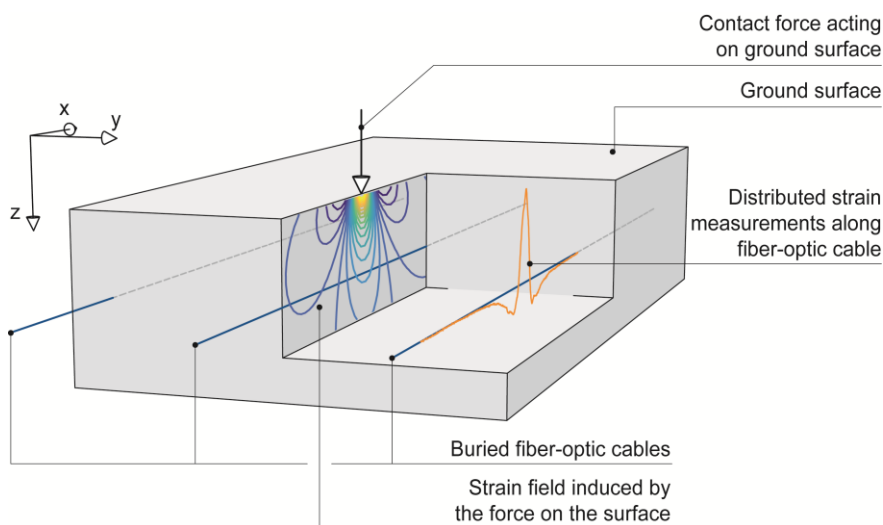


Figure 7-1. Basic principle of object identification using ground buried fibre-optic strain sensors (from Friedli et al. 2017).

In this chapter a different view on the small-strain nonlinearity is offered by the use of distributed strain measurements of ground-buried FOSs in a Boussinesq problem. First the experimental setup is introduced, the strain sensing layout and the loading assembly are explained. The results of the strain data measured with the FOSs is shown and discussed. The soil behaviour is discussed by comparing the experimental data to a finite-element model using four different linear and nonlinear elastic constitutive models. Triaxial test on soil excavated close to the buried FOSs with local strain measurements are presented and discussed. Finally the constitutive models and their parameters are compared to the triaxial test results.

7.3 Experiment

7.3.1 Experimental setup

A shallow trench with depth of 0.5m was excavated in the field. FOSs were buried at 0.2 m and 0.4 m depth in serpentine to achieve five parallel cable sections in a distance of 0.25 m to each other (Figure 7-2). The natural soil at the experimental site is classified as sandy silt with a small amount of clayey fines. The FOSs were prestrained and protected by a thin sand layer before the trench was refilled and compacted to its initial density using a vibrating plate. While one end of the FOS was placed in a shaft where it was connected to the strain sensing device, the second end was placed in a small shaft at the other end of the experiment.

7.3.2 Strain Sensing

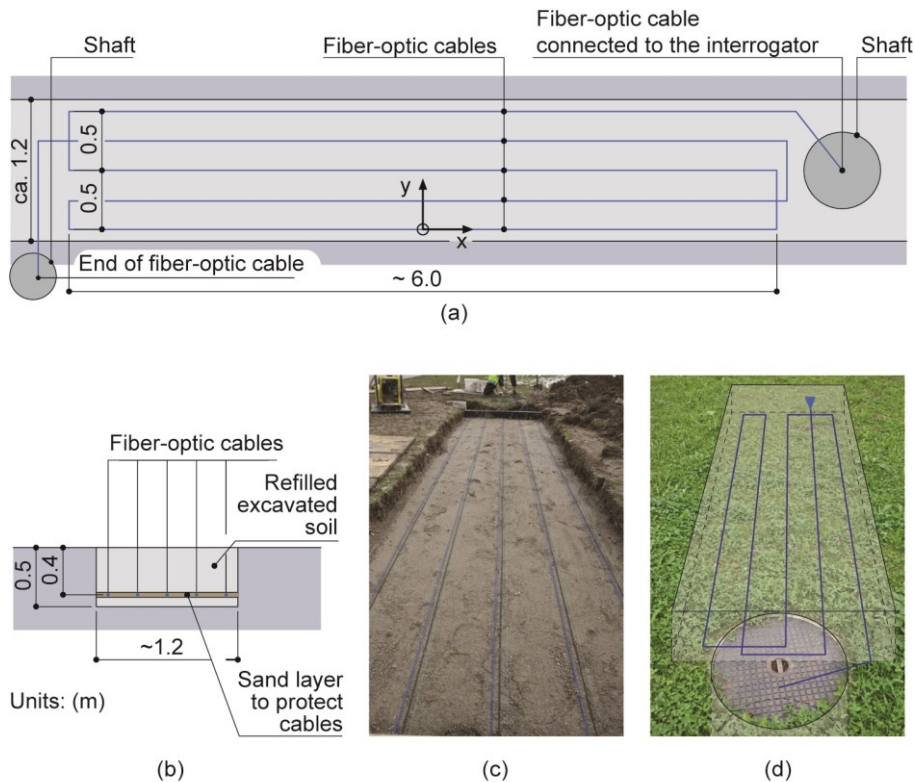


Figure 7-2. Layout of the fibre-optic sensors in the experimental setup: (a) plan view, (b) cross section, (c) fibre-optic cables before refilling, (d) ground surface few weeks after installation (from Friedli et al. 2017).

The FOSs buried in the experimental setup consists of a standard single mode fibre which is protected by a plastic coating from the harsh environment in the trench. The coating is tight buffered (that is, mechanically connected to the fibre in the centre) to ensure a good strain transfer from the coating to the fibre.

The distributed strain sensing in the experiment was achieved using the OBR 4600 device (Luna Inc., Roanoke, VA) which uses swept wavelength interferometry (SWI) based on measuring the Rayleigh scattering (Froggatt et al. 2006; Froggatt and Moore 1998; Gifford et al. 2007). A change of strain or temperature along the fibre causes a spectral shift in the Rayleigh backscatter. This shift is correlated to the applied strain and temperature change. SWI allows measuring the strain along standard fibres with high precision ($\sim 1 \mu\epsilon$) and high spatial resolution (5 mm) along sensors with length up to 70 m. As the temperature and strain both affect the measurement, strictly speaking they should be separated. This separation could be done for example by measuring the temperature independently. Furthermore, environmental effects, such as changes of humidity do also influence the measurement results. In this study, however, the time between reference measurements and measurements under load is short (in the range of a few minutes). Therefore the environmental effects and the temperature effects can be neglected.

7.3.3 Loading Assembly

The ground surface over the buried FOSs was loaded by a plastic barrel placed on a circular steel plate with 10 cm diameter (Figure 7-3). The plastic barrel was filled with water in steps of 5 kg up to 100 kg which was weighted before each loading step. After each loading step a strain measurement was taken along the FOSs. Wooden girders (Figure 7-3), supported more than 3 m from the FOSs to avoid influence on the sensors, were used to stabilise the barrel horizontally. A small gap between the barrel and the stabilisation girders, which was checked and re-opened manually after each loading step, ensured no load loss to the stabilisation structure. The water was brought into the barrel using an additional wooden bridge structure next to the stabilisation girders to avoid influencing the experiment by stepping onto the ground surface. Preliminary results of this experiment were presented in (Friedli and Puzrin 2015).

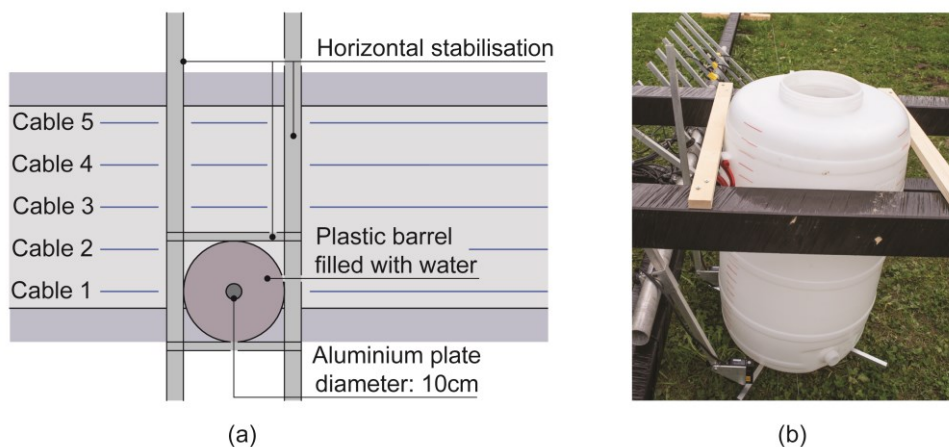


Figure 7-3. Loading assembly: (a) plan view, (b) photo of the plastic barrel and the horizontal stabilisation.

7.3.4 Results

The results of the strain measurements along the FOSs shows that directly underneath the load, at both depths of 0.2 m and 0.4 m, extension strains are measured (geotechnical sign convention is used, positive is compression). These extension strains decay quickly with increasing distance from the load and turn into compressive strains at a distance of $\sim 0.15 - 0.2$ m to the axis of the load. At the shallower depth of 0.2 m the distance between the zero crossings is narrower than at the depth of 0.4 m, which is a result of the wider stress distribution with depth. With increasing load the magnitude of the strain increases but the shape of the strain profile and in particular the distance between the zero crossings remains approximately constant. By following the extension peak at $x = 0$ it is observed that the scaling of the strain magnitudes with increasing load is not linear, which is a first indication of the nonlinear behaviour of the soil.

Assuming linear elastic soil behaviour allows the application of the well-known (Boussinesq 1885) solution for a half space loaded by a point load at the origin on the surface. The derivation of the solution can be found in text books (e.g., Green and Zerna 1968). The strain along a horizontal line is calculated from the derivative of the horizontal displacement. In Cartesian coordinates (x, y, z) this results in

$$\varepsilon_{xx} = \frac{P}{E} \cdot \frac{(1 + \nu)}{2\pi} \left[\frac{(1 - 2\nu) \left(2 + \frac{z}{R}\right) x^2}{R^2(R + z)^2} - \frac{(1 - 2\nu)}{R(R + z)} + \frac{(R^2 - 3x^2)z}{R^5} \right] \quad (7-1)$$

$$R = \sqrt{x^2 + y^2 + z^2}$$

Where P is the load magnitude, E is the Young's modulus and ν is the Poisson ratio. Using this solution allows to inversely calculate the Young's modulus E and Poisson ratio ν for each loading step. This is done by assuming that they are constant in the whole half space and using constrained nonlinear least squares optimisation (*fmincon* in Matlab Optimisation toolbox R2016b, (MATLAB 2016)) to minimise the error between the measured, $\varepsilon_{xx,meas}$, and the calculated strain, $\varepsilon_{xx,calc}$, which depends on the elastic parameters E, ν .

$$E_{opt}, \nu_{opt} = \arg \min_{E, \nu} \|\varepsilon_{xx,meas} - \varepsilon_{xx,calc}(E, \nu)\| \quad (7-2)$$

The evolution of this optimised equivalent E and ν with increasing load is presented in Figure 7-5. It is shown that the equivalent E decreases strongly from almost 70 MPa at the lowest applied load to below 20 MPa at the load with a mass of 100 kg. Note that the decay of E is strongest at the lowest applied loads and is in a similar range for both depths.

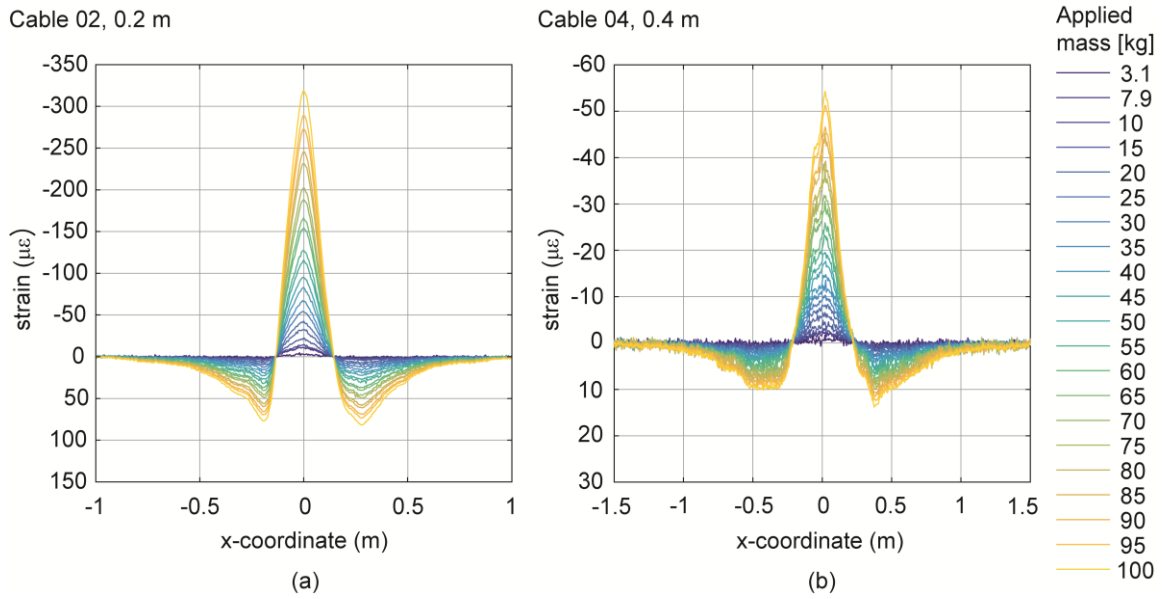


Figure 7-4. Measured strain profiles along cable 1 for loads corresponding to a mass between 3.1 kg and 100 kg: (a) at a depth of 0.2m, (b) at a depth of 0.4m.

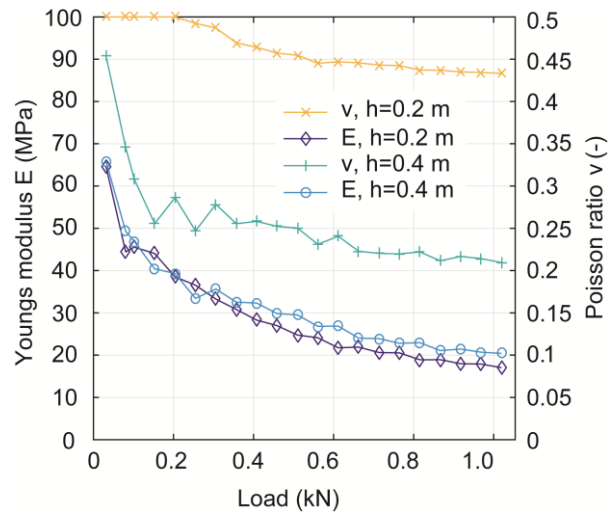


Figure 7-5. Optimised equivalent Young's modulus and Poisson ratio depending on the applied surface load.

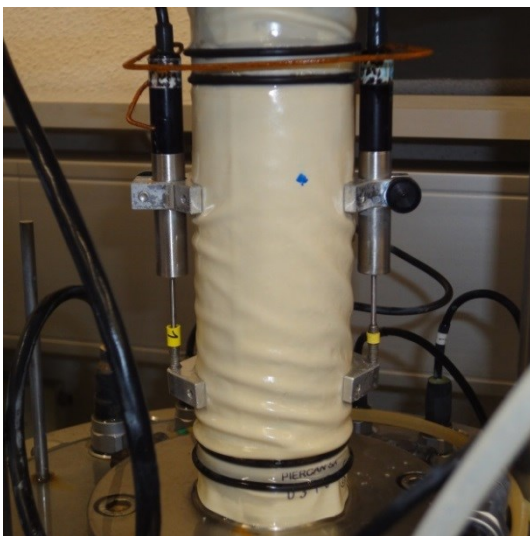
7.4 Triaxial Tests

7.4.1 Sample preparation

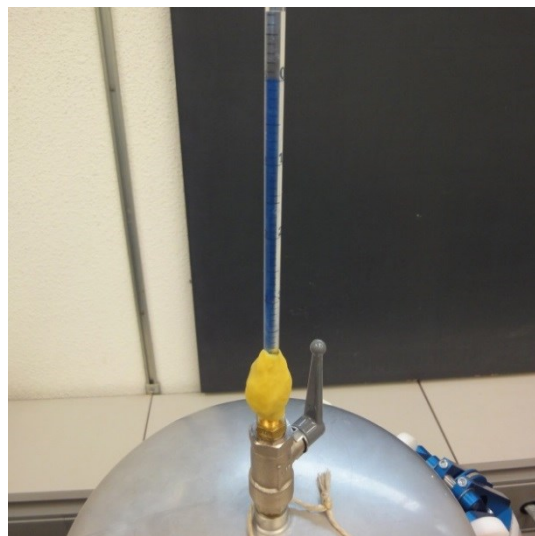
To have an independent measure of the soil behaviour in the field experiment triaxial tests were performed. A probe of soil close to the trench with the FOSs was excavated on the same day as the loading experiment was conducted. This ensured to have the same water content in the triaxial soil samples and the field experiment. The excavated soil was re-compacted inside of the rubber membrane in a mounting help. The re-compacted soil lied between 1.66-1.76 g/cm³ (details to the soil samples used are presented in in Appendix 7-1 (Table 7-1) and in Appendix 7-2). The final probes in the triaxial cell had a diameter of 56.4 mm and a height of 119 mm.

7.4.2 Test setup

The triaxial tests were performed on the triaxial testing apparatus of the geomechanics group at IGT (details on the used triaxial testing apparatus can be found for example in Messerklinger (2006)). The in-situ pressure at the depth of the FOSs is very low (~ 2.3 kPa at 0.2 m or ~ 4.5 kPa at 0.4 m). To perform a triaxial test at such low pressure level raises difficulties regarding the accuracy of the pressure regulation in the cell and the sensitivity of the volumetric strain measurement. To overcome these difficulties the tests were performed with a free water table in a burette fixated to the top of the cell (Figure 7-6 (b)) and the tap of the cell was closed. Due to the small diameter of the burette ($D=5.98$ mm) a change in the cell volume leads to a change of the water table in the burette and therefore a change of the water pressure in the cell which was measured with the pressure sensor. This procedure allows measuring the volume changes of the probe with higher resolution compared to direct measurement of the volume change. Note that not only the volume change of the probe but also the moving rods of the loading frame cause a change of the cell volume which had to be subtracted from the total volume change. Axial compression tests were performed.



(a)



(b)

Figure 7-6. Photos of the triaxial test: (a) probe after the test with LVDT's for local strain measurements, (b) burette on top of the triaxial cell with free water table.

Due to the applied procedure the radial stress changes slightly which leads to stress paths slightly deviating from the inclination $\Delta p/\Delta q = 1/3$. With the procedure low initial pressures at the bottom of the probe (~ 10 kPa) were achieved, which are however still a higher than the expected in-situ pressures at the depth of the FOSs. This may lead to an overestimation of the stiffness. Note that compared to the low pressure the pressure gradient over the height of the probe is high, which is to a smaller degree also the case in the field.

After installing the probe in the triaxial apparatus the water was raised to a level within the burette. During the filling of the cell and the burette with water it was attempted to prevent air bubbles within the cell. The axial stress was then increased slowly to the same level as the radial stress. Due to creep of the soil sample the axial stress reduced under constant displacement of the loading pedestal. This creep was compensated over the duration of approximately 12 hours in steps. After this time the axial stress stayed quite stable and the sample was sheared with a constant axial displacement rate. The loading rate was 0.001 mm/s which corresponds to an axial strain rate of 8.4 $\mu\epsilon/s$.

The triaxial tests were performed with local strain measurements using linear variable displacement transducers (LVDT) with an initial axial distance of 70 mm glued to the rubber membrane (Figure 7-6 (a)) to avoid errors caused by the compliance at the contact of the pedestal and the soil probe. These errors are most pronounced at very small strains and would lead to an underestimation of the stiffness. The used local strain sensing system is described in detail in (Messerklinger 2006).

7.4.3 Test results

The triaxial test results of three tests are presented in the relevant strain range compared to the field experiment (0-300 $\mu\epsilon$) in Figure 7-7. As expected the stress paths deviate slightly from the axial compression path due to the free water table in the burette which leads to small pressure changes caused by the volume changes in the cell. The deviatoric behaviour clearly shows a strong nonlinear behaviour of the soil at very small strains. The apparent tangent shear modulus decays from about 20'000 kPa to about 1'500-3'000 kPa at 1'000 $\mu\epsilon$. Similar to the inversely calculated stiffness from the FOSs in the field experiment the rate of the stiffness degradation is very fast at the origin and becomes smaller with increasing strains. The apparent tangent bulk modulus in the volumetric behaviour similarly degrades quickly from about 12'000-30'000 kPa to about 5'000-20'000 kPa at 1'000 $\mu\epsilon$. As Triax 3 seems not to show the exact same behaviour as Triax 1 and 2, the high stiffness values obtained from the Triax 3 test have to be treated with care. Triax 3 is still shown here for completeness. The strain paths in the relevant strain range seem to be almost linear, at least for Triax 1 and 2, which indicates that the decay of the shear modulus and the decay of the bulk modulus are somehow proportional.

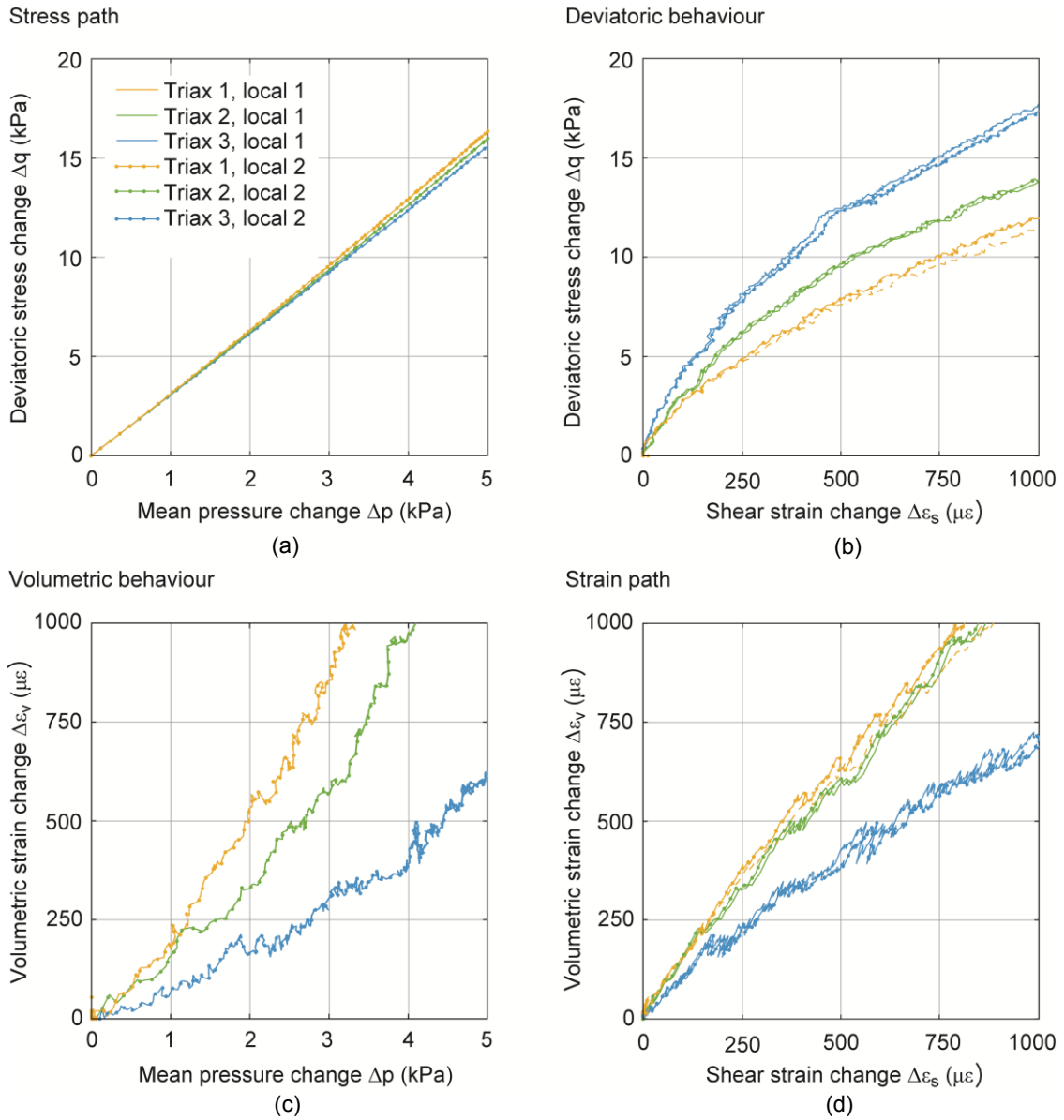


Figure 7-7. Results of the triaxial tests: (a) stress path, (b) deviatoric stress-strain behaviour, (c) volumetric stress-strain behaviour, (d) strain path.

7.5 Modelling

Four different constitutive models are used to investigate their effect on the response in the Boussinesq boundary value problem. The strains in the loaded half space are calculated using the finite-element (FE) method with the four constitutive models implemented. As only loading is considered and in the experiment small irreversible strains were observed after removal of the load and in particular because the inverse analysis for object identification benefits from a unique relation between the applied load and the measured strain only elastic (reversible) models are considered here. However, it is known that the small strain nonlinear behaviour is, at least partly, not reversible (*e.g.*, Puzrin et al. 2001; Puzrin & Burland 1998). The first model uses linear isotropic elasticity, where also an analytical solution for the loaded half space exists (*e.g.*, Boussinesq 1885). The other three models are nonlinear elastic constitutive models with nonlinear deviatoric behaviour and linear volumetric behaviour (Nonlinear 1), both nonlinear deviatoric and volumetric behaviour (Nonlinear 2) and coupled nonlinear deviatoric and volumetric behaviour (Nonlinear 3). The idea of coupling the volumetric and the deviatoric behaviour arised because of the proportional decay of the deviatoric and the volumetric stiffness observed in the triaxial tests and the fact that the zero crossings of the strain measurements in the field experiment are constant.

The nonlinear behaviour of all three models is based on a normalised stress-strain fitting curve. The response of the three nonlinear models is derived according to the hyperelastic approach from a strain energy density function or, following Houlsby & Puzrin (2007) from the Helmholtz free energy function. The stresses are derived from the derivative of the Helmholtz free energy with respect to strains.

7.5.1.1 Normalised stress-strain function

The logarithmic function presented by Puzrin & Burland (1996) is widely accepted to capture accurately the stress-strain curve in the small-strain region of soils in laboratory tests. It has, however, the drawback that the stress-strain function has to be split at the point where the limiting stress is reached and a second function has to be added tangentially (*e.g.*, a linear function). The function is used in the normalised form with the normalisation according to Hardin & Drnevich (1972) and Puzrin (2012), the normalisation is shown here examplarily for the deviatoric behaviour.

$$y = \frac{q}{q_L}; \quad x = \frac{\varepsilon_s}{\varepsilon_{sr}}; \quad \varepsilon_{sr} = \frac{q_L}{3G_0}; \quad x_L = \frac{\varepsilon_{sL}}{\varepsilon_{sr}} \quad (7-3)$$

Where q_L is the limiting stress at the strain ε_{sL} and G_0 is the initial stiffness.

The logarithmic function is defined as

$$y(x) = x - \alpha x (\ln(1 + x))^R \quad (7-4)$$

with the parameters

$$R = \frac{(1 + x_L) \ln(1 + x_L)}{(x_L - 1)} \left(\frac{1}{x_L} - b \right) \quad (7-5)$$

$$\alpha = \frac{x_L - 1}{x_L (\ln(1 + x_L))^R}$$

and

$$b = \frac{G_L}{G_0} \quad (7-6)$$

Where G_L is the stiffness at the limiting stress q_L . The normalised stress strain behaviour of the logarithmic function is shown, as an example, in Figure 7-8 (b).

The constitutive models used in this study are formulated in terms of total stress. As the soil is in a partially saturated state the evaluation using effective stresses is very cumbersome and not within the scope of the chapter. Although the model behaviour depends only on the stress and strain changes during loading of the ground surface, the initial stress and strain states are omitted in the notation (for example the mean stress change is denoted p and not $\Delta p = p - p_0$ and the volumetric strain change is ε_v and not $\Delta \varepsilon_v = \varepsilon_v - \varepsilon_{v0}$).

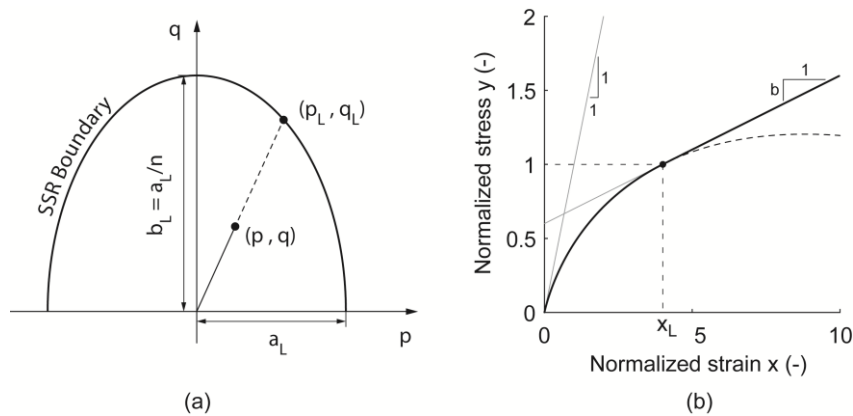


Figure 7-8. (a) Small strain region (SSR) as an ellipse in the p-q-stress space, definition of the limiting stresses p_L and q_L ; (b) Example of the normalised logarithmic stress strain function.

7.5.2 Non-linear elasticity 1: nonlinear deviatoric behaviour and linear volumetric behaviour

7.5.2.1 Triaxial stress-strain space

The Helmholtz free energy potential for this model in the triaxial space is (Puzrin 2012):

$$f(\varepsilon_v, \varepsilon_s) = K \frac{\varepsilon_v^2}{2} + \frac{q_L^2}{3G_0} \cdot \int_0^{\frac{3G_0\varepsilon_s}{q_L}} y(x) dx \quad (7-7)$$

Where K is the bulk modulus, q_L is the limiting deviatoric stress where the limiting stiffness G_L is reached, G_0 is the initial shear modulus and $y(x)$ is the normalised stress-strain function. The stresses are derived as the derivative of the Helmholtz free energy with respect to the strains.

$$\begin{aligned} p &= \frac{\partial f}{\partial \varepsilon_v} = K \varepsilon_v \\ q &= \frac{\partial f}{\partial \varepsilon_s} = q_L y\left(\frac{3G_0\varepsilon_s}{q_L}\right) \end{aligned} \quad (7-8)$$

7.5.2.2 Generalisation to 3D stress-strain space

As isotropic behaviour is assumed, the extension of the constitutive model to the full stress-strain space is done by substituting the strains in the Helmholtz free energy function by the definition of the strain invariants

$$\begin{aligned} \varepsilon_v &= I_1 = \varepsilon_{11} + \varepsilon_{22} + \varepsilon_{33} \\ \varepsilon_s &= \frac{2}{3} \sqrt{3I_{2D}} \end{aligned} \quad (7-9)$$

with

$$I_{2D} = \frac{1}{6} [(\varepsilon_{11} - \varepsilon_{22})^2 + (\varepsilon_{33} - \varepsilon_{22})^2 + (\varepsilon_{11} - \varepsilon_{33})^2] + \varepsilon_{12}^2 + \varepsilon_{23}^2 + \varepsilon_{31}^2 \quad (7-10)$$

This results in the Helmholtz free energy function for the general 3D stress-strain space.

$$f(\varepsilon_{ij}) = K \frac{I_1^2}{2} + \frac{q_L^2}{3G_0} \cdot \int_0^{\frac{2G_0\sqrt{3I_{2D}}}{q_L}} y(x) dx \quad (7-11)$$

The stresses in the general 3D space are derived from the derivation of (7-11) with respect to strains ε_{ij} .

$$\sigma_{ij} = \frac{\partial f}{\partial \varepsilon_{ij}} = K \delta_{ij} + \frac{q_L}{\sqrt{3I_{2D}}} y\left(\frac{2G_0\sqrt{3I_{2D}}}{q_L}\right) \frac{\partial I_{2D}}{\partial \varepsilon_{ij}} \quad (7-12)$$

Where δ_{ij} is the Kronecker delta which is 1 if i and j are equal and is 0 if they are not equal.

7.5.3 Non-linear elasticity 2: nonlinear deviatoric behaviour and nonlinear volumetric behaviour

7.5.3.1 Triaxial stress-strain space

The Helmholtz free energy potential for this model in the triaxial space is:

$$f(\varepsilon_v, \varepsilon_s) = \frac{p_L^2}{K_0} \cdot \int_0^{\frac{K_0|\varepsilon_v|}{p_L}} y_v(x_v) dx_v + \frac{q_L^2}{3G_0} \cdot \int_0^{\frac{3G_0\varepsilon_s}{q_L}} y_s(x_s) dx_s \quad (7-13)$$

Where K_0 is the initial bulk modulus, p_L is the limiting mean stress in the volumetric behaviour, G_0 is the initial shear modulus, q_L is the limiting deviatoric stress and $y_v(x_v)$ and $y_s(x_s)$ are the normalised stress-strain functions for the volumetric and the deviatoric behaviour, respectively.

The stresses are derived as derivation of the Helmholtz free energy with respect to the strains.

$$p = \frac{\partial f}{\partial \varepsilon_v} = \text{sgn}(\varepsilon_v) p_L y_v \left(\frac{K_0|\varepsilon_v|}{p_L} \right) \quad (7-14)$$

$$q = \frac{\partial f}{\partial \varepsilon_s} = q_L y_s \left(\frac{3G_0\varepsilon_s}{q_L} \right)$$

Where $\text{sgn}(\varepsilon_v)$ is the signum function which is 1 if the argument is positive, -1 if the argument is negative and 0 if the argument is 0.

7.5.3.2 Generalisation to 3D stress-strain space

Similar to the nonlinear 1 model the extension of the constitutive model to the full stress-strain space is done by substituting the strains in the Helmholtz free energy function by the definition of the strain invariants. This results in the Helmholtz free energy function for the general 3D stress-strain space.

$$f(\varepsilon_{ij}) = \frac{p_L^2}{K_0} \cdot \int_0^{\frac{K_0|I_1|}{p_L}} y_v(x_v) dx_v + \frac{2G_0\sqrt{3I_{2D}}}{q_L} \cdot \int_0^{\frac{q_L}{\sqrt{3I_{2D}}}} y_s(x_s) dx \quad (7-15)$$

The stresses in the general 3D space are derived from the derivation of the Helmholtz free energy function with respect to strains ε_{ij} .

$$\sigma_{ij} = \frac{\partial f}{\partial \varepsilon_{ij}} = \text{sgn}(I_1) p_L y_v \left(\frac{K_0|I_1|}{p_L} \right) \delta_{ij} + \frac{q_L}{\sqrt{3I_{2D}}} y_s \left(\frac{2G_0\sqrt{3I_{2D}}}{q_L} \right) \frac{\partial I_{2D}}{\partial \varepsilon_{ij}} \quad (7-16)$$

7.5.4 Non-linear elasticity 3, nonlinear elastic model with deviatoric and volumetric coupling

7.5.4.1 Triaxial stress-strain space

An elastic model is proposed which couples the non-linear deviatoric and the non-linear volumetric behaviour. As shown later, the coupling is achieved by defining the size of the small strain region (SSR) similarly to Puzrin et al. (2001) and Puzrin & Burland (1998) as an ellipse in the $p - q$ -stress plane. As the ellipse is defined in the stress space the constitutive behaviour is, in contrast to the other models, first derived from the Gibbs free energy potential. Following Houslyby & Puzrin (2007) the Gibbs free energy potential is

$$g(q, p) = -\frac{a_L^2}{K_0} \cdot \int_0^{\frac{p}{p_L(p,q)}} x_v(y_v) dy_v - \frac{a_L^2}{3G_0} \cdot \int_0^{\frac{q}{q_L(p,q)}} x_s(y_s) dy_s \quad (7-17)$$

Where $x_v(y_v)$ and $x_s(y_s)$ are the inverse of the normalised stress-strain functions for the volumetric and the deviatoric behaviour, respectively. The stresses p_L and q_L define the size of the small strain region (SSR) in the $p - q$ -stress plane and are functions of the current stress state and the parameters a_L and n which define the ellipse used to couple the deviatoric and the volumetric stress-strain behaviour. The two limiting stresses p_L and q_L are defined to lie on the intersection between the ellipse described by

$$\frac{p_L^2}{a_L^2} + \frac{q_L^2 n^2}{a_L^2} = 1 \quad (7-18)$$

and the radial projection of the current stress point (Figure 7-8 (a)). This leads to the following expressions for the limiting stresses.

$$p_L(p, q) = \frac{a_L p}{\pm \sqrt{p^2 + q^2 n^2}} \quad (7-19)$$

$$q_L(p, q) = \frac{q}{p} p_L(p, q) = \frac{a_L q}{\pm \sqrt{p^2 + q^2 n^2}}$$

For the further derivations only the positive sign is used. The strains are calculated by the derivative of the Gibbs free energy function with respect to the stresses.

$$\varepsilon_v = -\frac{\partial g}{\partial p} = \frac{p}{\zeta(p, q)} \left(\frac{x_v(\zeta(p, q))}{K_0} + \frac{x_s(\zeta(p, q))}{3G_0} \right) \quad (7-20)$$

$$\varepsilon_s = -\frac{\partial g}{\partial q} = \frac{qn^2}{\zeta(p, q)} \left(\frac{x_v(\zeta(p, q))}{K_0} + \frac{x_s(\zeta(p, q))}{3G_0} \right)$$

where

$$\zeta(p, q) = y_v = y_s = \frac{p}{p_L} = \frac{q}{q_L} = \frac{\sqrt{p^2 + q^2 n^2}}{a_L} \quad (7-21)$$

Note that the functions $x_v(y_v)$ and $x_s(y_s)$ do not have the same parameters and therefore, although their argument is the same, their functional value is different.

The ratio between volumetric and shear strains depends only on the ratio of the mean pressure, the deviatoric stress and the parameter n which defines the eccentricity of the limiting ellipse in the stress space. Proportional loading therefore results in a constant strain ratio.

$$\frac{\varepsilon_v}{\varepsilon_s} = \frac{\frac{p}{\zeta(p, q)}}{\frac{qn^2}{\zeta(p, q)}} = \frac{1}{n^2} \frac{p}{q} \quad (7-22)$$

For the implementation in finite-element (FE) software as user subroutine the stress has to be defined as a function of strains. The derivation is shown here starting from the corresponding Helmholtz free energy function.

$$f(\varepsilon_v, \varepsilon_s) = \frac{a_L^2}{K_0} \cdot \int_0^{\frac{K_0 \varepsilon_v}{p_L(\varepsilon_v, \varepsilon_s)}} y_v(x_v) dx_v + \frac{a_L^2}{3n^2 G_0} \cdot \int_0^{\frac{3G_0 \varepsilon_s}{q_L(\varepsilon_v, \varepsilon_s)}} y_s(x_s) dx_s \quad (7-23)$$

Where $y_v(x_v)$ and $y_s(x_s)$ are the respective normalised stress-strain functions for the purely volumetric and deviatoric stress paths and the limiting stresses p_L and q_L are functions of the strain

$$p_L(\varepsilon_v, \varepsilon_s) = \frac{a_L n \varepsilon_v}{\sqrt{\varepsilon_s^2 + n^2 \varepsilon_v^2}} \quad (7-24)$$

$$q_L(\varepsilon_v, \varepsilon_s) = \frac{\varepsilon_s}{n^2 \varepsilon_v} p_L(\varepsilon_v, \varepsilon_s) = \frac{\varepsilon_s n a_L}{n^2 \sqrt{\varepsilon_s^2 + n^2 \varepsilon_v^2}}$$

The stresses are derived as derivatives of the Helmholtz free energy with respect to volumetric ε_v and deviatoric strains ε_s .

$$p = \frac{\partial f}{\partial \varepsilon_v} = \frac{\varepsilon_v}{\xi} (y_v(K_0 \xi) + y_s(3n^2 G_0 \xi)) \quad (7-25)$$

$$q = \frac{\partial f}{\partial \varepsilon_s} = \frac{\varepsilon_s}{n^2 \xi} (y_v(K_0 \xi) + y_s(3n^2 G_0 \xi))$$

With

$$\xi = \frac{\varepsilon_v}{p_L} = \frac{\varepsilon_s}{n^2 q_L} = \frac{\sqrt{\varepsilon_s^2 + n^2 \varepsilon_v^2}}{n a_L} \quad (7-26)$$

7.5.4.2 Model response in the triaxial stress space

The model response for proportional loading paths is shown in Figure 7-9 calculated with the parameters shown in Table 7-2 in the Appendix 7-2. Note that due to the coupling of the volumetric and the deviatoric behaviour the stiffness parameters K and G do not correspond with the gradients of the volumetric and deviatoric behaviour. As the limiting stresses are coupled using an ellipse in the triaxial stress space, stress paths with more volumetric loading reach the limiting stiffness in the deviatoric behaviour faster than stress paths with more deviatoric loading. In contrast, in the volumetric behaviour stress paths with more volumetric loading reach the limiting stiffness slower than stress paths with more deviatoric loading. Note that, as shown in equation (7-22) the coupling of the deviatoric and the volumetric behaviour leads to straight strain paths for proportional loading.

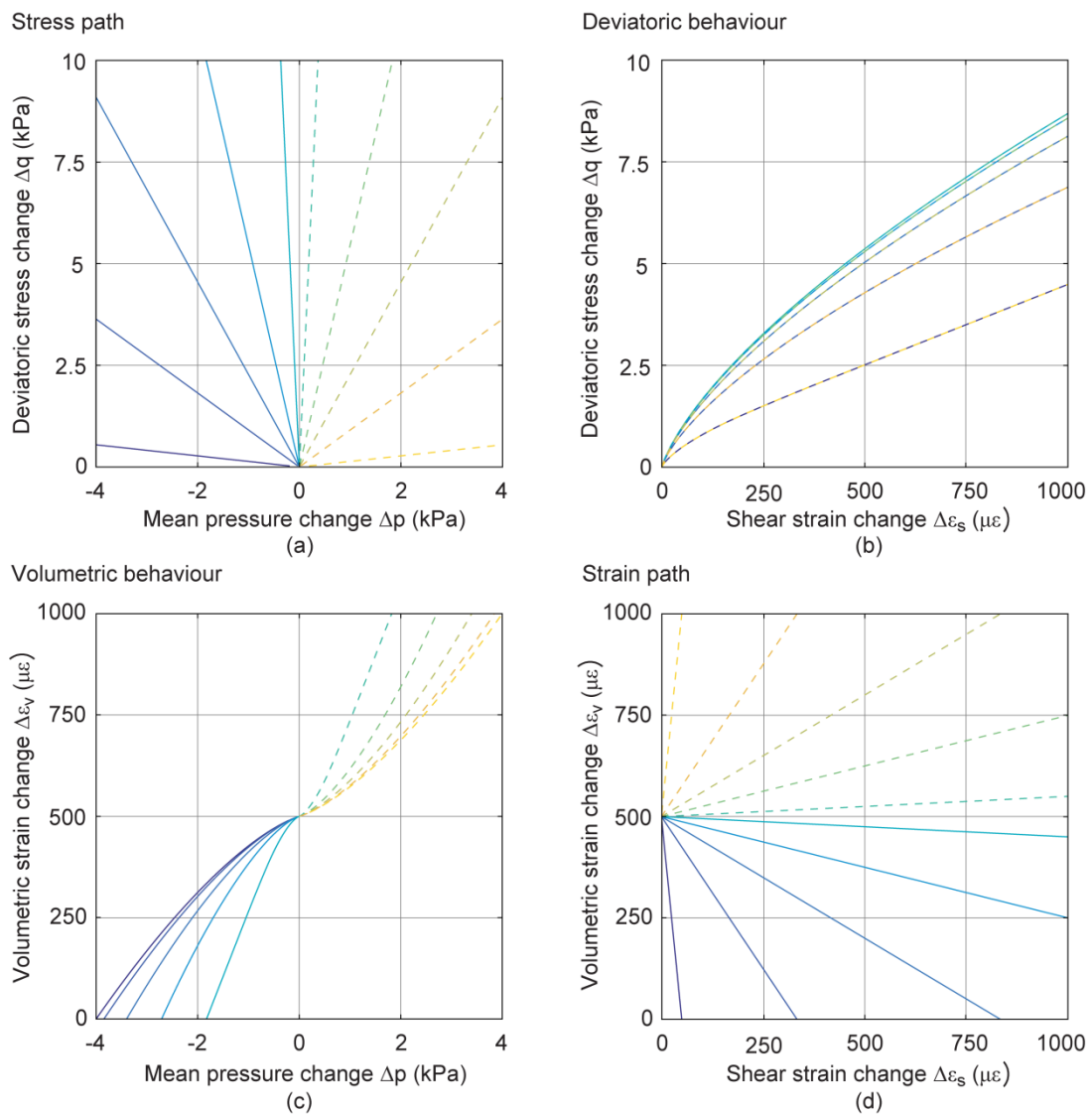


Figure 7-9. Model response in the triaxial stress space for different stress paths: (a) stress path; (b) deviatoric behaviour; (c) volumetric behaviour; (d) strain path

7.5.4.3 Generalisation to 3D stress-strain space

Similarly to the preceding models the extension of the constitutive model to the full stress-strain space is done by substituting the strains in (12) by the definition of the strain invariants. This results in the Helmholtz free energy function for the general 3D stress-strain space.

$$f(\varepsilon_{ij}) = \frac{a_L^2}{K_0} \cdot \int_0^{K_0\chi} y_v(x_v) dx_v + \frac{a_L^2}{3n^2G_0} \cdot \int_0^{3G_0n^2\chi} y_s(x_s) dx_s \quad (7-27)$$

where

$$\chi = \frac{\sqrt{\frac{4}{3}I_{2D} + n^2I_1^2}}{na_L} \quad (7-28)$$

The stresses are derived from the derivative of (25) with respect to strains ε_{ij} .

$$\sigma_{ij} = \frac{\partial f}{\partial \varepsilon_{ij}} = \frac{n^2I_1\delta_{ij} + \frac{2}{3}\frac{\partial I_{2D}}{\partial \varepsilon_{ij}}}{n^2\chi} [y_v(K_0\chi) + y_s(3G_0n^2\chi)] \quad (7-29)$$

7.6 Model responses in the Boussinesq problem

The application of the nonlinear elastic models to the Boussinesq problem studied in the experiment was done using the ABAQUS/explicit (Simulia, Dassault Systèmes, Providence, RI) finite element (FE) computing environment. The constitutive models were implemented with a user subroutine. The geometry of the axisymmetric FE model is shown in Figure 7-10. The loading was applied similar to the experiment on a stiff plate with diameter of 0.1 m. The interaction between the plate and the soil was modelled using a 'hard' normal contact and frictionless shear contact. As the comparison of the experiment and the model is done on the level of the buried FOSs the exact modelling of the contact is not of great importance.

It is assumed that the behaviour is independent of the initial stress state in the soil. Therefore no self-weight is applied to the soil. The load P on the stiff plate applied with a smooth step function to simulate quasi-static conditions which were checked by comparison of the kinetic energy and the applied external work. At the load steps corresponding to the experiment, virtual strain and

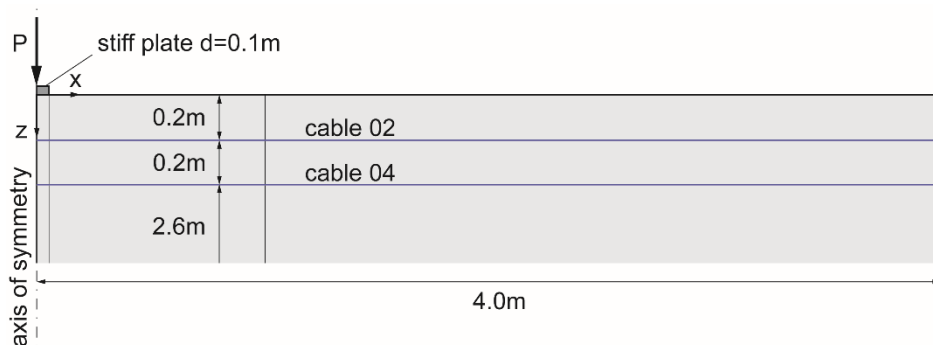


Figure 7-10. Geometry of the axisymmetric model in ABAQUS

stress measurements are recorded along horizontal lines at the depth of 0.2 m and 0.4 m corresponding to virtual FOSs.

The parameters of the constitutive models were optimised to fit the experimental data and are shown in Table 7-2 in the Appendix 7-2. This optimisation was performed manually by comparing the strain value directly under the load and the distance to the zero crossing of the strain profile. A comparison of the model responses with the triaxial tests performed is shown later. A validation of the FE model against the elastic solution with a point load on its surface is shown in Appendix 7-4.

7.6.1 Strains along the fibre-optic sensors

The resulting strains are shown in Figure 7-11 for the cable 02 at a depth of 0.2 m. All three constitutive models are able to capture the general strain profile with extension strain under the load and compressive strain further away. While the linear elastic model captures the ‘shape’ of the strain profile quite accurately it is not able to capture the nonlinearity. In contrast, all three nonlinear models capture the nonlinearly increasing strain with each load step but lead to a wider shape of the strain. In particular the nonlinear 1 model (nonlinear deviatoric and linear volumetric behaviour) produces a wider peak directly underneath the load. The nonlinear model 2 and 3 capture the width of the strain peak quite well but overestimate the compressive strain at around cable coordinate 0.5 m. However, they both capture the fast decay of compressive strain with increasing distance from the load. The ‘shapes’ of the measured and calculated strain profiles are also compared in Figure 7-11 (f) in a normalised way.

The resulting strains at the cable 04 at a depth of 0.4 m are shown in Figure 7-12. Similarly to cable 02, linear elasticity captures the ‘shape’ of the strain profile accurately. The nonlinear 1, although capturing the stiffness decay, leads to a wide and ‘flat’ strain peak underneath the load. The nonlinear 2, and in particular the nonlinear model 3 capture the narrow strain peak underneath the load better but both overestimate the compressive strain around cable coordinate 0.5 m. The ‘shapes’ of the measured and calculated strain profiles are also compared in Figure 7-12 (f) in a normalised way.

The constitutive models used are compared in Figure 7-13 by following distinct points of the strain profile throughout the loading process. In Figure 7-13 (a) and (c) the strain directly under the load is plotted against the applied load magnitude for cable 02 and cable 04, respectively. It is shown that all the nonlinear models are able to capture the behaviour observed in the field experiment quite accurately. In Figure 7-13 (b) and (d) the distance between the zero crossings of the strain profile are plotted against the applied load for cable 02 and cable 04, respectively. Note that the spatial resolution of the zero crossings shown in Figure 7-13 (b) was chosen equal to the spatial resolution of the FOS measurements. It is shown that this distance remains more or less constant during the experiment. In the linear elastic model this distance is purely defined by the Poisson ratio ν . As ν remains constant the distance between the zero crossings also remains constant. In contrast this distance increases with the nonlinear 1 model (in particular in cable 04) due to the increasing difference between the decaying tangent shear modulus $G(\varepsilon_s)$ and the constant bulk modulus K . With the nonlinear model 2 and in particular the nonlinear model 3 the distance between the zero crossings remains again more or less constant during the loading history. This is a result of the more proportional decrease of both shear and bulk moduli of these models.

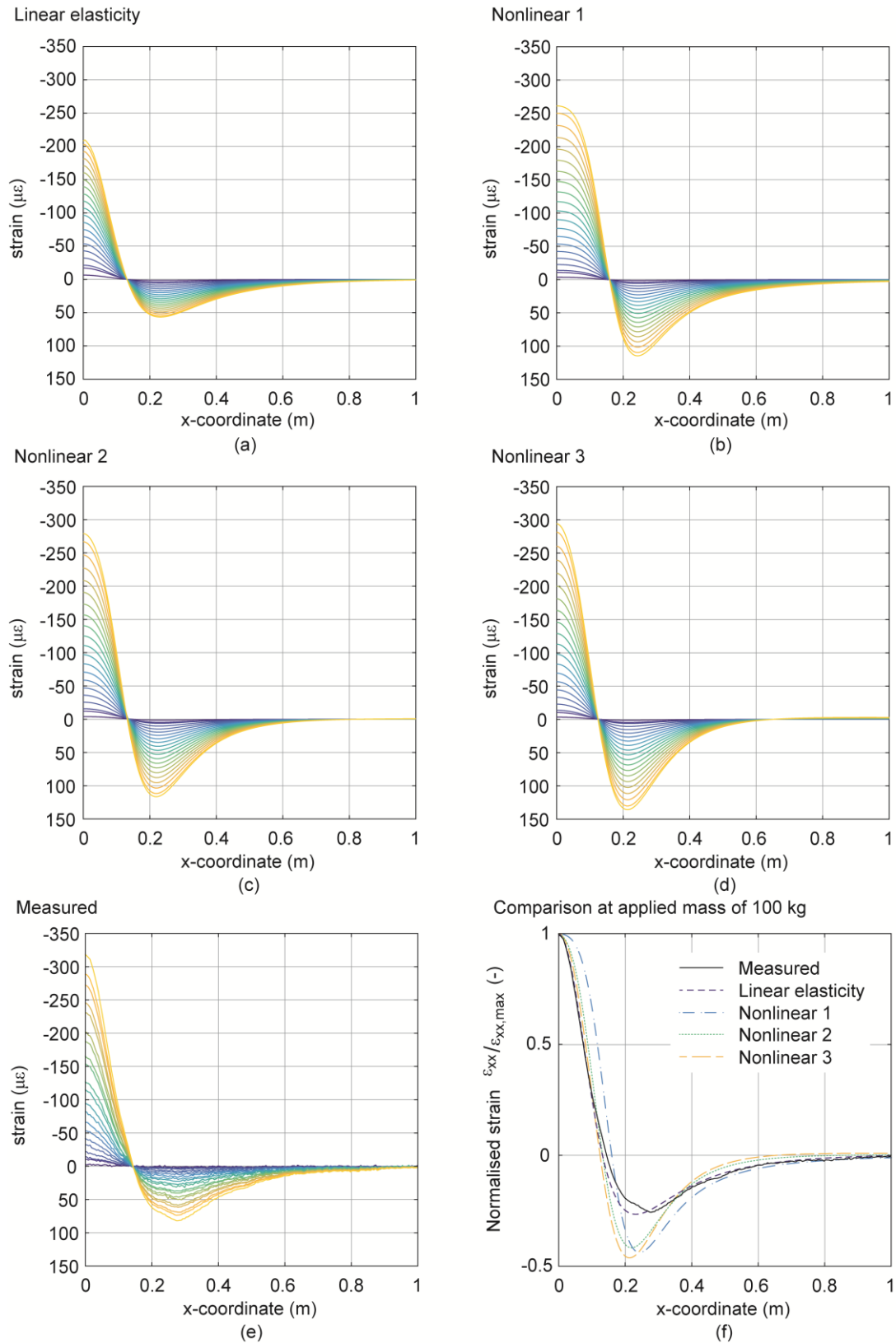


Figure 7-11. Horizontal strains ϵ_{xx} at the level of cable 02 (0.2 m) for the four different constitutive models: (a) linear isotropic elasticity; (b) nonlinear deviatoric and linear volumetric behaviour; (c) both nonlinear deviatoric and volumetric behaviour; (d) coupled nonlinear deviatoric and volumetric behaviour; (e) measured strain; (f) comparison of the strains at the load corresponding to a mass of 100 kg.

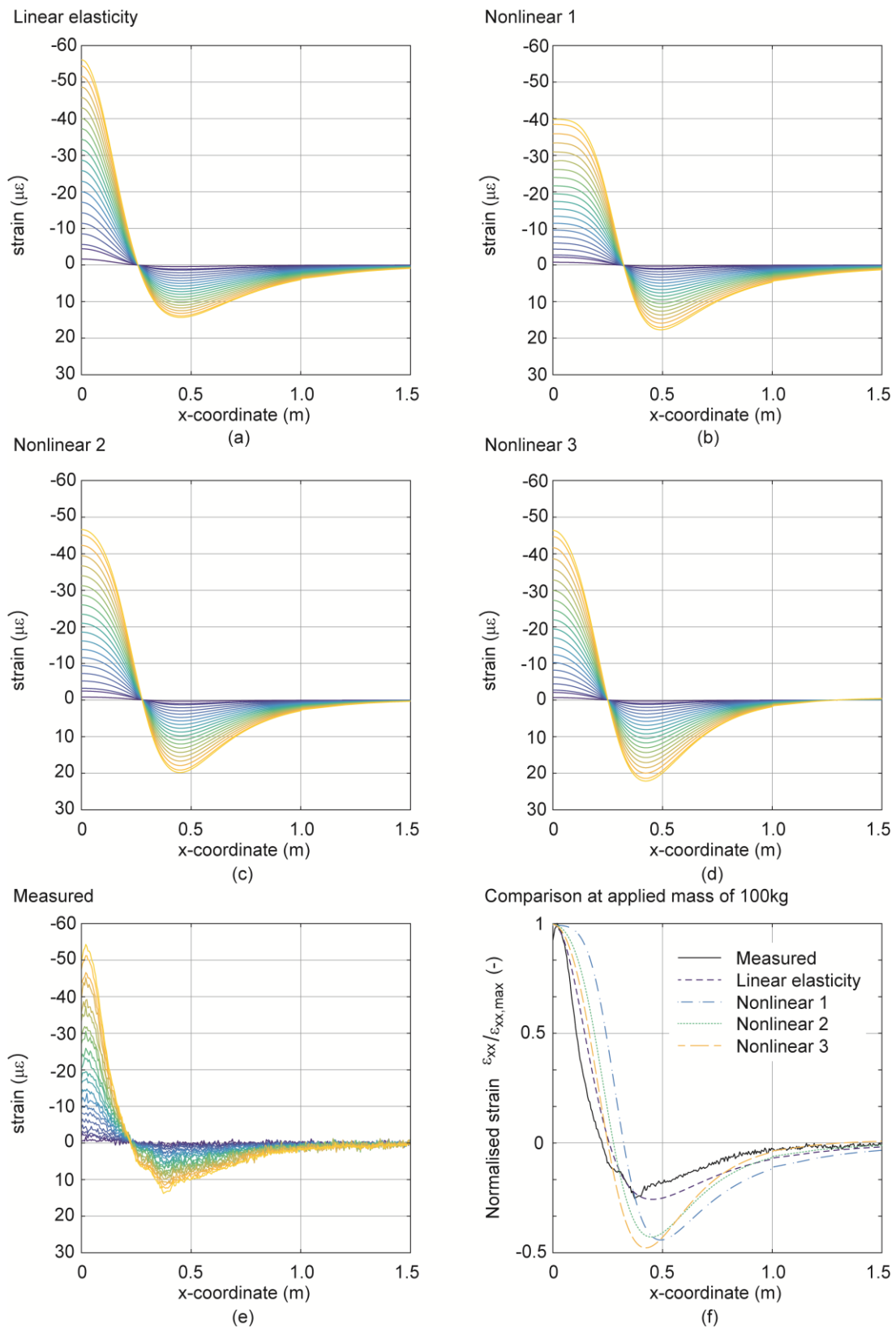


Figure 7-12. Horizontal strains ϵ_{xx} at the level of cable 04 (0.4 m) for the four different constitutive models: (a) linear isotropic elasticity; (b) nonlinear deviatoric and linear volumetric behaviour; (c) both nonlinear deviatoric and volumetric behaviour; (d) coupled nonlinear deviatoric and volumetric behaviour; (e) measured strain; (f) comparison of the strains at the load corresponding to a mass of 100 kg.

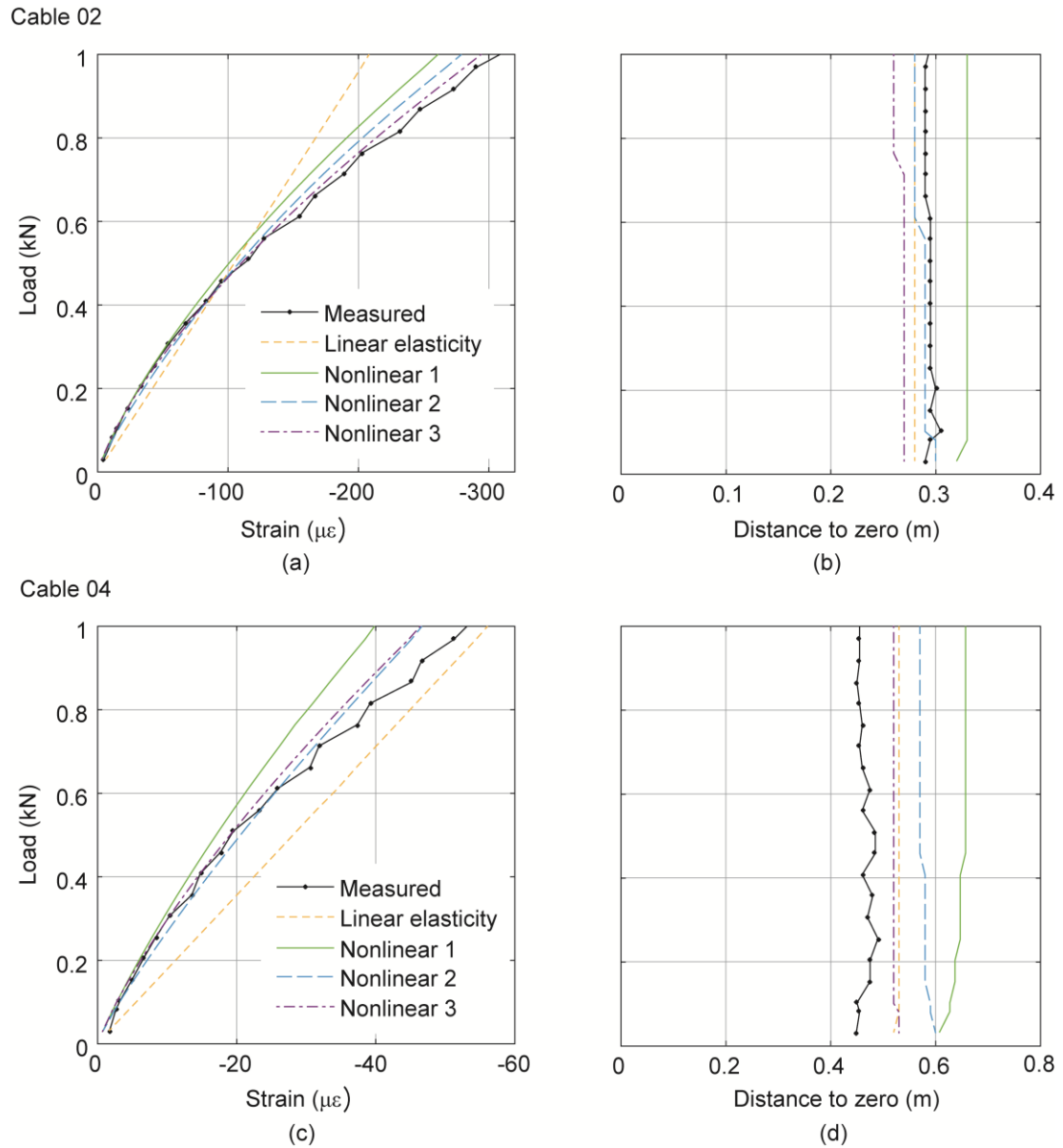


Figure 7-13. Comparison of distinct points of the strain profiles with increasing load: cable 02 (a) min. strain directly under the load vs. applied load; (b) distance from the load axis to the zero crossing of the strain profile; cable 04 (c) min. strain directly under the load vs. applied load; (d) distance from the load axis to the zero crossing of the strain profile.

7.6.2 Stress paths

To shed more light into the different behaviours of the used constitutive models in the Boussinesq problem the stress paths at the depth of the buried FOSs are evaluated (Figure 7-14 for cable 02 and Figure 7-15 for cable 04). It is shown that while with linear elasticity the stress paths of the evaluated points are linear and follow almost the same inclination of $\Delta q/\Delta p \sim 3.5$, with the nonlinear model 1 their inclination is spread between purely deviatoric paths underneath the load and $\Delta q/\Delta p \sim 2.8$. Furthermore the stress paths are curved. This can be explained by a redistribution of the stresses from the loaded axis towards larger distances with increasing strain. The same effect is observed with the nonlinear 2 model where due to the nonlinear volumetric behaviour the stress paths do not spread as strongly compared to the nonlinear 1 model. The nonlinear 3 model with its deviatoric-volumetric coupling leads, similar to the linear elastic model, to linear stress paths but their inclination is spread similarly compared to the nonlinear 2 model. Note that the magnitudes of the stress paths of all nonlinear models are significantly lower than the stress paths of the linear elastic model. This can be explained by wider distribution of the stresses away from the load axis and is reflected also in the wider strain profiles of the nonlinear 1 model and the overestimation of the compressive strain of all three nonlinear models (Figures 7-11 and 7-12).

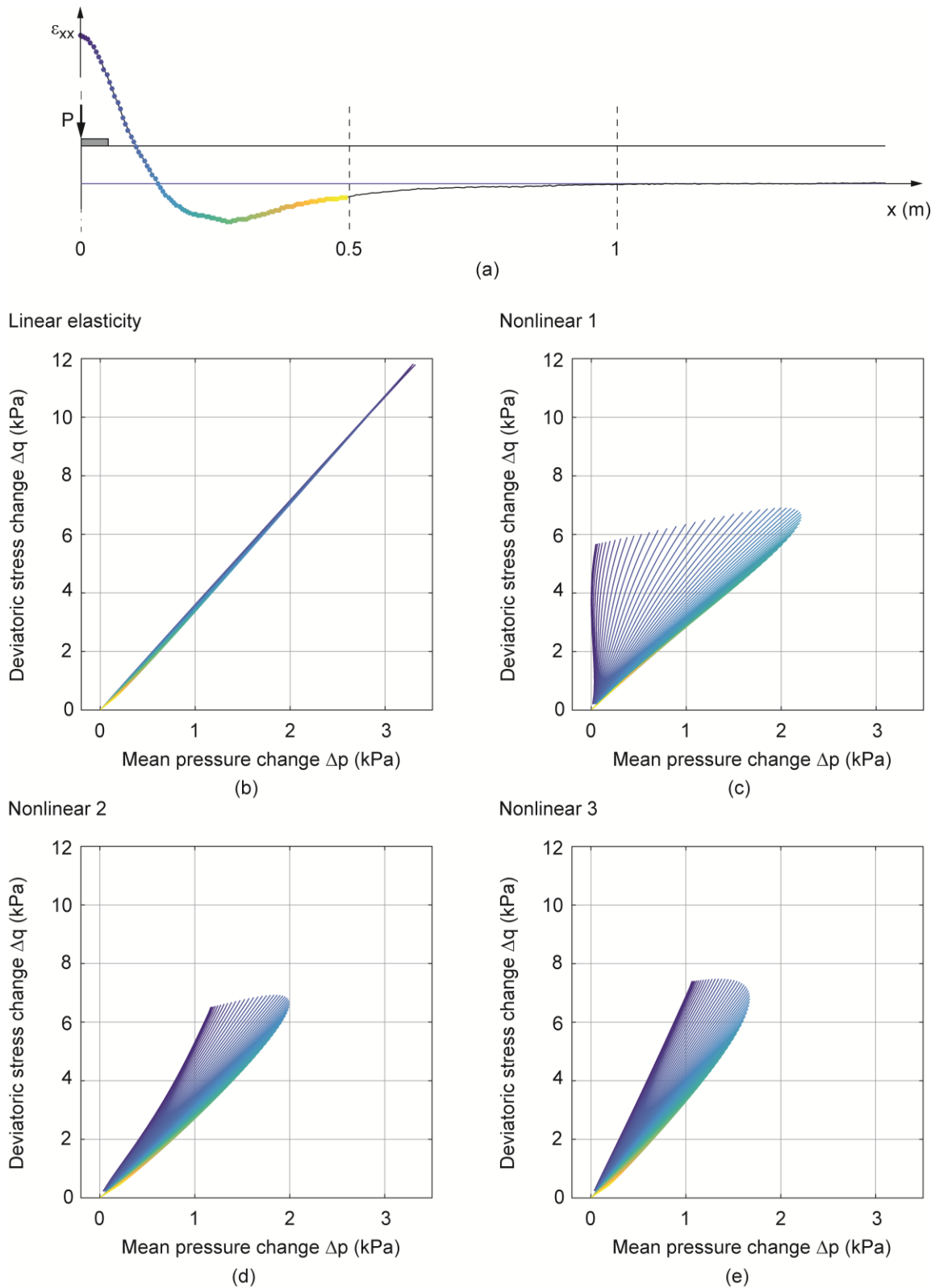


Figure 7-14. Comparison of the stress paths for the different constitutive models at points along cable 02; (a) location of the evaluated points; (b) linear elastic model; (c) nonlinear 1 model; (d) nonlinear 2 model; (e) nonlinear 3 model.

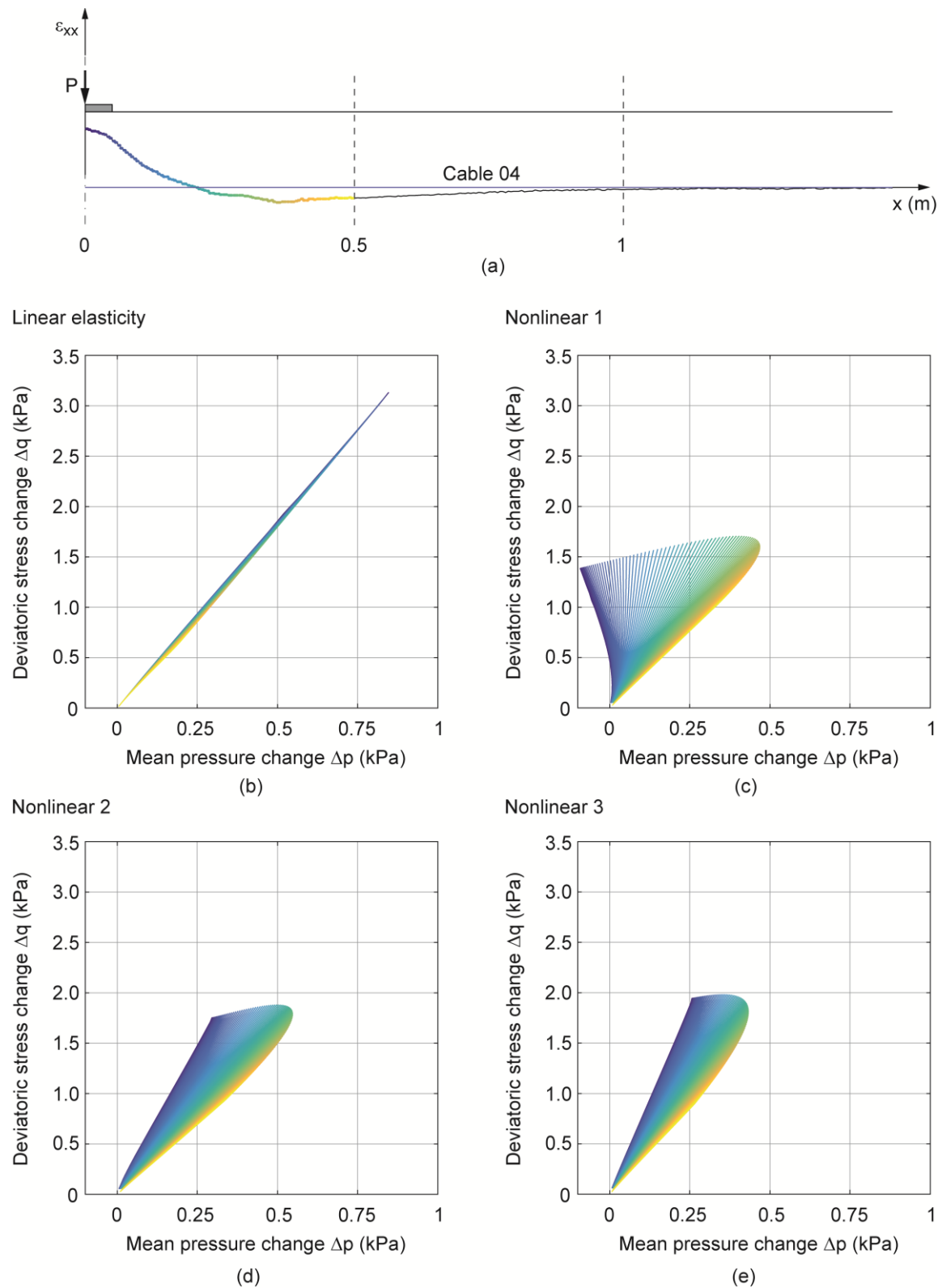


Figure 7-15. Comparison of the stress paths for the different constitutive models at points along cable 02; (a) location of the evaluated points; (b) linear elastic model; (c) nonlinear 1 model; (d) nonlinear 2 model; (e) nonlinear 3 model.

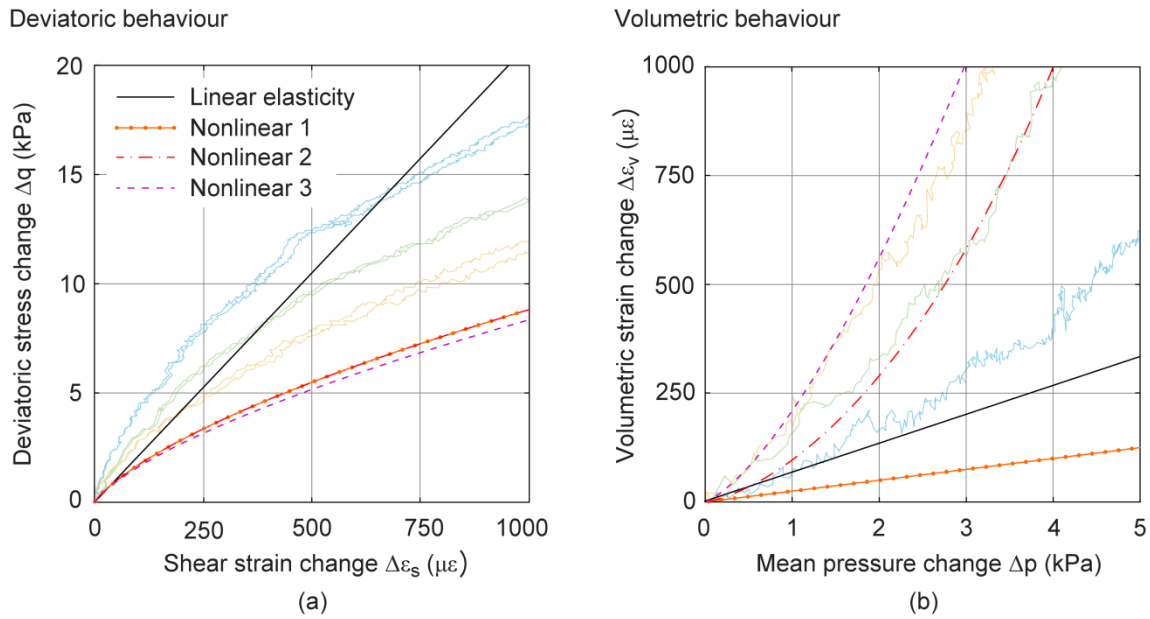


Figure 7-16. Comparison of the stress-strain behaviour of the four models with the parameters from Table 7-2 with the triaxial test results: (a) deviatoric behaviour; (b) volumetric behaviour.

7.6.3 Comparison with triaxial test results

The performed triaxial tests showed clear nonlinear stress-strain curves in both the deviatoric and the volumetric behaviour. The four constitutive models were fitted to match the measured strains along the buried FOSs accurately. Figure 7-16 shows the comparison of the deviatoric and volumetric behaviours of the models with the triaxial test results for an axial compression path (only the nonlinear 3 model is stress path dependent). It is shown that the linear elastic model only captures the ‘mean’ stiffness measured in the triaxial tests as a secant modulus. Still it is able to reproduce the strain measurements of the field experiment quite accurately. The nonlinear models follow almost the same deviatoric stress-strain curve, with a smaller stiffness compared to the triaxial tests. This difference is most likely a result of the too high radial stresses in the triaxial tests. The difference between the in-situ stiffness and the stiffness in the triaxial test can be approximated using the well-established power laws (*e.g.*, Janbu 1963; Ohde 1939) to take the influence of the confining stress into account.

$$\frac{G}{G_{ref}} = \left(\frac{p}{p_{ref}} \right)^m \quad (7-30)$$

With $m = 0.5$ for sands and silts this leads in this case to $G/G_{ref} \sim 0.48$ and ~ 0.67 for cable 02 and cable 04, respectively. These ratios may explain at least the magnitude of the difference between the best-fit constitutive models and the triaxial test results.

7.7 Conclusions

Fibre-optic sensors (FOSs) buried in the ground have been used in a field experiment to measure the strains in the ground caused by a small load acting on the surface (Boussinesq problem). During this experiment a significant nonlinearity of the soil stiffness was observed. The stiffness decreased significantly with increasing load and the rate of decrease is strongest at the smallest applied loads, which is a justification for the use of the logarithmic stress-strain function to model the soil behaviour at small strains. FOSs proved to be a suitable tool for the investigation of the soil behaviour at the very small strains caused by the surface loads. The experimental results shown in this chapter represent a unique direct measurement of the soil nonlinearity in a geotechnical boundary value problem in a field experiment.

The same nonlinear behaviour could be observed in triaxial tests performed at low confining stresses. Both the deviatoric and the volumetric behaviour show proportional degradation of stiffness at small strains.

The boundary value problem considered in the field experiment was modelled using the finite-element method with four different constitutive models. It was found that linear elasticity captures the ‘shape’ of the strain profiles in the Boussinesq problem accurately but can only fit the measured strain data at one particular load magnitude for which the stiffness parameters are optimised. To overcome this limitation the response using three nonlinear elastic models was investigated. It is shown that not only the nonlinear deviatoric but also the nonlinear volumetric behaviour is important to capture the strains measured in the field experiment.

To capture the measured strains at the FOSs buried at different depths in the ground the influence of pressure dependency could be implemented into the models. Although elastic models are able to capture the measured strains during the experiment accurately, the observed strains are partly irreversible. For more accurate modelling of the loading and unloading behaviour of a geotechnical boundary value problem at such small strains elastic-plastic kinematic hardening constitutive models should be used. Further improvement could also be achieved by the consideration of potential anisotropic soil behaviour, which may be significant at the very low vertical stresses close to the ground surface.

However, none of the nonlinear models matches the ‘shape’ of the strain profiles as close as linear elasticity. Therefore, for the application in surface object identification a model using linear elasticity with constant Poisson ratio and load-dependent Young’s modulus constant in the whole half space should provide the best results, although such a model is mechanically questionable.

7.8 Appendix 7-1: Details on the triaxial test samples

In table 7-1 the density and the initial stress values of the triaxial test samples is presented.

Table 7-1. Details on the triaxial test samples

Sample no.	Density ρ (g/cm ³)	Initial axial stress $\sigma_{1,init}$ (kPa)	Initial radial stress $\sigma_{3,init}$ (kPa)
1	17.6	12.5	10.3
2	16.6	10.9	10.5
3	17.4	10.3	10.8

7.9 Appendix 7-2: Grading of the soil

Figure 7-17 shows grading curve of the natural soil excavated at the experimental site in the field. Due to the significant amount of silt and fines the curve was built from a sieving analysis (for particle sizes over 0.125 mm) and laser diffraction (for particle sizes below 0.125 mm). The laser diffraction method only provides a volumetric measure of the particle size distribution which was converted into a mass by assuming grain density of 2.65 g/cm³ (corresponding to Quartz). The curve therefore represents only an approximation.

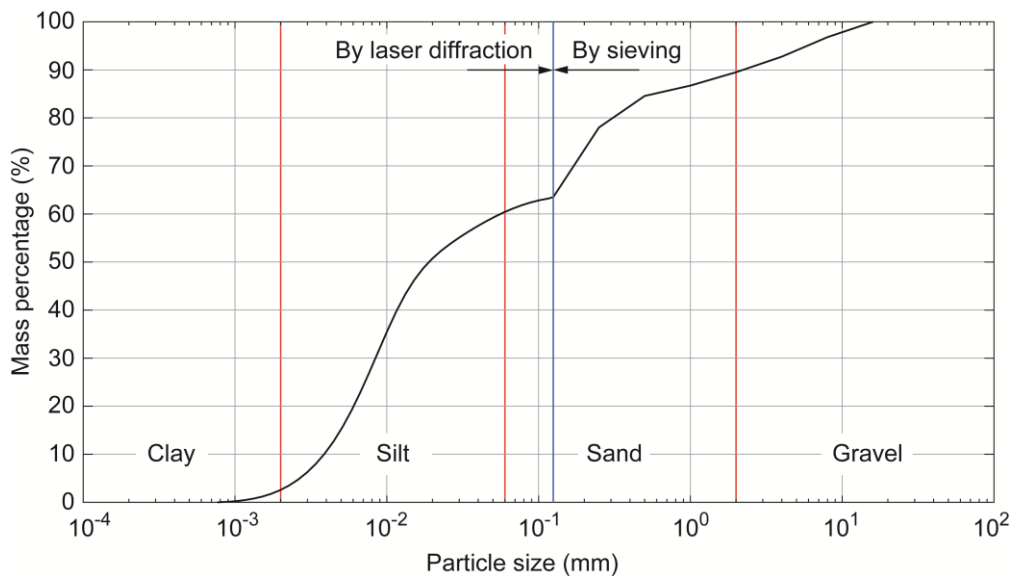


Figure 7-17. Grading curve

7.10 Appendix 7-3: Parameters of the constitutive models

The parameters of the used constitutive models are presented in table 7-2.

Table 7-2. Used parameters of the constitutive models

Linear elasticity				
E	ν	or	K	G
kPa	-		kPa	kPa
20'000	0.3		16'667	7'692

Nonlinear 1				
K	G_0	G_L	x_L	q_L
kPa	kPa	kPa	-	kPa
25'000	20'000	1'200	10.5	20

Nonlinear 2							
K_0	K_L	x_{vL}	p_L	G_0	G_L	x_{sL}	q_L
kPa	kPa	-	kPa	kPa	kPa	-	kPa
80'000	2'000	20	4	20'000	1'200	10.5	20

Nonlinear 3							
a_L	n	K_0	K_L	x_{vL}	G_0	G_L	x_{sL}
kPa	-	kPa	kPa	-	kPa	kPa	-
6	0.61	30'000	1'000	20	7'000	412	11

7.11 Appendix 7-4: Validation of the finite element solution

Figure 7-18 shows the comparison of the strain at the level of cable 02 calculated with the analytical point load solution and with the FE software ABAQUS using linear elasticity. In the FE solution the load was placed on top of a stiff plate with diameter of 0.1 m. The two solutions compare well, the small difference is most likely an effect of the difference between the point load with zero diameter and the small plate. The result validates the FE solution and the use of the elastic point load solution for object identification even if the applied loads are distributed over a small area.

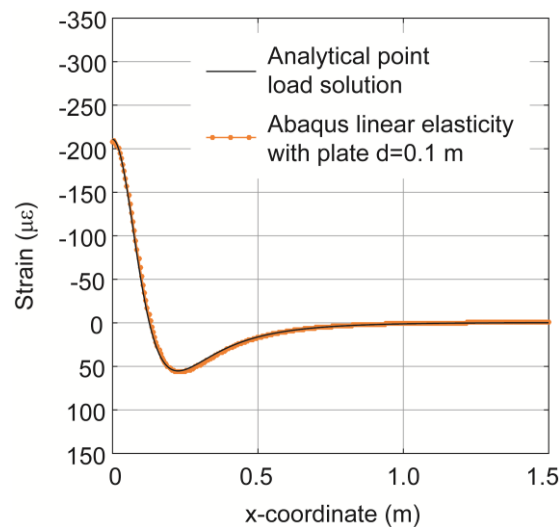


Figure 7-18. Comparison of the horizontal strain at the level of cable 02 calculated with the analytical point load solution and with the finite element method using linear elasticity.

7.12 Acknowledgment

I would like to thank Simon Vogler, Heinz Buschor, Andreas Kieper and René Rohr from the Institute for Geotechnical Engineering at ETH Zurich for their valuable help during the preparation and the conduction of the experiment as well as Dominik Hauswirth for his input on fibre-optic sensors.

7.13 Notation

a_L	Half-axis of the ellipse in the triaxial stress space for the nonlinear 3 model
b	Stiffness ratio
g	Gibbs free energy function
f	Helmholtz free energy function
h	Depth of the fibre-optic cables
m	Exponent in the power law
n	Eccentricity of the ellipse for the nonlinear 3 model
p	Mean pressure
p_L	Limiting mean pressure
p_{ref}	Reference mean pressure
q	Deviatoric stress
q_L	Limiting deviatoric stress
$\text{sgn}(\dots)$	Signum function
x_L	Normalised limiting strain
$y(x)$	Normalised stress-strain function
E	Young's modulus
G	Shear modulus
G_0	Initial (small-strain) shear modulus
G_L	Shear modulus at the limiting stress
G_{ref}	Reference shear modulus
I_1	First invariant of the strain tensor
I_{2D}	Second deviatoric invariant of the strain tensor
K	Bulk modulus
K_0	Initial (small-strain) bulk modulus
K_L	Bulk modulus at the limiting stress
P	Load magnitude
R	Parameter of the logarithmic stress-strain function
α	Parameter of the logarithmic stress-strain function
ε_{ij}	Strain tensor
ε_{xx}	Horizontal strain
$\varepsilon_{xx,meas}$	Measured horizontal strain
$\varepsilon_{xx,calc}$	Calculated horizontal strain
ε_s	Shear strain
ε_v	Volumetric strain
ζ	Substitution used in the coupled nonlinear 3 model
$\mu\varepsilon$	Microstrain, $\mu m/m$
ν	Poisson ratio
ξ	Substitution used in the coupled nonlinear 3 model
σ_{ij}	Stress tensor
χ	Substitution used in the generalized 3D coupled nonlinear 3 model

7.14 References

- Addenbrooke, T.I., Potts, D.M. & Puzrin, A.M. (1997) The influence of pre-failure soil stiffness on the numerical analysis of tunnel construction. *Géotechnique* **47**, No. 3, 693–712.
- Bellotti, R., Jamiolkowski, M., Lo Presti, D.C.F. & O'Neill, D.A. (1996) Anisotropy of small strain stiffness in Ticino sand. *Géotechnique* **46**, No. 1, 115–131.
- Boussinesq, J.V. (1885) *Application des potentiels à l'étude de l'équilibre et du mouvement des solides élastiques*. Gauthiers-Villars, Paris.
- Burland, J.B. & Hancock, R.J.R. (1977) Underground Car Park at the House of Commons, London: Geotechnical Aspects. *The Structural Engineer* **55**, No. 2, 87–100.
- Burland, J.B. (1989) Ninth Laurits Bjerrum Memorial Lecture: 'Small is beautiful'-the stiffness of soils at small strains. *Canadian Geotechnical Journal* **26**, No. 4, 499–516.
- Dyvik, R. & Madshus, C. (1985) Lab measurements of Gmax using bender elements. *Proceedings of the ASCE Convention, Advances in the Art of Testing Soils Under Cyclic Conditions*, V. Khosla, ed., American Society of Civil Engineers, Detroit, Michigan, USA, 186–196.
- Friedli, B., Pizzetti, L., Hauswirth, D. & Puzrin, A.M. (2017) Ground-buried fibre-optic sensors for object identification. *ASCE Journal of Geotechnical and Geoenvironmental Engineering*, in Review.
- Friedli, B. & Puzrin, A.M. (2015). Investigation of Soil Nonlinearity at Very Small Strains Using Ground Buried Fibre Optic Sensors. In *Proceedings of the 6th International Symposium on Deformation Characteristics of Geomaterials*. (eds. Rinaldi, V.A., Zeballos, M.E. & Clariá, J.J.) Buenos Aires, Argentina, 608–614.
- Froggatt, M.E., Gifford, D.K., Kreger, S., Wolfe, M. & Soller, B.J. (2006) Characterization of Polarization-Maintaining Fibre Using High-Sensitivity Optical-Frequency-Domain Reflectometry. *Journal of Lightwave Technology*, OSA, **24**, No. 11, 4149–4154.
- Froggatt, M. & Moore, J. (1998) High-spatial-resolution distributed strain measurement in optical fibre with Rayleigh scatter. *Applied Optics*, **37**, No. 10, 1735–1740.
- Gifford, D.K., Froggatt, M.E., Wolfe, M.S., Kreger, S.T., Sang, A.K., & Soller, B. J. (2007) Millimeter Resolution Optical Reflectometry Over Up to Two Kilometers of Fibre Length. *2007 IEEE Avionics, Fibre-Optics and Photonics Technology Conference*, IEEE, Dallas, Texas, USA, 52–53.
- Green, A. E., & Zerna, W. (1968). *Theoretical Elasticity*. Oxford University Press.
- Hardin, B.O. & Drnevich, V.P. (1972) Shear modulus and damping in soils: Design equations and curves. *ASCE Journal of the Soil Mechanics and Foundation Engineering Division*, **98**, No. 118, 667–692.
- Houlsby, G.T. & Puzrin, A.M. (2007) *Principles of Hyperplasticity*. Springer-Verlag, London.
- Janbu, N. (1963) Soil compressibility as determined by oedometer and triaxial test. *Proceedings of the European Conference on Soil Mechanics and Foundation Engineering*, Vol. 1, Wiesbaden, Germany, 19–25.
- Juarez, J.C., Maier, E.W. & Taylor, H.F. (2005) Distributed fibre-optic intrusion sensor system. *Journal of Lightwave Technology*, **23**, No. 6, 2081–2087.

- Kwon, I.-B., Baik, S.-J., Im, K. & Yu, J.-W. (2002) Development of fibre optic BOTDA sensor for intrusion detection. *Sensors and Actuators A: Physical*, **101**, No. 1–2, 77–84.
- Madsen, C., Bae, T. & Atkins, R. (2007) Long Fibre-optic Perimeter Sensor: Signature Analysis. *Conference on Lasers and Electro-Optics/Quantum Electronics and Laser Science Conference and Photonic Applications Systems Technologies, OSA*, paper PWA5 Baltimore, Maryland, USA.
- Madsen, C.K., Snider, T., Atkins, R. & Simcik, J. (2008) Real-time processing of a phase-sensitive distributed fibre optic perimeter sensor. In *Proc. SPIE 6943, Sensors, and Command, Control, Communications, and Intelligence (C3I) Technologies for Homeland Security and Homeland Defense VII* (eds. Carapezza, E.M.), 694310.
- MATLAB (2016) MATLAB and Optimization toolbox, Release 2016b. The MathWorks Inc., Natick, Massachusetts, United States.
- Messerklinger, S. (2006) *Non-linearity and small strain behaviour in lacustrine clay*. Dissertation No. 16512, ETH Zurich, Switzerland.
- Nikles, M. (2009) Long-distance fibre optic sensing solutions for pipeline leakage, intrusion, and ground movement detection. In *Proc. SPIE 7316, Fibre Optic Sensors and Applications VI*. (eds. Udd, E., Du, H.H. & Wang, A.) International Society for Optics and Photonics.
- Ohde, J. (1939) Zur Theorie der Druckverteilung im Baugrund. *Der Bauingenieur*, 451–459.
- Owen, A., Duckworth, G. & Worsley, J. (2012) OptaSense: Fibre Optic Distributed Acoustic Sensing for Border Monitoring. In *2012 European Intelligence and Security Informatics Conference*. IEEE, Odense, Denmark 362–364.
- Park, J. & Taylor, H.F. (2003) Fibre Optic Intrusion Sensor using Coherent Optical Time Domain Reflectometer. *Japanese Journal of Applied Physics*, IOP Publishing, **42**, No. 6, 3481–3482.
- Puzrin, A.M. (2012) *Constitutive Modelling in Geomechanics*, Chapter: Small Strain Nonlinearity. Springer, Berlin, Heidelberg, 155–166.
- Puzrin, A.M., & Burland, J.B. (1996) A logarithmic stress-strain function for rocks and soils. *Géotechnique*, **46**, No. 1, 157–164.
- Puzrin, A.M. & Burland, J.B. (1998) Non-linear model of small-strain behaviour of soils. *Géotechnique*, **48**, No. 2, 217–213.
- Puzrin, A.M., Friedli, B. & Hauswirth, D. (2013). *Fibre optic based intrusion sensing system*. European Patent Application, EP 2987151 A1.
- Puzrin, A.M., Houlby, G.T., & Burland, J.B. (2001) Thermomechanical formulation of a small-strain model for overconsolidated clays. *Proceedings of the Royal Society A: Mathematical, Physical and Engineering Sciences*, **457**, No. 2006, 425–440.
- Stokoe, K.H. & Woods, R.D. (1972) In Situ Shear Wave Velocity by Cross-Hole Method. *Journal of the Soil Mechanics and Foundations Division, ASCE*, **98**, No. 5, 443–460.
- Taylor, H.F. & Lee, C.E. (1993) *Apparatus and method for fibre optic intrusion sensing*. US Patent, US5194847 A.
- Woods, R.D. (1978) Measurement of dynamic soil properties. *Proceedings of the ASCE Geotechnical Engineering Division Specialty Conference – Earthquake Engineering and Soil Dynamics*, Pasadena, California, USA, 91–78.

8 Conclusions and outlook

8.1 Part A: Earth pressures in landslides

8.1.1 Main results and conclusions

In part A the earth pressures in landslides are investigated. It is shown that the earth pressures in landslides can be assessed as a limit state problem where the soil in the vicinity of a retaining structure or a building is at failure. The investigation of this limit state provides the highest possible earth pressure acting. Knowledge of this limiting pressure is important for the design of new and the assessment of existing structures. Similar to the classical earth pressure theories for stable ground no statement is possible about the evolution of the pressures during the movement of the landslide.

Based on the application of either the static approach or the kinematic approach, lower- or upper-bounds, respectively, are derived. Limit analysis proved to be a suitable tool for the investigation of such limit states as it provides not only a solution which is meaningful but additionally allows formulating a statement about the relation of the solution compared to the exact solution. If the derived earth pressures in landslides are used for the design of new or the assessment of existing structures it is interesting to note that the kinematic method, unlike in almost all other problems, provides solutions on the safe side, as the earth pressures acting on a structure are overestimated.

In chapter 3 the earth pressures acting on a constraining structure in a landslide (that is, a structure stabilising the landslide) are studied using limit analysis. This earth pressure is referred as the 'landslide pressure'. Rigorous upper- and lower-bounds of limit analysis were derived, which are shown to provide the exact solution for the special case of a planar landslide. The derived exact solution coincides algebraically with a solution for another problem derived by (Rankine, 1857), which represents a lower-bound for the passive earth pressure in stable, homogeneous ground with an inclined surface. It is, however, important to note that Rankine's passive earth pressure solution provides a good lower-bound only for special cases but underestimates the passive pressure significantly for steep slopes. While the passive earth pressure increases significantly with increasing slope Rankine's lower-bound decreases.

The influence of wall friction and inclination as well as soil dilatancy and the influence of ground-water on the landslide pressure are discussed, broadening the field of application of the derived solution. The comparison of the landslides pressure solution with existing solutions from the literature (Brandl and Dalmatiner, 1988; Haefeli, 1944) revealed significant discrepancies which are explained by the use of the limit equilibrium method and some simplifying assumptions in the existing solutions. The derived solution can be applied for the design of new retaining structures in landslides and the assessment of existing structures as an earth pressure load acting on the structures. Further it can be used to assess the highest possible stabilising force which can be transmitted from a stabilisation structure into the landslide body. However, it should be noted that in the latter case the upper-bound limit analysis does not provide a solution on the safe side.

In chapter 4 the landslide pressure solution was applied to three selected extensions of the boundary conditions, releasing some geometrical conditions of the landslide and the retaining structure. It was shown that the special case discussed in chapter 3, although using some restrictive assumptions, does also provide good earth pressure values in a wide range of arbitrary inclinations and frictions on the weak slip surface. However, in contrast to the solution in chapter 3 the landslide pressure acting on a retaining structure depends on the wall-friction if the simplifying condition of equal inclination and friction of the slip surface does not hold. The investigation of the closely related problem of a not fully mobilised slip surface in the vicinity of the structure, which is only possible for rigid structures installed before the landslide moved, showed that in such cases the landslide pressures can be significantly higher compared to the fully mobilised case. Regarding the design of the structure, this is a strong argument for compliant structures in landslides. Finally, it was shown that structures which are horizontally pinned but do not reach down to the slip surface are only able to evoke the landslide pressure mechanism if they are embedded deeper than a critical value. This critical embedment, which decreases with increasing slope inclination, can be used as an optimum criterion for the design of landslide stabilisation structures.

In chapter 5 the closely related problem of the earth pressures acting on buildings embedded in the compression zone of a moving landslide (that is, the displacement rates decrease towards the bottom end) are studied using limit analysis and the finite-element method (FEM). The difference in stiffness between a building and the landslide body can lead to a disturbance of the displacement field of the moving soil mass. This disturbance results in an increase of the loads acting on the building until eventually (when failure of the building is excluded) a limit state of the soil is reached. It is shown that in practical cases first a local limit state where the soil in the vicinity of the building fails is reached. Further compression of the landslide later leads to a global failure of the whole sliding body which is similar to the failure used to determine the landslide pressure in chapter 3 but may be altered by the building.

After the local failure is reached the loads on the building do not increase anymore. Therefore the evaluation of this limit state is used to evaluate the ultimate loads acting. Depending on the geometry of the slope and the building, the weight of the building as well as the strength of the soil and the interface between the soil and the building different mechanisms are proposed and evaluated using the kinematic method of limit analysis and the corresponding solutions for the ultimate loads are presented. Note that similar to the landslide pressure in chapter 3 the upper-bound solutions represent a safe estimate for the loads if used for the design and the assessment of the buildings.

Using the FEM it was shown for a case study, which is typical for permanently moving landslides in the Alps, that it is likely to reach the local limit state within the lifetime of a building. Therefore it is concluded that buildings in landslides should be designed in order to withstand the ultimate loads acting at this limit state. For temporary structures, such as construction pits, it may be overly conservative to design against these relatively high loads. The assessment of evolution of the loads over time is not within the scope of this thesis but should be topic of future research.

In general the findings provide an understanding of the most relevant factors which determine the limiting earth pressures in landslides. The developed earth pressure solutions should provide a tool for engineers for the assessment of existing and the safe design of new structures in landslides. The concepts used to determine these earth pressures (based on the investigation of the limit states) may also be applied to cases with other displacement fields (not only structures in the compression zone of constrained landslides) in future research and practice, for example for structures crossing the boundary of a landslide or structures in the extension zone at the top end of a landslide. The derived solutions will hopefully also contribute to codes and regulations dealing with retaining structures and buildings in landslides.

8.1.2 Future research

The developed solutions are based on the plane strain assumption, which at least for long retaining structures is a valid simplification. Other structures in landslides (*e.g.*, bridge piers or buildings) have a limited width perpendicular to the slope. It is known that for example the passive earth pressure is significantly higher in three-dimensional cases due to the larger amount of soil involved in the mechanisms. Therefore it is of high importance to extend the solutions shown here to three-dimensional conditions.

Although this work is based on sound geotechnical concepts it is purely theoretical. Therefore an experimental and field validation of the solutions is of high importance to increase the confidence and allow a broad practical application. Such a validation in the field is however not straight forward since absolute pressures would have to be measured on, for example, a retaining wall in a landslide and it has to be decided at which point in time the limit state is reached.

For the evaluation and the design of temporary structure (*e.g.*, construction pits) the consideration of the landslide displacement rate on the evolution of the loads is important. It is likely that in many cases with moderate displacement rates the loading of such structures is slow and that the derived ultimate loads at the limit state of soil failure are not reached within the lifetime. The evaluation of the load evolution will require a good understanding of the initial stress and displacement conditions of the landslide and the constitutive behaviour of the sliding body and the retaining structure has to be modelled accurately including the staged constructions. From an engineering view it is however more important to design robust structures which can cope with possible differences between the modelling and the reality. The safety of the structure should not be based purely on the correct modelling of such a complex problem.

As existing structures in landslides often show significant structural damage, which is likely to be the result of an underestimation of the landslide induced loads, it is also important to study the structural behaviour of the damaged buildings or retaining structures in particular also regarding their potential retrofitting.

8.2 Part B: Applications of fibre-optic sensors in Geomechanics

8.2.1 Main results

In Part B the application of distributed fibre-optic strain sensors (FOSs) in geomechanics is investigated. Distributed fibre-optic strain sensing with its unprecedented spatial and strain resolution proved to be a suitable tool for the investigation of the mechanical soil behaviour in geotechnical boundary value problems in previous work. Special fibre-optic cables with metal and plastic coatings, developed earlier at the Institute for Geotechnical Engineering at ETH Zurich (Hauswirth, 2015; Hauswirth and Iten, 2010), allow the use of FOSs buried directly in the soil. As with buried FOSs the deformations of the soil in geotechnical boundary value problems can be measured not only on the surface but along of a line within the soil new insight can be gained into the soil behaviour.

FOSs buried in a shallow trench in the ground enable the measurement of the deformations in the ground caused by an object moving on its surface. In chapter 6 a system is proposed which uses such measurements together with inverse analysis for the calculation of the contact force patterns acting between the object and the ground surface. The inverse analysis which is based on a mechanical model of the ground loaded at its free surface (elastic half space, *e.g.*, Boussinesq, 1885) and an algorithm similar to those used in image deblurring. The forward problem of calculating the strain along the FOSs from arbitrary load patterns is presented and it is shown that its discretisation leads to a linear system of equations. The inverse problem is ill-conditioned; therefore a numerical solution using regularisation is proposed and applied.

In a field experiment with ground-buried FOSs the strain caused by different static load patterns was measured. It is shown that the measurements together with the proposed inverse analysis are capable of identifying the load magnitudes and positions of the applied loads accurately. This seems rather remarkable as the ground is made of natural, non-engineered material containing certain non-homogeneity and shows non-linear mechanical behaviour.

The combination of such a system with high-temporal frequency sensing (which is already commercially available for small lengths) enable the identification of dynamic loads on the ground surface. This would open up a path for practical applications such as perimeter security systems with identification of the intruder, biodiversity measurements (from step lengths and the contact force magnitudes different species crossing could be discriminated) and dynamic weigh-in-motion systems for road traffic and airports.

In the field experiment significant non-linear behaviour of the soil at the very small strains induced by small surface loads (corresponding to a mass of 10 kg – 100 kg) was observed. This nonlinearity is further explored in chapter 7. The ground surface was loaded on a small plate in steps and the corresponding strains along the buried FOSs were measured. The results reveal that the stiffness of the soil decreases significantly with increasing load with the highest rate of decrease at very small strains. This effect is known in geotechnics as small strain nonlinearity. The measurements using FOSs represent a direct measurement of this nonlinearity in a boundary value problem.

The experiment was modelled using the finite-element method with four different constitutive models. Besides the linear isotropic elastic model, three non-linear models were investigated.

From the four applied models linear elasticity captures the ‘shape’ of the measured strain profiles best but is not able to capture the observed non-linearity. The response of the three other applied non-linear elastic models is discussed and it is shown that additionally to the non-linear deviatoric behaviour also the non-linear volumetric behaviour is important to capture the field measurements. A validation of the used constitutive models and their parameters against triaxial test results with local strain measurements shows good agreement of the non-linear behaviour. The soil behaviour is, however, stiffer in the triaxial tests. This is most likely the result of different levels of confining stress compared to the field conditions.

In general FOSs, installed directly into the soil, represent a unique possibility to study the soil behaviour in geotechnical boundary value problems from very small to mid-range strains.

8.2.2 Future research

The combination of the proposed system for surface object identification with high temporal frequency sensing opens up possibilities for several applications. To this date such sensing systems are only able to measure lengths of tens of meters with the necessary high spatial and strain resolution. With future improvements of fibre-optic interrogators the path towards further applications should be open. Amongst these applications the identification of specific objects from the different load patterns is crucial and should be pursued for example using a large set of classified measurements conducted with different objects at the surface and machine learning. As the use of high frequency measurements requires an inverse analysis of many measurement frames the speed of the algorithm becomes important. This is in particular the case in the application of a perimeter security system, where (almost) real-time results are a prerequisite.

The influence of environmental changes such as different weather, moisture content of the soil and temperature on the mechanical behaviour of the soil should be studied. The change of the mechanical behaviour might influence the robustness and accuracy of the inverse analysis of the surface loads. The study of these effects would, for example, require the loading of the ground surface and measurements along buried FOSs over a long period of time with parallel measurement of temperature and soil moisture.

In the conducted field experiments some small irreversible strains after load removal have been observed (no data published in this thesis). This unloading and also subsequent reloading and their effect on the inverse analysis need to be investigated. The soil behaviour in the loading and unloading cycles could be modelled using kinematic hardening models (*e.g.*, Puzrin and Burland, 1998). The comparison with the experimental data could serve as a validation of such models in a geotechnical boundary value problem. Furthermore it was observed that the irreversible strains diminish over time due to potential rate effects of the soil. This could be further explored with the objective of determining the time required to reach a new ‘virgin’ state (that is, a state where the soil behaves like in first loading) after unloading and whether such a state does even exist.

Another interesting future research would be to study the long-term behaviour of the buried fibre-optic cables. The choice of the cable for a commercial system is very important to ensure a reliably working system with no failure due to cable breakage caused, for example by rodents like mice. Further, the evolution of the plastic coating over time and whether the strain transfer to the fibre in the core is persistently working is not fully clear and needs investigation.

8.3 References

- Boussinesq, J.V. (1885) *Application des potentiels à l'étude de l'équilibre et du mouvement des solides élastiques*. Gauthier-Villars, Paris, France.
- Brandl H. & Dalmatiner J. (1988) *Brunnenfundierungen von Bauwerken in Hängen (insbesondere Brücken)*. Schriftenreihe Strassenforschung des Bundesministeriums für wirtschaftliche Angelegenheiten. Wien, Heft 352, Vienna, Austria.
- Haefeli R. (1944) Zur Erd- und Kriechdruck-Theorie. *Schweizerische Bauzeitung* **124**, 256–260.
- Hauswirth, D. (2015) *A study of the novel approaches to soil displacement monitoring using distributed fibre optic strain sensing*. Dissertation No. 22282, ETH Zurich, Switzerland.
- Hauswirth, D., Iten, M. & Puzrin, A. M. (2010) Fibre optic cable an micro-anchor pullout tests in sand, In *Proceedings of the 7th International Conference on Physical Modelling in Geotechnics (ICPMG 2010)* (eds. Springman, S., Laue, J. & Seward, L.), 337-342, Zurich, Switzerland.
- Puzrin, A.M., & Burland, J.B. (1998) Non-linear model of small-strain behaviour of soils. *Géotechnique*, **48**, No. 2, 217–213.
- Rankine W.J.M. (1857) On the Stability of Loose Earth. *Philosophical Transactions of the Royal Society of London* **147**, 9–27.

Curriculum Vitae

Personal details

Name: Balz Friedli
Address: Speerstrasse 34
8038 Zürich
Switzerland
Phone: +41 44 633 37 47
Email: balz.friedli@igt.baug.ethz.ch
Date of birth: 31.10.1986
Nationality: Swiss

Education

2012-2018 PhD in Geotechnical Engineering, ETH Zurich
2015-2016 CAS in Spatial Information Systems, Geoinformatics, ETH Zurich
2010-2012 MSc in Civil Engineering, ETH Zurich
2006-2009 BSc in Civil Engineering, ETH Zurich

Employment

2012-2018 Research assistant, Institute for Geotechnical Engineering, ETH Zurich
2010-2012 Civil Engineer, Fürst Laffranchi Bauingenieure (20%)
2009-2010 Intern, Civil Engineer, Fürst Laffranchi Bauingenieure

Language skills

German: Native language
English: Full professional proficiency
French: Limited working proficiency